UNIVERSITÀ DEGLI STUDI Dl NAPOLI FEDERICO II

D.I.I. – DIPARTIMENTO DI INGEGNERIA INDUSTRIALE

TESI DOTTORATO IN

INGEGNERIA INDUSTRIALE – XXXII CICLO

DEVELOPMENT OF ADVANCED ALGORITHMS BASED ON PHYSICAL THERMAL MODELS FOR THE ESTIMATION OF TYRE DYNAMIC BEHAVIOUR BY SMART TYRE DEVICES DATA

RELATORE
PROF. ING. RICCARDO RUSSO
PROF. ING. FRANCESCO TIMPONE

DOTTORANDO
ING. FRANCESCO CARPUTO

COORDINATORE
PROF. ING. MICHELE GRASSI

TUTOR AZIENDALE
P.H.D ING. ANDREA ZORZUTTI
PIRELLI S.P.A
ING. MASSIMILIANO SALLUSTI
PIRELLI S.P.A
ING. DIEGO MINEN
VI-GRADE

2020

Acknowledgments

The work described in the following pages is the result of an extremely stimulating PhD program thanks above all to all the people met during the entire period.

In particular, a special thanks goes to the Vehicle Dynamics group of the industrial engineering departments that assisted me during the entire PhD course.

I would like to thank Pirelli's Cyber^{TM} tyre group for their collaboration in this thesis project and for giving me the opportunity to work on a very stimulating project.

Thanks go to Vi-Grade with whom the PhD course ended.

Finally, a thank you to all the colleagues and friends who have supported me during these years.

Abstract

The theme of this work is part of the broad context of the industrial research development described by the challenges of the Horizon 2020 society, with particular reference to the "Digital Agenda, Smart Communities, Intelligent Mobility Systems" line.

It is inserted in the following areas:

- Intelligent urban mobility systems for logistics and people;
- Safety systems of the urban environment, environmental monitoring and prevention of critical or risk events;
- Embedded electronic systems, intelligent sensor networks, internet of things.

In particular, the huge technological progress achieved in past few years has contributed to give a great drive towards the development of advanced safety and monitoring systems for automotive applications.

In a context of great revolution in the transport system that the inhabitants of the planet are preparing to live, the primary targets are the raising of road safety standards and the creation of a vehicular network for the sharing of traffic information and the dynamic state of the car park.

The automotive sector is experiencing a phase of profound change, fuelled by the progressive establishment of embedded systems oriented to the well-known concept of smart and sustainable mobility, with the target set by autonomous driving systems on the horizon.

The object of the study are the innovative tyres called "smart tyres", characterized by a structure equipped with integrated sensors useful for acquiring information on the vehicle and on the road.

The smart tyre is an element of great innovation as it allows to increase the level of interaction between vehicle and driver and allows to observe the phenomena of tyre-road interaction. In fact, the availability of a measuring element located in the contact area, provides numerous points of use, both in science and industry such as monitoring of the tread wear level, evaluation of the friction level, monitoring of user behaviour and manoeuvres (aimed at studying traffic dynamics), etc.

These models allow great progress both in order to increase performance, but above all to safeguard the safety of passengers and pedestrians. Thanks to the continuous monitoring offered by a sensorized car park, it is possible to have information about, for

example, soil roughness mapping (useful in the planning of maintenance interventions), the management of emergency assistance in the event of accidents, the supply of intelligent traffic light networks, the offer of insurance rates based on the most frequent itineraries and driving style.

The development of physical and real-time algorithms would provide the additional level of predictability that such systems need in view of large-scale deployment.

The development of real-time simulation models related to the tyre / road interaction, the identification of the vehicle subsystems with which the smart tyres are appropriate to interact, as well as the evaluation of these interactions are aimed at optimizing the dynamic behaviour of the vehicle.

The integration of multiple subsystems will represent one of the added values providing important insights regarding the communication methodologies between physical systems and the related virtual representations.

The traditional approaches SIL (software-in-the-loop) and HIL (hardware-in-the-loop) will evolve in the direction of a scenario that foresees the human being as a central element in the testing and validation chain, arriving at configurations of the DIL type (driver-in the-loop). In perspective it is also expected that the driver can be replaced by an autonomous control system.

Table of contents

Objectives and Methods

The work was carried out in collaboration with Pirelli tyre S.P.A (company on the Italian territory) and with VI-grade (company on the foreign territory).

Nowadays, being safety and stability two of the main branches of research in which the automotive field is putting effort. International standards for road safety have become more and more strict and inflexible when it comes to road safeness.

The technological development of the last years has allowed electronics to become one of the main fields of innovation and the automotive sector makes use of electronics nearly into all its branches allowing a great improvement, both in terms of quantity and quality, of the safety equipment for vehicles.

The ADAS denomination (Advance Driver Assistance System) gathers all the systems which can improve the feeling of potentially dangerous situations and to interact with other active controls of vehicles.

The necessity for ADAS is generated by the need to produce safer vehicles and to reduce the number of road fatalities. Moreover, those same systems are becoming increasingly more powerful and more invasive.

Pirelli Tyres S.p.a operates into this scenario providing cars with high quality and high performance tyres which are also employed as an" intelligent" vehicle component with the aim of improving both active safety and manoeuvrability.

The so called Cyber™Tyre project carried out by Pirelli is based on the basic principle of providing the tyre with sensors that can exchange information and interact with the active safety controls of the vehicle.

The Cyber™Tyre system developed by Pirelli can surely be considered as a unique part of ADAS environment: in fact, by means of the installation of sensors into the tyre, the company aims to provide information regarding the tyre-road contact area with the goal of interacting with active control systems and providing useful information to the driver in terms of safety and vehicle dynamics.

This system allows the knowledge of the main dynamic entities featuring tyre-road interaction by means of the installation of suitable sensors inside the tyre.

Thanks to this solution Pirelli is now able to provide important information about parameters that are related to the contact area such as contact forces, contact patch length, deformed radius, center of gravity position and surface texture changes.

The current thesis work lies into this context and it is the product of a cooperation project between University of Naples, Pirelli Tyres S.p.a and VI-grade.

Part of this work is placed into the Cyber™Tyre context and it consists in the definition of a strategy for the introduction of thermal dependence in the numerical model for the calculation of features currently implemented, such as for example the estimates of contact forces. The objective is to increase the reliability of the estimate in all conditions, especially in cold tyre conditions.

Subsequently, the activity focused on the creation of real-time simulation models linked to the tyre/road interaction and to the identification of the vehicle subsystems with which the smart tyres are appropriate to interact, as well as to the evaluation of such interactions aimed at optimization of the dynamic behavior of the vehicle.

In fact, the validation of ADAS algorithms involves a significant number of realistic test cases and therefore would require so much time to make it incompatible with any significant time-to-market or return on investment of any new vehicle development plans. The complete simulation of the system, as soon as possible, is substantially mandatory.

VI-Grade produces high performance dynamic driving simulators. Given its proven experience in the development and implementation of complex simulative architectures, it can provide "driver in the loop" systems within which to test and validate the intelligent devices.

In particular, the work carried out in this area concerns the effects induced by temperature variations on the tyre/road interaction curves, and consequently on the dynamics of the global vehicle.

Specifically, the phases of the activity in question will concern the parameterization of vehicle models through which to analyze the data coming from the on-board control unit and from the smart tyres, obtaining experimental characterizations concerning the pneumatic-road interaction without the use of expensive and large test benches for tyre testing.

The study of the correlation between temperature, grip, wear and performance offered by tyres in the testing phase will lead to the development of physical models that reproduce trends and quantitative aspects, allowing the implementation of these

formulations and the consequent reproduction, with the many related advantages to be able to predict local distributions of temperature, friction coefficient and degree of removal of treads, giving life to an essential tool for the analysis, simulation and prediction of the complex phenomena inherent to the interaction between the vehicle and the ground.

The next lines describe the thesis structure and provide a brief description of each chapter.

- **Chapter 1 – Tyre Structure and Vehicle Dynamics:** In this chapter the structure of the tyre is analyzed by giving a brief description of its chemical composition. Furthermore, hints of vehicle dynamics are given, especially about tyre-road interactions.
- **Chapter 2 – The Temperature influence on the tyre:** In this chapter, a short description on the behaviour of viscoelastic materials will be done. In particular, how the temperature and frequency influence their mechanical properties will be discussed. Furthermore, the heat generation modes in a tyre (the friction power and strain energy loss) will be presented.
- **Chapter 3 – The Cyber™Tyre system description:** This chapter is dedicated to the hardware system description making a brief description of its main components. Subsequently, the procedure for estimating the vertical load is described as well as the need to introduce the thermal dependence in the estimation of such features.
- **Chapter 4 – The thermal model:** In the first part of this chapter, the standard thermal model UniNa is described. Subsequently the development of a suitable thermal model for the Cyber™Tyre system will be described. Finally, a whole series of indoor and outdoor tests will be presented in order to validate this model.
- **Chapter 5 – Correction of the vertical load estimation:** This chapter is dedicated to the strategies development for the introduction of thermal dependence in vertical load estimation. Various strategies are developed and compared in order to choose the one that most satisfies conditions of robustness, efficiency and ease of implementation.
- **Chapter 6 – The Temperature influence on Tyre/road interaction curves:** This work is chapter is dedicated to a sensitivity analysis of the influence of a series of quantities on the vehicle dynamic behavior. Numerous parameters are

considered (tread wear level, specific thermal conductivity and heat of the various layers etc.) which would require many tests. The work was carried out in collaboration with VI-grade which provides a simulation environment called *VI-Car Real Time*.

VI-CarRealTime provides a real-time vehicle simulation environment where the same simplified vehicle model can be used by vehicle dynamics and controls engineers to optimize vehicle and control system performance.

Chapter 1

Tyre Structure and Vehicle Dynamics

1.1 Introduction

The tyre is the element of contact between the vehicle and the road and is the most important component in the dynamics of the vehicle since the performance of the vehicle is strongly influenced by its characteristics.

Depending on their application, different constructive composite solutions are adopted employing significant quantities of canvas, steel wire and fabric reinforcements.

The tyres must perform some fundamental tasks, such as providing load capacity, ensuring the damping effect, correctly transmitting the driving and braking torques, providing cornering force and generating minimum noise and minimal vibrations [1] [2] [3].

It is an under pressure, inextensible and deformable casing, made of composite material of polymeric matrix (vulcanized rubber and additives such as carbon black and silica) with reinforcement plies of steel or synthetic fibers. It has a shape of a solid of revolution (toroid ring) and is built on an axially symmetrical element called rim.

The most common tyre in automotive industry is the tubeless type, lacking inner tube. The tyre and the rim of the wheel form an airtight container to seal the air as the tubeless tyre has an inner lining of impermeable halo butyl.

1.2 The Structure

The parts constituting a modern tubeless tyre are the following [4] [5] [6]:

- The tread: the most external surface of the tyre that is exposed to the road surface. It consists of a rubber compound, commonly styrene-butadiene (SBR) copolymers, whose surface is crossed by a pattern that must ensure a good grip in every condition.

- The shoulder: the zone between the edge of the tread and the beginning of the sidewall. It ensures a good heat dispersal.
- The sidewall: the area between the shoulder and the bead bundle and is the part that protects the carcass by lateral impacts. It is a thin rubber layer that gives rigidity to the tyre and improves the ride quality.
- The bead: the element that allows the tyre to remain fixed on the rim, preventing relative rotations. The core of a tyre bead is made up of several individually rubber coated steel wires formed into a hoop, that is then provided with a rubber apex. It is a very critical element from the mechanical point of view because every action that the tyre exchanges with the road is transferred to the vehicle through it. Therefore, it is subject to high levels of stress due to its small size.
- The inner liner: the area placed on the inner surface of the tyre. It consists of a special compound useful for improving the air retention.
- The belt plies: a strong reinforcement found between the tread and the carcass in a radial or belted bias tyre. It stabilizes the tread area and provides impact resistance. Varying the belt width and angles affects vehicle ride and handling characteristics.
- The carcass: the resistant structure, which is made up of by one or more layers of plies situated under the tread or under the belt plies.

They are shown in Figure 1.1.

Body plies arrangement gives the name to the structure of the tyre: nowadays the most commonly employed structure is the radial one, in which the carcass is composed of one or more plies disposed through the meridian planes of the toroid [5]. The radial tyre is characterized by better grip, more stability and a higher braking efficiency, acting as safer than conventional ones; they allow a greater level of comfort and a greater energetic saving.

The other type of structure, still used in some applications for trucks, trailers and farm implements, is called diagonal or bias because the plies cross on the carcass being disposed according to proper inclinations respect to equatorial plane called "crown angles". In this type of tyre, the belt plies are absent, making it easy to distinguish the different kinds of tyres.

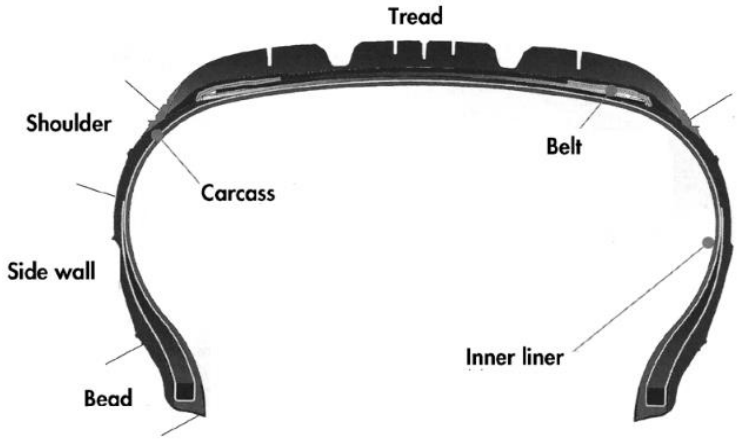

Figure 1.1 – Tyre structural component [7]

1.3 The Materials

There are more than a dozen specially formulated compounds that are used in the interior of the tyre. The basics ingredients are the following:

- Polymers are the backbone of rubber compounds. They consist of natural or synthetic rubber.
- Fillers reinforce rubber compounds. The most common filler is carbon black although other materials, such as silica, are used to give the compound unique properties.
- Softeners: Petroleum oils, pine tar, resins and waxes are all softeners that are used in compounds principally as processing aids and to improve tack or stickiness of unvulcanized compounds.
- Antidegradants: Waxes, antioxidants, and antiozonants are added to rubber compounds to help protect tyres against deterioration by ozone, oxygen and heat.
- Curatives: During vulcanization or curing, the polymer chains become linked, transforming the viscous compounds into strong, elastic materials. Sulfur along with accelerators and activators help achieve the desired properties.

Considering the many polymers, carbon blacks, silicas, oils, waxes and curatives, plus specialty materials such as colorants, adhesion promoters, and hardeners, the variety of compounds available is enormous. It is important to keep in mind that modifying a property affects the performance of the tyre in a specific area: making the tyre efficient on a wet track makes it less efficient in terms of fuel economy or on a dry road. The compounds need to be engineered or balanced to meet different requirements.

A tyre's reinforcing materials are the predominant load carrying members of the cord-rubber composite. They provide strength and stability to the sidewall and tread as well as contain the air pressure. The most used are the following:

- **Nylon** type 6 and 6,6 tyre cords are synthetic long chain polymers produced by continuous polymerization/spinning or melt spinning. The most common usage in radial passenger tyres is as cap, or overlay ply, or belt edge cap strip material, with some limited applications as body plies.
- **Polyester** tyre cords are also synthetic, long chain polymers produced by continuous polymerization or melt spinning. The most common usage is in radial body plies with some limited applications as belt plies.
- **Rayon** is a body ply cord or belt reinforcement made from cellulose produced by wet spinning. It is often used in Europe and in some run-flat tyres as body ply material.
- **Aramid** is a synthetic, high tenacity organic fiber produced by solvent spinning. It is 2 to 3 times stronger than polyester and nylon. It can be used for belt or stabilizer ply material as a light-weight alternative to steel cord.
- **Steel cord** is carbon steel wire coated with brass that has been drawn, plated, twisted and wound into multiple-filament bundles. It is the principal belt ply material used in radial passenger tyres.
- **Bead** wire is carbon steel wire coated with bronze that has been produced by drawing and plating. Filaments are wound into two hoops, one on each side of the tyre, in various configurations that serve to anchor the inflated tyre to the rim.

1.4 The Mechanics

1.4.1 Reference System

The study of the mechanics of tyres is of fundamental importance to the understanding of the performance and characteristics of ground vehicles. To describe the behaviour of a tyre and the forces and moments acting on it, it is necessary to define an axis system that serves as a reference for the definition of various parameters [8]. In order to describe the tyre-road interaction and its force system, a flat ground and attach a Cartesian coordinate frame at the center of the tyre print are assumed, as shown in the figure 1.2.

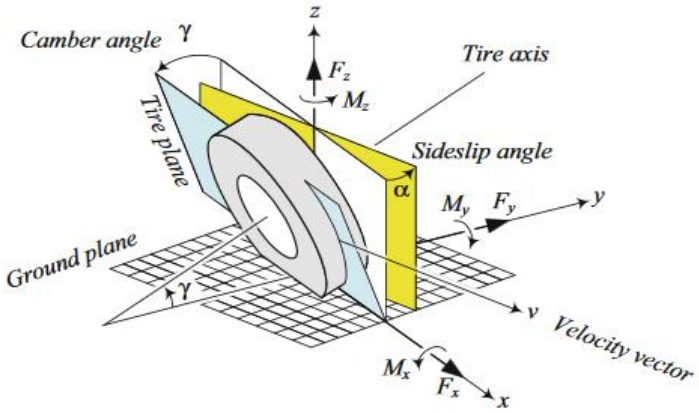

Figure 1.2 – ISO tyre reference system [9]

The origin (O) of the axis system it is located in the centre of the contact patch. The origin is the point defined by the intersection of three planes: horizontal (defined by xOy), longitudinal (defined by xOz) and vertical (defined by yOz).

The x-axis is contained in the wheel plane and it's parallel with the longitudinal axis of the vehicle. The positive direction of the x-axis is pointing towards the front of the vehicle. The *z* -axis is perpendicular to the ground and upward, and the *y*-axis makes the coordinate system a right-hand triad.

The tyre orientation is defined by two angles: the *camber* angle γ and the *sideslip* angle α.

The *camber* angle is the angle between the tyre-plane and the equatorial plane passing through the *x-axis*. The *sideslip* angle is the angle between the *x-axis* and the velocity vector *v*. To better understand the meaning can be useful to observe the figure 1.3.

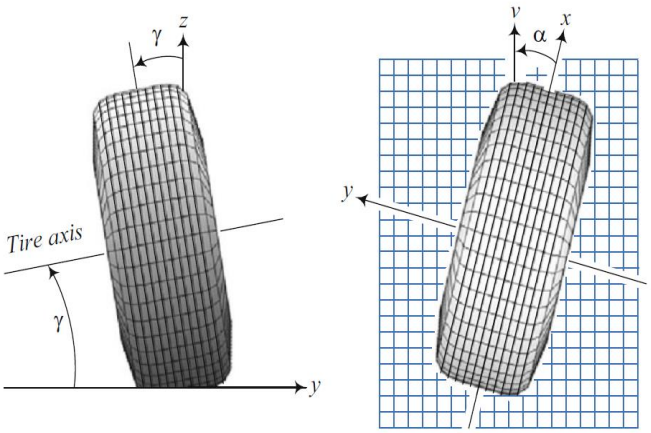

Figure 1.3 – Camber and sideslip angles [9]

The resultant force system that a tyre receives from the ground is assumed to be located at the center of the tyre-print and can be decomposed along x, y, and z axes.

Therefore, the interaction of a tyre with the road generates a three-dimensional force system including three forces and three moments, as shown in figure 1.3 [8] [9].

- *Longitudinal force Fx*. It is the force acting along the *x -axis*. Longitudinal force is also called forward force. The longitudinal force $Fx > 0$ if the vehicle is accelerating otherwise, if it is breaking $Fx < 0$.
- *Normal force Fz*. It is the vertical force, normal to the ground plane. Normal force is also called vertical force or wheel load. If the resultant force is upward $Fz > 0$.
- Lateral force *Fy*. It is the force, tangent to the ground and orthogonal to both *Fx* and *Fz.* The resultant $Fy > 0$ if is in the *y-axis* direction.
- *Roll moment Mx*. It is the longitudinal moment about the x *-axis*. The roll moment is also called the bank moment, tilting torque, or overturning moment. The moment $Mx > 0$ if it tends to turn the tyre about the *x -axis*.
- *Pitch moment My*. It is the lateral moment about the y-*axis*. The pitch moment is also called rolling resistance torque. The moment $My > 0$ if it tends to turn the tyre about the *y-axis* and moves it forward.
- *Yaw moment Mz*. It is the upward moment about the *z-axis*. The yaw moment is also called the aligning moment, self-aligning moment, or bore torque. The moment $Mz > 0$ if the tyre tends to be turned about the *z -axis*.

Another reference system can be used in the automotive field and is the coordinate system adopted by the *Society of Automotive Engineers SAE*. It is shown in figure 1.4.

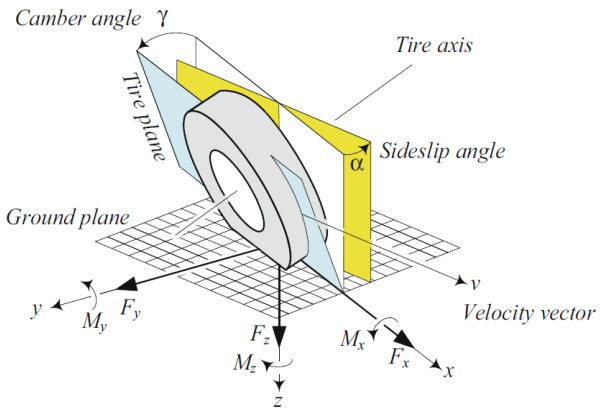

Figure 1.4 – SAE tyre reference system [9]

The *x-axis* is at the intersection of the tyre-plane and the ground plane. The *z-axis* is downward and perpendicular to the tyre-print. The *y-axis* is on the ground plane and goes to the right to make the coordinate frame a righthand frame.

The choice of one or the other reference system is indifferent if proper attention is paid to the signs of the interactions that are opposed between the two tyre coordinate systems.

1.4.2 Kinematics

In order to describe the wheel motion, the quantity called slip is used [10] [1] [11] [3] [12]. The slip ratio is different for the case when the vehicle is braking or accelerating, as given by following relationship:

$$s_x = \begin{cases} 1 - \dfrac{v_x}{\Omega r_r} & \Omega r_r > v_x \quad 0 < s_x < 1 \quad acceleration \\ \dfrac{\Omega r_r}{v_x} - 1 & \Omega r_r < v_x \quad -1 < s_x < 0 \quad deceleration \end{cases} \tag{1.1}$$

where v_x is the *x-axis* component of the wheel centre velocity, Ω is the angular velocity of the wheel, and r_r is the tyre rolling radius.

The quantity Ωr_r is defined pure rolling velocity and matches with the wheel centre velocity as soon as the tyre works in pure rolling conditions.

The quantity s_x is called *longitudinal slip* and it is possible to differentiate the following cases [13]:

- Wheel working in pure rolling condition: there are any differences between the wheel centre and each rim point velocity.

$$s_x = 0 \iff \Omega r_r = v_x$$

- Wheel working in global slip condition (traction phase): the tyre rotates among the wheel axis, but the vehicle does not move forward.

$$s_x = -\infty \iff v_x = 0$$

- Wheel working in global locking condition (braking phase): the tyre behaves as a rigid body during the vehicle-braking phase.

$$s_x = -1 \iff \Omega r_r = 0$$

Similarly, it is possible to define the lateral slip angle as:

$$s_y = \frac{v_y}{v_x} = \tan\alpha \approx \alpha \tag{1.2}$$

However, considering what happens in the contact patch, the tyre tread usually works in pseudo – sliding condition.

Actually, the tread of a tyre is deformable, whereas its belt is not stretchable. Consequently, for example, when a vehicle brakes, the road surface pulls the contact

patch backwards, but only the tread is distorted. The tread blocks recline, and this outcomes in a relative movement between the bottom of the rubber block, in contact with the road surface, and the belt. This is the shear phase (or pseudo – sliding), which occurs at the leading edge of the contact patch. [14]

As the rubber tread block gets closer to the trailing edge of the contact patch, the stress increases and the rubber block, whilst remaining sheared, goes into effective sliding condition with the road surface. This means that a mismatch in the velocity value occurs between the points of the tread in contact with the road and the road surface ones.

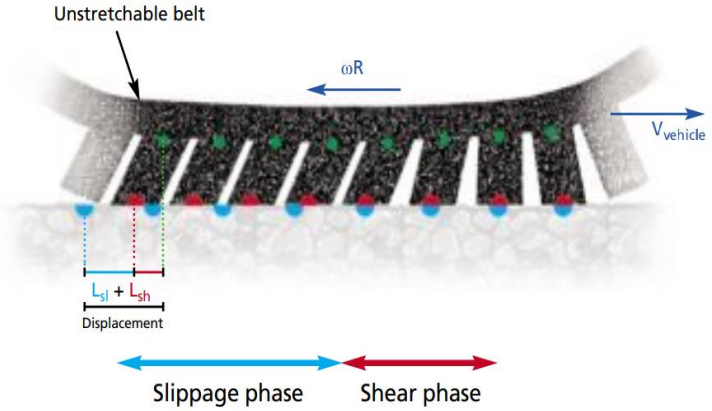

Figure 1.5 – Tyre in pseudo - sliding.

1.4.3 Dynamics

The vehicle performances are highly influenced by the grip and the deformability of the tyres: this underlines the importance to study the interactions between the tyre and the road and what forces are involved during the motion.

The tyre is subjected to three different force systems during its motion [4] [15]:

- The *gravitation field*, to which every system on the Earth is subjected.
- The *aerodynamical forces field*, that is generated by the fluid in relative motion respect the vehicle.
- The *tyre-road interactions*. They generate because of the application of a machine or brake torque about the axis and a force on the centre of each wheels. This system of forces is transmitted by the tyre to the ground through the contact patch.

In the vehicle dynamics and in particular in the tyre road contact the study of the interactions becomes of fundamental importance. Regardless of the degree of roughness of the road, the distributed normal and tangential loads in the contact patch yield a resultant force ***F*** and a resultant torque vector ***M*** [1]***:***

$$\begin{cases} \boldsymbol{F} = F_x\,\boldsymbol{i} + F_y\,\boldsymbol{j} + F_z\,\boldsymbol{k} \\ \boldsymbol{M} = M_x\,\boldsymbol{i} + M_y\,\boldsymbol{j} + M_z\,\boldsymbol{k} \end{cases} \tag{1.3}$$

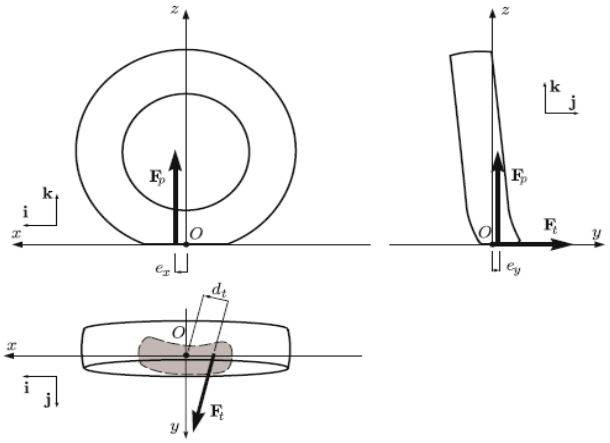

Figure 1.6 – Forces acting on the tyre from the road [1]

Commonly, the forces system 1.3 is schematized with two perpendicular forces:

$$\begin{cases} \boldsymbol{F_t} = F_x\,\boldsymbol{i} + F_y\,\boldsymbol{j} \\ \boldsymbol{F_p} = F_z\,\boldsymbol{k} \end{cases} \tag{1.4}$$

so that:

$$\begin{cases} M_x = F_z\,e_y \\ M_y = -F_z\,e_x \\ M_z = \sqrt{F_x^2 + F_y^2}dt = |\boldsymbol{F_t}|dt \end{cases} \tag{1.5}$$

Here the forces *Fx*, *Fy*, and *Fz* are separately analyzed, with particular attention to the dependence on the grip coefficient.

Longitudinal force F_x

The longitudinal force is strongly linked to the acceleration or braking of the vehicle, therefore to the longitudinal dynamics. The longitudinal force is generated at the tyre-print (or contact patch) when a moment is applied to the spin axis of the tyre and a slip ratio occurs. The forward force is proportional to the normal load *Fz* [9] [8]

$$\boldsymbol{F_x} = F_x\,\boldsymbol{i} \tag{1.6}$$

$$F_x = \mu_x(s)F_z \tag{1.7}$$

In the equation 1.7 μ_x is the *longitudinal grip coefficient* and is function of the *slip ratio s*, as shown in the figure 1.6.

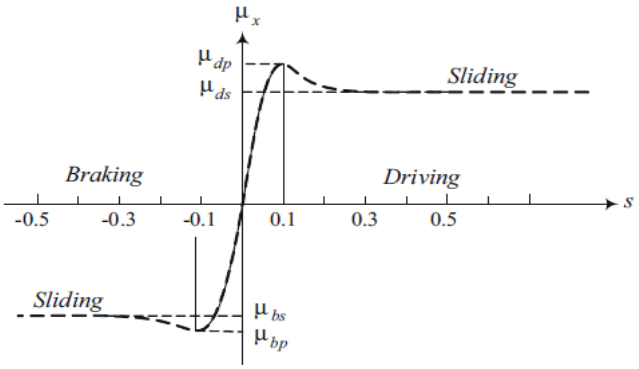

Figure 1.7 – Longitudinal grip coefficient as a function of slip ratio s, in driving and braking [8]

The grip coefficient reaches a driving peak value μ_{dp} at $s \approx 0.1$, before dropping to an almost steady-state driving slide value μ_{ds}. The grip coefficient $\mu_x(s)$ may be assumed proportional to *s* when *s* is very small:

$$\mu_x(s) = C_s\, s \tag{1.8}$$

Where C_s is the *longitudinal slip coefficient*.

The tyre will spin when $s \geq 0.1$ and the grip coefficient remains almost constant. The same phenomena happen in braking at the values μ_{bp} and μ_{bs}. The frictional force F_x between a tyre and the road surface is a function of normal load F_z, vehicle speed v_x, and wheel angular speed Ω. In addition to these variables there are several parameters that affect F_x, such as tyre pressure, tread design, wear, and road surface conditions. It has been determined empirically that a contact friction force of the form $F_x = \mu_x(\Omega, v_x)F_z$ can model experimental measurements obtained with constant v_x, Ω.

A simplified model is usually employed in computer calculation because is safe and exact enough; it is illustrated in figure 1.8 [8] [9].

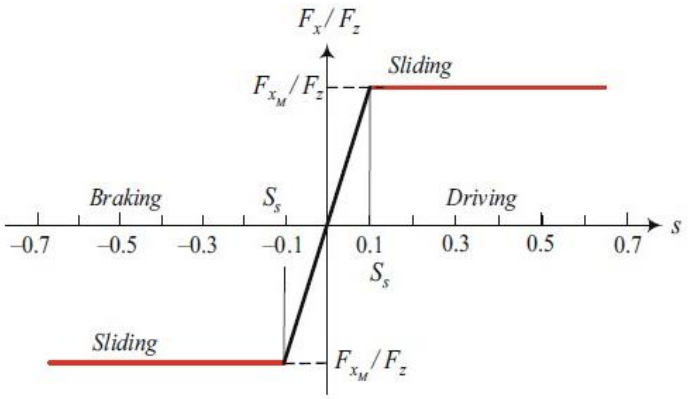

Figure 1.8 – The simplified model of longitudinal tyre force Fx/Fz in vehicle dynamics [8]

This model can be expressed by the following equations:

$$\frac{F_x}{F_z} = \begin{cases} C_s\, s, & -S_s \le s \le S_s \\ \dfrac{F_{xM}}{F_z} = C_s S_s = \mu_x s & s > S_s \; or \; s < -S_s \end{cases} \tag{1.9}$$

In the figure 1.9 is illustrated the free-body diagram of a tyre [8]. In *x-direction* the longitudinal force F_x and the rolling resistance force F_R can be noticed. In *z-direction* the normal load F_z is balanced by the ground reaction while the torque T is applied in the *y-direction.*

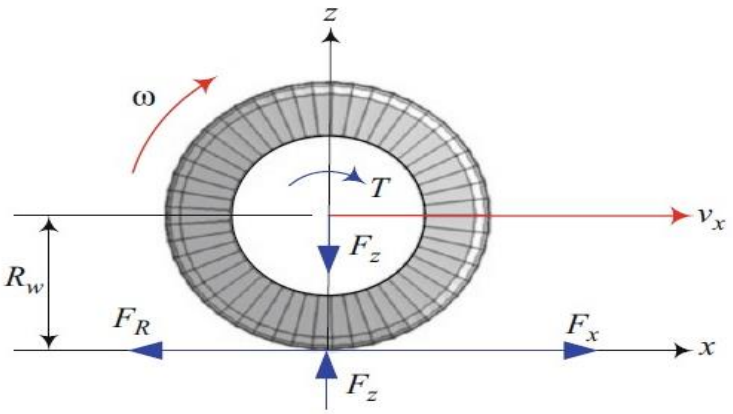

Figure 1.9 – Free-body-diagram of a wheel [8]

The motion equations are:

$$\begin{cases} m_w\, \dot{v}_x = F_x - F_R \\ I_w \dot{\omega}_w = T - (F_x - F_R) R_w \end{cases} \tag{1.10}$$

where m_w is the wheel mass, ω_w is the wheel angular velocity, I_w is the mass moment of the wheel and R_w is the tyre effective radius.

Lateral force F_y

The tyre motion path on the road makes an angle α, the *sideslip angle* with respect the tyre-plane, under a vertical load F_z and a lateral force F_y. The angle is proportional to the force F_y [8]:

$$\boldsymbol{F_y} = F_y \boldsymbol{j} \tag{1.11}$$

$$F_y = -C_\alpha \alpha \tag{1.12}$$

where C_α is the *cornering stiffness* of the tyre:

$$C_\alpha = \left|\lim_{\alpha \to 0} \frac{\partial F_y}{\partial \alpha}\right| \tag{1.13}$$

The lateral force F_y at the tyre-print is at a distance $a_{x\alpha}$ behind the tyre-print centerline and makes a moment M_z, the self-aligning moment:

$$\boldsymbol{M_z} = M_z \boldsymbol{k} \tag{1.14}$$

$$M_z = F_y \, a_{x\alpha} \tag{1.15}$$

For small α, the aligning moment M_z tends to turn the tyre about the *z-axis* and make the *x-axis* align with the velocity vector **v**.

The tyre acts as a linear spring under small lateral forces F_y with a lateral stiffness k_y:

$$F_y = k_y \Delta y \tag{1.16}$$

The wheel starts sliding laterally when the lateral force reaches a maximum value F_{yM}. At this point, the lateral force approximately remains constant and is proportional to the vertical load:

$$F_{yM} = \mu_y F_z \tag{1.17}$$

where, μ_y is the tyre grip coefficient in the *y*-direction. As the wheel rolls forward, undeflected treads enter the tyre-print region and deflect laterally as well as longitudinally. When a tread moves toward the end of the tyre-print, its lateral deflection increases until it approaches the tailing edge of the tyre-print [8].

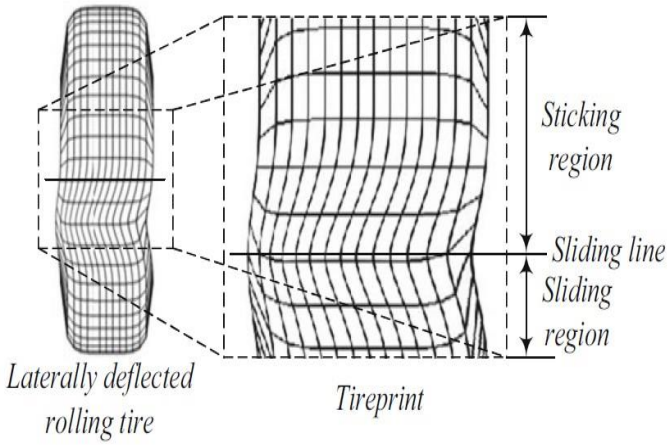

Figure 1.10 – View of a laterally deflected and turning tyre [8]

The normal load decreases at the tail of the tyre-print, so the friction force is lessened and the tread can slide back to its original position when leaving the tyre-print region. The point where the laterally deflected tread slides back is called sliding line.

Lateral distortion of the tyre treads is a result of a tangential stress distribution τ_y over the tyre-print, as shown in the figure 1.11.

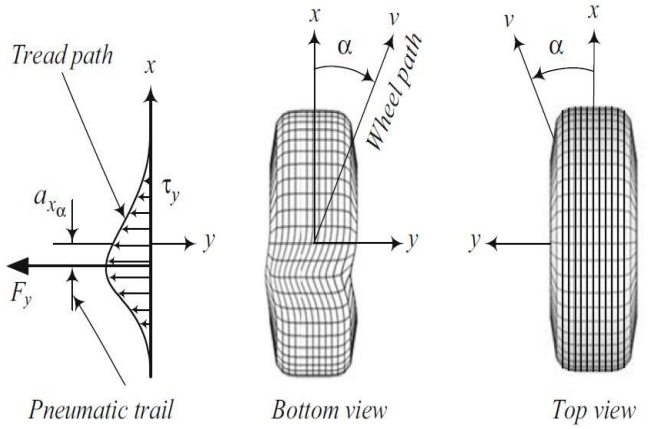

Figure 1.11 – The stress distribution τ_y, the lateral force F_y for a positive slip angle α

A slip moment M_x generates because a lateral shift in the tyre of the normal force F_z linked to the slip angle α:

$$\boldsymbol{M_x} = -M_x \boldsymbol{i} \tag{1.18}$$

$$M_z = F_x \, a_{y\alpha} \tag{1.19}$$

The slip angle $\alpha > 0$ if the tyre should be turned about the z-axis to be aligned with the velocity vector v. A positive slip angle α generates a negative lateral force F_y.

In the figure 1.12 the lateral force *Fy* as a function of the sideslip α is shown.

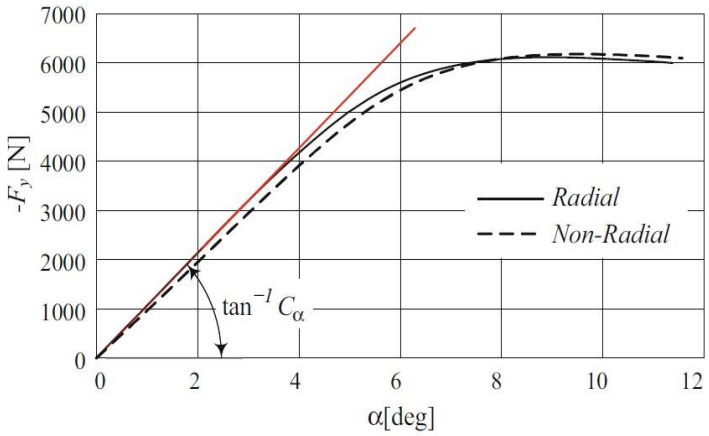

Figure 1.12 – The lateral force F_y as a function of the sideslip angle α [8]

If the vector **v** is written as $\boldsymbol{v} = v_x\boldsymbol{i} + v_y\boldsymbol{j}$ then the sideslip angle α can be expressed as follow:

$$\alpha = \tan^{-1}\frac{v_y}{v_x} \tag{1.20}$$

In the figure 1.13 the normal load F_z effects on the lateral force F_y as function of the sideslip angle α is shown.

Increasing the load not only increases the maximum attainable lateral force, it also pushes the maximum of the lateral force to higher slip angles.

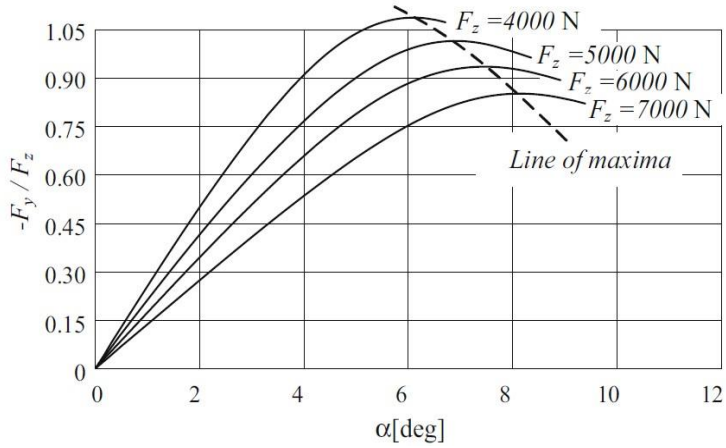

Figure 1.13 – Effect of load on lateral force as a function of slip angle α [8]

Tyre Force

Tyres may be considered as a force generator with two major outputs: forward force F_x, lateral force Fy, and three minor outputs: aligning moment M_z, roll moment M_x, and pitch moment My. The input of the force generator is the tyre load F_z, sideslip α, longitudinal slip s, and the camber angle γ [8] [9].

$$F_x = F_x(F_z, \alpha, s, \gamma) \tag{1.21}$$

$$F_y = F_y(F_z, \alpha, s, \gamma) \tag{1.22}$$

$$M_x = M_x(F_z, \alpha, s, \gamma) \tag{1.23}$$

$$M_y = M_y(F_z, \alpha, s, \gamma) \tag{1.24}$$

$$M_z = M_z(F_z, \alpha, s, \gamma) \tag{1.25}$$

The trends of the forces with respect to the slip s and the slip angle α are presented below.

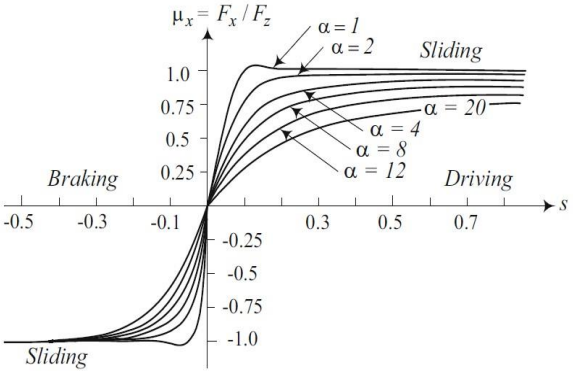

Figure 1.14 – Longitudinal force ratio F_x/F_z as a function of slip ratio s for different sideslip α [9]

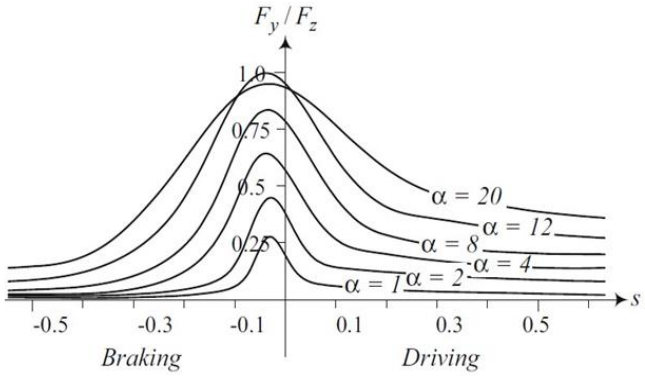

Figure 1.15 – Lateral force ratio F_y/F_z as a function of slip ratio s for different sideslip α [9]

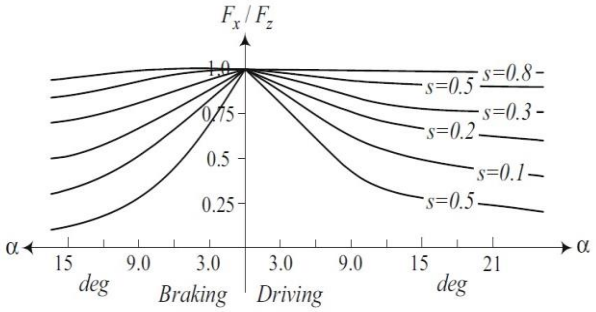

Figure 1.16 – Longitudinal force ratio F_x/F_z as a function of sideslip α for different slip s [9]

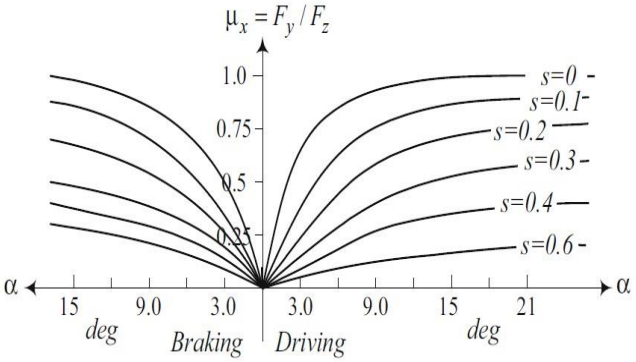

Figure 1.17 – Lateral force ratio F_y/F_z as a function of sideslip α for different slip s [9]

When the tyre is under both longitudinal slip and sideslips, it is under combined slip.

The shear force on the tyre-print of a tyre under a combined slip can approximately be found using a grip ellipse model, as shown in figure 1.18.

$$\left(\frac{F_y}{F_{yM}}\right)^2 + \left(\frac{F_x}{F_{xM}}\right)^2 = 1 \tag{1.26}$$

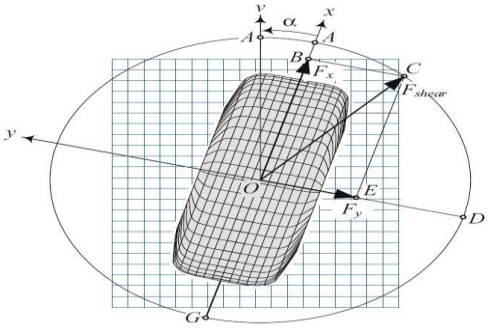

Figure 1.18 – Ellipse model [9]

1.5 Tyre Models Overview

During the past 20 years, enormous progress has been made in chassis engineering and driveability. Modern vehicles are significantly safer and more comfortable than their predecessors. In a context for which it is necessary assured and intensify the maturity of the product, despite wider ranges of models and shorter development times, the significance of modelling and simulation of the tyre behaviour becomes increasingly important.

In recent years, different types of mathematical models have been developed in order to model tyre behaviour. Of course, depending on the purpose of the specific model, different levels of accuracy can be introduced.

The existing automotive tyre models can be broadly classified into 3-4 categories shown in figure 1.19 [16] [17]

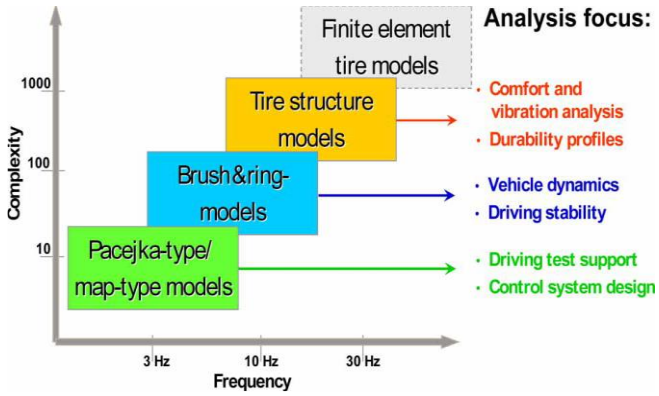

Figure 1.19 – Tyre model categories and main fields of application [18]

The division into categories is based on the growing complexity of the formulation and on the frequency range of the input/output signals covered by the model.

The first category is comprised of the models based on mathematical expressions which best fit the measurement results of real tyres, e.g. a polynomial or the Pacejka model [18].

The second and third categories include models formulated based on the available knowledge of the tyre, but they differ as to the complexity (analytical models). An example of the model from the second category is the Dugoff model [19], and from the third category the FTyre model [20].

Finally, the fourth category includes accurate finite element models, which, however, can rarely be used for vehicle dynamics studies due to computational complexity.

Chapter 2

The Temperature influence on the tyre

2.1 Introduction

In this chapter a short dissertation is carried out on the behaviour of viscoelastic materials since the tyre consists mainly of rubber.

The heat generation modes in a tyre (the friction power and strain energy loss) will be presented and how the temperature and frequency influence their mechanical properties will be discussed.

In fact, through the wheels, the vehicle exchanges forces with the track [2] [21]which depend on the structure of the tyres [22] and on their adherence, strongly influenced by temperature [23] [24].

2.2 The concept of the Viscoelasticity

Many mechanical systems are made of viscoelastic materials to avoid instability and to limit vibrations.

Viscoelasticity is widely studied since decades: considering works of Ferry (1961), Vinh (1967), Caputo and Mainardi (1971), Lakes (1999), Chevalier and Vinh (2010) and Balmès and Leclère (2009). Viscoelasticity is a causal phenomenon for which the force always pre-cedes the displacement. This behaviour can be described by the relaxation function or the creep function [25].

A polymeric material, with viscoelastic behaviour, presents a material structure formed by reticular cross-linked chains.

This structure type is the cause of the strong temperature dependence due to the different chain mobility level. Therefore, below the glass transition temperature, the material exhibits a high stiffness value while above this temperature, the stiffness decreases considerably.

A similar effect is observed when the material is cyclic loaded with high and low frequency, respectively.

Polymers differ from other materials in inherent rheological or viscoelastic properties: the stress-strain bond strongly influenced by time, even at room temperature.

The viscoelastic material is a deformable material with a behaviour which lays between a viscous liquid and an elastic solid. Their behaviour deviates from Hooke's law and exhibits elastic and viscous characteristics at the same time.

A viscoelastic material will return to its original shape after any deforming force has been removed, even though it will lake lime to do so. The reason of this phenomenon is that the deformation energy is not totally stored, but partially dissipated through hysteretic mechanism. Contrariwise, when a perfectly elastic solid, like a spring, is subjected to a force, it distorts instantaneously in proportion to the applied load. Then, as soon as the force is no longer ap-plied, the body returns to its initial shape.

To better understand the mechanical behaviour in viscoelastic materials, two main types of experiment are usually carried out: transient and dynamic. While static characterization regards the quasi-static application of load or deformation, transient and dynamic testing procedures concern the analysis of material response to a time applied deformation or load function (elongation or shear).

Two important categories, regarding the transient material testing, are commonly performed: creep experiment and stress relaxation experiment.

Creep consists in a progressive increasing of deformation under uniform load applied on the material specimen (Figure 2.1a) while in a stress relaxation experiment, a sample is rapidly strained to a fixed length at constant temperature and the stress is recorded as a function of time (Figure 2.1b).

It can be described in integral form by the following equation:

$$\varepsilon(t) = \frac{\sigma}{E} + \int_0^t J(t-\tau)\dot{\sigma}(\tau)d\tau \qquad (2.1)$$

In the creep experiment, the *creep compliance modulus J* is defined as the ratio between the strain, obtained at definite instant of time, and the load step applied (Figure 2.1a):

$$J(t) = \frac{\varepsilon(t)}{\sigma_0} \qquad (2.2)$$

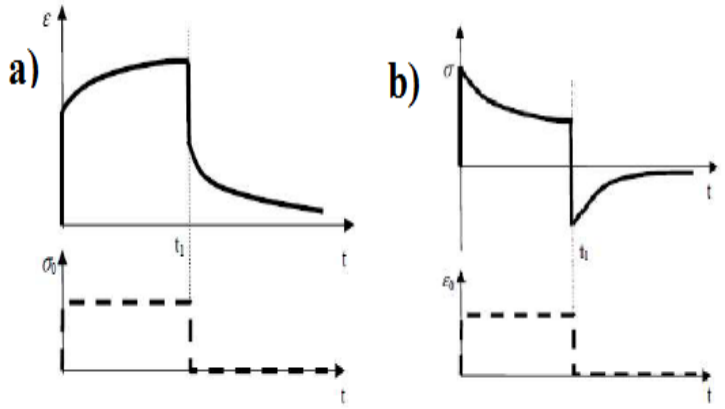

Figure 2. 1– Creep experiment (a) and stress relaxation experiment (b)

While, relaxation is when stress changes during time at an imposed deformation, and is expressed as:

$$\sigma(t) = E\ \varepsilon(t) + \int_0^t K(t-\tau)\dot{\varepsilon}(\tau)d\tau \tag{2.3}$$

In the relaxation experiment, the *relaxation modulus K* is expressed as (Fig.2.1 b):

$$K(t) = \frac{\sigma(t)}{\varepsilon_0} \tag{2.4}$$

From the eq. 2.1 it is clear that creep compliance is time dependent. In particular, the material behaves as a glassy solid if the load is applied with higher frequency values and it is like a rubbery solid if the load is applied quasi-statically. In the middle time-range, the compliance shows a linear slope where the solid behaves as a viscoelastic material. In particular, in the middle time-range which characterizes the linear viscoelastic slope trend, the creep compliance proportionally increases with time (Figure 2.2a).

Similarly, the stress relaxation material modulus is time-dependent, and it is also possible to distinguish the rubbery and glassy plateaus, in which the material exhibits quite opposite behavior (Figure 2.2b).

Another important testing procedure class, able to describe the viscoelastic behaviour, consists in the dynamic experiments. These tests are commonly employed to analyse the material reaction to cyclic stress or strain applied:

$$\sigma(t) = \sigma_0 \sin \omega t \tag{2.5}$$

where ω represents the angular frequency of an applied sinusoidal stress and depends on the time.

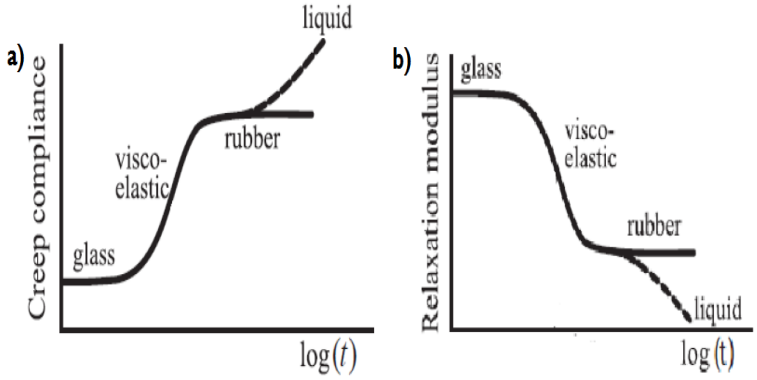

Figure 2.2 – Creep material compliance (a) and stress relaxation material modulus (b)

In quasi-elastic materials, the strain generated by the stress also exhibits a sinusoidal trend with the same phase of the applied load. On the opposite side, in viscoelastic materials, the strain reaction shows a time delay towards the applied stress, characterized by a phase angle δ.

Therefore, the strain response is given by (Figure 2.3):

$$\varepsilon(t) = \varepsilon_0 \sin(\omega t - \delta) \tag{2.6}$$

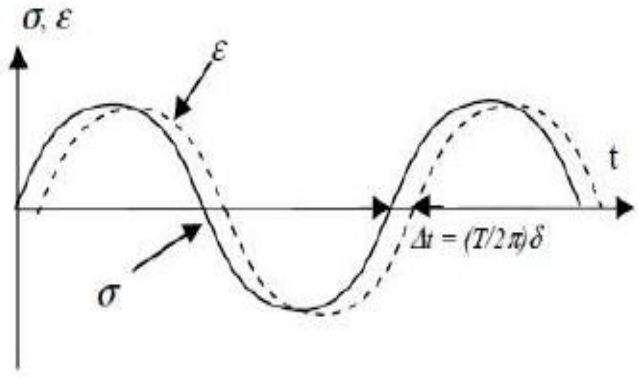

Figure 2.3 – Strain – stress trend

In the frequency domain it is introduced the complex modulus expressed as:

$$\frac{\sigma(\omega)}{\varepsilon(\omega)} = E(\omega)^* = E'(\omega) + E''(\omega) \tag{2.7}$$

where $E'(\omega)$ is the storage modulus [Pa] and $E''(\omega)$ is the loss modulus [Pa].

These above quantities are deeply linked to the way the material dissipates a part of energy provided by means of a load/stress time function. Therefore, the both moduli are related to the phase angle δ, according to the vector diagram in the Fig. 2.4:

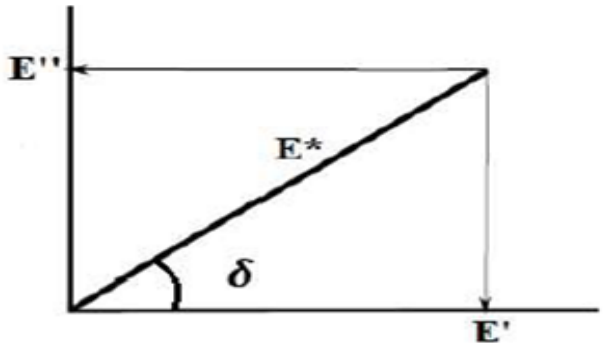

Figure 2.4 – E* vector diagram

Loss factor is defined as:

$$\frac{E''(\omega)}{E'(\omega)} = \tan\delta \tag{2.8}$$

It is important to see that all the quantities, referring to the viscoelastic behaviour, are function of the frequency at which the sinusoidal load/deformation is applied.

More precisely, the modulus, the energy loss and hysteresis of a viscoelastic material change in relation to two parameters: the frequency with which the force is applied and the material temperature the phenomena are evaluated on. It is important to point out that load frequency and material temperature produce opposite effects on the rubber behaviour, as represented in Figure 2.5 and Figure 2.6.

The moduli of viscoelastic materials can be characterized, for example, by Dynamic mechanical analysis (D.M.A.).

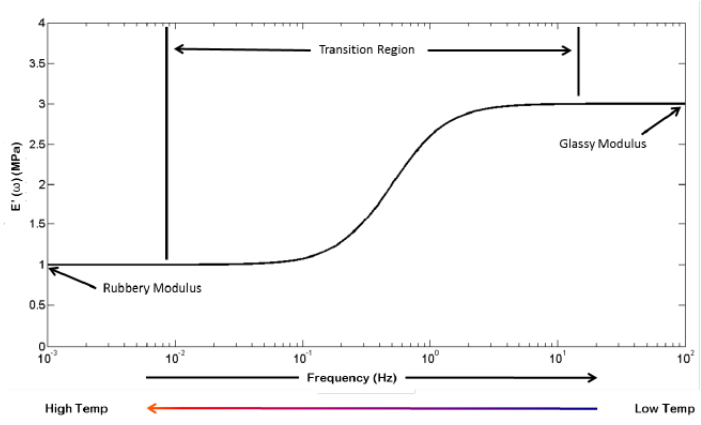

Figure 2.5 – Storage moduli of sample viscoelastic material (semi-log scale) [26]

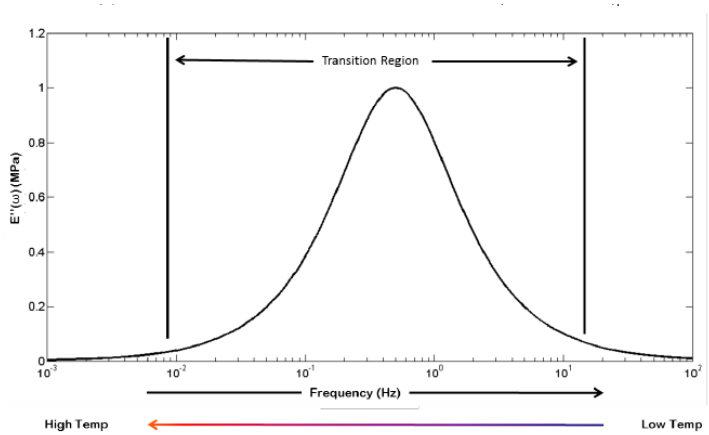

Figure 2.6 – Loss moduli of sample viscoelastic material (semi-log scale) [26]

A sinusoidal stress is applied and the strain in the material is measured, allowing one to deter-mine the complex modulus. The temperature of the sample or the frequency of the stress are often varied, leading to variations in the complex modulus.

However, the measurements which can be performed on most commercial DMA equipment are limited to the low-frequency domain (typically up to a few hundred Hz). In order to characterize the material on a broader frequency range, the time–temperature superposition (TTSP) is applied (Williams–Landel–Ferry, 1980) [27].

This principle relates the material response at a given time t (or frequency ω) and at a given temperature T to that at other conditions (denoted by subscript r):

$$\omega_r = a_T(T, T_r)\omega \tag{2.9}$$

$$E'(\omega_r, T_r) = b_T(T, T_r)E'(\omega, T) \tag{2.10}$$

$$E''(\omega_r, T_r) = b_T(T, T_r)E''(\omega, T) \tag{2.11}$$

where $a_T(T, T_r)$ and $b_T(T, T_r)$ are coefficients which indicate the amount of horizontal and vertical shifting (respectively) to be applied to isotherms of storage and loss moduli measured at a temperature T in order to estimate the material properties at a reference temperature T_r (Figure 2.7).

The horizontal shift factors $a_T(T, T_r)$ describe the temperature dependence of the relaxation time and usually follow the empirical Williams-Landel-Ferry (WLF):

$$\log_{10} a_T(T, T_r) = -\frac{C_1(T - T_r)}{C_2 + (T - T_r)} \tag{2.12}$$

where C_1 and C_2: empirical constants whose order of magnitude is about 10 and 100 K, respectively.

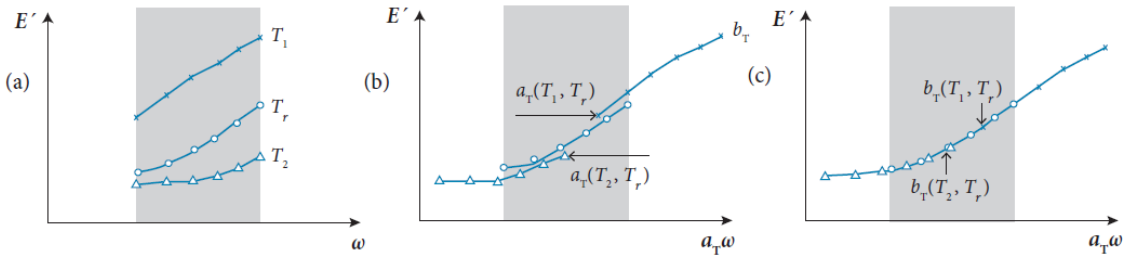

Figure 2.7 – (a) Isotherms of storage modulus on the frequency range measurable by DMA, at temperatures T1, T2 and Tr, with T1 < Tr < T2; (b) Isotherms of storage modulus after application of the horizontal shift factors, taking Tr as the reference temperature; (c) Isotherms of storage modulus after application of both horizontal and vertical shift factors, taking Tr as the reference temperature [28]

The vertical shift factors $b_T(T, Tr)$ are related to thermal expand which for most polymers can be neglected.

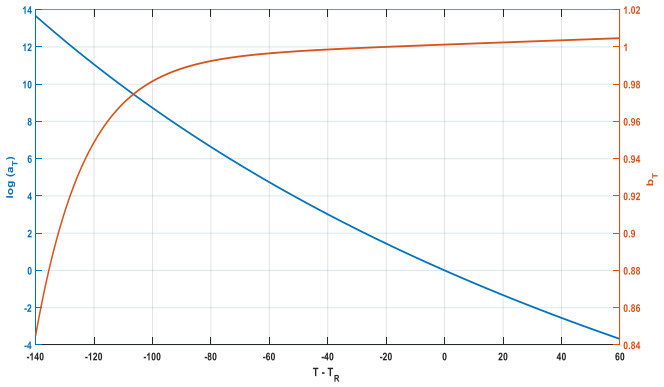

Figure 2.8 — Typical trend of a_T and b_T

2.3 The Strain Energy Loss

When the tyre is subject to a vertical load, it is deflected that means it is always deformed during its exercise (Figure 2.9).

Many parameters affect the entity of this deflection, such as vertical load, inflation pressure, carcass stiffness, etc.

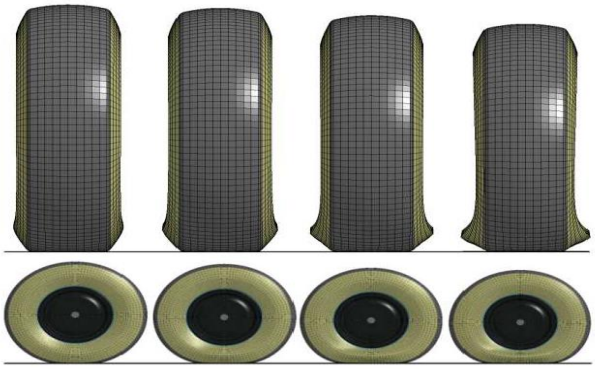

Figure 2.9 – Tyre deflection under different vertical load level [29]

A rolling pneumatic tyre exhibits both elastic and viscous characteristics due to embedded rubber compounds and therefore every part of it that deflects every revolution is subjected to a hysteresis cycle. This means that not all energy is returned when the material relaxes because part of it is dissipated in the heat (Figure 2.10).

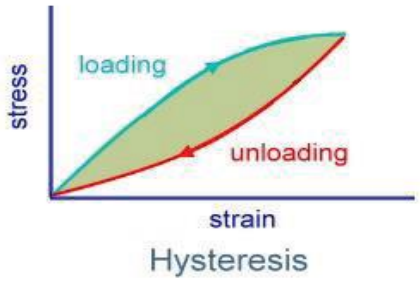

Figure 2.10 – Hysteresis cycle [30]

Because in a hysteretic cycle the unloading phase is not equal to the loading phase the contact pressure distribution along the contact patch is not uniform so the resultant force is not aligned with the contact patch centre, but it is always ahead [30] (Figure 2.11).

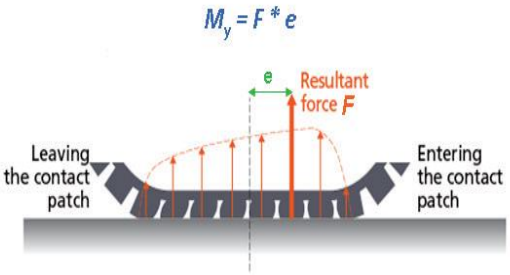

Figure 2.11 – The concept of tyre rolling resistance [30]

The analysis of the figure shows the presence of a resistant moment that contrasts the motion and that establishes the *rolling resistance* of the tyre.

When the tyre is in free-rolling conditions, the power dissipated in hysteresis can be computed as:

$$\dot{E_{diss}} = M_y \, \omega \, [W] \tag{2.13}$$

where:

- M_y = Rolling Resistance Moment [N m]
- ω = angular speed of the tyre (rad/s)

At each operating temperature, the ratio of loss strain energy to the total strain energy of the rubber, can be estimated by experimental methods. According to the results obtained by Lin and Hwang [31], it is reasonable to take this ratio 0.1 for vast variety of operating temperatures (Figure 2.12).

When the tyre is in traction – or braking – or when the tyre is in cornering, the deformations are more complex than the simple tyre deflection exposed above and these deformations concur to the strain energy loss generation of course (Figure 2.13).

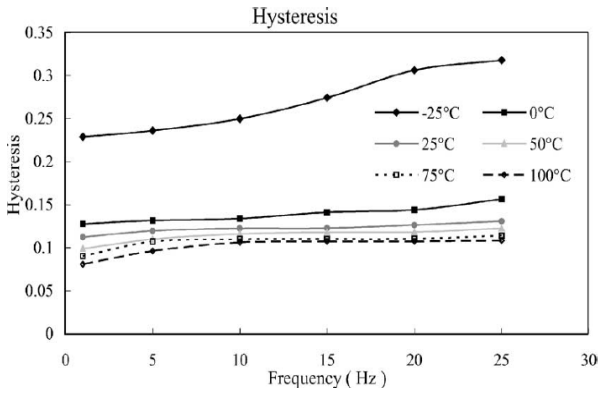

Figure 2.12 – Hysteresis for tread compound of bias tyre varying with temperatures and frequencies

Figure 2.13 – Tyre deformation in corner

Because the tyre is usually in pseudo-sliding conditions – that means part of the contact patch slides against the road surface and therefore a certain amount of heat is always generated at the interface between the tread and the roadway.

The power dissipated, called "*friction power*", can be written as:

$$FP = F_x v_{sx} + F_y\, v_{sy}\ [W] \tag{2.14}$$

where:

- F_x is the longitudinal interaction force [N]
- F_y is the lateral interaction force [N]
- v_{sx} is the longitudinal sliding velocity [m/s]
- v_{sy} is the lateral sliding velocity [m/s]

A part of this thermal power is transferred to the tyre and the remaining to the asphalt. This is considered by means of a partition coefficient CR calculated using the following expression [32]:

$$CR = \frac{k_T}{k_R}\sqrt{\frac{\alpha_t}{\alpha_R}} \tag{2.15}$$

in which thermal diffusivity α can be expressed as $\alpha = \frac{k}{\rho c_v}$.

Considering the following road properties:

$$k_R = 0.55\ \frac{\mathrm{W}}{mK} \tag{2.16}$$

$$\rho_R = 2200\ \frac{\mathrm{kg}}{\mathrm{m}^3} \tag{2.17}$$

$$Cv_R = 920\ \frac{\mathrm{J}}{\mathrm{kg\ K}} \tag{2.18}$$

and the properties of the SBR (Styrene and Butadiene mixture used for the production of passenger tyres), available in literature [33] [34], the resulting calculated value of CR is about 0.55, which means that the 55% of the generated power is directed to the tyre.

Since in general, the thermal conductivity of the rubber varies with the temperature, also the CR coefficient will be a function of the tyre temperature.

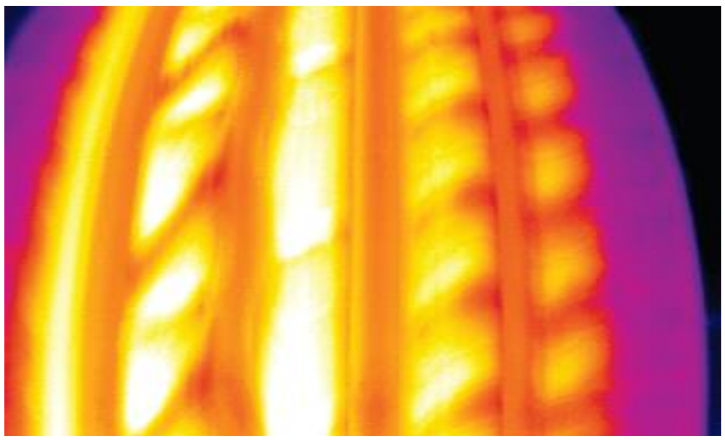

Figure 2.14 – The tyre surface temperature measured by thermo camera [30]

2.4 How the temperature influences the handling performance

The working temperature of a tyre usually depends on different aspects, as well as on the type of tyre itself, the way the vehicle is driven and the ambient temperature.

In general, the internal temperature of a standard passenger tyre is between 20 and 60 °C. Clearly, the temperature of the tyres increases as soon as the outside temperature is higher. In normal working temperature conditions, the amount of energy dissipated by the tread compound, which exhibits a viscoelastic behaviour, if subjected to a cyclic load, decreases with increasing temperature, as shown in the Figure 2.15.

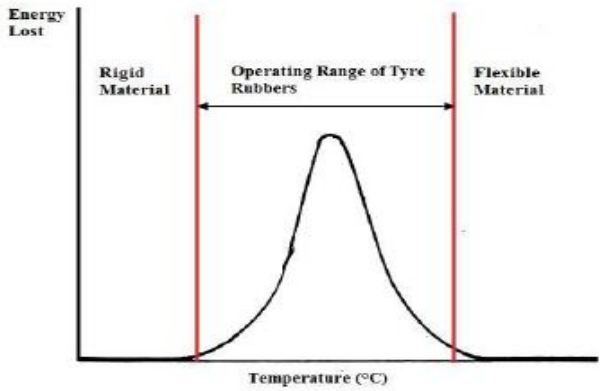

Figure 2.15 – Temperature effect on viscoelastic compound dissipation

The working range of the suitable temperature corresponds to the maximum area of energy loss due to viscoelastic behaviour so that the friction coefficients are high. Very low temperatures transform the behaviour of the tread into a rigid one.

The temperature influence on rubber friction has been known for at least 60 years when Schallamach [35] experimentally observed the decrease in "pulling force" with the temperature increasing (Figure 2.16).

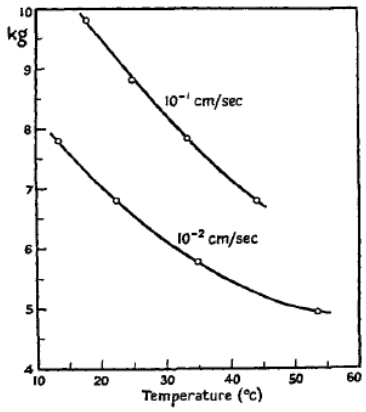

Figure 2.16 – Temperature influence on Schallamach studies [35]

In general, the rubber friction should be due to different contributions: an adhesive component, a hysteretic component and a contribution due to the wear (the third component is in general negligible) [36]

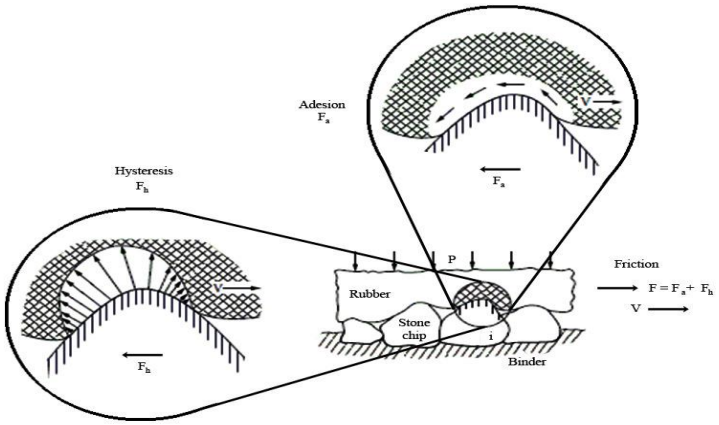

Figure 2.17 – Kummer's model for rubber friction mechanisms

So, in dry conditions the friction force can be written as

$$F_T = F_A + F_{HB} + F_C \tag{2.19}$$

F_T is the total frictional resistance, F_A is the adhesive contribution due the Van der Waals' forces between the two surfaces, F_{HB} is the contribution due to the bulk deformation hysteresis in the rubber and F_c is the contribution due to the removal of the rubber material by the road asperities (that seems to weigh no more than 2%).

For what concern the first two contributions Kummer considered them not independent because adhesion increases the extension of the contact area and consequently the zone affected by hysteretic deformations.

Persson [37] hypothesized that the different components are predominant on different scales: the hysteretic contribution is associated with the long-wavelength surface roughness while the adhesion deforms the rubber at short-wavelength roughness.

The friction is directly related to the viscoelastic properties of the rubber itself and shows similar trend of the loss Modulus E'' ($tan\,\delta$) of the compound. Thus, increasing the temperature involves in a decreasing of the friction (hysteretic component).

Considering the Figure 2.18: when the temperature decreases, even if the δ increases (until 0°C in this case), the E' (or G') increases too involving in a reduction of the real contact area. So, even decreasing the temperature the tyre friction reduces.

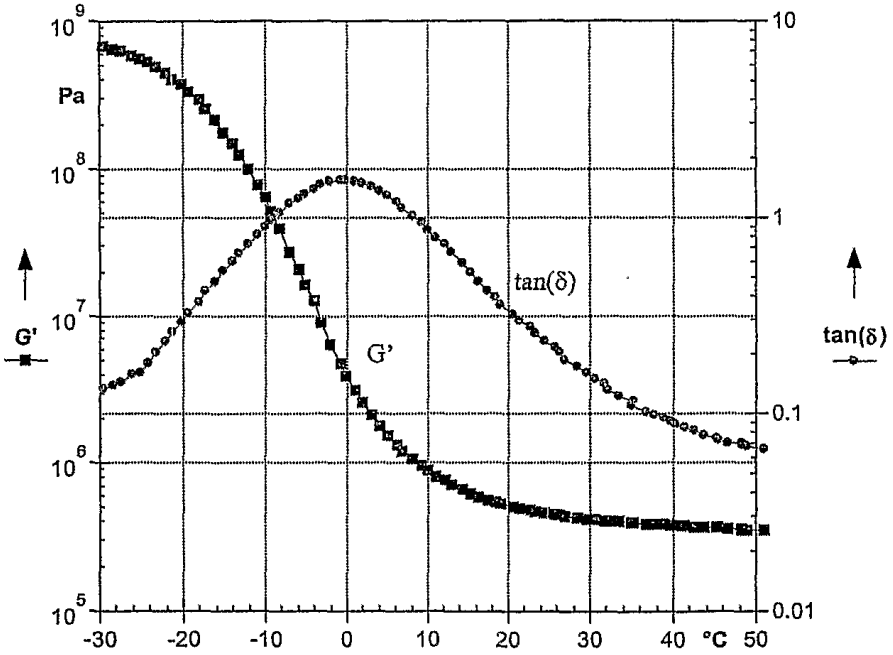

Figure 2.18 – G' and tanδ curves in dependency on temperature

Evidently an optimal combination of $tan\,\delta$) and E' that maximizes the tyre friction exists.

Since hysteretic deformations dissipate heat, it is clear that the friction between rubber and road is always associated with the generation of heat at the interface. This concept is clearly explained by Persson [38] which also introduces the concept of flash temperature.

Since the friction correlated to the characteristics of the tread compound, it is clear that all these considerations refer to the surface temperature, that is to the temperature of a

very thin layer of the outer surface of the tyre. This temperature is deeply different from the *bulk temperature* namely the temperature of the core of the tyre.

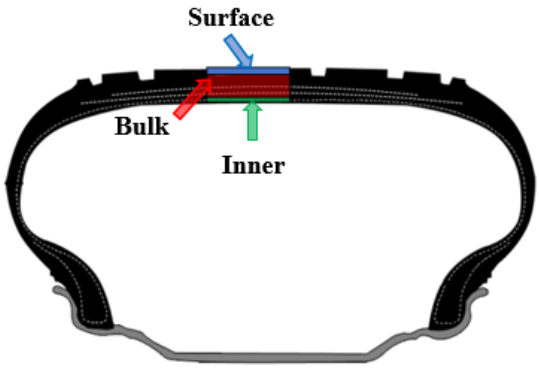

Figure 2.19 – The surface, the bulk concept and the inner concept

2.5 Influence of the temperature on tyre stiffness

Tyre structure is known for a laminated style with a shell structure of rubber that is strengthened by the number of ply.

Tyre performance is influenced by inflation pressure and depends on the mechanical characteristics of the tyre, includes sidewall stiffness.

Tyre is one of pressure vessels and inflation pressure is dominant in sidewall stiffness. Therefore, it can be said that tyre sidewall stiffness derives from the tension of inflation pressure and the structural dynamic characteristics, including the properties of the rubber material.

An example of tyre stiffness representation is shows in the Figure 2.20.

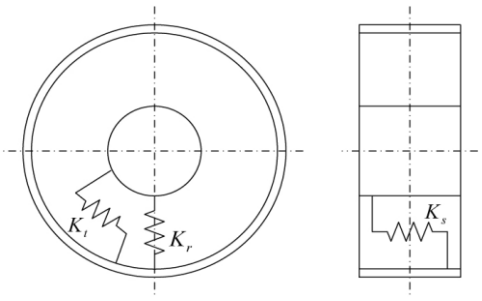

Figure 2.20 – Spring bedded ring model of radial tyre [39]

where:

- K_s is the spring of lateral direction;
- K_t is the spring of the tangential direction;
- K_r is the spring of the radial direction;

The tyre stiffness can be considered as the sum of three contributions: the first part of the stiffness arises from the tension in the sidewall cords. This tension is present because of the inflation pressure, so this part of the stiffness is referred to as the pneumatic part; the second part regards the structural contribution of sidewalls (depending on operating temperature); the third part is linked to the centrifugal effects [39] [40] [41] [42].

The structural part of stiffness is very depending on the tyre temperature because they are related to the elastic modulus [43] (Young Modulus in case of steel belt and Storage Modulus in case of rubber) that is well known temperature dependent at least for viscoelastic materials.

In the Figure 2.21 is shows the tyre temperature effect on the vertical stiffness while the Figure 2.22 and Figure 2.23 show the tyre temperature effect on the Bracking and Cornering stiffness respectively.

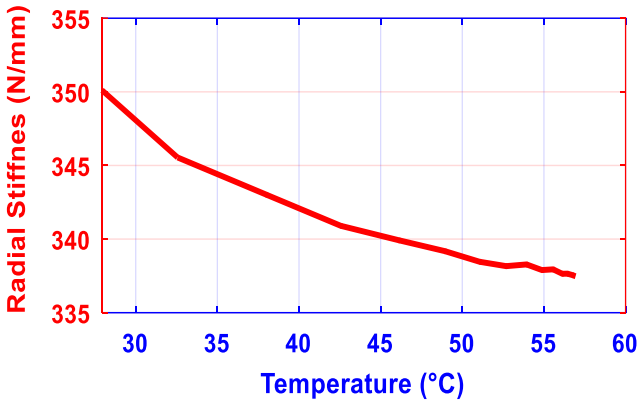

Figure 2.21 – Tyre temperature effect on the vertical stiffness

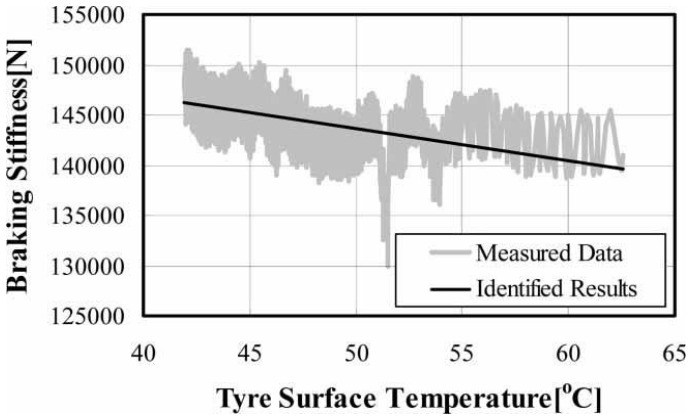

Figure 2.22 – Tyre temperature effect on the Braking stiffness [44]

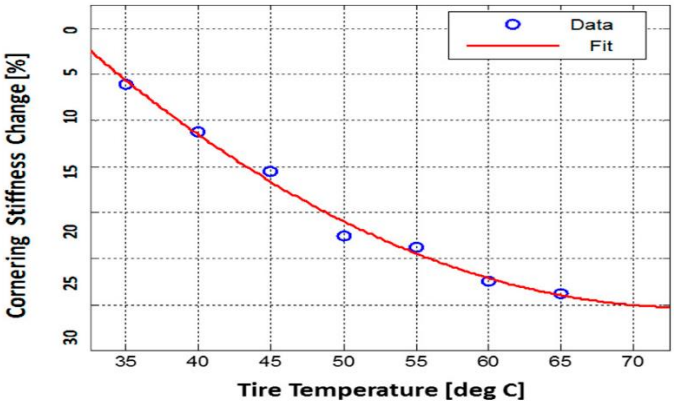

Figure 2.23 – Tyre temperature effect on the Cornering stiffness [45]

Figure 2.24 shows the influence of temperature on the longitudinal and lateral interaction curves (the data represented has been adimensionalized due to confidentiality agreements with the motorsport research partner).

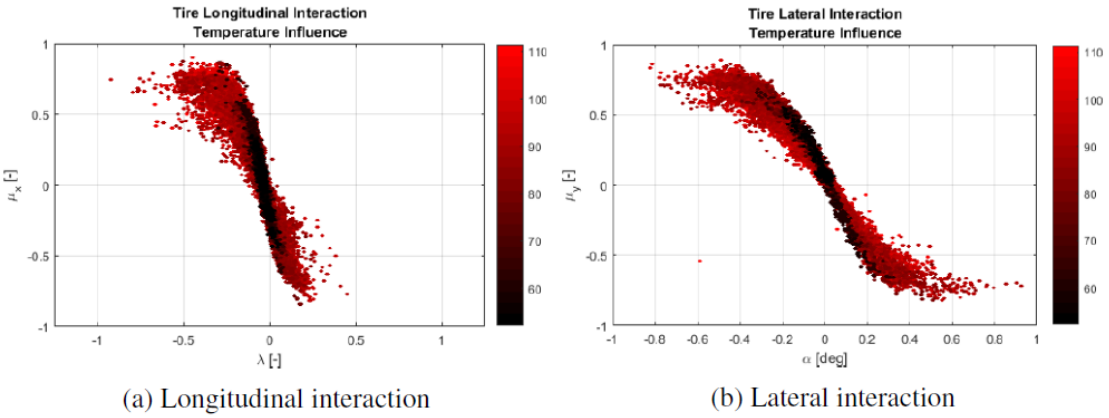

(a) Longitudinal interaction (b) Lateral interaction

Figure 2. 24 – Temperature influence on tyre interaction characteristics curves [13]

In recent years, the ever-increasing interest in intelligent tyre technology has led to the formulation of different empirical models correlating deformation measurements provided by the sensors with tyre dynamics.

Thanks to the introduction of a sensor inside the tyre is possible to senses a lots of useful information (features) like the vertical load, lateral and longitudinal forces.

In general, the evaluated of these features is the result of a series of calibration using experimental data obtained at a steady-state temperature (generally after a warm-up phase).

The importance of introducing a temperature correction on the features (like vertical load, longitudinal Forces and lateral Forces) is evident.

The first part of this work focused precisely on this aspect and it consists in the in the definition of a strategy for the introduction of thermal dependence in the numerical model for the calculation of features currently implemented, such as for example the estimates of contact forces. The objective is to increase the reliability of the estimate in all conditions, especially in cold tyre conditions.

Chapter 3

The Cyber^{TM}Tyre system description

3.1 Introduction

Ground vehicle motion is primarily determined by tyre forces, therefore, knowledge of they, is required in order to understand and predict the vehicle behavior and safety.

Moreover, ground vehicle safety is also significantly related to road conditions, which can be quantified from the perspective of the vehicle as the tyre/road friction coefficient.

The longitudinal and lateral forces that a tyre can produce are a function of the vertical force and the friction coefficient between the tyre and the road. Since the vertical force and the coefficient of friction are both limited, there is a limit to how much longitudinal and lateral force a tyre can develop.

Real-time sensing of tyre forces is highly desirable in a vehicle, since knowledge of these forces can be used to determine the fraction of tyre force capacity already expended.

The measured forces of tyres may be used by a vehicle safety control system to mitigate the effects of unreasonable and unattainable tyre force demands on the driver, especially in rapidly changing road conditions.

Estimates of the tyres forces used by current vehicle safety control systems are usually obtained through state observers, in which vehicle states are acquired by existing vehicle sensors such as torque and steering wheel angle measurements, wheel steering sensors, accelerometers and others [46].

The main problem with the tyre force assessment systems based on the observer is that they require a change in the longitudinal or lateral force to make an estimate [47].

Indeed, these systems prefer highly dynamic, short time duration, high-amplitude inputs to vehicle controls by the driver in order to make good estimates. In addition to this disadvantage, the accuracy of tyre forces estimated using an observer-based system may be insufficient [48].

In order to improve the systems for estimating the force of existing tyres, the challenge is to find a tyre force sensor capable of measuring tyre forces in real time during all vehicle modes of operation.

A smart tyre (or intelligent tyre) is a tyre capable of monitoring itself using sensors inside it and providing information on conditions such as temperature, inflation pressure, road tyre friction, forces and conditions aquaplaning etc.

Generally, except for inflation pressure, the direct measurement of quantities such as contact forces, require bulky and expensive instrumentation.

These quantities can be evaluated starting from some measures like those summarized in the table:

Table 3.1 – Raw Sensor Measurements

Symbol	Description
$\boldsymbol{u}$	Displacement
$\boldsymbol{\ddot{u}}$	Acceleration
$\boldsymbol{\varepsilon}$	Strain
$\boldsymbol{\theta}$	Wheel Angular Position
$\boldsymbol{\omega}$	Wheel Angular Speed

Pirelli Tyres S.p.a operates into this scenario providing cars with high quality and high -performance tyres which are also employed as an" intelligent" vehicle component with the aim of improving both active safety and manoeuvrability.

The so called Cyber^{TM} Tyre project carried out by Pirelli is based on the basic principle of providing the tyre with sensors that can exchange information and interact with the active safety controls of the vehicle.

The company aims to provide information regarding the tyre-road contact area with the goal of interacting with active control systems and providing useful information to the driver in terms of safety and vehicle dynamics.

This system allows the knowledge of the main dynamic entities featuring tyre-road interaction by means of the installation of suitable sensors inside the tyre.

Thanks to this solution Pirelli is now able to provide important information about parameters that are related to the contact area such as contact forces, contact patch length, deformed radius, center of gravity position and surface texture changes.

3.2 Existing Tyre Force Measurement Methodologies

A major impetus for the development of passenger car tyre pressure measurement methods is the regulation (EU) 2012/523 which has made mandatory the TPMS (Tyre Pressure Monitoring System) on all cars registered, sold and put into circulation, from 1 November 2014.

The system is supposed to identify dangerously low air pressure conditions, and not necessarily small decreases in air pressure.

TPMS can be divided into two different types: direct (dTPMS) and indirect (iTPMS). The target of a TPMS is avoiding traffic accidents, poor fuel economy, and increased tyre wear due to under-inflated tyres through early recognition of a hazardous state of the tyres.

Indirect TPMS do not use physical pressure sensors but measure air pressures by monitoring individual wheel rotational speeds and other signals available outside of the tyre itself.

Direct TPMS physically measure the tyre pressure in each tyre and report it to the vehicle's instrument cluster or a corresponding monitor. Some units also measure and alert temperatures of the tyre as well. These systems can identify under-inflation in any combination, be it one tyre or all, simultaneously.

In [49], an extensive review of technologies and estimation methods for intelligent tyre systems has been presented. Many research applications about intelligent tyres adopt sensors installed on the inner liner and are divided into strain-based and acceleration-based [50] [51].

Further interesting systems are present in the literature. For example, Magori et al. [52], using ultrasonic sensors, can monitor deformation, temperature and other characteristics of the contact impression.

Tuononen [53] has conducted many studies to measure tyre crushing through the use of optical sensors.

Tyre radial displacement can be measured between the wheel and the tyre inner liner, and displacement of the tyre sidewall can also be measured. Radial displacement measurement devices reported in the literature range from a very simple string potentiometer device [54]all the way to a sophisticated optical system using a light source and a lens [46].

In general, tyre displacement sensors are reasonably efficient, but durability may be a concern.

Tyre acceleration is a desirable raw sensor measurement since the accelerometers used to measure it are widely available, small and they are mechanically designed to operate at high acceleration levels, such as those reached in a rolling tyre.

Tyre strain is also a desirable raw output since traditional foil-type strain gages are small and easy to obtain. However, the stiffness of these sensors (and their adhesive) is much higher than tyre rubber. To address this incompatibility, specially designed tyre strain sensors with elastomer substrates have been suggested [55].

The Cyber^{TM} Tyre system developed by Pirelli Tyres S.p.a has the goal to evolve the tyre into an "intelligent" part of the vehicle (Smart Tyre) by making it able to interact with the vehicle control units and its active controls.

It involves the installation of one or more accelerometric sensors inside the tyre: the characteristics of the quantities to be acquired, as well as the operating conditions of the sensor itself, have led previous studies to analyse different hardware solutions.

Even with a view to mass production, the sensor must be able to provide good reliability and robustness and must be able to acquire the quantities required in the various operating conditions of a rolling tyre, both during cornering and potentially up to maximum homologated tyre speed.

For these reasons, the most suitable solution is a triaxial accelerometric sensors placed on the inner liner of the tyre, able to detect the acceleration to which it is subjected at the moment of impact with the ground: from these measurements it will then be possible to trace the conditions of deformation of the tyre in the tyre footprint and the consequent information useful for the study of vehicle dynamics.

The main element of the system is the Sensor Node that is composed by a MEMS triaxial accelerometer, a RF (Radio Frequency) antenna for data transmission and other auxiliary electronic components for the management and pre-processing of the signals, which will be sent wirelessly to a control and management unit on board the vehicle.

Thanks to the acquired accelerometric signals it is possible to retrieve mathematically the estimation of several information regarding the dynamics of the vehicle, such as for example the contact forces between the tyre and the road surface in the three directions detected by the sensor. The estimation of these quantities is carried out through empirical models obtained from experimental data, collected in tests carried out indoors on the interest tyre:

they are statistical models based on regressive approach. Polynomial coefficients are obtained through a calibration procedure

The first prototype of the system is called *SAMPLE A*. This prototype was intended for internal use and feature development. The continuous research carried out by Pirelli and

the development of technology has produced a new version of the already existing system that is now identified as *SAMPLE B*, that can be considered still a prototype but also a significant step forward to industrialization. At the moment Pirelli has reached Sample C maturity prototype, a technology at industrialization level. Sample C technology will not be disclosed in the present work due to confidentiality reasons. All the testing activities in the present work have been carried out using SAMPLE A and SAMPLE B prototypes. The description of the two solutions will be discussed in the current chapter.

3.3 The hardware system

The innovative solution developed by Pirelli Tyres S.p.a can be schematized, independently from the Sensor Node configuration, according to the following layout:

- Mechanical part, whose task is to carry out the measurements of the acceleration signals coming from the rolling tyre.
- An electronic part, dedicated to data conditioning and transmission to an external acquisition unit, installed outside the tyre.
- A control unit (VEU - Vehicle Elaboration Unit) for signals elaboration that is also responsible for monitoring and management of the interaction among the devices constituting the system.

3.3.1 The Sensor Node SAMPLE A

This first solution developed by the Cyber^{TM} Tyre team is composed by the *MEMS* triaxial accelerometer equipped with the RF antenna for data transmission, protected by a rubber housing and mounted onto the inner liner as shown in Figure 3.1.

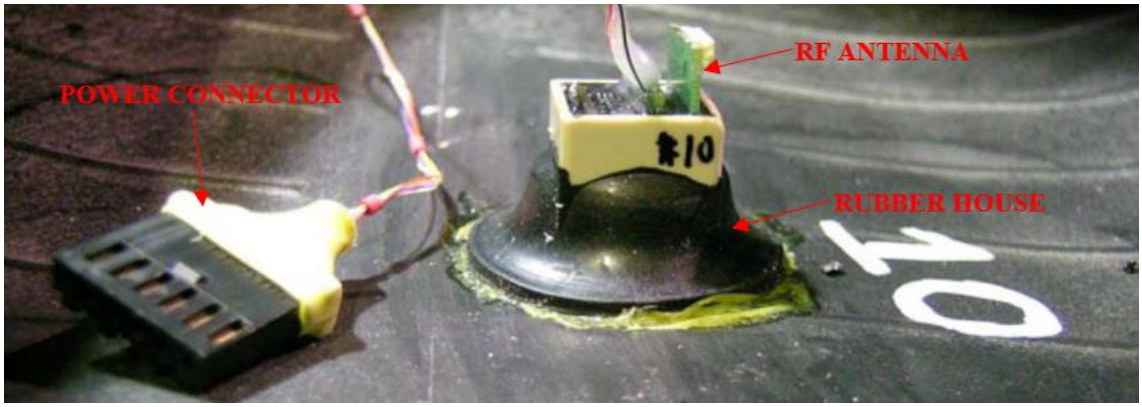

Figure 3.1 – Sensor Node^{TM} SAMPLE A installed on the inner liner [56]

The Sensor Node is fed by an external lithium-ions battery mounted on the wheel and connected to it by means of cables and a proper connector.

The cubic housing of the SAMPLE A contains the triaxial accelerometer and the related electronic parts. All the components are dipped into a resin called potting which has the task of keeping the part in place.

The connection between the sensor node and the tyre is realised by means of the rubber house [57], a specific casing that is produced by Pirelli Tyres S.p.a itself. The rubber house is realized with a polymeric compound featured by high tangential stress, wear, fatigue and temperature resistance. The Sensor Node is fixed into the rubber house which, in turn, is connected to the inner liner through a high-performance glue.

The SAMPLE A accelerometer is featured by its own reference frame which is a right-handed system featured by the x axis parallel to the direction of travel, the z axis directed towards the wheel radius and the y axis oriented accordingly, as depicted in Figure 3.2 a.

It is possible to install up to 3 accelerometers into the same tyre, aligned along the transversal direction (Figure 3.2 b).

The conditioning operation (filtering and amplification) carried out using the components present inside the Sensor Node and are the result of an in-depth analysis carried out by previous studies and thesis works ([57], [58], [59]) in the context of the activity with Pirelli S.p.A.

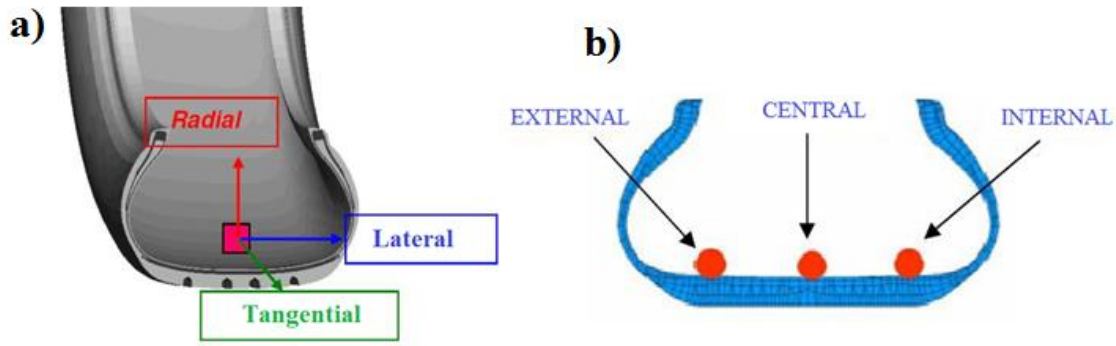

Figure 3.2 – a) Sensor reference system [56]; b) accelerometers positions

The acquired signals sent to the elaboration unit can be sampled by means of two different methods:

- **Asynchronous sampling**: The sampling frequency f_s is kept fixed, therefore, the time lapse between two subsequent samples is constant and equal to $\Delta_t = 1/f_s$.

- **Synchronous sampling:** The sampling frequency is varied according to the tyre angular velocity in order to have a constant number of samples for each revolution.

The physical phenomenon of interest is the tyre deformation during the contact with road. Since this phenomenon is periodic with the tyre revolution, the synchronous sampling seems to be the more suitable acquisition method. In that scenario, the number of samples per period identifies the maximum harmonic component that can be appreciated.

However, previous thesis works have verified [60] that it is possible to employ asynchronous sampling method without loss of information with a sampling frequency equal to 5 kHz, avoiding the use of an auxiliary signal for the angular speed identification (which is necessary in case of synchronous sampling).

The SAMPLE A acquires the accelerometric signal on the whole tyre turn (Figure 3.3), so if the Fourier's transform of the signal is numerically computed (FFT), the angular velocity of the tyre is found as the amplitude of the first point of the spectrum (zero frequency component) while the first harmonic component corresponds to the second point in the same array.

Figure 3.3 – SAMPLE A: acquisition window [61]

3.3.2 The Sensor Node SAMPLE B

The SAMPLE B represents the second version of the Sensor Node developed by Pirelli and it is now close to the industrialization phase.

The triaxial accelerometer is the same as that used for SAMPLE A while there are differences in terms of shape, energy supply and electronic components. In fact, the new Sensor Node is equipped with a replaceable 3V battery integrated into the housing,

making the system completely wireless. The electronic parts have been redesigned in order to satisfy a correct compromise between performance and costs.

Figure 3.3 shows the system architecture of the SAMPLE B.

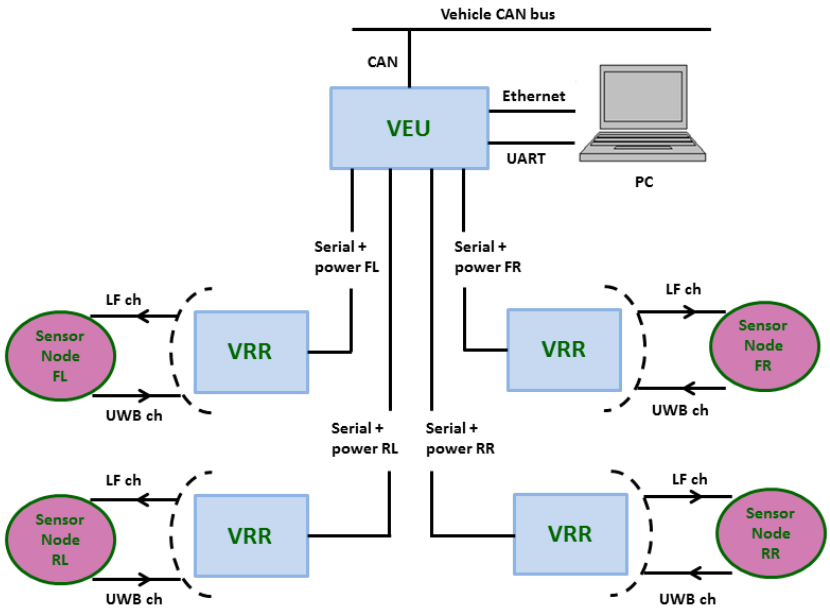

Figure 3.4 – SAMPLE B system layout [62]

Each sensor is connected in wireless with a dedicated intermediate electronic receiver called VRR (Vehicle Radio Receiver) which, in turn, is connected to the VEU that is the main elaboration unit. The sensor node is constituted by the accelerometer and the electronic parts necessary for data transmission such as an Ultra -Wide Band antenna and a LF (Low radio Frequency) antenna responsible for the reception of the commands from the VRR.

The VRR unit is the intermediary between the VEU and the Sensor Node. The dialog with the latter one is realized, as already mentioned, in wireless through UWB and LF radio connections. One VRR for each node is necessary and it is usually mounted on the wheel arch. On the other side, the VRR is connected to the VEU by means of a bi-directional serial channel.

Finally, the VEU is in charge of the signal elaboration and features extraction. Being equipped with a dual-core embedded processor it is also able to manage all the activities that are carried out by the other components. The VEU is also featured by an ethernet port and 2 CAN bus ports for the connection with the vehicle electronic systems.

The Sensor Node is positioned inside a tyre so as to conveniently coincide the measurement directions of the MEMS accelerometer with the tyre interest directions: using a right-handed triad, the Z direction of the transducer is made to coincide with the radial direction of the tyre, the X direction of the transducer with the longitudinal direction, the Y direction of the transducer with the lateral direction (Figure 3.2).

The node SAMPLE B is now featured by circular shape and it is inserted into a dedicated support (rubber house) shown in the Figure 3.5. The connection is not unremovable since the node is kept fixed by means of a plastic clip that can be exported in order to change the node battery or to perform maintenance.

The way through which the rubber house is connected to the tyre inner liner is the same as the one already mentioned for the *SAMPLE A*.

The available mounting configurations are (Figure 3.6):

- One single node placed at the center of the inner liner.
- 2 nodes, one in central position and the other close to the external part of the tyre, placed at 180 degrees with respect to the first one.

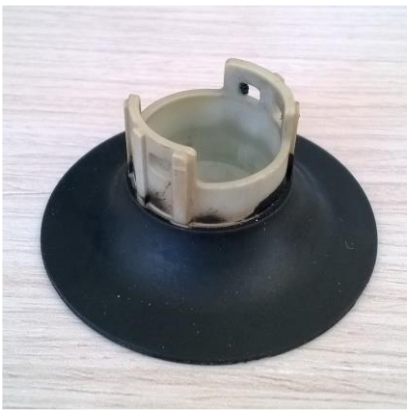

Figure 3.5 – Rubber House

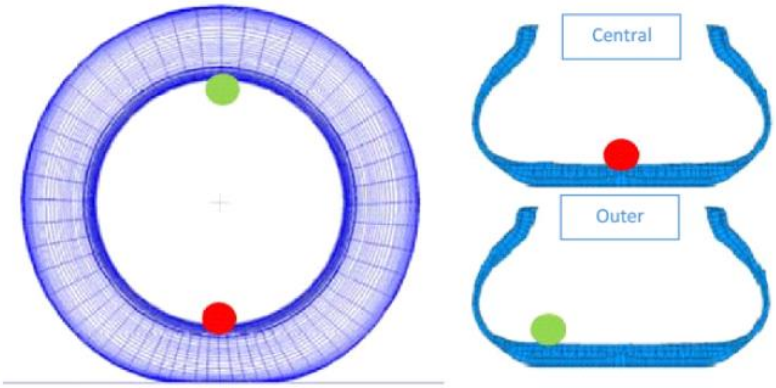

Figure 3.6 – SAMPLE B: mounting configurations

While the *SAMPLE A* acquires signals on the whole wheel turn, the SAMPLE B acquires only 120 degrees as shown in Figure 3.7, symmetric with respect to the contact patch. This solution allows the signal transmission and elaboration during the residual portion of the tyre turn without any overlapping of operations.

Figure 3.7 – SAMPLE B: acquisition window [61]

Another fundamental difference with respect to the SAMPLE A is the acquisition method which is now synchronous in the case of the SAMPLE B. The acquisition period varies according to the tyre angular velocity and the sampling frequency is not fixed.

Under the assumption of constant rolling radius R, the time lapse between 2 samples is given by:

$$\Delta t\ (s) = \frac{\Delta\theta(\text{rad})R(\text{m})}{v\ (\frac{\text{m}}{\text{s}})} \tag{3.1}$$

While the corresponding frequency resolution is:

$$\Delta f(\text{Hz}) = \frac{1}{\Delta t\ (\text{s})} \tag{3.2}$$

Unlike *SAMPLE A*, *SAMPLE B* is also equipped with a temperature sensor.

3.4 Description of the treated signals

The accelerometric signals acquired by the Sensor Node require a treatment process before they can be used to obtain quantities useful for calculating the required features.

Signal processing is represented by:

- **wheel turn validation**: control over the quality of the signal itself. The validation is carried out on the signals acquired during a whole wheel revolution: if these signals are not considered valid, they are discarded.
- **filtering in the frequency domain**: carried out to eliminate high frequency contributions (due to factors such as dynamics of the tread blocks at the entrance and exit from the tyre footprint, presence of road irregularities, etc.). This operation is carried out transporting the signals in the frequency domain through the application of the Fourier Transform
- **Integration and reconstruction of signals in the time domain**: the filtered signal is integrated twice in order to obtain the movements. The calculation of these quantities turns out to be necessary as some of the fundamental quantities used for estimating the contact forces are derived from these.

The filtered and processed accelerometric signals represent the starting point for the extraction of the indicators necessary for the contact forces estimation.

Considering the Figure 3.8, during a wheel revolution, it is possible to identify four distinct areas in the tyre:

1. Leading edge of the tyre footprint
2. Tyre footprint
3. Trailing edge of the tyre footprint
4. out of contact area

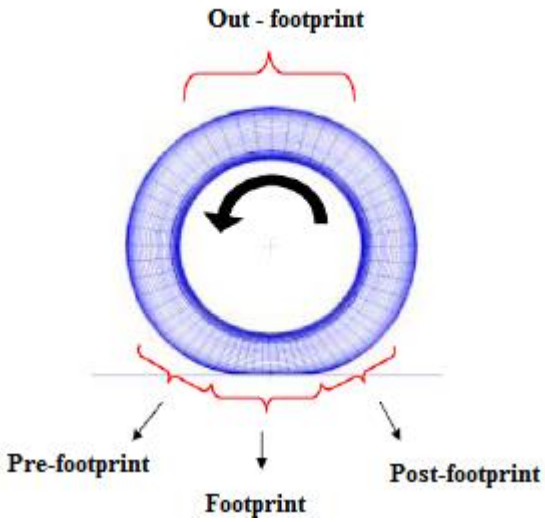

Figure 3.8 – Characteristic sectors of the wheel turn

From the analysis of accelerometer signals (in the first 3 zones) it is possible to extract indicators used both for estimating contact forces and as a basis for extracting more complex indicators.

These indicators can be divided, according to their physical meaning and independently of the signal analysed, into two macro-categories:

- Indicators related to the amplitude of the signals, obtained by studying the trend of the peaks of the signals or their peak-to-peak differences.
- Indicators related to the temporal duration of the signal, calculated instead by observing the temporal distance between two suitable reference points. The temporal delta thus observed is directly related to a spatial quantity.

3.4.1 Radial Signal

Among the three signals acquired, the one in the radial direction is the most robust and reliable in terms of repeatability [62].

The figure 3.9 shows the characteristics zones of wheel turn:

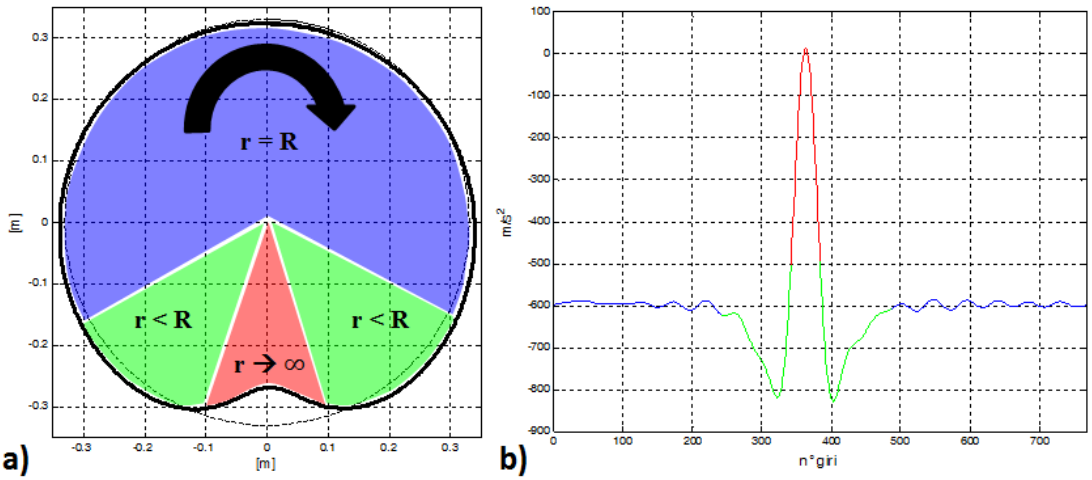

Figure 3.9 – a) Characteristic zones of a turn wheel b) Corresponding zones in a radial acceleration signal

During tyre rotation, the sensor is subjected to a radial acceleration comparable to that of a point that moves on a trajectory with a radius of curvature *r*.

Depending on the zone where the sensor is located, the curvature radius *r* takes on a different value:

- in the blue area, (zone out of tyre footprint) the value of *r* is equal to the value of the radius of the inflated tyre *R*.
- in the green area (Leading edge and Trailing edge of the tyre footprint) the deformations undergone by the covering lead to a decrease in the curvature radius r, with a consequent increase in radial acceleration.

- in the red area (in correspondence with the footprint) the rolling radius *r* tends ideally to infinity, with zero radial acceleration. This area is the one in which the maximum radial deformation occurs. The counter-curve visible in the footprint center can be associated more with the filtering operation than with the physics of the contact.

From the radial speed it is possible to obtain information on the shape of the contact footprint: the two peaks (minimum and maximum) present in the signal correspond to the entry and exit points of the sensor from the footprint (Figure 3.10 a).

Finally, the radial displacement (Figure 3.10 b) signal plays a very important role in defining the vertical load estimation.

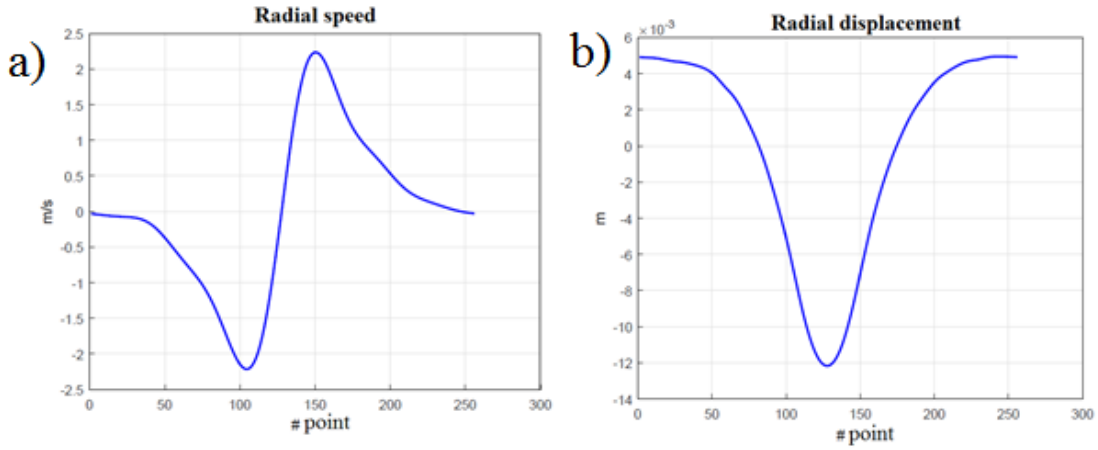

Figure 3.10 – a) Radial speed (post post-processing) b) radial displacement

3.4.2 Tangential signal

The accelerometric signal in tangential (or longitudinal) direction has a shape similar to that of the radial speed signal: in fact, it has two peaks, one of minimum and one of maximum, in correspondence with the zones of entry and exit of the sensor from the footprint. The first peak (minimum) is recorded in correspondence of the deformation undergone by the tyre at the entry footprint: here the sensor encounters a state of deformation (compression) which leads to a decrease in its rotation speed and to a consequent variation in tangential acceleration. Similarly, the second peak (maximum) is characterized by a state of deformation (extension) which is seen by the sensor (in its passage) as an increase in its angular velocity and a consequent further variation of the measured tangential acceleration (Figure 3.11 a).

3.4.3 Lateral signal

The lateral acceleration signal has a much less repeatable and constant form compared to the other two acquired values. Even its frequency spectrum is highly variable, and for these reasons, the extraction of indices is difficult [62]. Moreover, it is observed that, in conditions of drift angles imposed zero, a modest lateral acceleration is always measured due to phenomena such as ply-steer (Figure 3.11 b).

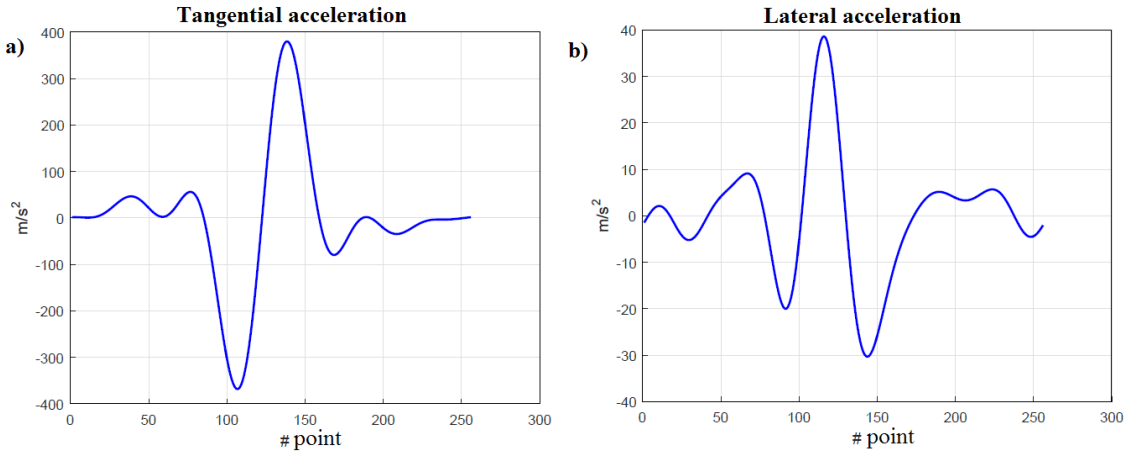

Figure 3.11 – a) Tangential acceleration b) Lateral acceleration

3.5 Statistical approach to the contact forces estimation

The contact forces estimation, takes place through a first phase in which characteristic quantities are identified, extracted from the analysis of the signals, which show a high degree of correlation with the forces themselves. A calibration procedure based on indoor tests brings to a calibration formula through a least square estimate on the calibration dataset. The choice of the calibration formula is based on experimental evidence obtained from indoor tests and on the analyst's experience.

A new approach to calibration has been developed in previous thesis activities [63] which allows many information from the data to be analysed methodically. It is based on the theory of multi-parameter linear regression models combined with an ANOVA (Analysis of Variance) and residue analysis [64] regression scheme.

3.5.1 Multiparameter linear regression methods

An application example of these techniques is summarized in the table 3.2. The regression algorithm, through suitable hypothesis tests, provides indispensable statistical information for the determination of the calibration formula and the multipliers of the indices contained therein (regressors). For a more detailed analysis of the method, see [57] and [64].

The use of these techniques is fundamental for the calibration phase: for each tyre specification used, the same as the interpolating polynomial, corresponds a set of multipliers (coefficients) of the specific regressors. The calibration procedure consists precisely, once the shape of the interpolating polynomial has been established, in calculating, through linear regression techniques, the multiplier coefficients, starting from datasets constructed with indoor tests.

Table 3.2 – Example of an ANOVA table for the statistical analysis of a linear regression model

Linear regression model:
Fz ~ 1 + omega:DR + DR:P + omega^2 + DR^2 + P^2

Estimated Coefficients:

	Estimate	SE	tStat	pValue
(Intercept)	1028.9	65.007	15.828	5.2251e-56
omega	5.3095	0.038295	138.65	0
DR	-1.9672e+05	1154.6	-170.38	0
P	-12.365	0.42747	-28.925	1.9984e-179
omega:DR	105.02	1.5908	66.018	0
DR:P	1804.7	3.3057	545.93	0
omega^2	-0.014473	0.00017404	-83.159	0
DR^2	-1.1519e+07	19464	-591.81	0
P^2	0.025246	0.00070476	35.822	1.5156e-270

Number of observations: 16234, Error degrees of freedom: 16225
Root Mean Squared Error: 35.9
R-squared: 1, Adjusted R-Squared 1
F-statistic vs. constant model: 8.32e+06, p-value = 0

Analysing in detail the table 3.1, the formula of the interpolating polynomial with which to estimate the quantity of interest is shown on the first line.

In the lower part are present:

- **Column 1**: list of regressors used within the interpolating polynomial.
- **Column 2**: value assumed by the multiplier coefficients of each regressor.
- **Column 3**: standard deviation of the coefficients.
- **Column 4**: *tSat* value associated with each individual coefficient. The *tSat* value is calculated as the ratio between the value of the coefficient itself and that of its standard deviation. Accurate estimates of the coefficient correspond to high *tSat* values.
- **Column 5**: value of the p-value associated with each coefficient. It represents the smallest significance level that leads to rejecting, in the hypothesis test on the single coefficient, the null hypothesis H0 (hypothesis that the coefficient is equal to zero and therefore that the significance of the relative covariate within the regression is negligible). The lower the value of the p-value, the greater the significance of the coefficient associated with it.

In the following lines there is then reported the number of observations contained in the regression dataset, the number of degrees of freedom of the error and its mean square value, the values of R^2 and R^2_{adj}, the term *fstat* and its relative *p- value*.

The terms R^2 and R^2_{adj}, positive and minor of the unit, represent the proportion between the variability of the data and the correctness of the statistical model used: the closer they are to unity, the more correct the model will be.

The formula of the interpolating polynomial in Table 3.2 was written using Wilkinson's notation, shown below (table 3.3):

Table 3.3 – Wilkinson notation

Wilkinson notation	Standard Notation	Type
$\boldsymbol{A + B}$	A, B	Single terms
$\boldsymbol{A \cdot B}$	A, B, A - B	Single plus interaction
$\boldsymbol{A{:}B}$	$A{\cdot}\,B$	Interaction only
$\boldsymbol{A^2}$	A, A^2	Single and square
$\boldsymbol{A \cdot B - B}$	$A, A{\cdot}\,B$	Subtraction of a term

In the final analysis, a further tool to verify the quality of the regression model is represented by the analysis of the residues. In applying a linear regression model, we hypothesize that the distribution of the residuals is Gaussian, that is, with zero mean and variance σ^2: the verification of the correctness of this hypothesis therefore allows us to receive further information on the goodness of the regression model.

This verification is usually carried out by observing the residual plots and the normal probability plot: from the first, particular residual trends are easily identifiable, a sign of their non-Gaussian distribution, while from the second it is possible to observe, through a histogram and a graph of the percentiles, the comparison between the distribution of residues and that of a normal with zero mean and variance σ^2.

3.5.2 Vertical load F_z

The vertical load estimation is carried out by observing the radial acceleration signal coming from the central sensor: from this it is possible to obtain quantities closely related to the radial deformation of the tyre (direct cause of the vertical force on it) and sufficiently disconnected from other external conditions (how could the radial signal coming from the external sensor be).

The quantities useful for vertical load estimation can be:

- **PL** (*patch length*): represents the length of the footprint calculated through the signals coming from the central sensor like

$$PL = \omega\, R\, \Delta t = \omega\, R \frac{N_{pi}}{f_s} \tag{3.3}$$

where ω is the angular speed in rad/s, R the rolling radius of the tyre, N_{pi} the number of samples acquired between the trailing edge and the leading edge of the footprint and f_s la sampling frequency with which the acquisition was made.

- **DR**: represents the minimum of the radial displacement and is calculated, at each wheel revolution, through the study of the radial displacement signal (obtained starting from the radial acceleration signal as described in 3.4.1).

Previous thesis work [57] has shown how the use of the DR regressor is able to give better and more robust results.

In the Figure 3.12 and 3.13 is possible to see how the trend of the *DR* regressor (depending on the vertical load) is less dispersed and noisy than the PL regressor.

Moreover, it is possible to notice that both have a strong dependence on the tyre inflation pressure: as the inflation pressure increases, the radial stiffness of the tyre increases and consequently the tyre deflection (and the patch length) is reduced to the same vertical load applied.

The typical formulation of the estimate polynomial for the vertical load is:

$$F_z = F_z(\omega, P, DR) \tag{3.4}$$

where ω is the angular speed (rad/s), P is the inflation pressure (kPa).

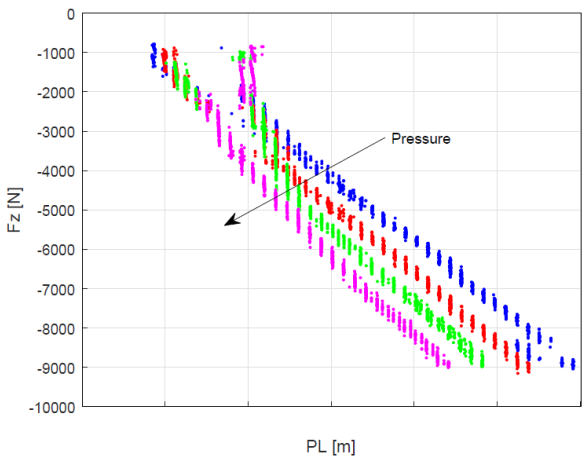

Figure 3. 12 – PL regressor as a function of the vertical load F_z and the inflation pressure P

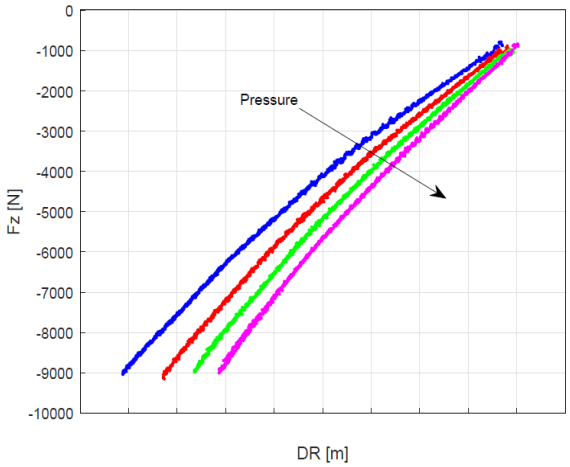

Figure 3. 13 – DR regressor as a function of the vertical load F_z and the inflation pressure P

3.5.3 Longitudinal Load F_x

Similarly to the estimate of the vertical load, also the longitudinal force is estimated through the study of the radial accelerometric signal. Observing the trend of the radial speed, the trailing edge and the leading edge of the footprint are easily identifiable, and the patch length can be estimated.

From the observation of this, it is easy to understand how the application of a longitudinal load involves a displacement of footprint in the direction of the applied force (Figure 3.14).

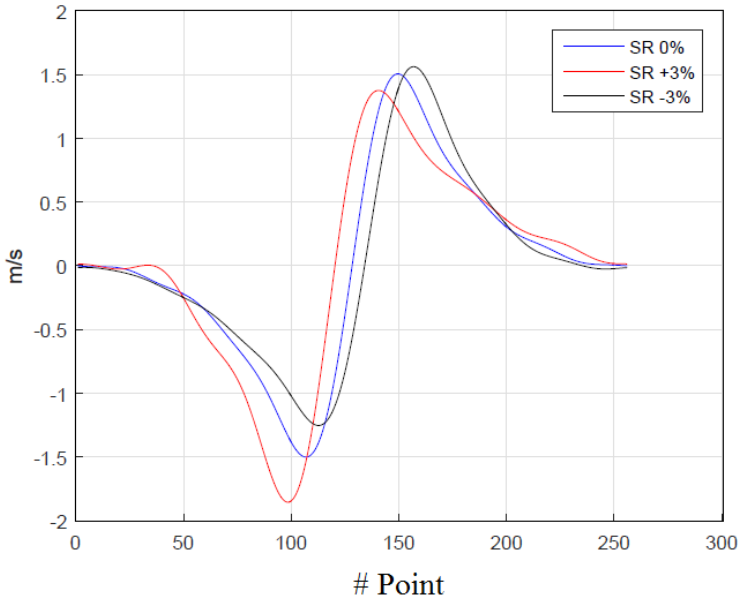

Figure 3.14 – Radial speed as the longitudinal slip varies (MTS indoor test at 100 km / h, vertical constant load at 5000 N, camber 0 °, slip angle 0 °)

The regressor studied for the estimation of the longitudinal load is indicated with *DRCV* is based on these considerations and is calculated as follows starting from the quantities obtained from the radial acceleration signal acquired by the central sensor:

$$DRCV = \frac{v_{r,out} - v_{r,in}}{2\omega R} \tag{3.5}$$

where $v_{r,out}$ and $v_{r,in}$ represent respectively the radial speed at trailing edge and the leading edge of the footprint, ω is the angular speed of the tyre in rad/s and R its rolling radius.

Figure 3.15 shows the trend of the longitudinal load in function of the *DRCV* regressor: it is noted that the points are decidedly more dispersed than the relation *vertical load-DR*.

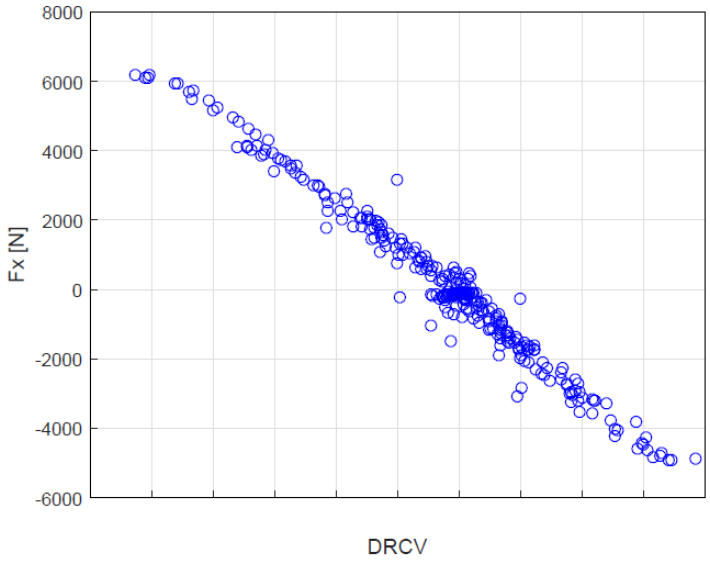

Figure 3.15 – Longitudinal load trend as a function of the DRCV regressor (MTS test of longitudinal sliding sweep at 100 km/h and 3 different vertical loads)

The typical formulation of the estimate polynomial for the longitudinal load is the following:

$$F_x = F_x(\omega, P, DRCV, DR) \tag{3.6}$$

where ω is the angular speed of the tyre in rad/s, P is the inflated pressure (kPa).

3.5.4 Lateral Load F_y

A study on the possibility of extracting information on the lateral load from the lateral accelerometric signal is reported in [63]. It is possible to extract indices from the lateral signal based on logics both double and single sensor, but without obtaining sufficiently robust results from an application point of view on outdoor tests.

The main causes can be identified as:

- High noise/signal ratio
- Poor repeatability of the signal spectrum with consequent difficulty in applying a filtering method
- It is necessary to eliminate (for calculation reasons) the first harmonic, with the consequent elimination of the Coriolis acceleration contribution [62].

The previous considerations led to the development of methodologies based on radial signal analysis, which proved to be the most robust and repeatable.

Analysis carried out with the finite element method made it possible to understand the state of deformation of the tyre (in the area corresponding to the contact footprint) following the application of a force in the lateral direction.

Two phenomena have emerged:

- Manifestation of a triangulation of the footprint in the load application direction (Figure 3.16)
- Generation of a three-dimensional deformation state

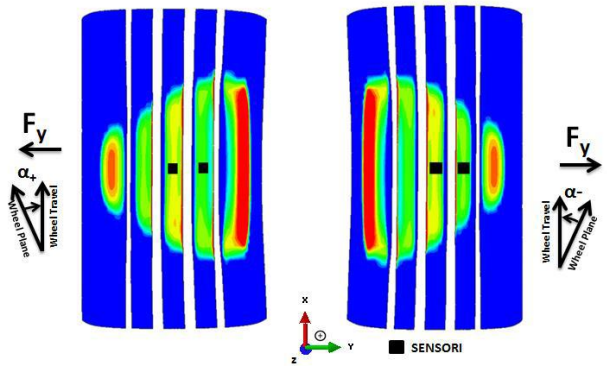

Figure 3.16 – Triangularization of the footprint by applying a load in a lateral direction

Consequently to these results, logics for the lateral load estimation based on the radial signal analysis acquired by several sensors positioned differently along the transverse direction of the liner, have been developed.

Considering a double sensor configuration, the regressor chosen for the lateral load estimation is the $PPV\ R_d$ and is calculated as:

$$PPV\ R_d = \frac{PPV\ R_c - PPVR_e}{\omega} \tag{3.7}$$

where ω is the angular speed (rad/s), $PPV\ R_c$ and $PPVR_e$ represent the peak-to-peak distance between maximum and minimum of the radial speed signal respectively measured by the central and internal sensors (Figure 3.17).

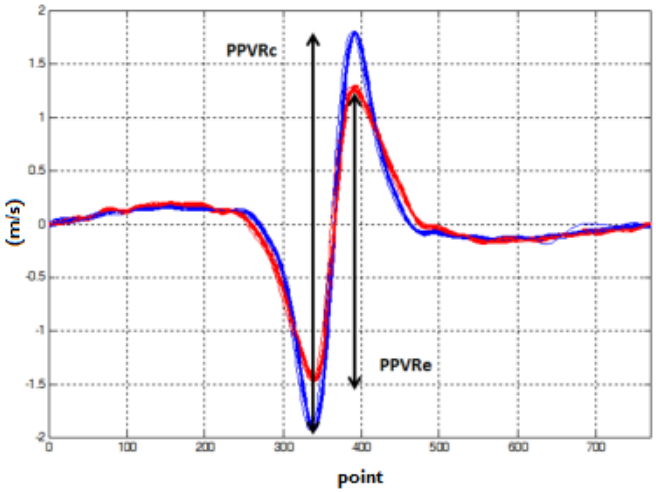

Figure 3.17 – PPV_R measured starting from the signals acquired by the central sensor (blue) and external sensor (red)

The Figure 3.18 shows the correlation between the regressor $PPV\ R_d$ and the lateral load.

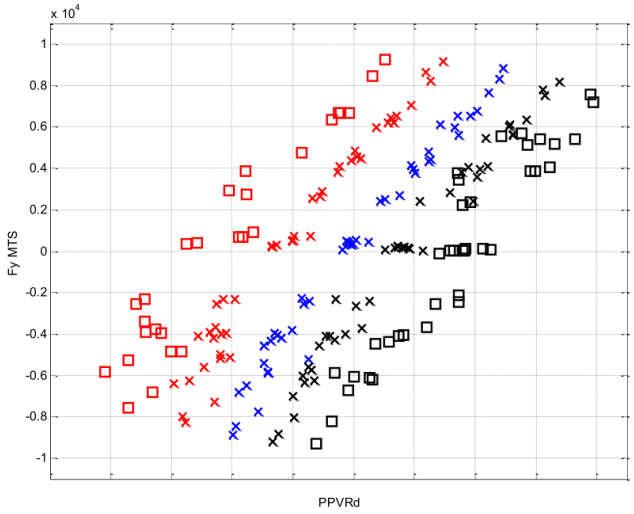

Figure 3.18 – Trend of lateral load F_y as a function of PPV Rd. MTS test with constant vertical load of 3000, 5000 and 7000 N, slip angle and camber variable. In red positive camber angles (crosses + 2 °, squares + 4 °), in blues null camber angles and in black negatives camber angles (crosses -2 °, squares -4 °) [62]

From this image we note the dependence of the camber angle on the lateral load (with equal drift and vertical load, a change in the camber angle leads to a change in the lateral force).

Previous studies ([57]) have introduced an additional regressor indicated by DR_r:

$$DR_r = \frac{DR_e}{DR_c} \tag{3.8}$$

This, based on a two-sensor logic (external and central), is calculated as the ratio between the DR obtained from the signals acquired from the external sensor (DR_e) and that obtained from the central sensor (DR_c).

Subsequent studies ([63]), have shown that the use of $PPV\ R_d$, DR_r and other indices allows obtaining a good estimate of the side load.

Further problems encountered in estimating the contact force in the lateral direction can be identified in the following causes:

- Presence of ply-steer and conicity phenomena: they lead to the presence of a non-zero lateral force even in null drift situations.
- Lack of correlation at some well-defined points for medium-low loads: phenomenon caused in situations of medium-low vertical load and high values of camber and drift, i.e. situations in which the lifting of the external sensor can occur.
- Sensitivity Variation of the $PPV\ R_d$ index with respect to the lateral force with the vertical load

3.6 Vertical Load calibration

Critical phase for the regression model creation is the data collection that will populate the starting dataset on which the model will be calibrated.

The data collected in these test are recorded both by the Cyber^{TM} Tyre system and by the flat belt machine: in this way it is possible to use, during the calibration of the model, the data collected by the machine (which can also measure the forces of contact) as the actual value of the estimated parameter. By comparing these data with the estimates made by the model, it will be possible to calibrate the multiplicative coefficients of the individual terms in the estimate polynomial.

3.6.1 The MTS Flat Track® machine and the of the Cyber^{TM}Tyre system measurement layout

The MTS Flat Track® (Figure 3.19) is a special machine specifically designed to test tyres: a peculiar feature is the presence of a flat belt in motion at a speed set by the user and controlled by the machine. The belt can be equipped with abrasive paper in order to simulate road friction. The tyre is mounted on a dynamometric hub that allows to measure the contact forces and moments involved between the belt and the tyre.

Figure 3.19 – MTS Flat Track® Machine

The machine can control in real time a series of quantities, shown in the table 3.4:

Table 3.4 – Measured quantities controlled in real time by the MTS Flat Track®

Quantities	**Symbol**	**Quantities**	**Symbol**
Slip Angle	α	Vertical load	F_z
Camber	γ	Longitudinal load	F_x
Slip ratio	ε	Lateral load	F_y
aligning torque	M_z	Overturning moment	M_x
Drive or braking torque	M_y	Angular speed	ω
Inflation pressure	P	Loaded radius	R_L
Rolling radius	R_r	Temperature	T

The tested tyres are all fitted with one or more sensor nodes, depending on the type of test to be performed. A specifically designed trigger system allows you to start the acquisition by both measurement systems (MTS and Cyber^{TM} Tyre) at the same time, thus making the comparison easier.

The types of tests carried out are the following:

- **Vertical load step** tests with speed, camber and slip angle controlled by the machine and with inflation pressure kept constant. The speed of execution of the manoeuvre is maintained such as to be able to assimilate the phenomenon as an almost static phenomenon. This type of test is used to calibrate the vertical load estimation model.

- **Slip angle sweep tests** with speed, vertical load and camber controlled by the machine and with inflation pressure kept constant. These tests are used for the calibration of the lateral force estimation model.

- **Slip ratio sweep tests** with speed, vertical load, drift and camber controlled by the machine and with inflation pressure kept constant. These tests are usually used for the calibration of the polynomial for estimating the longitudinal force.

Finally, reference and warm-up manoeuvres are carried out: the last ones are carried out with the aim of bringing the tyre to thermal steadiness.

In fact, the temperature influence on the tyre behaviour (during the tests just described) is often not negligible and of importance.

For asymmetrical tyres all tests are carried out for two rolling directions: clockwise and counter clockwise. This is due to the fact that the same tyre, if mounted on the left side or on the right side of the vehicle, given a fixed direction of advancement of the latter, experiences opposite rolling directions.

In the following chapters we focus on vertical load step tests and in particular on the temperature influence on the tyre behaviour.

3.6.2 Calibration phase: data collection procedures

Data collection campaigns, carried out for the calibration of the coefficients of its interpolating polynomial, are nowadays made up of vertical load step manoeuvres.

These tests, carried out on the MTS Flat Trac® machine, subject the tyre (instrumented with Cyber^{TM} Tyre system) to a series of vertical loading steps, generally from 1000 N to 9000 N (or in any case depending on the type of tyre).

During the test, the MTS machine keeps the tyre inflation pressure at a constant value, as well as the speed and other parameters, such as slip angle, camber angle and slip ratio. In particular, slip angle and slip ratio are kept null.

The loading steps are repeated for 4 different levels of inflation pressure and rotation speed.

In summary:

- 9 levels of vertical load
- 4 levels of speed (generally 50,100,150 and 200 Km/h)

- 4 level of inflation pressure (depending on the operating value at which the tyre will be working)
- 2 directions of rotation

In total there will be $9 \times 4 \times 4 \times 2 = 288$ tests.

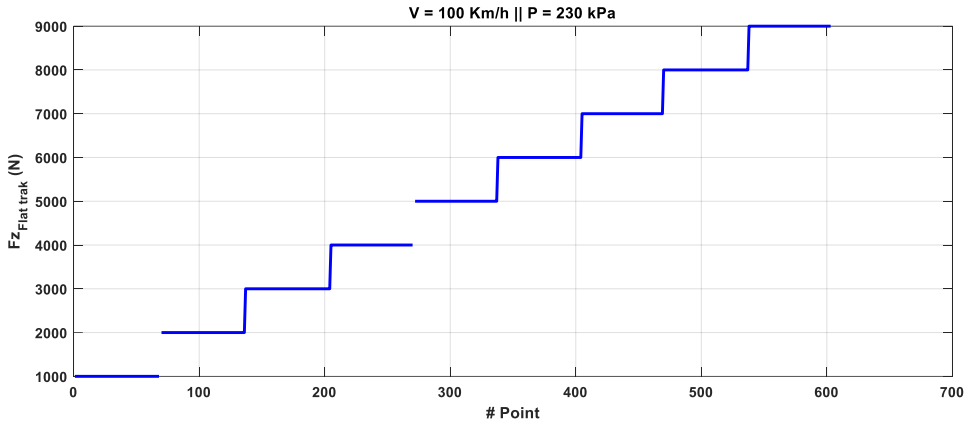

Figure 3.20 – Step of vertical load: V = 100 Km/h and P = 230 kPa

In order to increase test robustness and take into account the effects of uncertainty sources introduced by tyre itself (mainly uniformity) and the test setup, more than one sensor is used during calibration tests. Up to four sensors can be used.

3.6.3 Calibration phase: coefficients identification

Collected data, we apply the multiparameter linear regression method to characterize the regression formulas of forces.

As described in the previous chapters, the regressors that are most significant in vertical load estimation are:

- ***DR*** (minimum of the radial displacement)
- ***ω*** (angular speed)
- **P** (Inflation pressure)

The formula used to estimate the vertical load is:

$$F_z = \beta_0 + \beta_1\omega + \beta_2 D_R + \beta_3 P + \beta_4 \omega D_R + \beta_5 \omega P + \beta_6 D_R P + \beta_7 \omega^2 + \beta_8 D_R^2 + \beta_9 P^2 \qquad (3.9)$$

The *Stepwise regression with backward* technique is used. It is a stepwise regression approach that begins with a full (saturated) model and at each step gradually eliminates variables from the regression model to find a reduced model that best

explains the data. The stepwise approach is useful because it reduces the number of predictors, reducing the multicollinearity problem and it is one of the ways to resolve the overfitting.

The Figure 3.21 shows the result of the fitting model on one of the tyres analysed during the activity (the tyre model is not reported due to confidentiality).

Table 3.5 – ANOVA summary table

```
Linear regression model:
    Fz ~ 1 + DR_filtMain*P + DR_filtMain*omega + P*omega + DR_filtMain^2 + P^2 + omega^2

Estimated Coefficients:
                        Estimate          SE          tStat       pValue
                        ________    __________    _______    ____________

    (Intercept)           750.24        36.221     20.713     2.1693e-94
    DR_filtMain        -1.3342e+05        983.04    -135.72              0
    P                     -8.5381       0.25076    -34.049    1.3017e-247
    omega                  6.2413       0.12424     50.236              0
    DR_filtMain:P            1756        2.7342     642.25              0
    DR_filtMain:omega       43.944        2.3466     18.727     1.2235e-77
    P:omega              0.0029406    0.00033198     8.8576     8.7861e-19
    DR_filtMain^2      -1.0299e+07         20569    -500.72              0
    P^2                    0.017797    0.00044389     40.094              0
    omega^2               -0.035731    0.00042708    -83.664              0


Number of observations: 21767, Error degrees of freedom: 21757
Root Mean Squared Error: 58.4
R-squared: 0.999,  Adjusted R-Squared 0.999
F-statistic vs. constant model: 4.73e+06, p-value = 0


n° iteration = 6
```

In general, when applying a linear regression model, make a series of hypotheses among which the strongest concerns the Gaussian distribution of the residues [63].

The normal probability plot is the most effective tool for determining the normality of residues (Figure 3.22).

Another way to check the normality of the residues is to analyse the Q-Q plot. In this graph, the quantiles calculated on the actual observations (and therefore deriving from the regression model) are compared with those of a normal to zero mean. The points on the straight line with unitary slope satisfy this hypothesis.

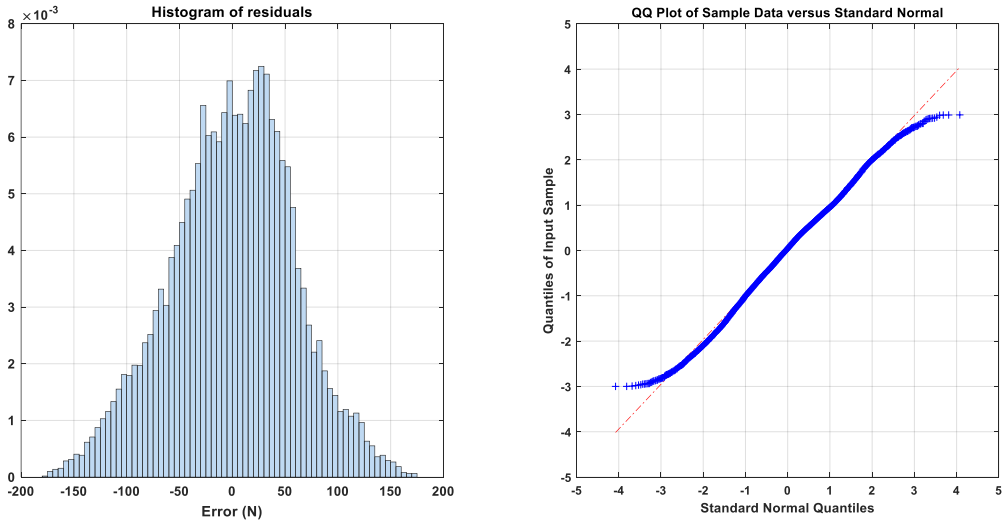

Figure 3.21 – Residual Histogram and QQPlot

In the figure 3.23 is reported the compare between the experimental F_z and the modelled F_z.

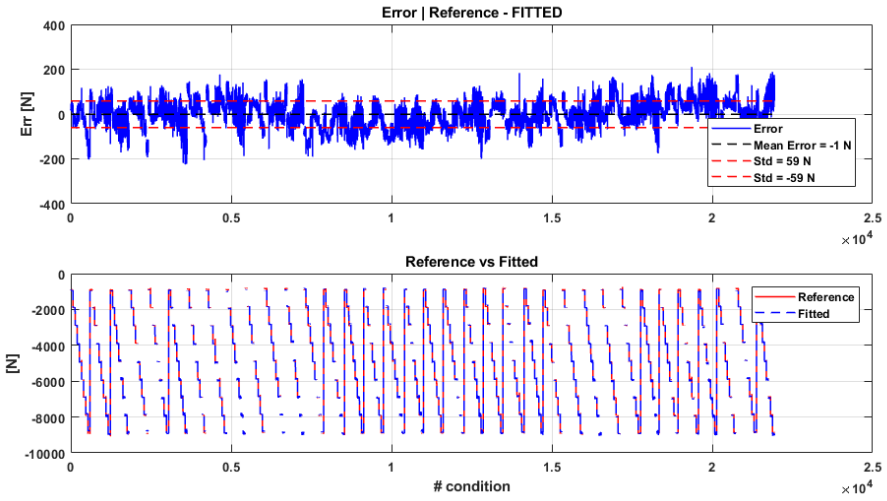

Figure 3.22 – Residual error and Reference Force vs Fitted Force

During the tests, the temperatures of some zones of the tyre are also measured (Figure 3.24).

In the same way we proceed for all the other tyres tested during this activity.

3.6.4 Tyre temperature influence on the DR regressor

The first investigations of the temperature effect on the DR regressor are reported in [62] and [65].

A test procedure consisting of a series of 12 continuous and identical F_z sweeps, performed at the velocity of 200 km/h and the same tyre internal pressure, in a free-rolling state and without a warmup is reported in [62].

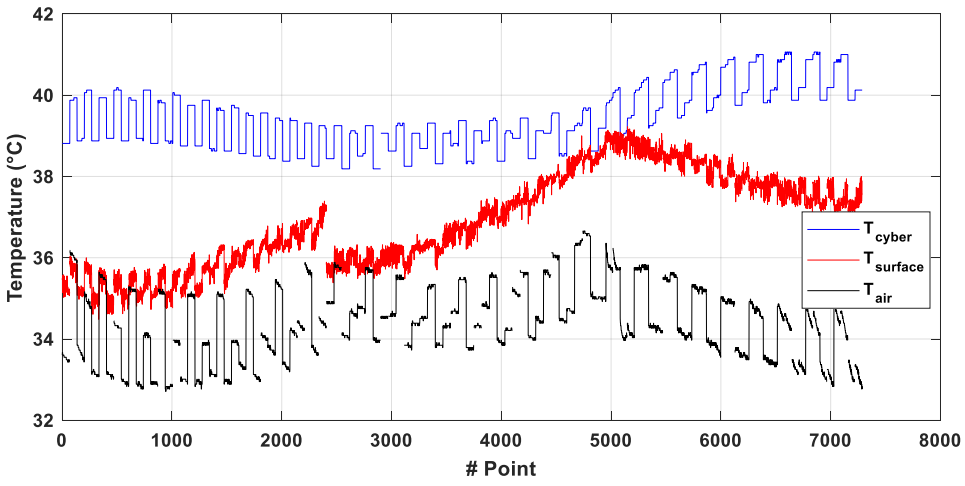

Figure 3.23 – Trend of the temperatures of some zones of the tyre

It follows the loading sweeps followed by a stretch of free rolling, lasting 10 minutes, at a constant vertical load equal to the reference load of the tyre and speed of 200 km/h.

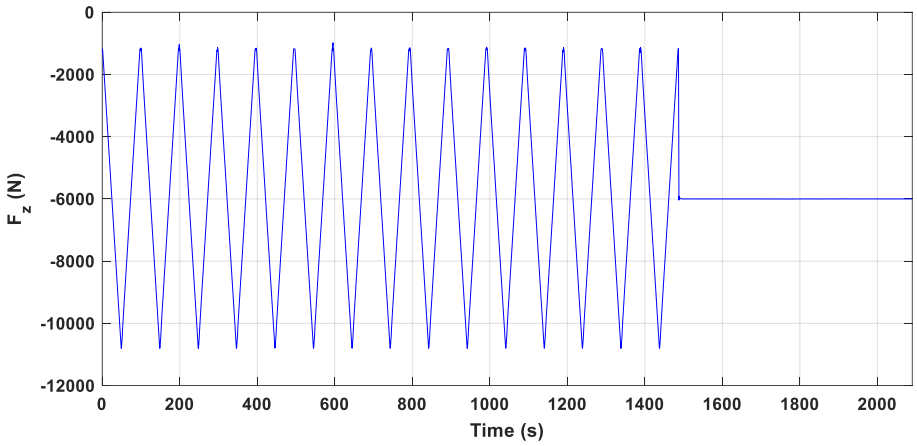

Figure 3.24 – Sweep of Fz: P = 250 kPa V = 250 km/h

Figure 3.26 shows the comparison between measured load and load obtained by polynomial for the considered test.

Analysing the input quantities of the polynomial (Figure 3.27), we note that the speed and the pressure remain constant (the test required it). On the other hand, by analysing the *DR* it is noticed that the maximum value increases passing from sweep 1 to sweep 15 (Figure 3.28).

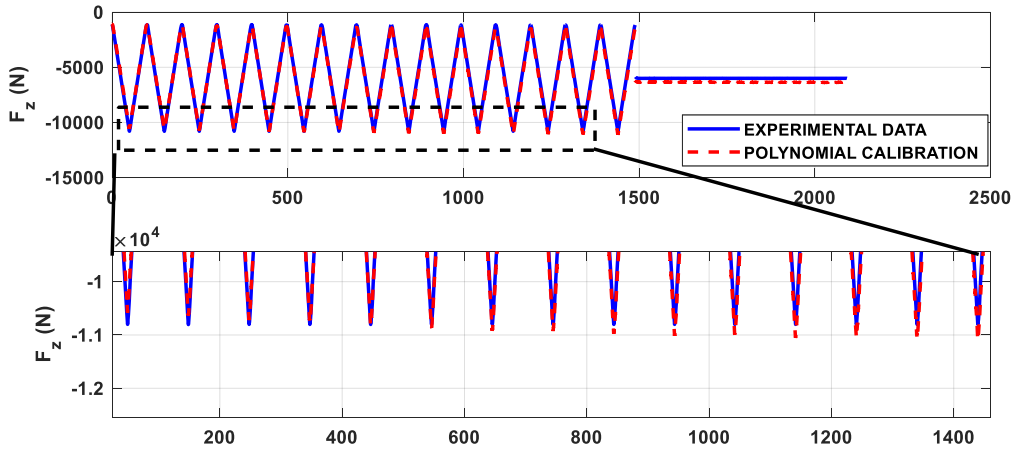

Figure 3.25 – Comparison between measured load and polynomial calibration

Analysing the input quantities of the polynomial (Figure 3.27), we note that the speed and the pressure remain constant (the test required it). On the other hand, by analysing the DR it is noticed that the maximum value increases passing from sweep 1 to sweep 15 (Figure 3.28).

Finally, analysing figure 3.29 it can be seen that at the time moments for which the temperature is lower than the calibration temperature, the polynomial tends to underestimate the vertical load. Vice versa at the time moments for which the measured temperature is greater than that of calibration. The error is minimal precisely at the calibration temperature.

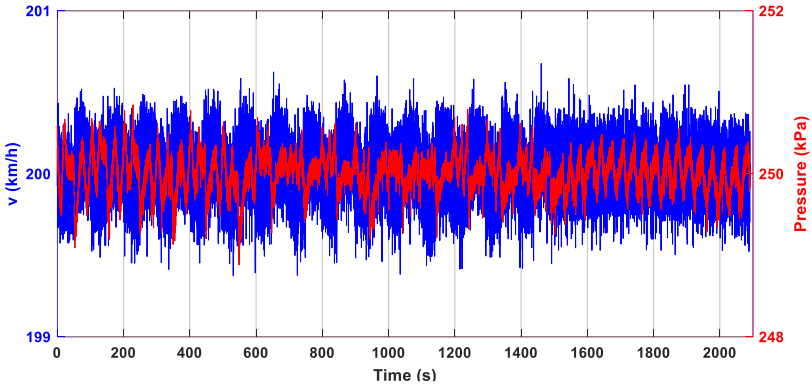

Figure 3.26 – Pressure and speed during the test

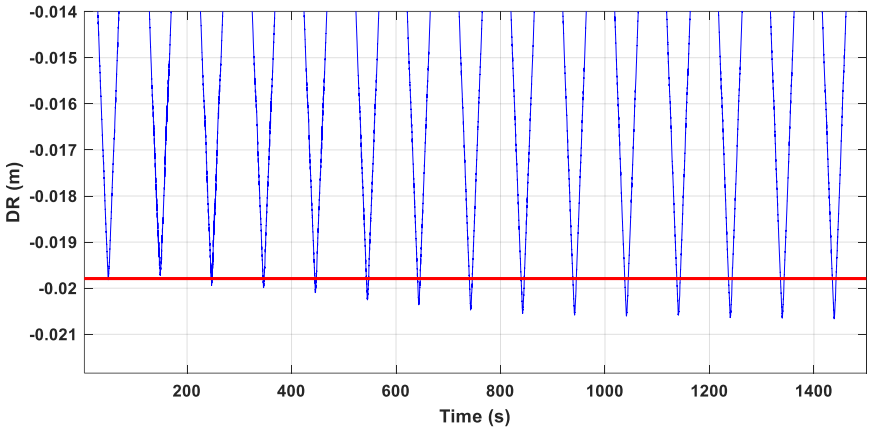

Figure 3.27 – DR trend during loading sweeps

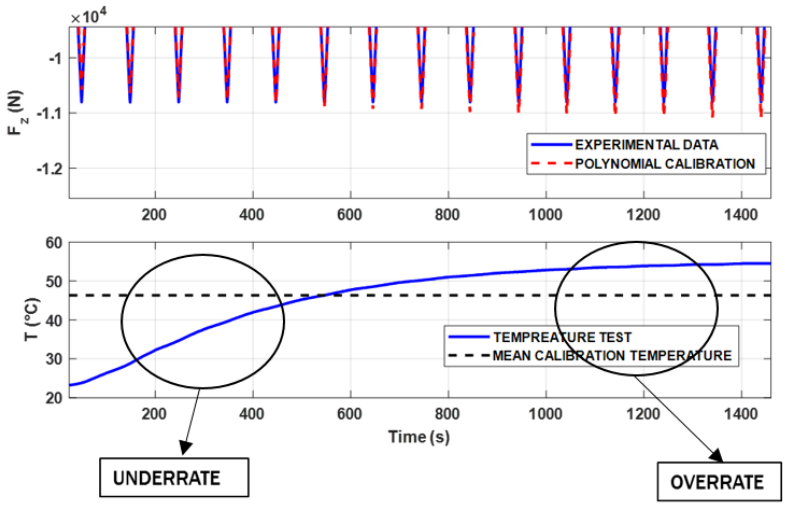

Figure 3.28 – Temperature measured during the sweep test compared to the same during calibration tests

The importance of considering the temperature in the estimation of the vertical load is also clear. Furthermore, as seen in 2.6, braking stiffness and cornering stiffness are also strongly influenced by it.

The work is structured as follows:

- Development of a thermal model which, by exploiting some inputs coming from the cyber tyre, allows to evaluate the temperature of the various zones of the tyre.
- Study of the effect of temperature on the behaviour of the tyre, preliminarily on the normal interaction characteristic, in order to identify the temperature of the area of the tyre that mostly correlates with the phenomenon.

Thanks to the thermal model, it is possible to obtain the temperature (indicated with T_{eq}) that most correlates to the phenomenon using the diagram shown in the Figure 3.30.

Moreover, the tyre interaction stiffness and transient behaviour variation are deeply linked with thermal effects concerning the deepest tyre layers.

Furthermore, the tyre tread bulk temperature, usually not measurable online but providable by means of a specifically developed tyre thermal model, is a crucial additional data channel to evaluate the tyre optimum thermal range and therefore to optimize the tyre performance in different ambient conditions and upon diverse track pavements.

In the next chapter we will discuss the development of the thermal model and all the steps that led to its validation (indoor and outdoor tests).

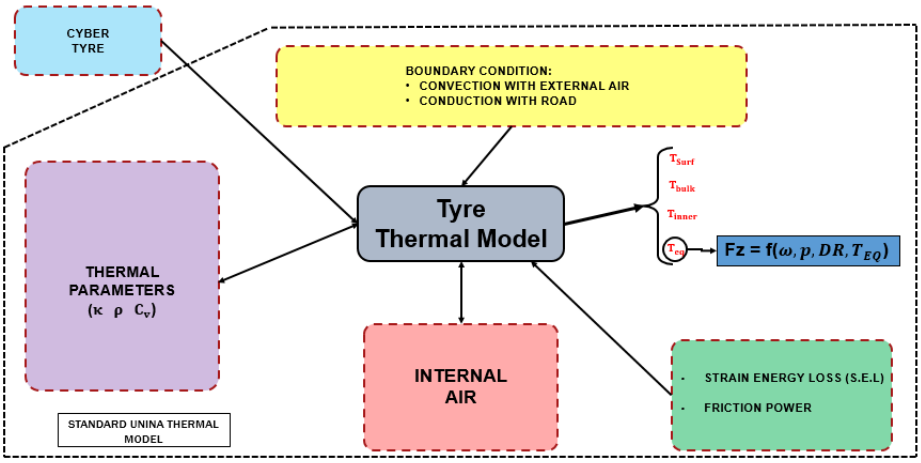

Figure 3.29 – Flow diagram of the thermal model

Chapter 4

The Thermal model

4.1 Introduction

In this chapter a thermal model is developed which, by receiving some information coming from the Cyber^{TM} tyre, allows to evaluate the temperature of the various zones of the tyre. One of the main advantages of having a thermal model is that of being able to evaluate the temperature of some zones of the tyre that can hardly be measured using sensors (such as bulk temperature) and which, however, have a great influence on the tyre behaviour.

The development of this thermal model requires some activities:

- **Cyber^{TM} Tyre thermal characterization**: thermal parameters identification such as *density* ρ, *specific heat* c_v and *thermal conductivity k* of the sensor node + rubber house
- **Tyre thermal characterization**: thermal parameters identification such as *density* ρ, *specific heat* c_v and *thermal conductivity k* of the tyres analysed during this activity
- **Indoor rolling resistance tests**: In order to characterize the S.E.L
- **Indoor MTS Flat Trac® tests**: In order to characterize the natural convection
- **Outdoor tests**: In order to characterize the forced convection and the conduction with road

The main feature that this thermal model must have is that it must be implemented on a control unit (VEU) to work in real time.

This is the reason for some choices regarding the discretization of the tyre made in order to find a trade-off between reliability and computational burden.

4.2 Physical thermal model

The developed thermodynamic tyre model is based on the use of the diffusion equation of Fourier applied to a three-dimensional heterogeneous domain [66] [67]

$$\frac{\partial T}{\partial t} = \frac{\dot{q}_G}{\rho \cdot c_v} + \frac{1}{\rho \cdot c_v}\left(\frac{\partial^2 k(x,y,z,T)\cdot T}{\partial x^2} + \frac{\partial^2 k(x,y,z,T)\cdot T}{\partial y^2} + \frac{\partial^2 k(x,y,z,T)\cdot T}{\partial z^2}\right) \quad (4.1)$$

Where:

- $\dot{q}_G$ is the energy generation rate per unit per unit volume (W/m^3)
- ρ is the density of material (Kg/m^3)
- c_v is the specific heat of material (J/KgK)
- k is the thermal conductivity of material (W/mK)
- x, y, z are the coordinates of the points

When studying the tyre from a thermal point of view, the following phenomena must be addressed (as represented in the Fig. 4.1):

- heat generation due to tyre-road tangential interaction, known as Friction Power
- heat generation due to effect of tyre cyclic deformation during the rolling, known as SEL (Strain Energy Loss)
- heat exchange with the external environment due to thermal conduction between the tread and the road
- heat exchange with the external environment due to convection of the tread layer with the outside air
- heat exchange with the external environment due to convection of the innerliner layer with the inner air
- heat conduction between the tyre layers due to the temperature gradient

From a thermal point of view the tyre can be schematized in three layers (Figure 2.19):

- Surface
- Bulk;
- Inner.

that is the external surface, the carcass and the internal surface.

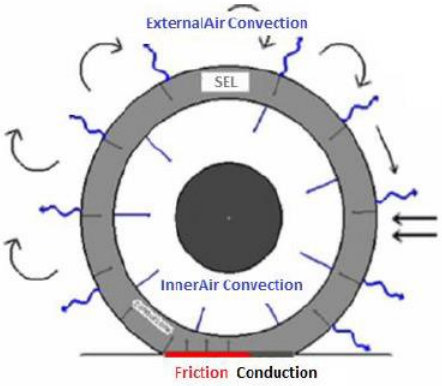

Figure 4.1 – Different heat phenomena occurring at a tyre during operation and divided in heat generation and heat exchange

This subdivision is linked to the temperatures that we are interested in knowing about the tyre system. These are the temperatures that influence the behaviour, increasing or less the grip and therefore the maxima forces occurring in the contact area between road and surface.

In order to modelling the tyre from point of thermal view, the following hypotheses are made:

- The road is isotropic and homogeneous in all its features, without irregularities, schematized as a geometric plane whose surface temperature is equal to Tr
- The tyre is considered as unrolled in the circumferential direction; therefore, it has a parallelepiped shape, without sidewall and grooves, divided into a series of parallelepiped-shaped elements.
- A Cartesian reference system is chosen with coincident origin in a vertex of the parallelepiped, *X axis* with the same direction in which the tyre is unrolled
- The contact area is considered as rectangular, with a width equal to W (equal to the width of the tread) and length La, depending on the radial rigidity of the tyre and the normal load.
- Radiation exchange mechanisms are neglected.

4.2.1 The Tyre and Cyber^{TM} Tyre discretization

The tyre is considered as unrolled in the circumferential direction (and then parallelepiped-shaped), lacking sidewalls and grooves (so the tyre is modelled as slick), discretized with series of nodes representing the points in which the temperature will be determined instant by instant.

In the standard thermal model developed by UniNa, the tyre is discretized by means of a grid and the parallelepiped was constituted by three layers in the radial direction (Figure 4.2).

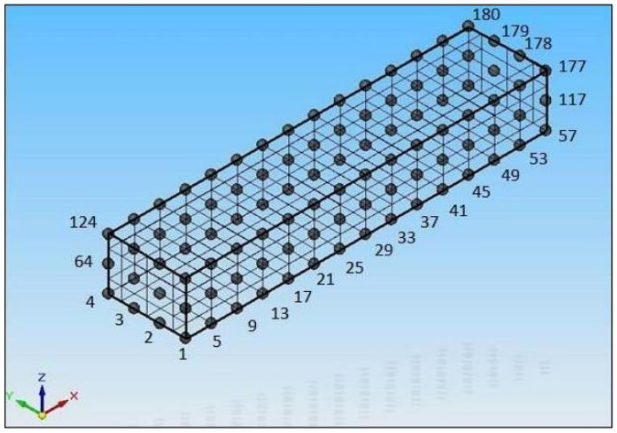

Figure 4. 2– Discretization of the tyre in the standard thermal model

In this application, to reduce the computational burdens, it was decided to discretize the entire tyre with 3 layers (surface, Bulk and Inner) and 6 masses (Figure 4.3)

- 3 masses represent the part below the rubber house
- 3 masses represent the remaining part

The cyber tyre^{TM} system, including the Sensor Node and the rubber house, was modelled with 5 masses (Figure 4.3). This last choice is linked to the strong heterogeneity of the sensor node (in terms of thermodynamic properties).

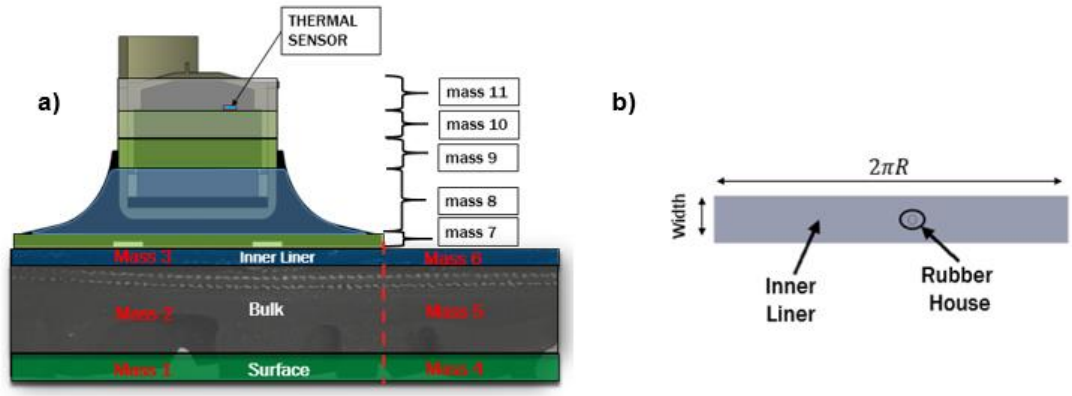

Figure 4.3 – Tyre and Cyber tyre^{TM} discretization a); unrolled tyre concept b)

The equation 4.1 is solved using the finite difference method arriving at a system of 11 coupled differential equations.

In typical state form:

$$\begin{Bmatrix} \frac{\Delta T_1}{\Delta t} \\ \frac{\Delta T_2}{\Delta t} \\ \vdots \\ \frac{\Delta T_{11}}{\Delta t} \end{Bmatrix} = \begin{Bmatrix} b_1 \\ b_2 \\ \vdots \\ b_4 \end{Bmatrix} + \begin{bmatrix} a_{1,1} & \cdots & a_{1,11} \\ \vdots & \ddots & \vdots \\ a_{11,1} & \cdots & a_{11,11} \end{bmatrix} \begin{Bmatrix} T_1 \\ T_2 \\ \vdots \\ T_{11} \end{Bmatrix} \tag{4.2}$$

For the writing of the equations we must consider that:

- The mass 1 exchanges heat by conduction with the mass 4, the mass 2, part of it with the road and part of it exchanges heat by convection with the external air;
- The mass 2 exchanges heat by conduction with the mass 1, the mass 3 and the mass 5;
- The mass 3 exchanges heat by conduction with the mass 2, the mass 6 and the mass 7;
- The mass 4 exchanges heat by conduction with the mass 1, the mass 5 part of it with the road and part of it exchanges heat by convection with the external air;
- The mass 5 exchanges heat by conduction with the mass 4, the mass 2 and the mass 7;
- The mass 6 exchanges heat by conduction with the mass 3 and exchanges heat by convection with internal air;
- The mass 7 exchanges heat by conduction with the mass 3, the mass 8 and exchanges heat by convection with internal air;
- The mass 8 exchanges heat by conduction with the mass 7, the mass 9 and exchanges heat by convection with internal air;
- The mass 9 exchanges heat by conduction with the mass 8, the mass 10 and exchanges heat by convection with internal air;
- The mass 10 exchanges heat by conduction with the mass 9, the mass 11 and exchanges heat by convection with internal air;
- The mass 11 exchanges heat by conduction with the mass 10 and exchanges heat by convection with internal air;

Moreover, in the equations related to masses 1 and 4 the term friction power appears while in the equations related to masses 2 and 5 the term strain energy loss appears.

Therefore, for example, the equation for mass 1,2 and 6 becomes:

$$\rho_{srf} \cdot C_{v,srf} \cdot V_1 \cdot \frac{\Delta T_1}{\Delta t} = \frac{k_{1,2}}{\Delta \mathrm{zm}_{,1,2}} \cdot (T_2 - T_1) \cdot A_{cond,1,2} + 2 \cdot \frac{k_{surf}}{\Delta \mathrm{xm}_{1,2}} \cdot (T_4 - T_1) \cdot A_{cond,1,4} + H_{ext} \cdot (Tair_{ext} - T_1) \cdot A_{conv,1} + H_c \cdot (T_r - T_1) \cdot A_{cont} + C_R \cdot (F_x \cdot v_{sx}) + C_R \cdot (F_y \cdot v_{sy}) \quad (4.3)$$

$$\rho_{blk} \cdot C_{v,blk} \cdot V_2 \cdot \frac{\Delta T_2}{\Delta t} = \frac{k_{1,2}}{\Delta \mathrm{zm}_{,1,2}} \cdot (T_1 - T_2) \cdot A_{cond,1,2} + 2 \cdot \frac{k_{blk}}{\Delta \mathrm{xm}_{2,5}} \cdot (T_5 - T_2) \cdot A_{cond,2,5} + \frac{k_{2,3}}{\Delta \mathrm{zm}_{,2,3}} \cdot (T_3 - T_2) \cdot A_{cond,2,3} + S.E.L \quad (4.4)$$

$$\rho_{inn} \cdot C_{v,inn} \cdot V_6 \cdot \frac{\Delta T_6}{\Delta t} = \frac{k_{5,6}}{\Delta \mathrm{zm}_{,5,6}} \cdot (T_5 - T_6) \cdot A_{cond,5,6} + 2 \cdot \frac{k_{inn}}{\Delta \mathrm{xm}_{3,6}} \cdot (T_3 - T_6) \cdot A_{cond,3,6} + H_{int} \cdot (Tair_{int} - T_6) \cdot A_{conv,6} \quad (4.5)$$

where:

- C_R is the heat partition coefficient [68]. It takes into account the percentage of the generated friction power that effectively warms up the tyre. The rest of this power flows into the road
- H_{ext} is the convection coefficient relative to the exchange with external air [W/m^{2}K]
- H_{int} is the convection coefficient relative to the exchange with internal air [W/m^{2}K]
- H_c is the track-tyre exchange coefficient [W/m^{2}K]
- Tr is the track temperature
- $Tair_{ext}$ is the external air temperature
- A_{cont} is the contact patch
- $A_{conv,i}$ is the area related to exchange by convection of the mass-i

The terms $k_{1,2}$, $k_{2,3}$ etc. are the equivalent thermal conductivity evaluated by 4.6 considering the Figure 4.4.

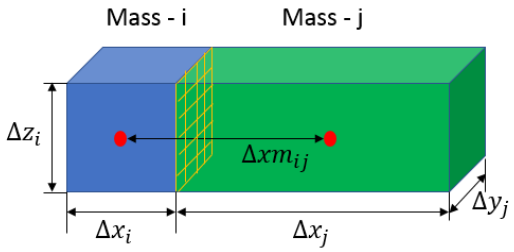

Figure 4.4 – Heat exchange between mass-i and mass-j

The mass-i and the mass-j exchange heat by conduction through the interface (yellow lattice in the Figure 4.4) whose area is equal to: $A_{cond,i,j} = \Delta y_i \cdot \Delta z_i = \Delta y_j \cdot \Delta z_j$.

$$k_{i,j} = \frac{1}{\frac{\Delta x_i}{2 \cdot k_i} + \frac{\Delta x_j}{2 \cdot k_j}} \cdot \Delta xm_{i,j} \tag{4.6}$$

where $\Delta xm_{i,j}$ is the distance between the between the barycenter of the two masses:

$$\Delta xm_{i,j} = \frac{\Delta x_i}{2} + \frac{\Delta x_j}{2} \tag{4.7}$$

Similarly, $\Delta zm_{i,j}$ is the is the distance between the between the barycenter of the two masses along the *z* direction.

The thermal parameters are identified with a method developed by Department of Industrial Engineering of University of Naples Federico II illustrated in 4.3.

In a first phase of the activity we concentrate only on the part relating to the SEL. In a second phase the term relating to friction power will also be introduced.

4.3 The Thermal Parameters evaluation

The Department of Industrial Engineering of University of Naples Federico II has conducted an interesting activity on the thermal conductivity evaluation through indirect measurements on tyre [69].

The concept is to use a particular in-house thermal model [70]to identify an equivalent thermal conductivity able to simulate the thermodynamically behavior of the entire tyre.

As known the tyre is a composite material characterized by different layers with different properties: different synthetic rubbers for tread, under-tread etc., plastic fibers (rayon, nylon etc.) for carcass, steel for belt and others.

Even if each of these materials is characterized by different thermodynamically properties, the experimental activity conducted by DIME showed that the thermodynamic behavior can be well described using a finite number of equivalent thermal conductivities.

The heat is directly supplied on the tyre tread surface trough a specifically powered laser, while two thermal cameras acquire temperatures reached on both the outer and the inner layers. Using the above instrumentation layout to acquire the tyre radial and circumferential temperature gradients and a specifically developed mathematical TRTLab model based on the use of Fourier's equation of diffusion applied to a three-dimensional domain, allows to estimate the tyre thermal diffusivity.

As represented in Fig. 4.5, a 2D plant of the experimental test rig layout, specifically designed for this purpose, is consists of the following instrumentation:

- a specific powered laser emitter, pointing on the tyre tread layer
- two IR cameras, directly facing the interior and the exterior tyre surfaces, to measure the both tread and inner-liner circumferential temperature gradients
- two IR cameras, directly facing the interior and the exterior tyre surfaces, to measure the both tread and inner-liner circumferential temperature gradients
- a convergent lens, placed between the laser emitter and the tyre, to obtain a constant laser beam diameter of 10 mm upon the tread surface

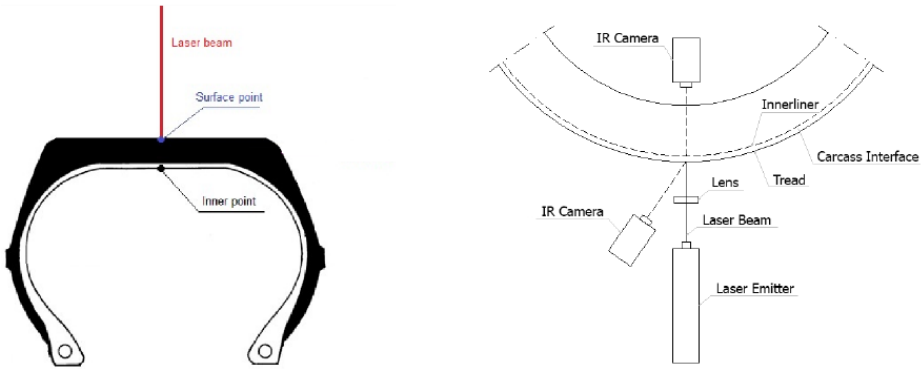

Figure 4.5 - Tyre thermal characterization layout

The tyre tread external layer is warmed-up with different power values in steady state conditions by a continuous Argon laser.

The laser emitter used for the test procedure is an argon ion Stabilite 2017 (Figure 4.6), produced by Spectra-Physics company. The tread surface is heated via the laser beam, expanded and collimated with the lens, with a specifically developed power values sequence, ranged between 0.5-2W.

The Laser emitter (in the Fig. 4.6a) consists of a controller, power supply and laser head, where the last two components have to be fluid-cooled, needing a supplemental water tube connection.

The IR thermocamera adopted is FLIR E60. In addition to the temperature trend acquisition of the inner and outer tyre surfaces, their specific purpose is the detecting the area of the circumferential temperature gradient extension to correctly choose the value of the tyre portion to mesh within the TRTLab model afterwards.

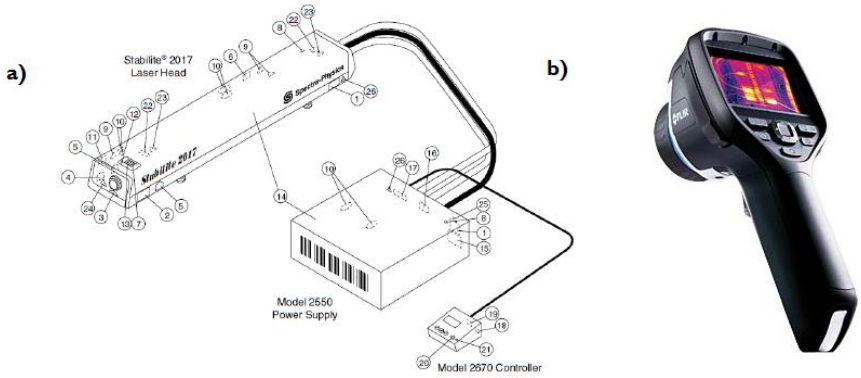

Figure 4.6 – Thermal test rig instrumentation: a) Laser emitter b) IR camera

Before performing the tests, all the tyre surfaces, interest of IR measure, are properly cleaned and an accurate value of the laser power emitted is measured using a power meter with an accuracy ±0.1%.

4.3.1 Data Acquisition and Processing

A standard test consists of three principal steps:

- idle phase: laser is switched off; a correct functioning of all the instrumentation is monitored
- heating phase: laser emitter is turned on; the heat propagation in all directions is acquired. During this step, transient temperature trends are particularly relevant to evaluate the node inertia values [71] within the TRTLab model and to estimate the thermal diffusivity as a function of temperature. The heating phase finishes when all the temperature gradients are stable with no more significant heat exchanges in time between the different tyre layers
- cooling phase: laser is switched off; the natural convection remains the only heat transport mechanism within the tyre thermal system

These tests were carried out both on the only Cyber^{TM}Tyre (Figure 4.7) and on the Cyber^{TM}Tyre fixed onto the inner liner (Figure 4.8).

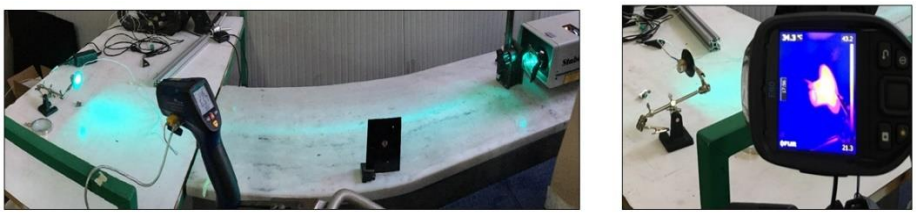

Figure 4.7 – Thermal tests carried out on the cyber tyre

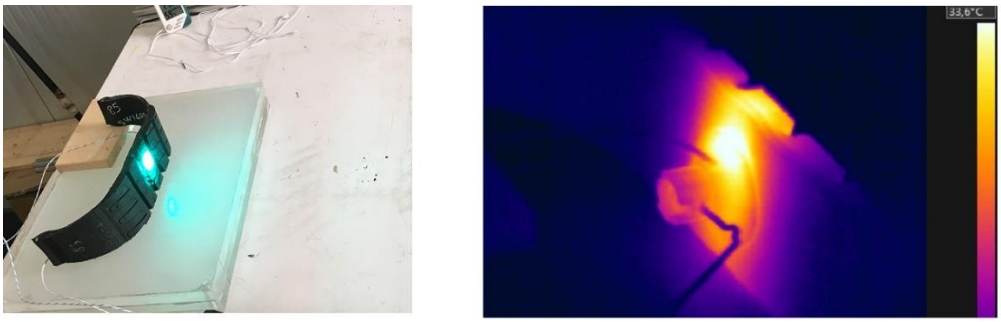

Figure 4.8 – Thermal tests carried out on the cyber tyre fixed to inner liner

Figure 4.9 shows the temperature trend for different laser power levels. T_{RH} is the temperature of the rubber house where the laser beam impacts while T_{cyber} is the temperature of the sensor node.

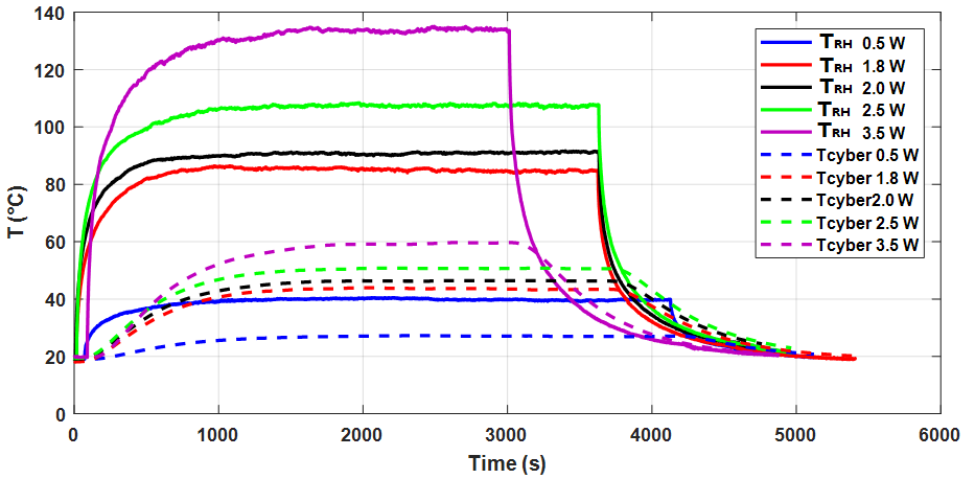

Figure 4.9 – Temperatures trend for different laser power levels (only cyber tyre)

In the case of thermal characterization of tyre + sensor node, 4 different spec have been analysed whose names are not reported for reasons of confidentiality and which are therefore indicated with $tyre_1$, $tyre_2$, $tyre_3$ and $tyre_4$ (Figure 4.10).

The data acquired with IR cameras have been processed using the "FLIR IR Research software" with an accuracy ±0.1 ◦C.

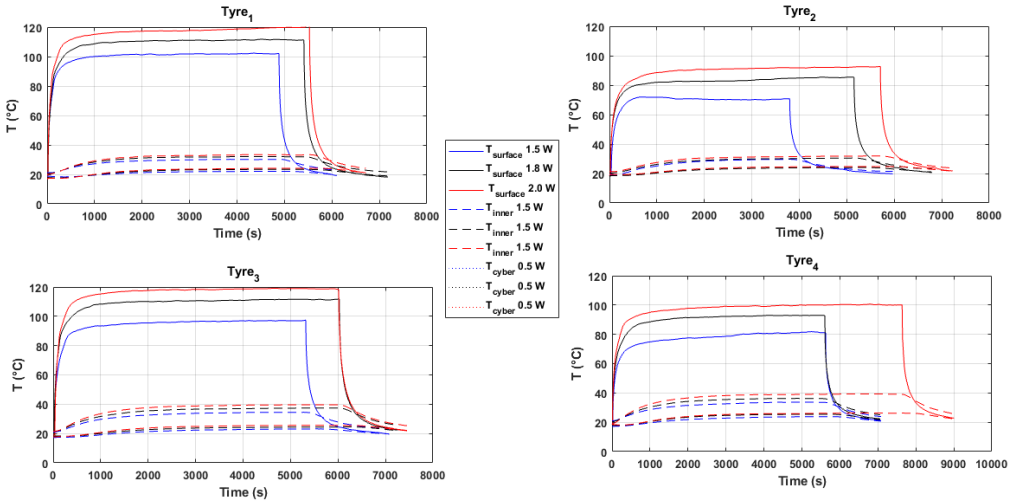

Figure 4.10 – Temperatures trend for different laser power levels (Tyre + sensor node)

4.3.2 TRTLab model

Each tyre is distinct considering both the structural characteristics and the peculiar thermal properties, so that a specific set of physical parameters has to be identified to properly describe the tyre thermo-inertial behaviour [72] [73].

The evaluation of the thermal diffusivity is complicated and delicate, since the whole tyre thickness consists of a highly composite structure where different layers wit disparate characteristics interact with each other throughout the heat propagation. Additionally, it has to be highlighted that the intrinsic temperature dependence also represents complicating matter.

Moreover, this is precisely why the TRTLab model needs the greatest possible number of tests at different laser powers to have more data in transient and steady state conditions to evaluate both the physical diffusivity of different tyre layers and the tyre thermal inertias.

Thermo Racing Tyre Laboratory model version is derived on the basis of a second order differential equation able to describe the thermal phenomenon dynamics, particularly suitable to be integrated numerically [74]:

$$q = -k\nabla T \tag{4.8}$$

Applying the first thermodynamics law to an infinitesimal volume dV_i and applying the Gauss theorem (so that a surface integral governing the heat exchange surface term becomes a volume integral), the expression of the Fourier's diffusion equation can be carried out:

$$\rho \cdot dV \cdot c_v \cdot dT = \dot{q_g} \cdot dV + div(k \cdot \nabla T) \cdot dV \cdot dt \tag{4.9}$$

To be numerically integrated, the above equation is rewritten in a state-space representation matrix form, as follows:

$$\frac{\partial T}{\partial t} = \frac{\partial \dot{q_g}}{\rho \cdot c_v} + \frac{div(k \cdot \nabla T)}{\rho \cdot c_v} \tag{4.10}$$

The heat generation term $\dot{q}_g$ in Eq. 4.18 is related to the laser thermal flux at the tread nodes. Supposing negligible the radiation mechanism, the tyre heat exchanges with the external environment become the following:

- Natural Convection
- Laser Beam

4.3.2.1 Natural Convection

Natural convection is a heat transport mechanism, in which the fluid motion is not externally generated since it is the consequence of the density differences due to the temperature gradient within the fluid [75]. A dimensionless Grashof number governs the flow regime in natural convection, representing the ratio of buoyant forces to viscous ones, so that it provides the main criterion to discriminate laminar and turbulent flows:

$$Gr = \frac{g\beta(T_{terad} - T_\infty)\delta^3}{\nu^3} \tag{4.11}$$

where:

- g is gravity acceleration $\left(\frac{\mathrm{m}}{\mathrm{s}^2}\right)$
- β is the cubic expansion coefficient of the fluid $\left(\frac{1}{\mathrm{K}}\right)$
- δ is the characteristic length of the problem in exam (m)
- T_{terad} is the surface temperature (K)
- T_∞ is the air temperature
- ν is the air kinematic viscosity $\left(\frac{\mathrm{m}^2}{\mathrm{s}}\right)$

The natural convection thermal exchange term between the tyre tread and inner-liner surfaces and the surrounding fluid is equal to:

$$\dot{Q}_{conv} = h_{nat} \cdot A \cdot (T_{tread} - T_\infty) \tag{4.12}$$

where:

- h_{nat} is the mean coefficient of thermal exchange of the surface for natural convection
- A is the heat exchange surface area

Natural convection coefficient h is obtained by the dimensionless analysis, as follows:

$$h_{nat} = \frac{Nu \cdot k_{air}}{\delta} \tag{4.13}$$

The simplest empirical relation to express the Nusselt dimensionless number *Nu* considers the geometry characteristics, the Rayleigh number *Ra* and the Pradtl number *Pr*:

$$Nu = \left\{ 0.825 + \frac{0.387 \cdot Ra^{\frac{1}{6}}}{\left[1 + \left(\frac{0.492}{Pr}\right)^{\frac{9}{16}}\right]^{\frac{8}{\pi}}} \right\}^{2} \tag{4.14}$$

4.3.2.2 Laser Beam

Thermal flux quantity $\dot{q}_g$ concerning the laser beam power affecting the tread surface is supposed to be equal to the power measured with the energy meter during the tests. This heat generation term is assigned only to the tread nodes located within the laser spot area, as shown in in the Figure 4.11.

The entire heating flux power is subdivided to singular nodes in relation to laser spot area portion (the Fig. 4.11 in yellow) directly impacting upon the singular node area within the x-y plane. Therefore, only a part of the total laser power is assigned to each tread node within the heat balance equations. In the Fig. 4.11, three tyre inertia layers are represented: tread in blue, belt-plies in green and inner-liner in red.

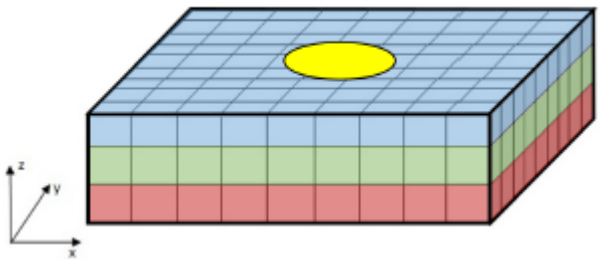

Figure 4.11 – Laser beam impacting on the external tread surface

The Thermo Racing Tyre Laboratory model requires the following input data to operate properly: the laser emitter power for laser beam modelling, the external air temperature for natural convection modelling and the pre-heating temperatures of the external tyre layers as initial conditions necessary for the integration of the heat balance equations.

As an example, the heat balance equations for the most significant node configurations, taking into account the thermal exchanges along the all directions, are further reported.

- Surface node hit by the laser spot:

$$\frac{\partial T}{\partial t} = \frac{1}{\rho c_v}\left(\frac{\dot{Q}_{laser}}{\Delta x \Delta y \Delta z_{m,srf}} + \frac{h_{nat}}{\Delta z_{m,srf}}(T_{air} - T) + \frac{\partial^2 k(z,T)\cdot T}{\partial x^2} + \frac{\partial^2 k(z,T)\cdot T}{\partial y^2} + \frac{\partial^2 k(z,T)\cdot T}{\partial z^2}\right) \quad (4.15)$$

- Surface node not hit by the laser spot

$$\frac{\partial T}{\partial t} = \frac{1}{\rho c_v}\left(\frac{h_{nat}}{\Delta z_{m,srf}}(T_{air} - T) + \frac{\partial^2 k(z,T)\cdot T}{\partial x^2} + \frac{\partial^2 k(z,T)\cdot T}{\partial y^2} + \frac{\partial^2 k(z,T)\cdot T}{\partial z^2}\right) \quad (4.16)$$

- Bulk node

$$\frac{\partial T}{\partial t} = \frac{1}{\rho c_v}\left(\frac{\partial^2 k(z,T)\cdot T}{\partial x^2} + \frac{\partial^2 k(z,T)\cdot T}{\partial y^2} + \frac{\partial^2 k(z,T)\cdot T}{\partial z^2}\right) \quad (4.17)$$

- Inner-liner node in contact with air

$$\frac{\partial T}{\partial t} = \frac{1}{\rho c_v}\left(\frac{h_{nat}}{\Delta z_{m,inner}}(T_{air} - T) + \frac{\partial^2 k(z,T)\cdot T}{\partial x^2} + \frac{\partial^2 k(z,T)\cdot T}{\partial y^2} + \frac{\partial^2 k(z,T)\cdot T}{\partial z^2}\right) \quad (4.18)$$

4.3.3 TRTLab Results

Thanks to the cad model of the sensor node and the rubber house it was possible to evaluate the volumes and the heat exchange surfaces (Figure 4.12).

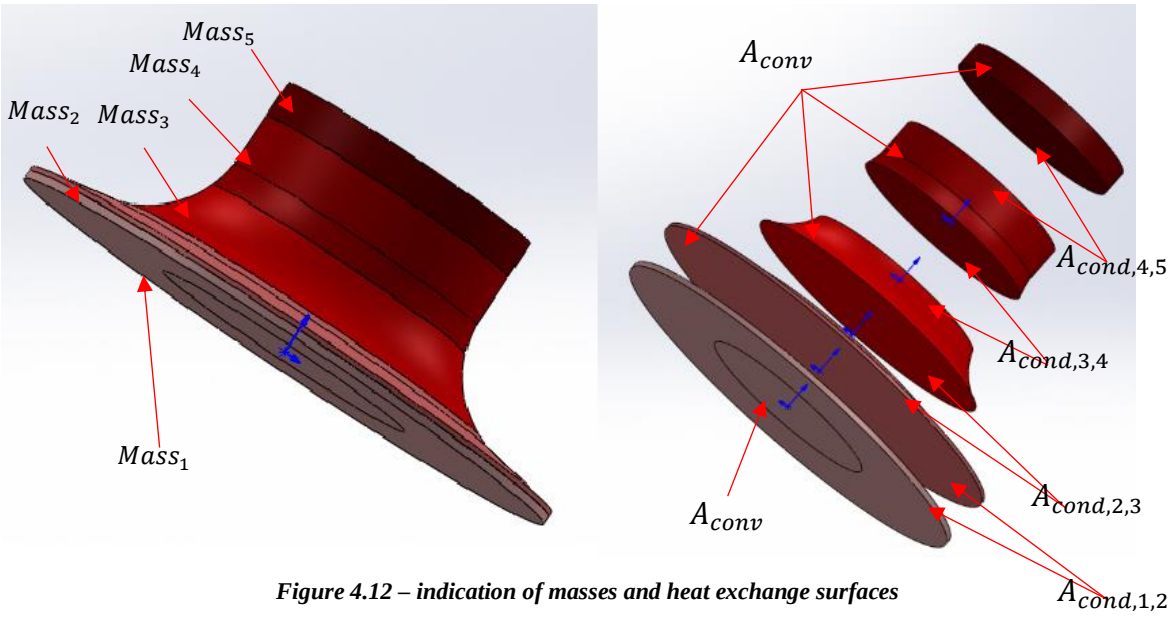

Figure 4.12 – indication of masses and heat exchange surfaces

Table 4.1 shows the subdivision of the masses based on the constituent material:

Table 4.1 – Material constituting the masses of the cyber tyre

Masses	**Material**
Masse 1	$Rubber$
Masse 2	$Rubber + plastic$
Masse 3	$Litium\ battery + plastic$
Masse 4	Resin + electronic circuit
Masse 5	Resin + electronic circuit + plastic

Figure 4.13 shows the identification results while in Table 4.2 the values of the identified thermal parameters are shown.

The identification procedure consists of reducing the error between the simulated temperature of the mass 5 and the temperature measured by the sensor node. The Figure 4.14 showes the Error between T_{cyber} measured and $T_{cyber,simulated}$. The max error is 4.7 °C corresponding to a percentage error of 5.6 %.

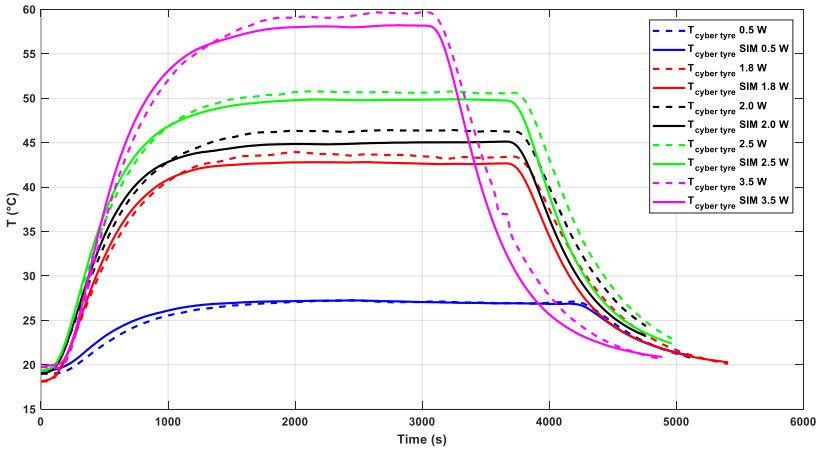

Figure 4. 13 – Cyber tyre thermal parameters: identification results

Table 4.2 – Cyber tyre thermal parameters identified

Masses	**Density ρ $\left({}^{kg}/_{m^3}\right)$**	**Specific heat c_v $\left({}^{J}/_{kg\ K}\right)$**	**Thermal conductivity $\left({}^{W}/_{m\ K}\right)$**
Masse 1	1140	1450	0.198
Masse 2	1140	1450	0.168
Masse 3	860	980	0.085
Masse 4	1120	720	0.182
Masse 5	1150	780	0.173

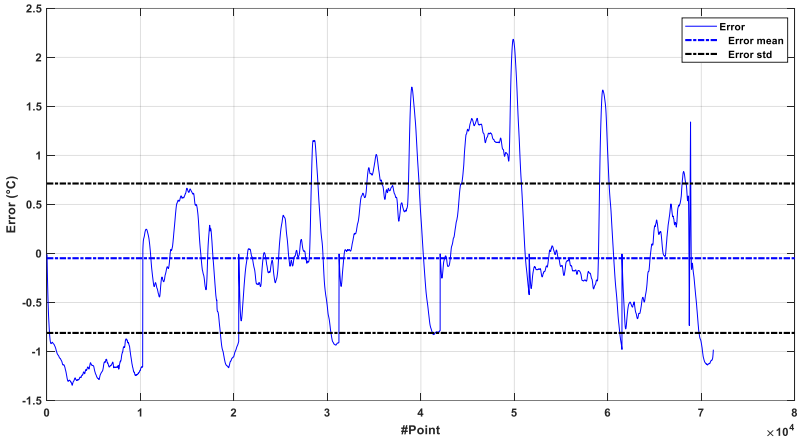

Figure 4.14 – Error between T_{cyber} measured and $T_{simulated}$

The next step was to identify the thermal parameters (with the same technique) of the various tyres to be tested.

Figure 4.15 shows the identification results for the tyre 1. Similar results were obtained for the other tyres.

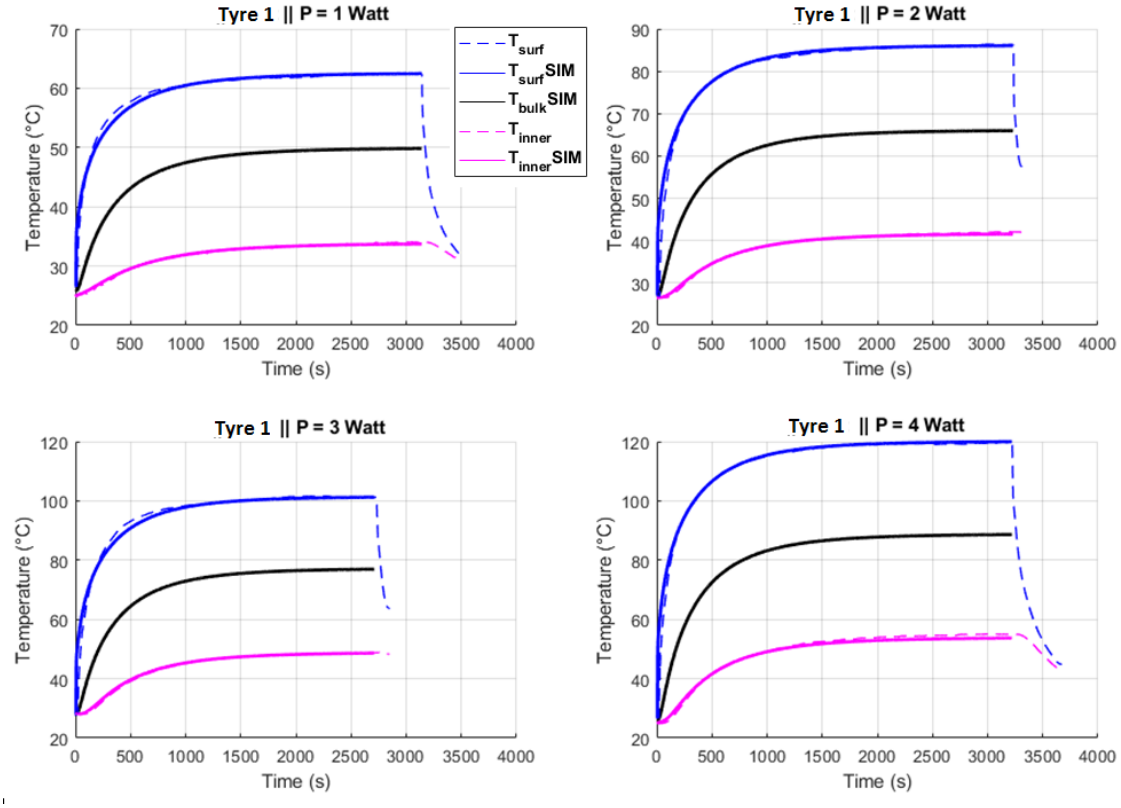

Figure 4.15 – Identification results for the Tyre 1

Both the thermal conductivity and the specific heat show a quadratic trend with the temperature as shown in Figure 4.16.

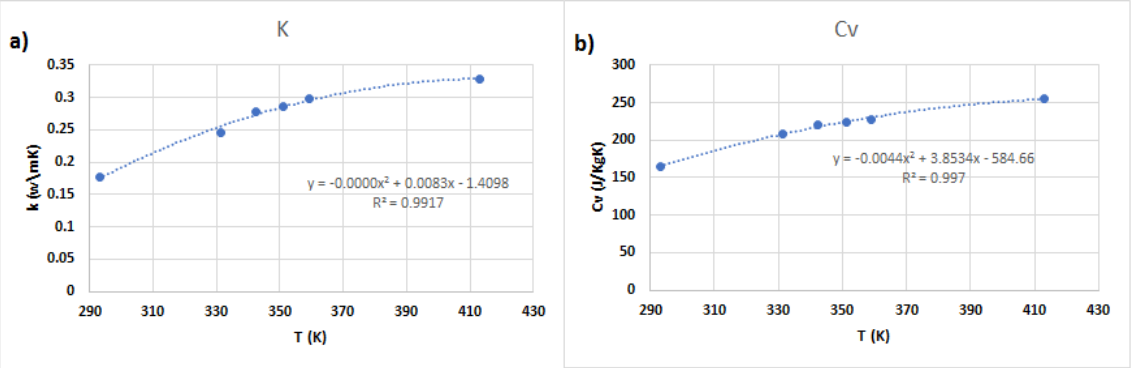

Figure 4.16 – quadratic trend of thermal parameters: a) thermal conductivity b) specific heat

4.4 Indoor rolling resistance tests

In order to characterize the strain energy loss, a series of tests were performed on a rolling resistance measurement machine (Figure 4.17).

Figure 4.17 – Rolling resistance test equipment

The purpose is to evaluate the performance of the strain energy loss in relation to:

- Vertical load
- Speed
- Inflation pressure

For this purpose, a test procedure is developed which includes (Figure 4.18):

- 3 vertical load levels (2000, 5000 and 8000 N)
- 3 speed levels (50, 100 and 150 Km/h)
- 3 levels of inflation pressures (200, 250 and 300 kPa)

For each condition of pressure, speed and vertical load, the test consists of three phases:

1. warm-up: In order to obtain the thermal regime (15 minutes)
2. rolling resistance acquisition with relative vertical load (3 minutes)
3. rolling resistance acquisition with a vertical load of 200 N (called skim load) in order to evaluate the passive resistance of the machinery (2 minutes)

For each conditions, the rolling resistance value is given by the difference between the full load and skim load conditions.

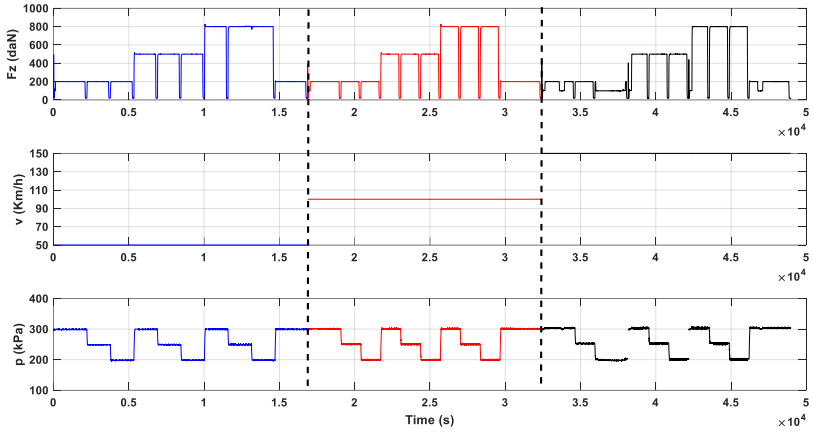

Figure 4.18 – Rolling resistance procedure tests

During the tests, the temperatures of some areas of the tyre were acquired:

- Internal air temperature
- Inner liner temperature
- Surface temperature
- Cyber^{TM} Tyre temperature

The internal air temperature was acquired through a thermocouple which accesses the internal chamber through a second valve obtained on the rim (Figure 4.19).

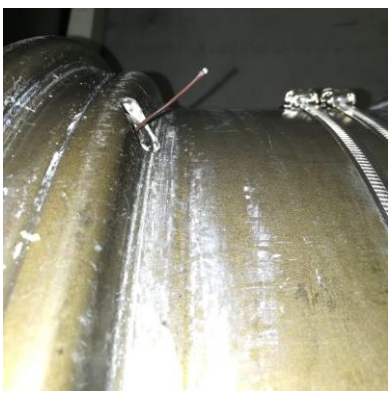

Figure 4.19 –Thermocouple for measuring the internal air temperature

The inner liner temperature was measured by an infrared sensor equipped with 8 measurement spots (Figure 4.20).

It is a wireless sensor produced by Texense which facilitated assembly inside the chamber without cables. Thanks to the presence of 8 laser spots, it was possible to measure the temperature of the inner liner from the left shoulder to the right one.

For the mounting of this sensor on the rim, a special casing has been designed.

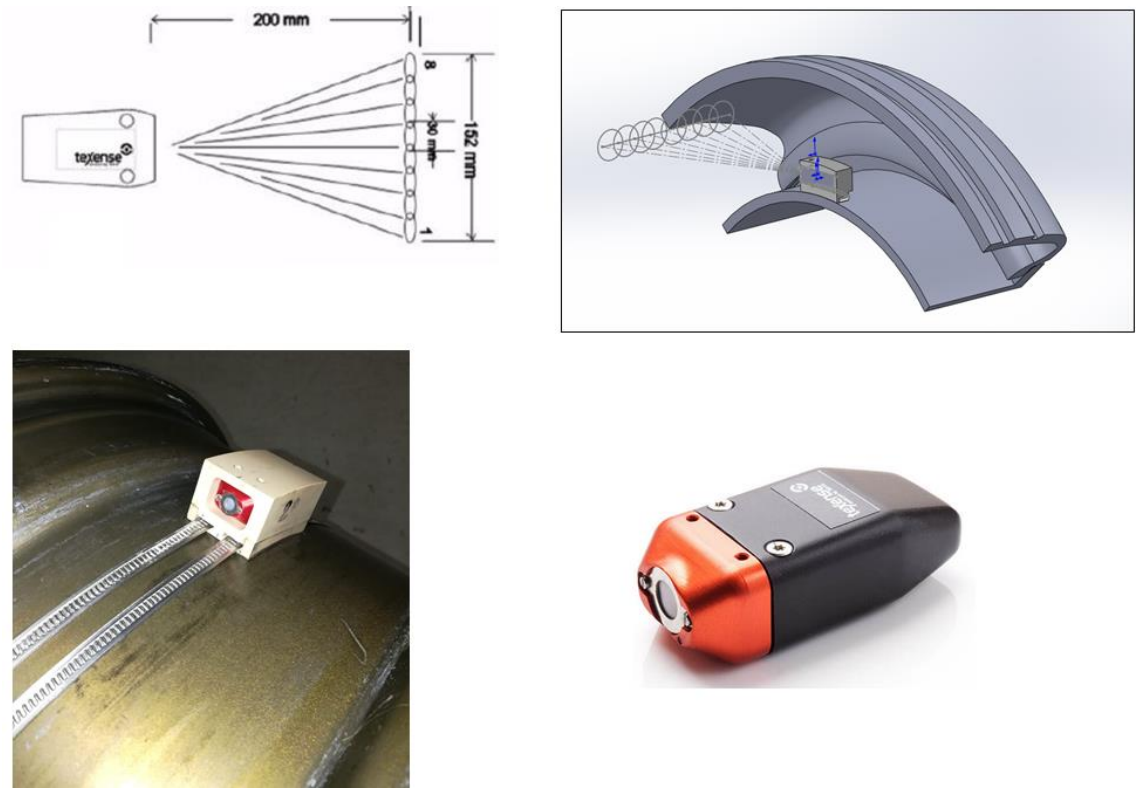

Figure 4.20 – Sensor IRN8WS for Inner liner temperature measurement

The surface temperature was measured using a IR camera (E60 produced by Flir).

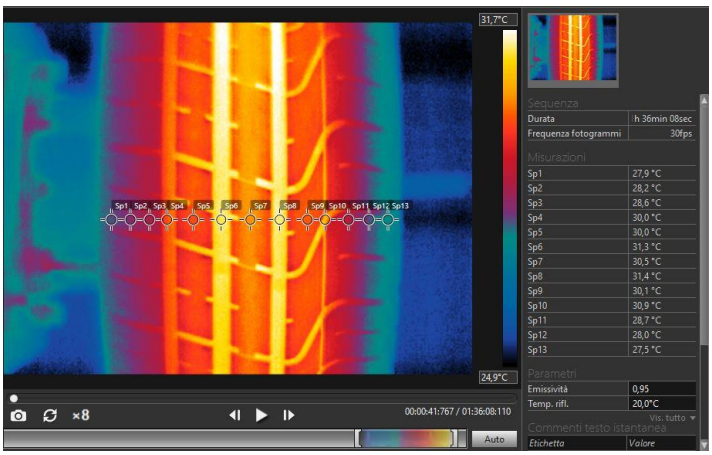

Figure 4.21 – Surface temperature measured by IR camera

All data have been acquired by a Dewesoft Dewe43 (Figure 4.22) connected via USB to a common laptop. The acquired data is saved on a hard disk and then processed later.

Figure 4.22 – The Dewe 43 acquisition unit

4.4.1 Rolling resistance data elaboration

After each condition, the machine issues a report containing some information including:

- Deflection f
- Loaded radius R_L
- Rolling resistance force F_R (in full and skim load)
- Rolling Radius R_R

From the knowledge of these quantities it is possible to obtain (Figure 4.23):

$$SEL = F_R R_L \omega = \frac{F_R R_L}{R_R} V \quad (W) \tag{4.19}$$

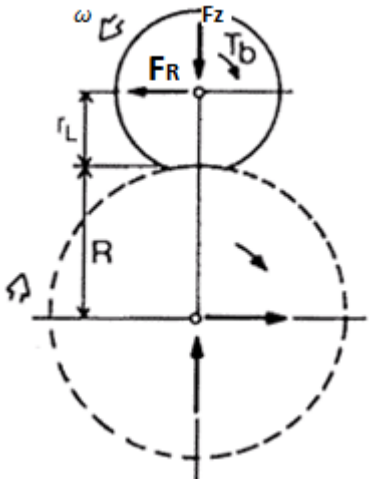

Figure 4.23 – Indication of the quantity contained in the formula 4.18

From 4.18 we get the power dissipated in the whole tyre. Generally, the various zones of the tyre contribute differently to the dissipation of energy (Figure 4.24) and this is

considered in the thermal model (the nodes present in the different zones will have a certain percentage of SEL).

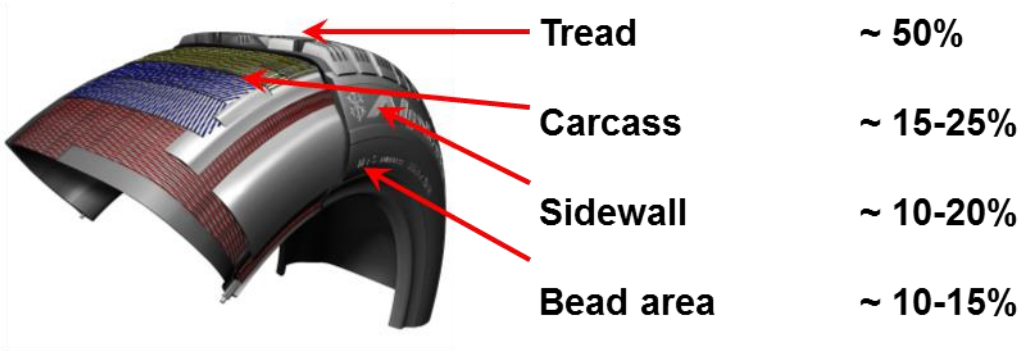

Figure 4.24 – Contributions to the SEL of the different areas of the tyre

Figure 4.25 shows the comparison between the 4 specs in the various operating conditions.

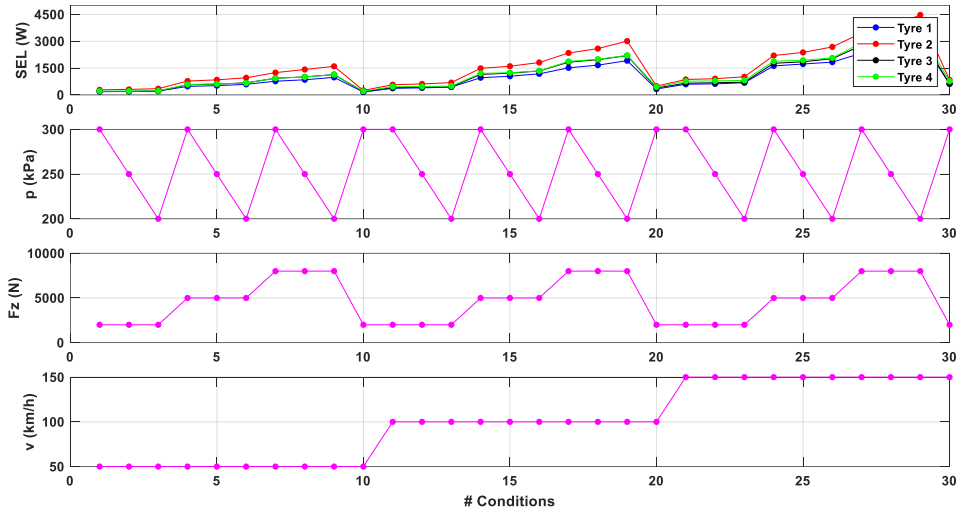

Figure 4.25 – Comparison between the 4 specs in the various operating conditions

Another aspect to keep in mind is that the load condition on the drum is more onerous than in the case on a flat road. To take this aspect into account, a corrective formula is used which allows the value of the rolling resistance assessed on the drum to be corrected:

$$Coef_R = \sqrt{\frac{\frac{R_1}{R_2}(R_2 + r_t)}{(R_1 + r_t)}} \tag{4.20}$$

where:

- R_1 is the radius of drum where the rolling resistance is evaluated
- R_2 is the radius of the drum with respect to which the rolling resistance value is to be corrected

- r_t is the radius of the tyre

In the case of the flat road, $R_2 = \infty$:

$$\boldsymbol{Coef_R} = \sqrt{\frac{R_1}{R_1 + r_t}} \tag{4.21}$$

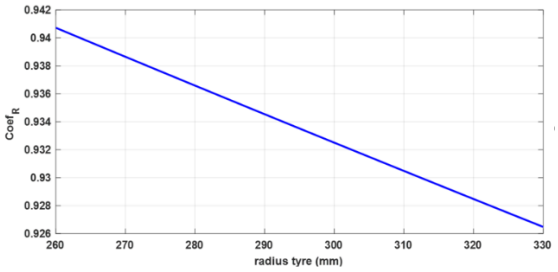

Figure 4.26 – Rolling resistance corrective coefficient in case of flat road

The purpose of this test is to evaluate a relationship between the dissipated power and the operating conditions such as vertical load, angular velocity and inflation pressure.

These conditions are also provided by the cyber tyre and this makes it possible to evaluate, at any time, the value of SEL (input of the thermal model).

This relationship has been evaluated by multi-parameter linear regression method:

$$SEL = f(F_z, p, v) \tag{4.22}$$

Figure 4.27 shows the results of the model for the 4 specs.

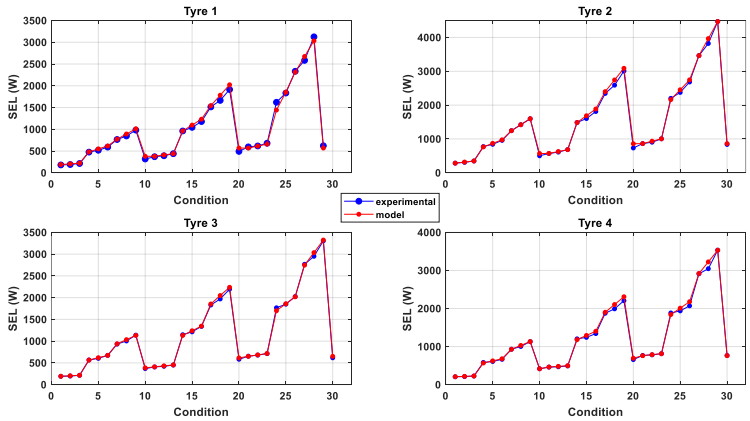

Figure 4.27 – Results of the model for the 4 specs

4.4.2 Thermal model: S.E.L implementation

Considering the equations described in chapter 4.2.1, it is possible to write the heat exchange equations for the 5 masses of cyber tyre and tyre masses.

The following hypotheses are made:

- The only heat generation term, represented by the SEL, is attributed to the bulk mass

- The surf mass, in part, exchanges heat by convection with the external air and partly exchanges heat by conduction with the drum. The conduction exchange takes place in the contact area evaluated directly by the regressor *PL* provided by the cyber tyre.
- The tyre is modelled without grooves. Their contribution is entered through a factor called *grooved factor* which reduces the contact are (assumes unit value for slick tyre).

The external convection coefficient is evaluated using the classical dimensionless analysis.

$$H_{ext} = \frac{k_{air} \cdot Nu}{L} \tag{4.23}$$

where:

- k_{air} is the thermal conductivity of the air
- Nu is the Nusselt number
- L is the characteristic length evaluated as $L = \frac{1}{\frac{1}{D}+\frac{1}{W}}$ where D is the overall diameter and W the tyre width

Basing on the article [76], the Nusselt number is evaluated as:

$$Nu = 0.11 \cdot [(0.5 \cdot Re^2 + Gr) \cdot Pr]^{0.35} \qquad 1000 \leq Re \leq 8000 \tag{4.24}$$

where:

- Gr is the Grashof number
- Pr is the Prandtl number
- Re is the Reynolds number

This quantity is evaluated as:

$$Gr = \frac{g \cdot \beta \cdot (T_s - Tair_{ext}) \cdot L^3}{\nu_{air}^3} \tag{4.25}$$

$$Pr = \frac{cp \cdot \mu_{air}}{k_{air}} \tag{4.26}$$

$$Re = \frac{\omega \cdot R_r \cdot L}{\nu_{air}} \tag{4.27}$$

where:

- g is the gravity acceleration (m/s^2)
- β is the air Thermal Expansion Coefficient $(1/K)$
- T_s is surface temperature (K)

- ν_{air} is the air Kinematic Viscosity (m^2/s)
- μ_{air} is the air Dynamic Viscosity $(kg/m \cdot s)$
- cp is the air Specific Heat $(J/kg\ K)$
- ω is the angular speed of tyre (rad/s)
- R_r is the rolling radius of the tyre (m)

Basing on the article [77], the internal convection coefficient is evaluated as:

$$H_{int} = \frac{k_{air} \cdot Nu_{int}}{L_{int}} \tag{4.28}$$

where:

- L_{int} is the characteristic length evaluated considering the tyre radius at the inner liner

Nu_{int} is evaluated as:

$$Nu = \frac{\xi/8 \cdot Re \cdot Pr}{K_1(\xi) + K_2(Pr) \cdot \sqrt{\xi/8} \cdot \left(P_r^{\frac{2}{3}} - 1\right)} \tag{4.29}$$

where ξ is the friction factor evaluated as:

$$\xi = (1.82 \cdot log_{10}(Re) - 1.64)^{-2} \tag{4.30}$$

while $K_1(\xi)$ and $K_2(Pr)$ are evaluated as:

$$K_2(Pr) = 11.7 + 1.8 \cdot \mathrm{Pr}^{-\frac{1}{3}} \tag{4.31}$$

$$K_1(\xi) = 1 + 3.4 \cdot \xi \tag{4.32}$$

The figure 4.28 shows the results of the thermal model relating to tests 50, 100 and 150 km / h for one of the 4 tyres. Among the various outputs of the model, there is also the temperature corresponding to that of the cyber tyre which was compared with that measured by it.

Figure 4.29 shows the error trend for both T_{inner} and T_{cyber}.

A similar trend is obtained for the other tyres tested.

Subsequently to the rolling tests on the drum, a series of tests on the MTS Flat Track® are carried out. These texts have been useful for calibrating the thermal model since the flat belt represents a condition more similar to tyre-road contact.

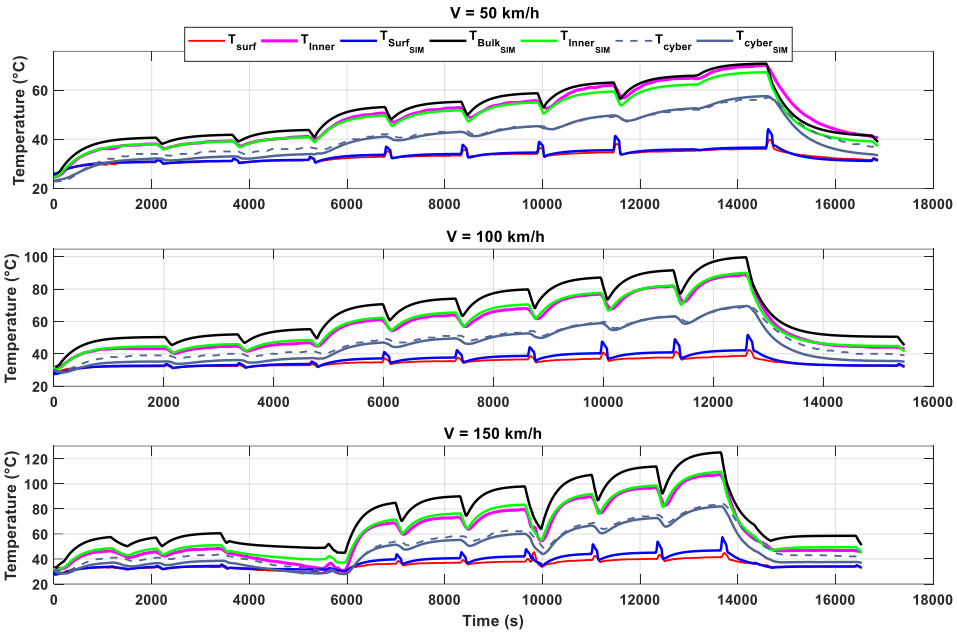

Figure 4.28 – Results of thermal model for rolling resistance tests

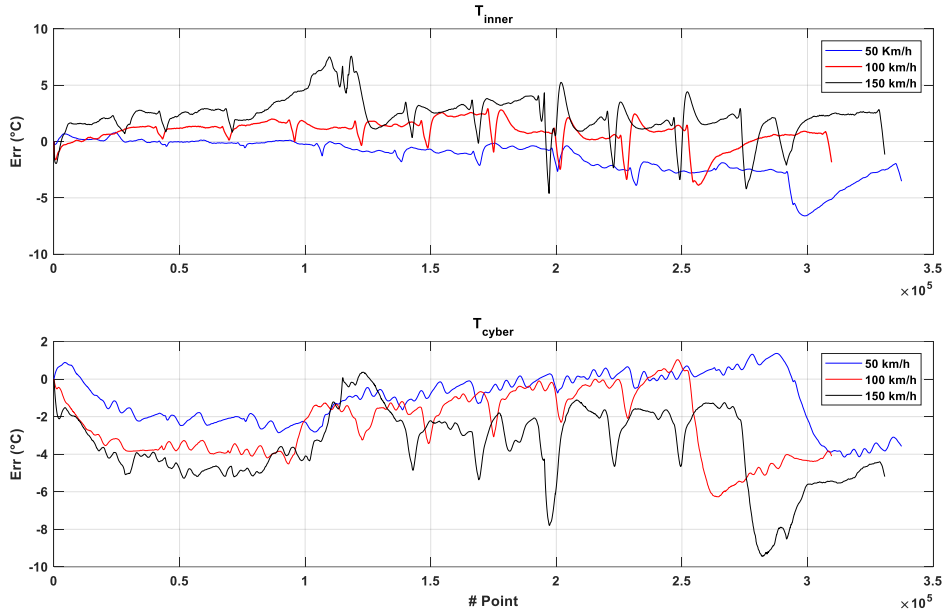

Figure 4.29 – Error between $T_{meausred}$ and $T_{simulated}$

4.4.3 Indoor MTS Flat Trac® tests

The MTS Flat Trac® has been described in 3.6.1. These tests were carried out in order to validation the thermal model in indoor conditions on a flat belt.

During these tests the same temperatures as the drum tests were acquired. In addition, special sensors have been used to measure the bulk temperature. It is a system developed

by the German TÜV Automotive department composed of by the sensitive elements constituted by thermo resistances that can be drown into the bulk on the shoulders (Figure 4.28).

Figure 4.30 – The T3M sensors

The sensitive elements can change linearly their electrical resistance in dependence on temperature. The sensors are connected through steel cables to an I/O unit able to transmit via Bluetooth technology up to 8 signals to a receiver connected via CAN bus to an acquiring system.

For this application, 4 *T3M* sensors were mounted as shown in Figure 4.29.

The tests carried out were the following:

- Free rolling test at low speed (50 Km/h)
- Free rolling test at high speed (200 Km/h)

During the tests the pressure was not controlled (free to evolve) and was measured by TPMS.

The table summarizes the measured temperatures and the instruments used.

Figure 4.31 – Tyre with T3M sensors

Table 4.3 – Temperature measured and instrument used

Zone	Instrument	N° of measurement points
Inner	IR sensor	8
Surface	IR sensor	3
Bulk	T3M	4
Internal Air	Thermocouple	-
External Air	Thermocouple	-

The results of the thermal model are shown in the Figure 4.32.

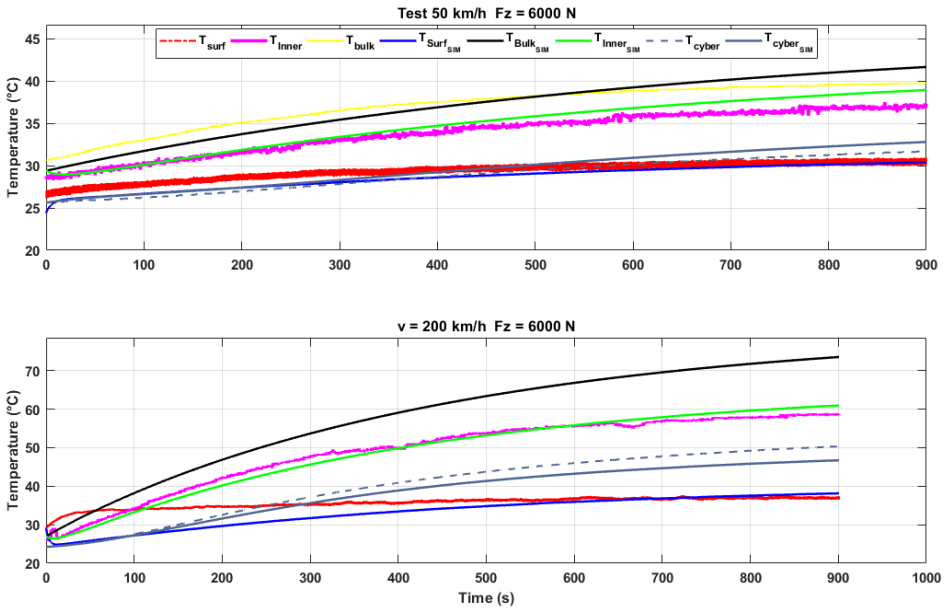

Figure 4.32 – Flat trac tests results

Figure 4.33 shows the error trend for both Tinner and Tcyber.

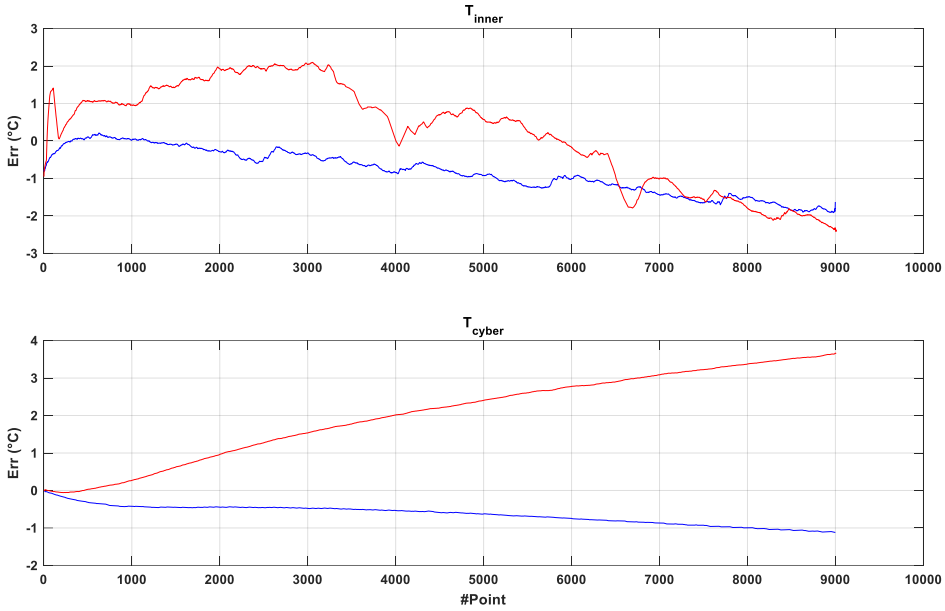

Figure 4.33 – Error between Tmeausred and Tsimulated

4.4.4 Outdoor Tests

During outdoor tests the tyre is working in the most realistic condition. These tests were necessary for the characterization of forced convection with external air and conduction with the road.

Furthermore, the reason of this activity was to confirm everything investigated in indoor.

Three types of tests were conducted:

- Outdoor tests in hot condition (cannot be reproduced in indoor tests) on the circuit of Nardò (NTC – Nardò Technical Center)
- Outdoor tests in cold condition (cannot be reproduced in indoor tests) on the Artic Driving Center in Finland
- Outdoor tests in medium condition (like the indoor tests) on the circuit of Nardò

Figure 4.34 – Nardò Technical Center a) Artic Driving Center b)

For all the tests, two vehicles were instrumented in order to acquire all the quantities useful for the activity:

- Inner-liner temperature by IR sensor (8 spot)
- Inner Air temperature by TPMS
- Internal pressure by TPMS and cyber tyre
- External temperature by thermocouple
- Surface temperature by IR sensors
- Bulk temperature by T3M sensors.
- Road temperature by IR sensors

Special supports have been designed to mount these sensors (Figure 4.34).

other quantities are acquired from the vehicle can bus:

- angular speed of the wheels
- steering angle
- Lateral and longitudinal acceleration
- Yaw rate
- Ambient temperature

All data have been acquired by a Dewesoft Dewe43 (Figure 4.22) connected via USB to a common laptop. The acquired data is saved on a hard disk and then processed later.

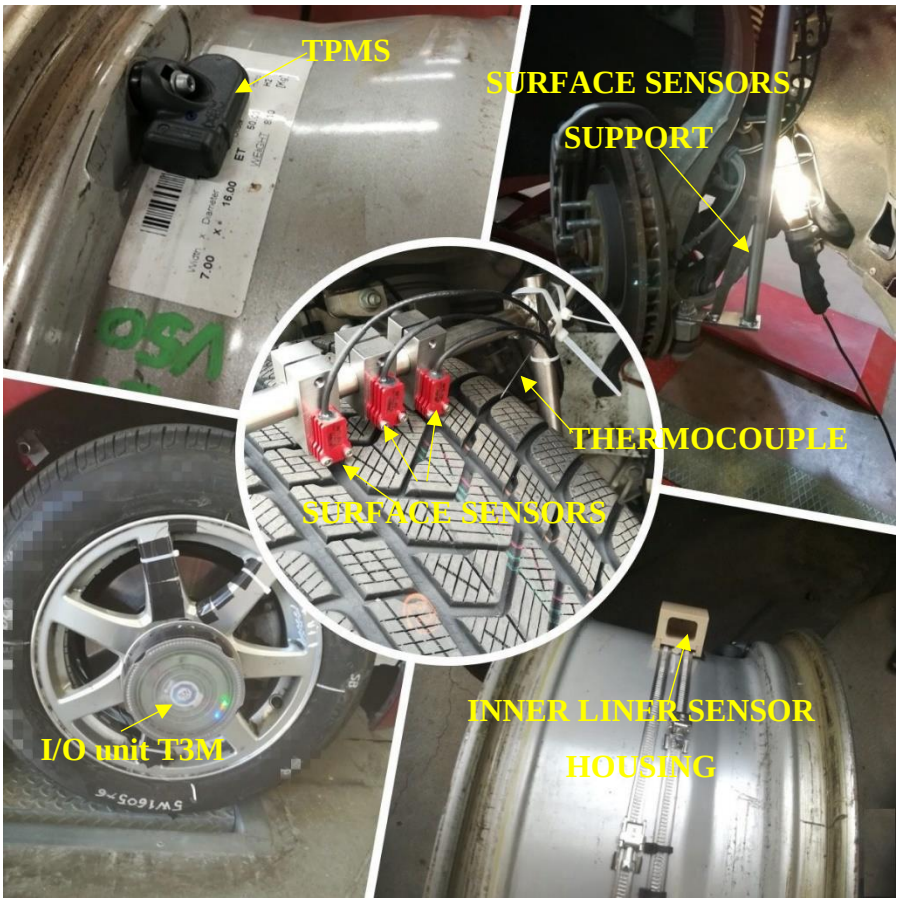

Figure 4.35 – Sensors with respective supports

Three kinds of tests have been conducted to investigate thermal behaviour of the tyres:

- Test 1: constant low speed (30 km/h for Rovaniemi and 50 km/h for Nardò) for 30 minutes on the oval
- Test 2: constant High speed (80 km/h for Rovaniemi and 160 km/h for Nardò) for 30 minutes on the oval
- Test 3: constant low speed (30 km/h for Rovaniemi and 50 km/h for Nardò) for 30 minutes on the oval.

The tests were carried out in the following sequence:

- 50-160-50 for Nardò: heating – heating – cooling (Figure 4.36)
- 80-30-80 for Rovaniemi: heating-cooling-heating (Figure 4.37)
- 50-160 for Nardò (medium condition): heating-heating (Figure 4.38)

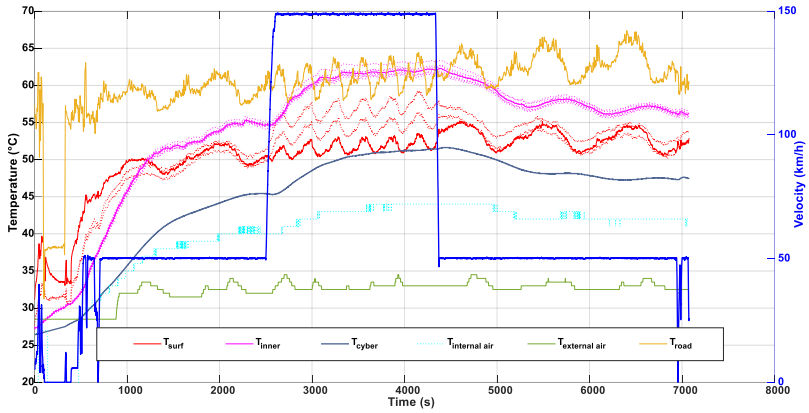

Figure 4.36 – Temperature measured (Hot test)

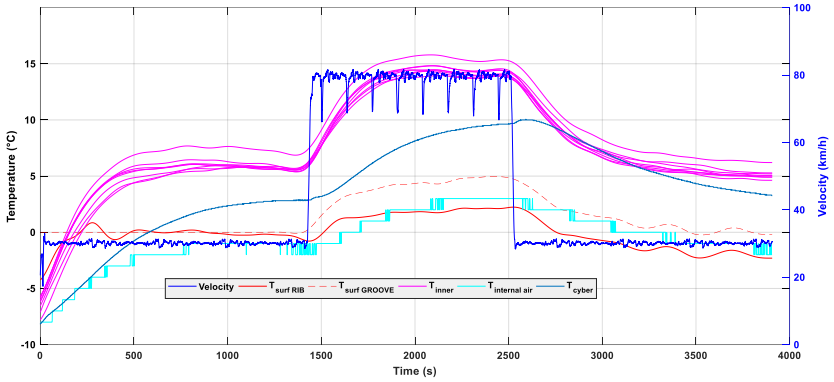

Figure 4.37 – Temperature measured (Coldt test)

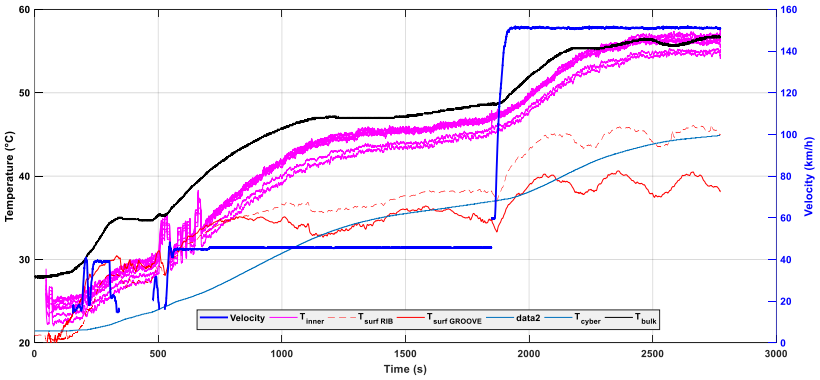

Figure 4.38 – Temperature measured (medium test)

The relation 4.22 allows to evaluate the SEL during the indoor tests, where the imposed vertical load was known. For outdoor tests, the tyre deflection has been linked with the Cyber^{TM}Tyre DR and Angular Velocity Regressors, so we have the following relationship:

$$SEL = f\left((\omega_{cyber}, p_{cyber}, RL(DR, \omega_{cyber})\right) \tag{4.33}$$

Starting from indoor data, a relationship between RL omega and DR was evaluate:

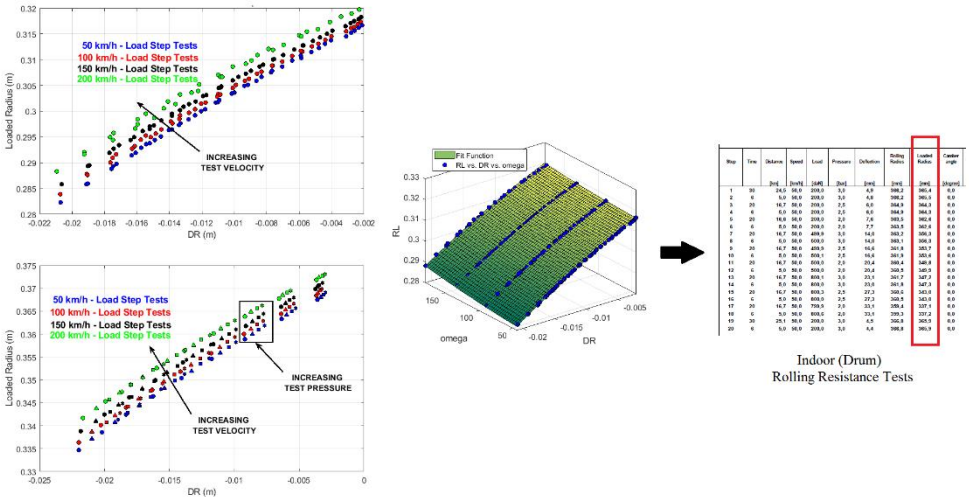

Figure 4.39 – Relationship between RL omega and DR

In addition, a model was developed to evaluate the internal air temperature based on the gas law considering the presence of humidity.

Moist air is a mixture of dry air and water vapor:

$$p_D = \rho_D \cdot R_D \cdot T \; for \; dry \; air \tag{4.34}$$

$$p_W = \rho_W \cdot R_W \cdot T \; for \; water \; vapor \tag{4.35}$$

Applying Dalton's law:

$$p_{tot} = p_D + p_W \tag{4.36}$$

is obtained:

$$\rho_0 = \frac{p_0}{\left\{R_D \cdot \left[1 + \frac{\varepsilon \cdot \varphi \cdot p_{sat}}{p_0 - (1-\varepsilon) \cdot \varphi \cdot p_{sat}}\left(\frac{1}{\varepsilon} - 1\right)\right] \cdot T_0\right\}} \tag{4.37}$$

Where:

- $T_0 = f(T_{cyber}(t = 0s))$
- $p_0 = p_{cyber}(\mathrm{t} = 0\mathrm{s})$
- φ is the relative humidity [0 1]
- R_D is the individual gas constant of dry air
- p_{sat} is the water vapor saturation pressure (Figure 4.40)

- $\varepsilon = \frac{R_D}{R_W} = 0.621$

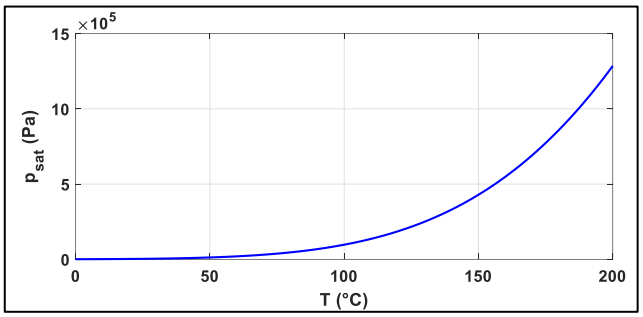

Figure 4.40 – Water vapor saturation pressure

Figure 4.41 shows the trend of air density in function of pressure and temperature for different value of relative humidity.

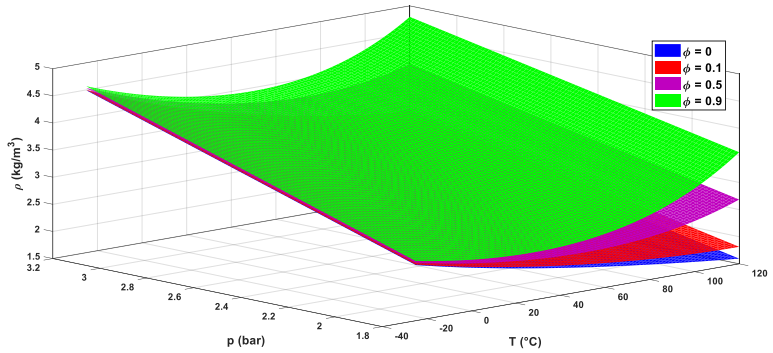

Figure 4.41 – Air density in function of temperature and pressure

Starting from ρ_0 and pressure measured by cyber tyre, it is possible to evaluate the evolution of the internal air temperature:

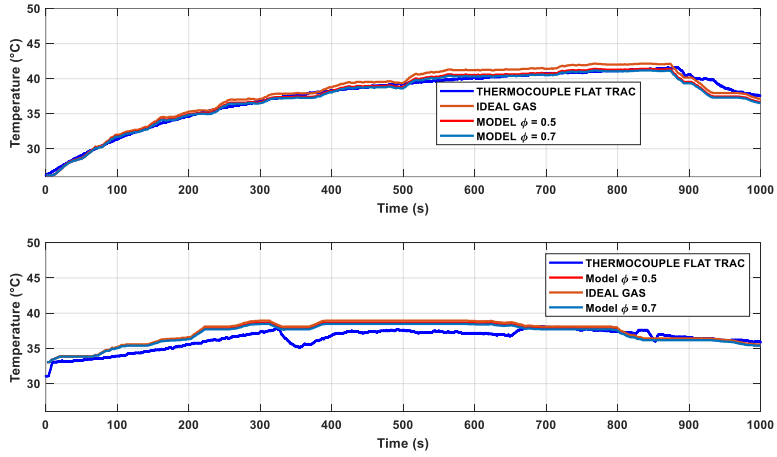

Figure 4.42 – Air Temperature model (indoor tests)

Figures 4.39 4.40 4.41 and 4.42 show the results of the thermal model for the carried out tests.

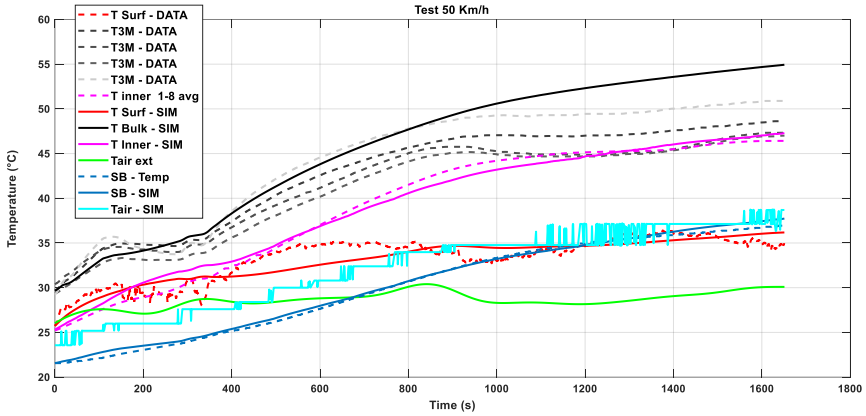

Figure 4.43 – Thermal model results for medium tests (50 Km/h)

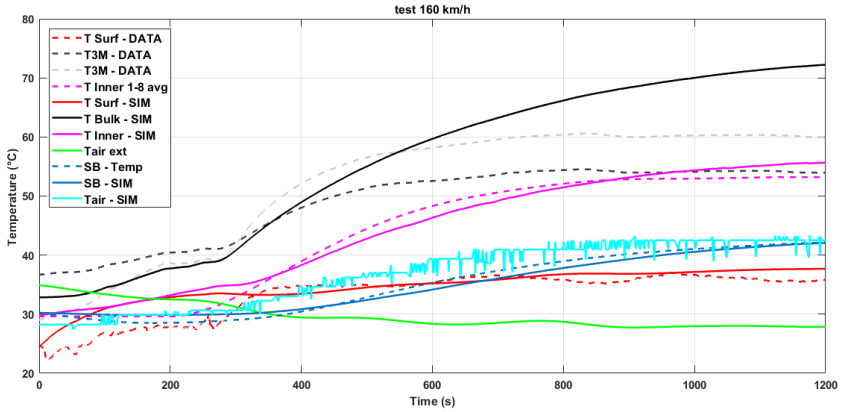

Figure 4.44 – Thermal model results for medium tests (160 Km/h)

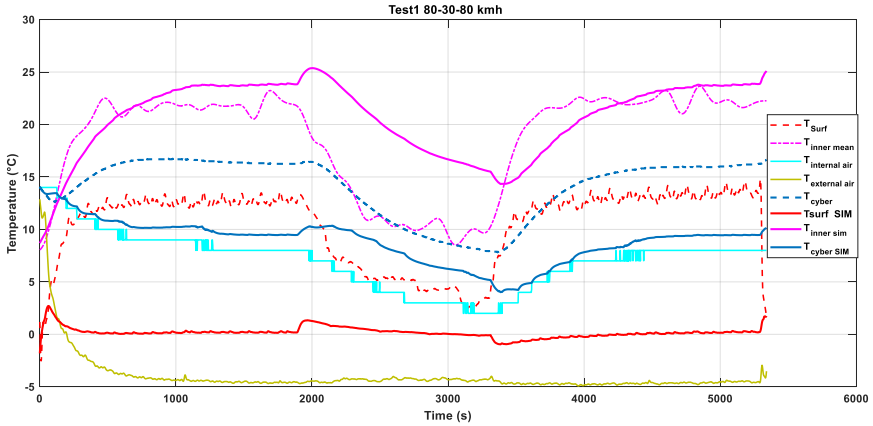

Figure 4.45 – Thermal model results for cold tests (80-30-80)

For the cold tests, the SEL Function rightly works considering the Bulk Layer Temperature evolution and Inner Liner one in steady conditions (80km/h).

During the vehicle speed transitions, the model does not correctly reproduce the temperature variations. This is due to thermal masses mesh (low computational cost).

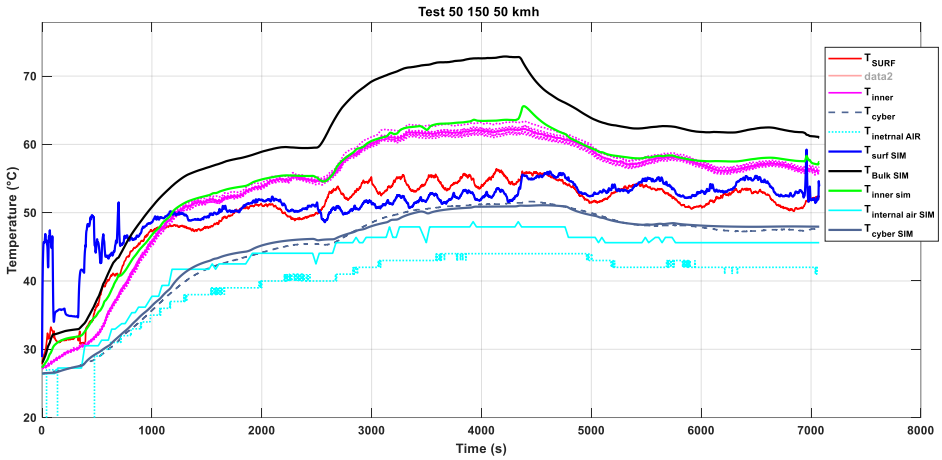

Figure 4.46 – Thermal model results for cold tests (80-30-80)

Chapter 5

Correction of the vertical load estimation

5.1 Introduction

In 3.1 the vertical load calibration procedure was described. It has been shown that from this calibration a polynomial is obtained which is able to estimate the vertical load starting from some quantities coming from the Cyber^{TM}Tyre (angular velocity, inflation pressure and DR).

This polynomial is very performing in a wide range of vertical load, inflation pressure and speed.

However, for temperature conditions other than calibration, underestimate or overestimate of the vertical load occurs (Figure 3.29).

This phenomenon is attributable to the viscoelastic character of the material and how the radial stiffness of the tyre is influenced by temperature (Figure 2.21).

There was therefore the need to implement a correction procedure for the estimate of the vertical load in conditions other than calibration. For this purpose, a thermal model was first developed which, starting from the temperature measured by the cyber tyre and other quantities, allows to evaluate the temperature of tyre zone that most influences the phenomenon.

The next step is to develop a vertical load estimation correction procedure. Two strategies will be compared:

1. New calibration polynomial having, in addition to the standard inputs (inflation pressure, angular velocity and DR), also the temperature.

2. Procedure that provides for the correction of the DR according to the temperature. This DR represents the input of the standard polynomial.

The two procedures are shown in figure 5.1.

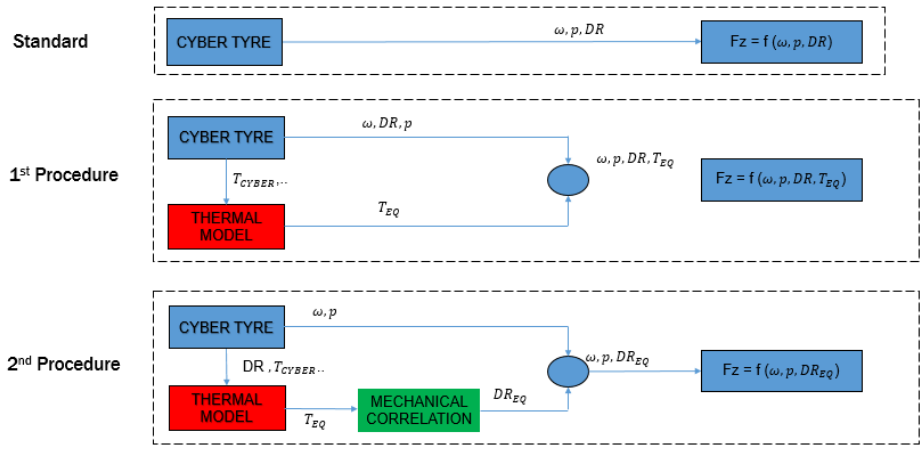

Figure 5.1 – Flow chart of the two correction procedures

5.2 Correction of the vertical load: characterization test

In order to develop the correction procedures, a series of Flat Trac® tests were needed in order to characterize the phenomenon in a wide range of temperatures:

1. warm-up test: from the ambient temperature to the operating temperature corresponding to the average calibration temperature
2. heating up to about 100 ° C
3. cooling down to the average calibration temperature

During the tests, the temperatures of some areas of the tyre were acquired:

- Internal air temperature
- Inner liner temperature
- Surface temperature
- Cyber^{TM} tyre temperature

Table 5.1 - – Temperature measured and instrument used

Zone	Instrument	N° of measurement points
Inner	IR sensor	8
Surface	IR sensor	3
Internal Air	Thermocouple	-
External Air	Thermocouple	-

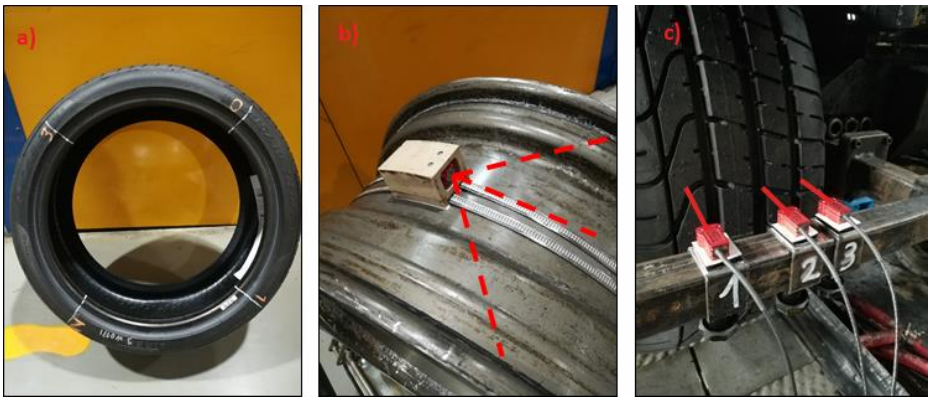

Figure 5.2 – 4 cyber tyre in central position a) Inner liner IR sensor b) Surface RIB, Groove internal and Groove external c)

The warm-up condition was carried out with a vertical load of 5000 N, a speed of 100 Km/h and an inflation pressure of 260 kPa.

The warm-up condition was carried out with a vertical load of 6000 N, a speed of 100 Km/h, an inflation pressure of 260 kPa and a series of slip angle sweeps.

The cooling condition was carried out in the same way as in the warm-up phase (Figure 5.3).

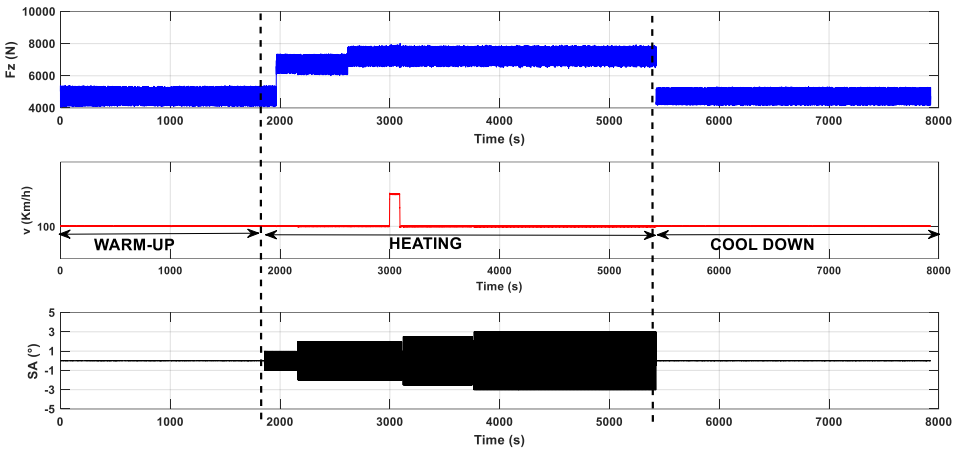

Figure 5.3 – Test conditions

Figure 5.4 shows the trend of temperatures corresponding to the three phases.

During the second phase, in addition to the *SEL* contribution, there is also the friction power contribution. Initially, only the first and third phases are considered where only the *SEL* contribution is present.

By applying the standard calibration polynomial, the results shown in the figure are obtained.

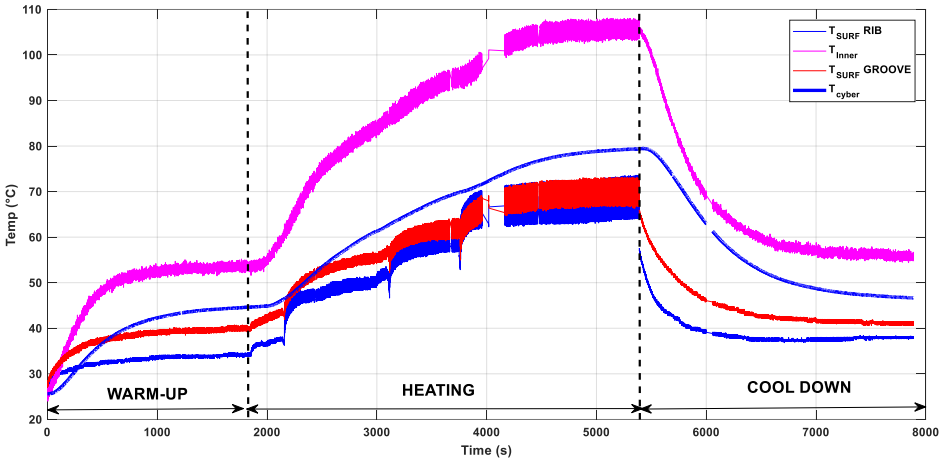

Figure 5.4 – Trend of temperatures corresponding to the three phases

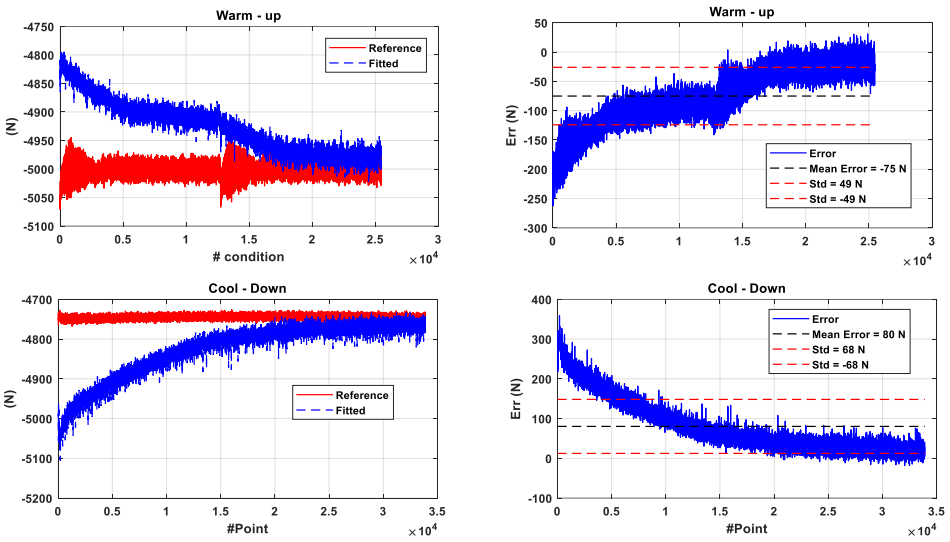

Figure 5.5 – Results of the standard polynomial applied to phase 1 and 3

During the warm-up phase, the polynomial tends to underestimate the value of the vertical load with an error that tends to decrease with increasing temperature. On the contrary, during the cooldown phase, the polynomial tends to overestimate the vertical load with an error that tends to decrease as the temperature decreases.

Figure 5.6 shows the trend of the *DR* during the cool-down phase. DR_{REF} indicates the value assumed by the *DR* at the same load, pressure and speed of the cooldown but at the calibration temperature.

The trend of the DR and the temperature explain the trend of the error reported in Figure 5.5. In fact, during the cool-down, the temperature regimes at a higher value than the calibration one and the polynomial, even at steady state, slightly overestimates the vertical load value. Instead for warm-up, the polynomial tends to underestimate the value

of the vertical load with an error that decreases as the temperature converges to the calibration value.

Finally, figure 5.7 shows the trend of radial stiffness during the cool-down phase. Note that as the temperature decreases, the tyre increases stiffness.

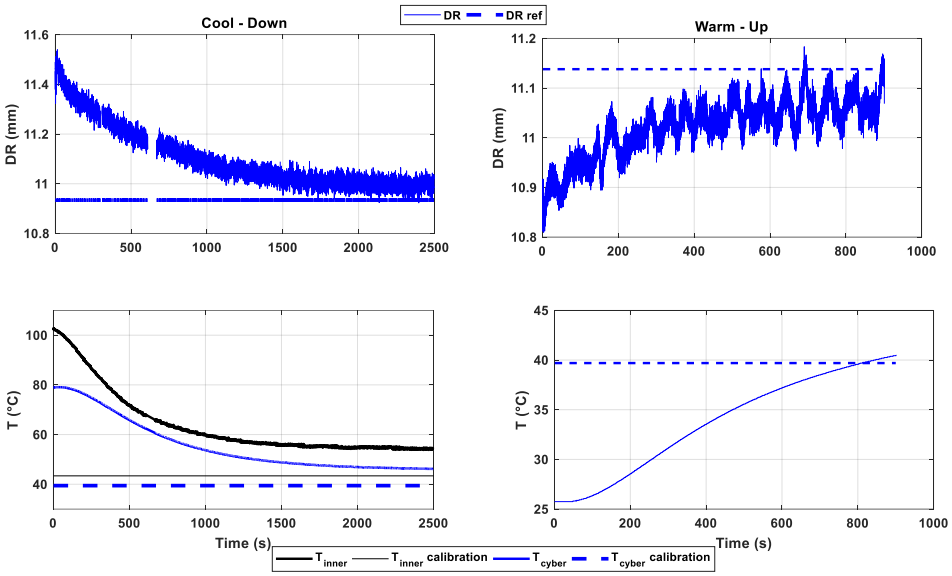

Figure 5.6 – Trend of the DR during the cool-down and warm – up phases

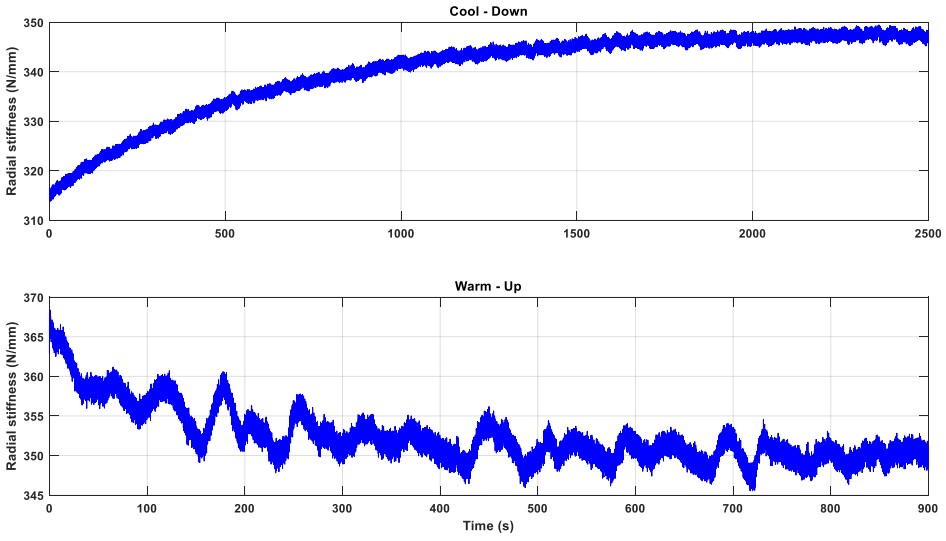

Figure 5.7 – Trend of radial stiffness during the cool-down and warm – up phases

Figure 5.8 shows the trend of radial stiffness as a function of temperature. It can be seen how perfect continuity exists between warm-up and cool-down.

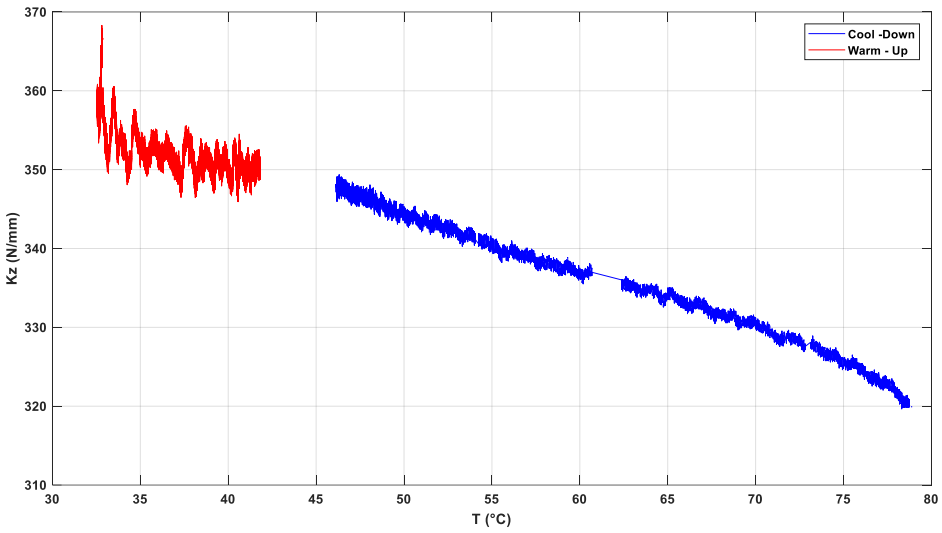

Figure 5.8 – Trend of radial stiffness as a function of temperature

The warm-up and cool-down phases were simulated using the thermal model (Figure 5.9).

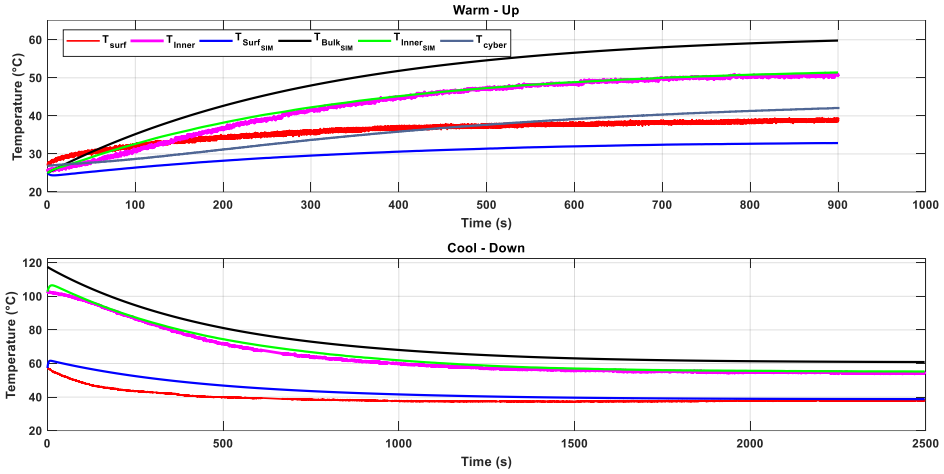

Figure 5.9 – Thermal model results

5.3 Correction of the vertical load: first correction strategy

The first strategy is to directly introduce the temperature into the calibration polynomial. It is a matter of carrying out a new calibration with the same method reported in 3.6.3 but introducing, in addition to the DR, speed and internal pressure, also the temperature as input.

The effect of the following temperatures is studied:

- Bulk temperature
- Inner Temperature
- Cyber Temperature

These temperatures have different dynamics during the same phase; the aim is to evaluate the temperature whose dynamics are similar to that of the variation of the normal stiffness.

5.3.1 First correction strategy with T_{inner}

The calibration polynomial takes the following form:

$$F_z = F_z(\omega, P, DR, T_{inner}) \tag{5.1}$$

The multiparameter linear regression method is applied to characterize the vertical force regression formula.

For training, the standard dataset (described in 3.6) is provided accompanied by a warm-up phase and a cool-down phase:

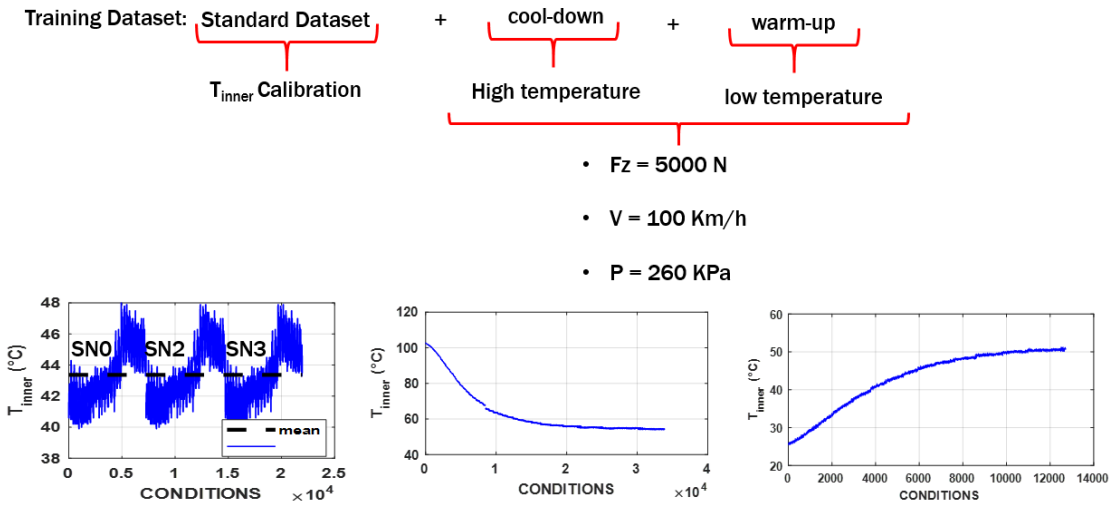

Figure 5.10 – Training Dataset

Figure 5.11 shows the results of the method. The final polynomial is quadratic and consists of 15 terms (4 predictors).

Finally, figure 5.12 shows the comparison between polynomials with and without correction for both warm-up and cool-down.

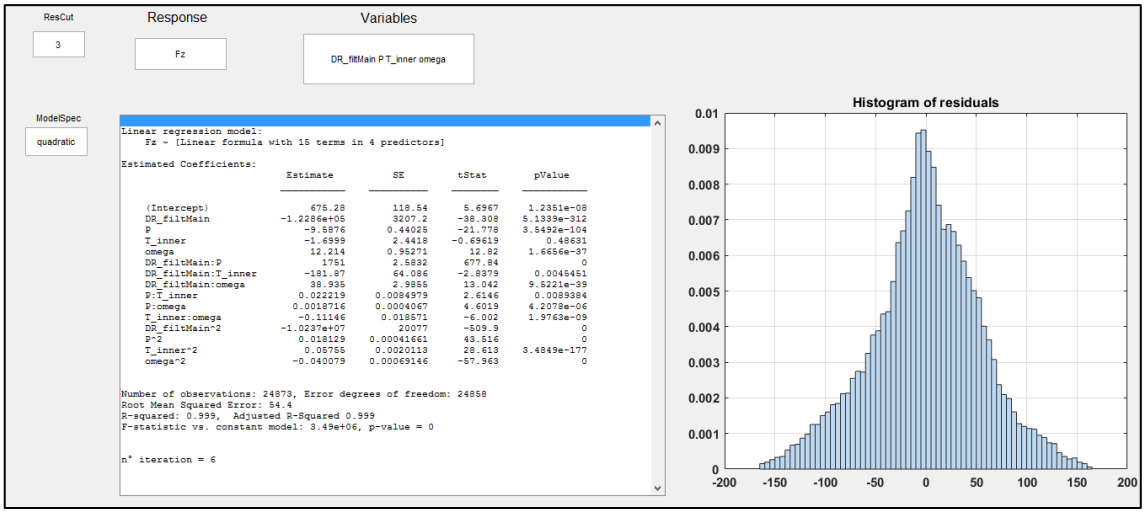

Figure 5.11 – Histogram of residual

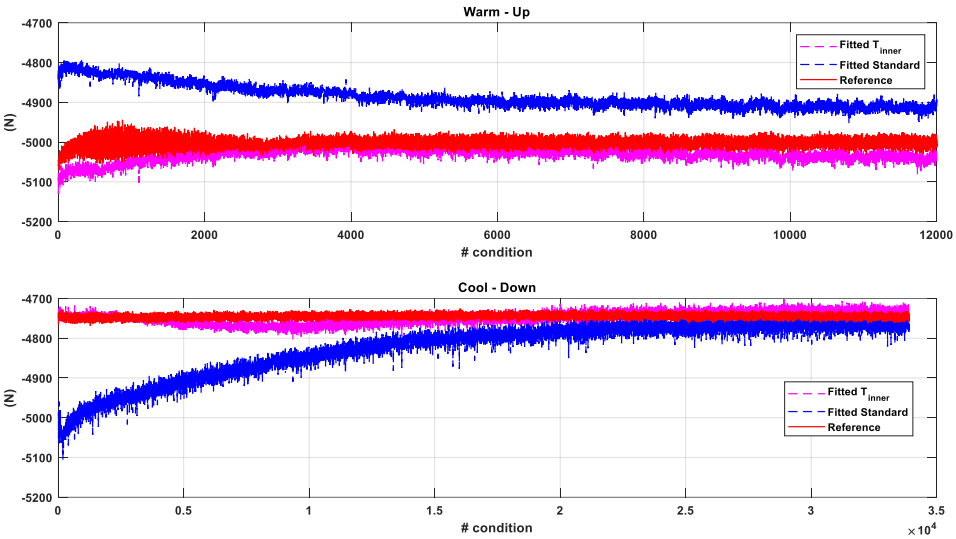

Figure 5.12 – Comparison between polynomials with and without correction

5.3.2 First correction strategy with Tcyber

The calibration polynomial takes the following form:

$$F_z = F_z(\omega, P, DR, T_{cyber}) \tag{5.2}$$

For training, the standard dataset (described in 3.6) is provided accompanied by a warm-up phase and a cool-down phase.

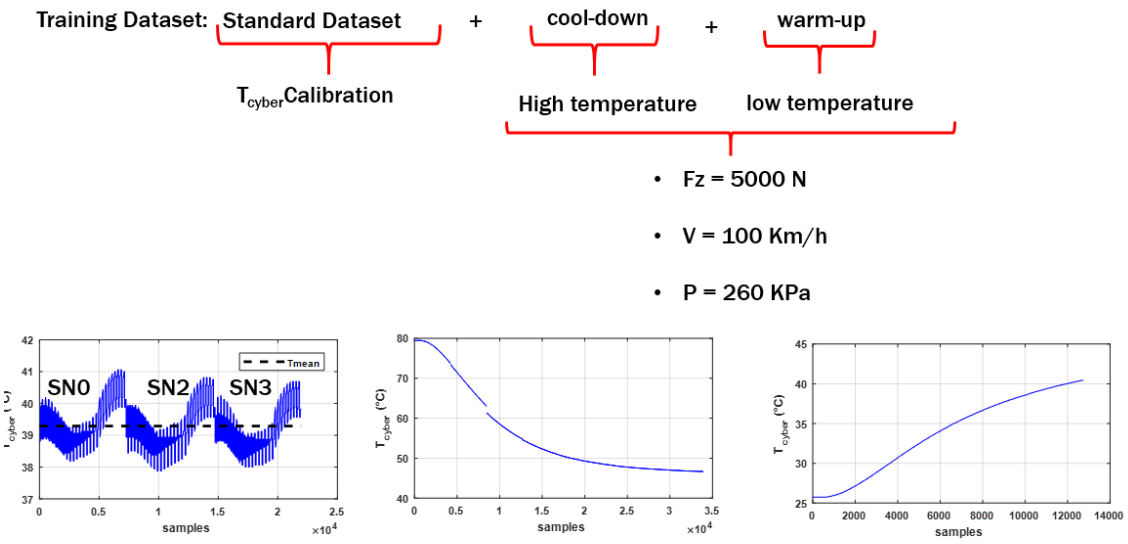

Figure 5.13 – Training Dataset

Figure 5.14 shows the results of the method. The final polynomial is quadratic and consists of 15 terms (4 predictors).

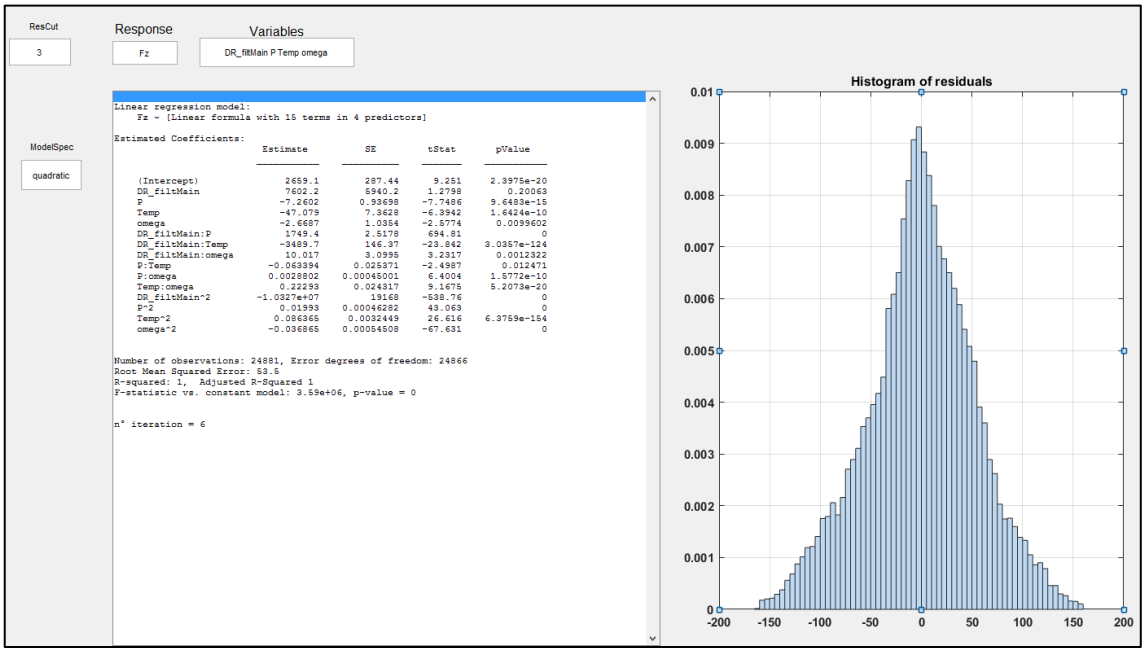

Figure 5.14 – Histogram of residual

Finally, figure 5.15 shows the comparison between polynomials with and without correction for both warm-up and cool-down.

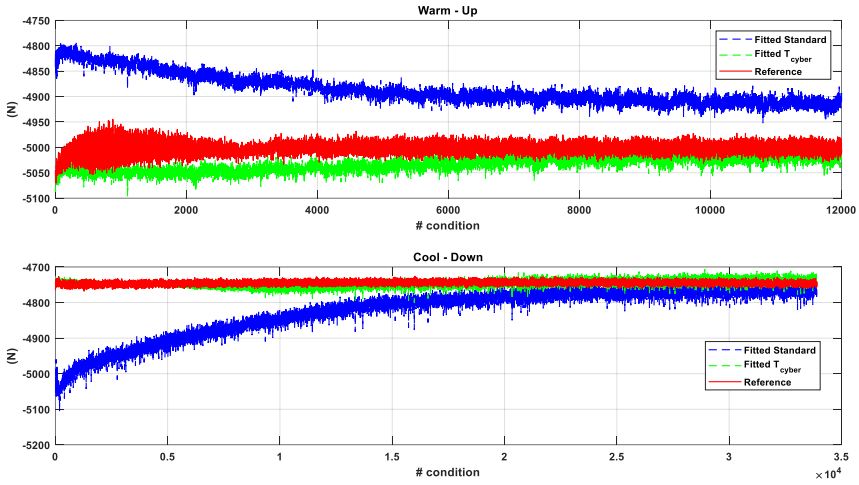

Figure 5.15 – Comparison between polynomials with and without correction

5.3.3 First correction strategy with Tbulk

Since during this test session the T3M sensors were not present, the bulk temperature used is that obtained from the thermal model.

The calibration polynomial takes the following form:

$$F_z = F_z(\omega, P, DR, T_{bulk}) \tag{5.3}$$

For training, the standard dataset (described in 3.6) is provided accompanied by a warm-up phase and a cool-down phase.

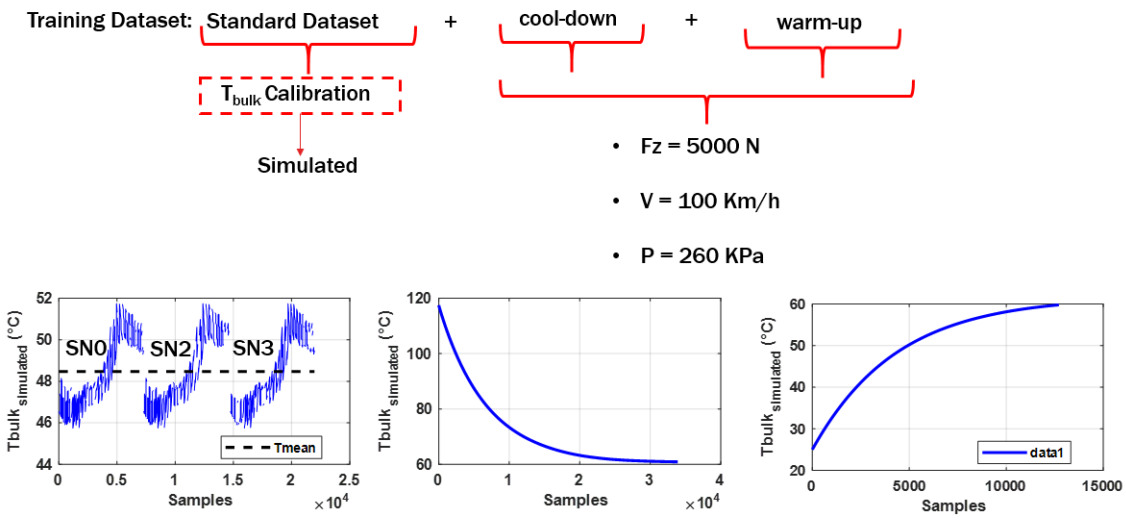

Figure 5.16 – Training Dataset

Figure 5.17 shows the results of the method. The final polynomial is quadratic and consists of 15 terms (4 predictors).

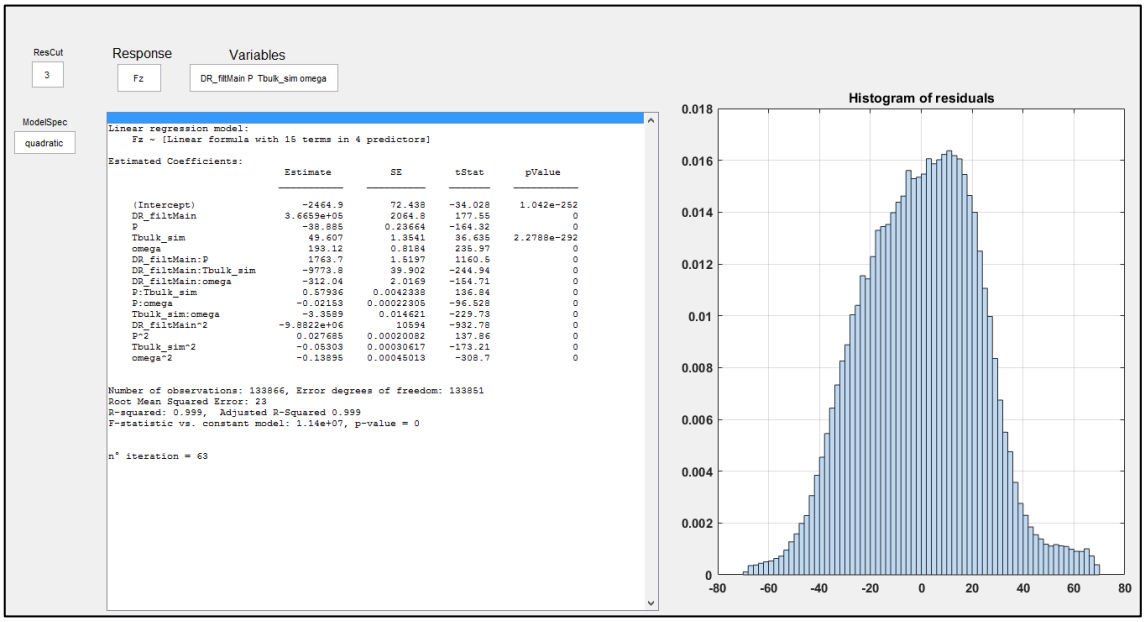

Figure 5.17 – Histogram of residual

Finally, figure 5.18 shows the comparison between polynomials with and without correction for both warm-up and cool-down.

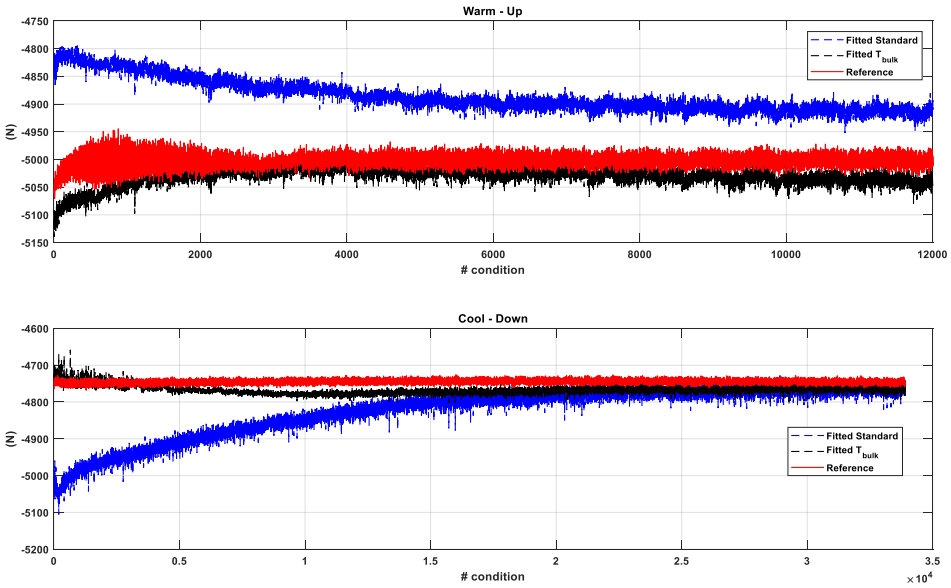

Figure 5.18 – Comparison between polynomials with and without correction

5.3.4 First correction strategy with T simulated

Unlike the T_{cyber} which is supplied directly by the cyber tyre, the T_{inner} and the T_{bulk} are measured only during these specific tests. The usefulness of the thermal model is precisely that of being able to have temperatures in other zones of the tyre starting from data measured by the cyber tyre.

In 5.3.3 the simulated Tbulk was treated; the simulated Tinner will be analyzed.

Then, the calibration polynomial takes the following form:

$$F_z = F_z(\omega, P, DR, T_{inner}sim) \tag{5.4}$$

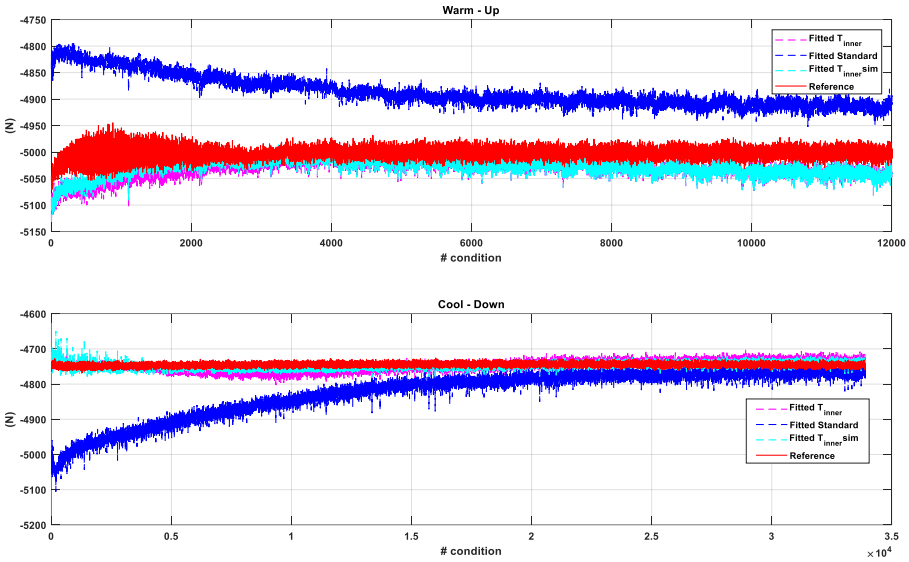

Figure 5.19 – Comparison between polynomials with and without correction

Table 5.2 summarizes the results obtained with the first strategy:

Table 5.2 – First strategy results

	TYPE CALIBRATION	METHOD	TYPE DATASET TRAINING	std (N)	mean error (N)
1	STANDARD	STANDARD	STANDARD	68	80
2	TCYBER	1ST STRATEGY	STANDARD + FULL COOL-DOWN +FULL WARM-UP (ALL SENSOSRS)	22	-1
3	TGROOVE	1ST STRATEGY	STANDARD + FULL COOL-DOWN +FULL WARM-UP (ALL SENSOSRS)	16	1
4	TINNER	1ST STRATEGY	STANDARD + FULL COOL-DOWN +FULL WARM-UP (ALL SENSOSRS)	26	0
5	TINNER sim	1ST STRATEGY	STANDARD + FULL COOL-DOWN +FULL WARM-UP (ALL SENSOSRS)	16	1
6	Tbulk sim	1ST STRATEGY	STANDARD + FULL COOL-DOWN +FULL WARM-UP (ALL SENSOSRS)	18	2
7	Tgroove sim	1ST STRATEGY	STANDARD + FULL COOL-DOWN +FULL WARM-UP (ALL SENSOSRS)	13	0

5.4 Correction of the vertical load: second correction strategy

This approach is based on the hypothesis of attributing the whole error to the DR. In fact, the standard calibration takes place in a certain temperature range and therefore with the same load, lower temperatures correspond to lower DR values and vice versa.

The idea is to bring the DR value measured at a certain temperature back to the reference value measured at the calibration temperature. This corrected DR represents the input of the standard calibration polynomial obtained with methods described in 3.6.3.

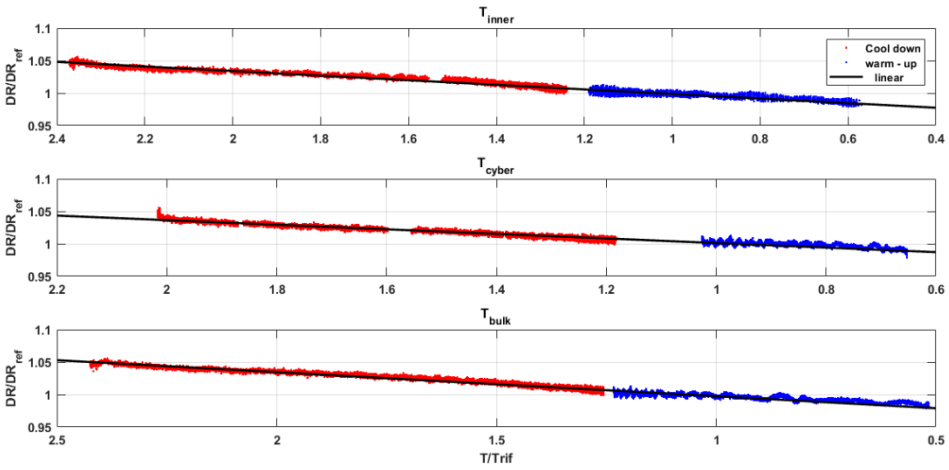

Figure 5.20 – DR dimensionless trend compared to the dimensionless temperature

$$DR_{target} = f_1\,(DR, Temperature) \tag{5.5}$$

$$F_z = F_z(\omega, P, DR_{target}) \tag{5.6}$$

f_1 is a function that allows to transform the measured *DR* at a certain temperature, into the DR_{target} corresponding to the calibration temperature:

$$DR_{ref} = a_0 + a_1 DR + a_2 T + a_3 DR * T \tag{5.7}$$

Figure 5.21 shows the effect of the correction on the *DR* while figures 5.22, 5.23 and 5.24 show the comparison between polynomials with and without correction for both warm-up and cool-down.

Finally, table 5.3 summarizes the results obtained with the first strategy.

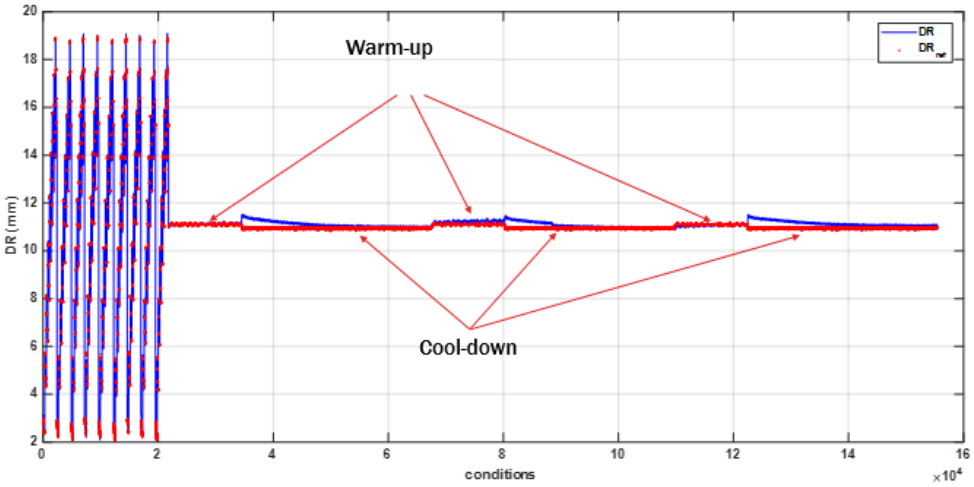

Figure 5.21 – DR_{target} vs $DR_{corrected}$

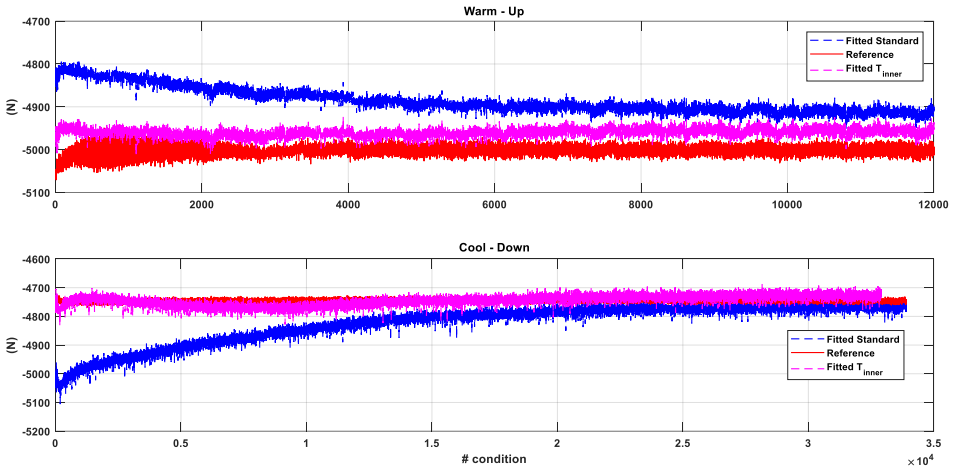

Figure 5.22 – Comparison between polynomials with and without correction (Tinner)

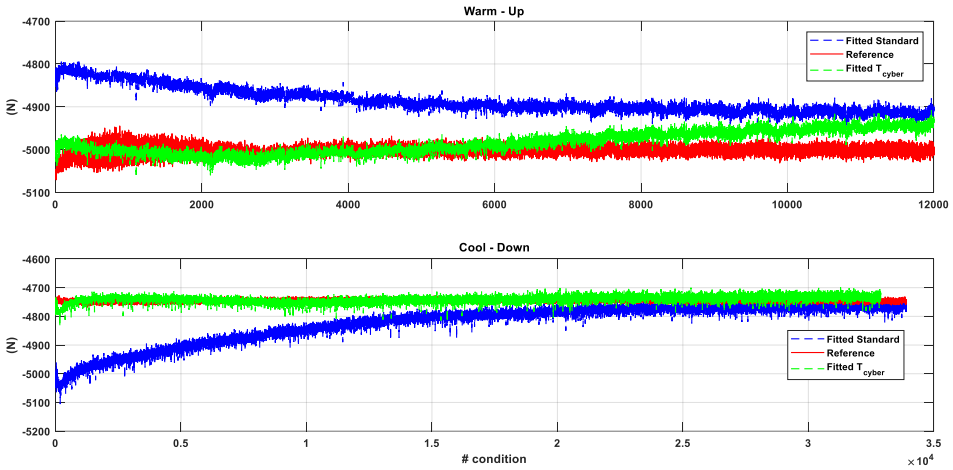

Figure 5.23 – Comparison between polynomials with and without correction (T_{cyber})

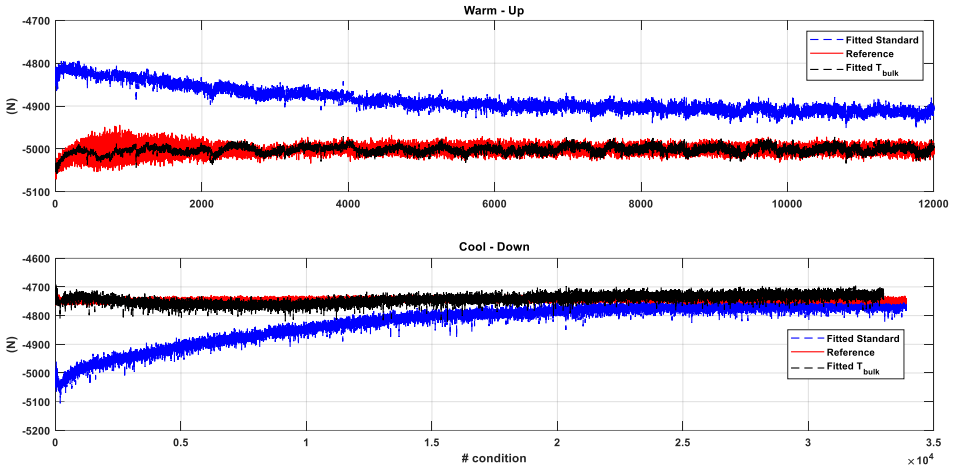

Figure 5.24 – Comparison between polynomials with and without correction (T_{bulk})

Table 5.3 – Second strategy results

	TYPE CALIBRATION	METHOD	TYPE DATASET TRAINING	std (N)	mean error (N)
1	STANDARD	STANDARD	STANDARD	68	82
2	TCYBER	2ND STRATEGY	STANDARD + FULL COOL-DOWN +FULL WARM-UP (ALL SENSOSRS)	-6	14
3	TGROOVE	2ND STRATEGY	STANDARD + FULL COOL-DOWN +FULL WARM-UP (ALL SENSOSRS)	-7	22
4	TINNER	2ND STRATEGY	STANDARD + FULL COOL-DOWN +FULL WARM-UP (ALL SENSOSRS)	-6	19
5	TINNER sim	2ND STRATEGY	STANDARD + FULL COOL-DOWN +FULL WARM-UP (ALL SENSOSRS)	25	-5
6	Tbulk sim	2ND STRATEGY	STANDARD + FULL COOL-DOWN +FULL WARM-UP (ALL SENSOSRS)	25	-4
7	Tgroove sim	2ND STRATEGY	STANDARD + FULL COOL-DOWN +FULL WARM-UP (ALL SENSOSRS)	24	-7

5.5 Correction of the vertical load: sensitivity analysis

An analysis is carried out on the variation of the estimate of the vertical load due to a variation of the estimate of the temperature (Figure 5.25):

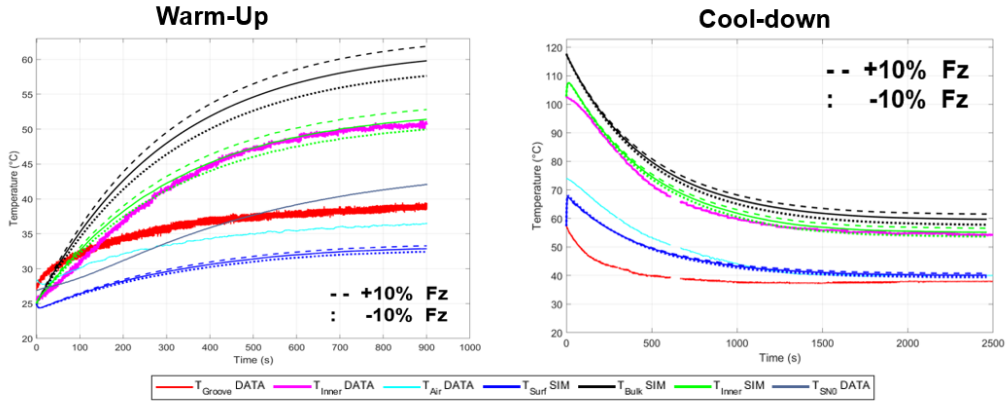

	+ 10% Fz	- 10% Fz
Surface	+1.22%	-1.13%
Bulk	+3.35%	-3.60%
Inner	+2.74%	-2.80%

	+ 10% Fz	- 10% Fz
Surface	+1.62%	-1.72%
Bulk	+3.05%	-3.17%
Inner	+2.60%	-2.68%

Figure 5.25 – Effect of Fz variation on the Temperature estimation

The following analyses are carried out for both strategies:

- T_{inner} with $Fz_{nom} \pm 10\%$
- T_{bulk} with $\mathrm{Fz_{nom}} \pm 10\%$

The analysis is carried out using the following parameter:

$$\Delta\% = \frac{Fzcorect\ Nom\ - \overline{Fzcorrect}}{Fzcoorect\ Nom} \tag{5.8}$$

where:

- $Fzcorect\ Nom$ is the vertical load correct with nominal Temperature
- $\overline{Fzcorrect}$ is the vertical load correct with nominal Temperature obtained with Fz $\pm$**10**%

Figure 5.26 shows the results for both strategies.

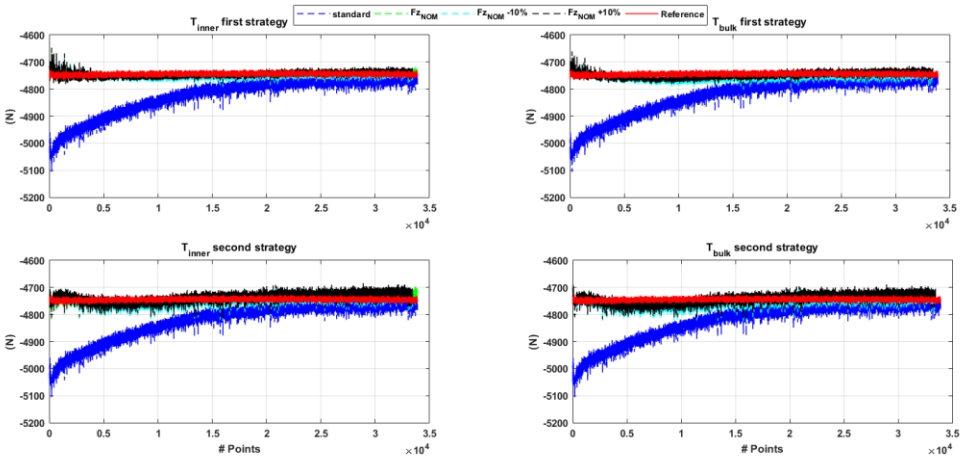

Figure 5.26 – Sensitivity analysis results

Finally, table 5.6 summarizes the values assumed by Δ.

Table 5.4 – Δ values

	+ 10% Fz	**- 10% Fz**
T_{inner} 1st strategy	0.13%	-0.15%
T_{inner} 2nd strategy	0.14%	-0.13%
T_{bulk} 1st strategy	0.34%	-0.42%
T_{bulk} 2nd strategy	0.13%	-0.14%

5.6 Correction of the vertical load: some considerations

Two vertical load correction strategies have been developed. The first strategy concerns the direct insertion of the temperature into the calibration procedure obtaining a calibration polynomial with 4 inputs. The second strategy concerns the prior correction of the DR with temperature. This corrected DR then represents the input of the standard polynomial (with 3 input).

For both strategies, different temperatures were analysed for different areas of the tyre (surface, inner, bulk and Tcyber).

Basically, for both strategies and for the various temperatures, a clear improvement in the estimate of the vertical load was obtained and therefore, on the basis of this it would be difficult to make a choice on the best strategy.

As for the strategies, from an application point of view, the second strategy represents the least invasive as it leaves the standard polynomial (this type of polynomial is the result of numerous years of study by the company and is very reliable) while the second strategy involves the modification of the entire polynomial and therefore a series of studies to arrive at an acceptable level of reliability.

As for the choice of temperature, based on the only test available, it is not possible to reach a definitive conclusion. In fact, the test carried out has a very slow thermal dynamics and therefore, it is necessary to carry out a series of tests in different dynamic conditions. Since the various areas of the tyre will have a different thermal dynamic, the choice will go to the one that most closely follows the dynamic of the DR.

5.7 Conclusions and next steps

The activity carried out in collaboration with Pirelli tyre SPA aimed to study the thermal behaviour of sensorized tyres called intelligent tyres.

The so called Cyber^{TM} Tyre project carried out by Pirelli allows the knowledge of the main dynamic entities featuring tyre-road interaction by means of the installation of suitable sensors inside the tyre.

Thanks to this solution Pirelli is now able to provide important information about parameters that are related to the contact area such as contact forces, contact patch length, deformed radius, centre of gravity position and surface texture changes.

The work consisted in the in the definition of a strategy for the introduction of thermal dependence in the numerical model for the calculation of features currently implemented,

such as for example the estimates of contact forces. The objective is to increase the reliability of the estimate in all conditions, especially in cold tyre conditions.

For this purpose, a thermal model was first developed capable of providing the temperature of some areas of the tyre starting from some sizes measured directly by the Cyber^{TM} Tyre (including the temperature at its position).

A series of tests were carried out both indoors and outdoors to characterize the various phenomena of heat exchange (convection, conduction, heat generation, etc.).

Subsequently, the activity concentrated on the effect of temperature on the estimate of the vertical load in conditions of pure rolling (only heat generation due to the viscoelastic effect of the material).

Two correction strategies have been developed:

1. Direct introduction of the temperature in the calibration polynomial
2. Preliminary correction of the DR and use of the standard calibration polynomial.

For both strategies, various temperatures corresponding to different areas of the tyre were used.

Both strategies led to a clear improvement in the estimate. Between the two strategies, the choice falls on the second as it results to be less invasive leaving the standard calibration polynomial unchanged.

Figure 5.26 shows schematically, in the form of a flow chart, how the thermal model is introduced into the cyber tyre measurement chain.

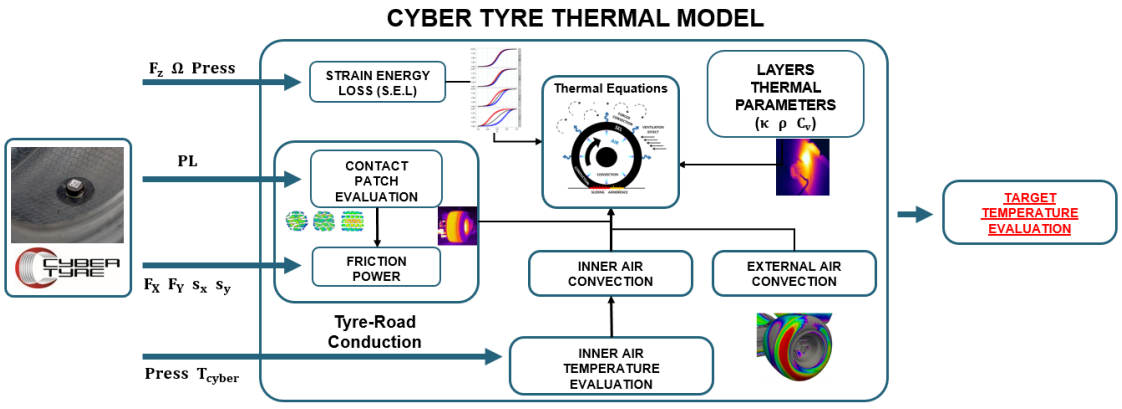

Figure 5.27 – Input-output flow chart of the thermal model

About the next steps:

1. validation of the methodology on tests with different vertical load values, internal pressure and speed
2. Carry out a series of tests in different dynamic conditions in order to identify the temperature that most correlates with the phenomenon.
3. Introduction of Friction power
4. Extend the study to other features such as lateral and longitudinal load

Chapter 6

The Temperature influence on tyre/road interaction curves

6.1 Introduction

In automobile racing world, where reaching the limit is the standard and the time advantage in an extremely short time period is a determining factor for the outcome, predicting in advance the behaviour of the vehicle system in different conditions is a pressing need.

The tyre performance is widely influenced by its operating internal temperature distribution and inflation pressure; the description from a thermodynamic point of view of a tyre is therefore of fundamental importance as regards the dynamics of the vehicle.

In this view, the importance of having a model that estimates temperature distribution inside the different tyre layers is evident, as well as the importance of defining how and how much this temperature distribution affects tyre performance.

Pacejka's Magic Formula tyre model is a standard in automotive word as a semi-empiric model employed for predictive performance analyses. To more deeply predict tyre behaviour, MF model must become sensitive to tyre temperature and inflation pressure, meaning that MF interaction curves must be able to be drawn at different temperature or pressure values.

However, the Pacejka's Magic Formula, is able to describe the tyre dynamics in a very strict range of operating condition (fixed temperature, internal pressure, asphalt characteristics, wear level and so on).

Based on this, a formulation, called MF-evo, has been developed, able to consider the internal air pressure and the temperature of the different layers, instantly changing the dynamic characteristics of the tyre.

The additional physical variables are co-simulated thanks to specifically developed tyre physical thermodynamic and grip model, able to estimate in real time the tyre layers' temperature and the internal air pressure.

The purpose of this work is a sensitivity analysis of the influence of a series of quantities on the vehicle dynamic behaviour.

Numerous parameters are considered (tread wear level, specific thermal conductivity and heat of the various layers etc.) which would require many tests.

The work was carried out in collaboration with VI-grade which provides a simulation environment called *VI-Car Real Time*.

VI-CarRealTime provides a real-time vehicle simulation environment where the same simplified vehicle model can be used by vehicle dynamics and controls engineers to optimize vehicle and control system performance.

It is a Software-in-the-Loop simulations:

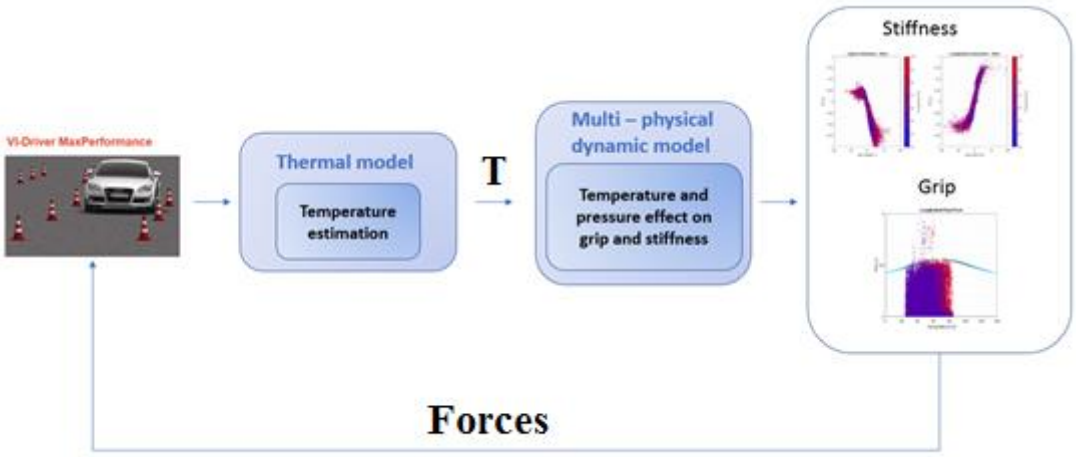

Figure 6.1 – Software in the loop simulation

6.2 Pacejka Magic Formula

This is a semi-empirical method that requires a campaign of experimental tests in order to characterize the tyre-road system.

This model is very useful to simulate the steady-state behaviour by providing a set of mathematical formulae, which are partly based on a physical background. It calculates the forces (Fx, Fy) and moments (Mx, My, Mz) acting on the tyre under pure and combined slip conditions, using longitudinal and lateral slip (k, α), wheel camber (γ) and the vertical force (Fz) as input quantities (Figure 6.2).

In addition to the Magic Formula description, a set of differential equations is defined, representing the transient behaviour of the tyre with respect to handling at frequencies up to 8 Hz [78] [79].

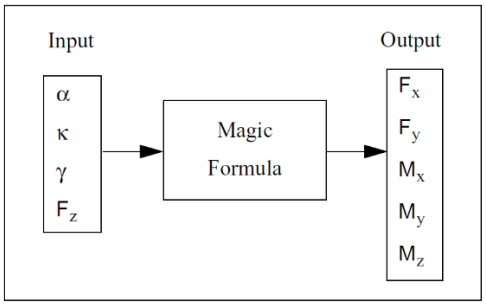

Figure 6.2 – Input and Output variables of the Magic Formula Tyre Model

Before the description of the formulation, all the units of the parameters and variables used in MF – Tyre, in agreement with SI units, are provided:

Variable Type	Name	Abbreviation	Unit
angle	Slip angle Camber angle	α γ	rad
Force	Longitudinal force Lateral force Vertical force	F_x F_y F_z	N
Moment	Overturning moment Rolling resistance Self-aligning moment	M_x M_y M_z	Nm
speed	Longitudinal speed Lateral speed Longitudinal slip speed Lateral slip speed	V_x V_y V_{sx} V_{sy}	m/s
Rotational speed	Tyre rolling speed	Ω	rad/s

The general expression of the MF is [78]:

$$y(x) = D \cdot \sin[C \cdot \arctan\{B_x - E \cdot (B_x - \arctan B_x)\}] \tag{6.1}$$

with:

$$Y(x) = y(x) + S_v \tag{6.2}$$
$$x = X + S_h \tag{6.3}$$

where:

- $Y(x)$ is the output (Fx, Fy or Mz)
- X is the input (slip ratio or slip angle)
- B is the rigidity factor
- C is the shape factor
- D is the peak value

- E is the bending factor
- S_v is the vertical shift
- S_h is the horizontal shift

The result, shown in figure 6.3, is a curve that passes through the origin (unless the imposed translations), reaches a peak value and then assumes a horizontal asymptotic pattern. The 6 coefficients listed above are called Pacejka's macro parameters and govern the trend of the curve.

The BCD product corresponds to the slope of the curve in the origin. C controls the shape of the curve and governs the abscissa of the maximum and the curvature in its surroundings. The shifts allow to translate the curve and to contemplate the contribution of camber, hysteresis, asymmetry and taper of the tyre.

It is important to note that for C≤1 the maximum value of the curve coincides with the asymptote and that for E> 1 the curve degenerates (the model is infeasible).

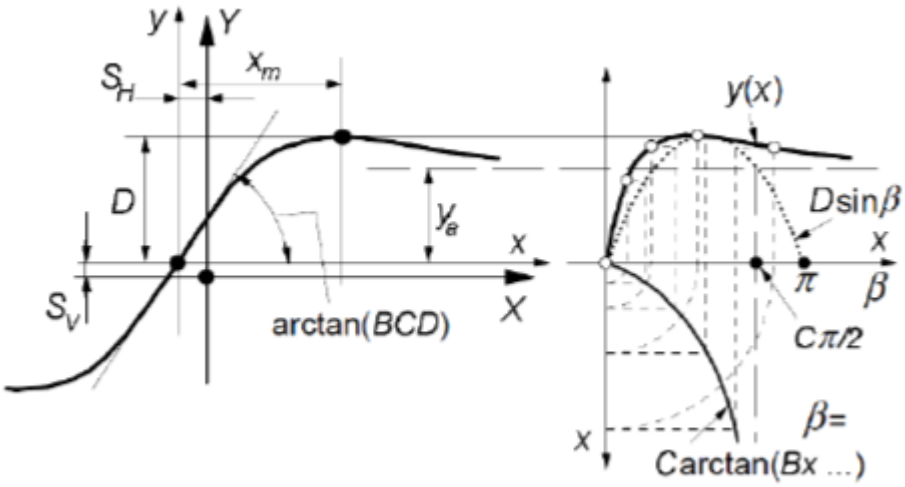

Figure 6.3 – Curve produced by the original sine version of the Magic Formula

The expression just described allows to represent the characteristics of pure interaction.

In combined interaction, at the same load, total sliding condition occur for smaller value of slip (ratio or angle), since part of the available adherence is engaged by the complementary interaction. This observation led to the development and implementation of the "cosine version" of the Pacejka formula.

The first expression elaborated was:

$$G = D \cdot \cos[C \cdot \arctan(B_x)] \tag{6.4}$$

$$x = X + S_h \tag{6.5}$$

With B, C, D and Sh distinct from the previously defined macro parameters. As shown in Figure 6.4, parameter D represents the maximum value (slightly less than 1 in the presence of offset), C determines the position of the horizontal asymptote placed at the base of the curve, B governs the shape and intercepts with the axis of the abscissas.

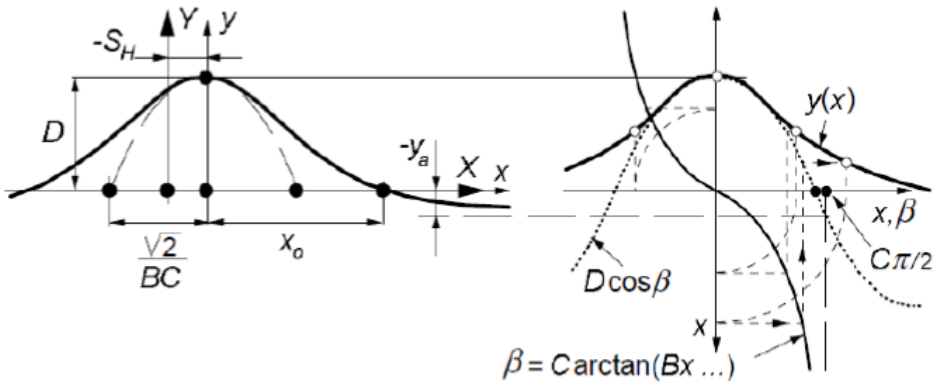

Figure 6.4 – Curve produced by the cosine version of the Magic Formula

This expression is also known as the "hill function" due to the bell-like performance that characterizes it.

Parameter G, multiplied by pure interaction, returns the combined interaction. This is evidently a weight function, a reduction factor that has a physical sense only if it is within the range [0,1].

The most recent expressions of the formula, particularized for longitudinal and lateral interaction, are:

$$G_{x\alpha} = \frac{\cos[C_{x\alpha} \cdot \arctan\{B_{x\alpha}\alpha_s - E_{x\alpha}(B_{x\alpha}\alpha_s - \arctan(B_{x\alpha}\alpha_s))\}]}{\cos[C_{x\alpha} \cdot \arctan\{B_{x\alpha}S_{Hx\alpha} - E_{x\alpha}(B_{x\alpha}S_{Hx\alpha} - \arctan(B_{x\alpha}S_{Hx\alpha}))\}]} \tag{6.6}$$

$$G_{yk} = \frac{\cos[C_{yk} \cdot \arctan\{B_{yk}k_s - E_{yk}(B_{yk}k_s - \arctan(B_{yk}k_s))\}]}{\cos[C_{yk} \cdot \arctan\{B_{yk}S_{Hyk} - E_{yk}(B_{yk}S_{Hyk} - \arctan(B_{yk}S_{Hyk}))\}]} \tag{6.7}$$

6.2.1 Magic Formula Particularization

In general, the interaction characteristic, i.e. the law that binds the force (longitudinal or lateral) to the slip (ratio or angle), varies according to the vertical load, the camber angle, the inflation pressure, the spin. It also depends on the construction characteristics,

the thermo-mechanical and tribological properties of the tyre, as well as on the road surface conditions. The subject is further complicated by the non-linear behaviour of the system under examination.

To introduce dependence on all these factors into the economy of the equation, the macro parameters have been expressed as a combination of micro-parameters. Over the last few years, the modelling work has been focused on the development and optimization of the expressions that link macro and micro-parameters, without prejudice the general formulation.

Before proceeding it should be noted that Magic Formula is defined in the privileged reference system according to the ISO convention.

MF-Tyre conforms to the TYDEX STI conventions described in the TYDEX-Format and the Standard Tyre Interface (STI).

Two TYDEX coordinate systems with ISO orientation are particularly important, the C- axis and W-axis systems as detailed in Figure 6.5.

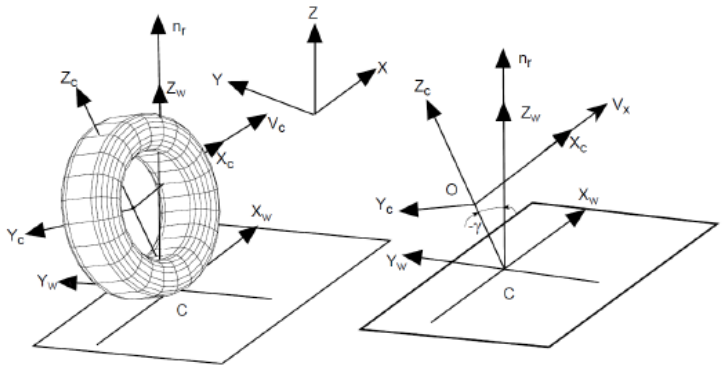

Figure 6.5 – TYDEX C – and W- Axis Systems used in MF-Tyre, according to TYDEX

The C-axis system is fixed to the wheel carrier with the longitudinal xc – axis parallel to the road and in the wheel plane ($xc- zc$ – plane). The origin O of the C-axis system is the wheel centre.

The origin of the W-axis system is the road contact-point (or point of intersection) C defined by the intersection of the wheel plane, the plane through the wheel spindle and the road tangent plane. The orientation of the W-axis system agrees to ISO.

The forces and torques calculated by MF-MC Tyre, which depend on the vertical wheel load *Fz* along the zw- axis and the slip quantities are projected in the W-axis system. The xw- yw- plane is the tangent plane of the road in the contact point C.

The geometrical and kinematical quantities involved are so defined:

- V, wheel centre speed;

- Vx and Vy, respectively longitudinal and lateral speed of the wheel centre;
- Ω, the peripheral speed of the wheel around its own kinematic axis;
- Re, pure rolling radius;
- $Vsx = Vx - \Omega Re$, longitudinal sliding speed, that is the speed difference between centre and periphery of the wheel that occurs during the braking or the acceleration phases;
- $Vsy = Vy$, lateral sliding speed, it occurs when the velocity vector does not lie on the equatorial plane of the wheel, i.e. when the vehicle is engaged in a curve;
- $\kappa = -\frac{\mathrm{Vsx}}{\mathrm{Vx}}$, slip ratio, it constitutes the abscissa of the longitudinal interaction characteristic (the "-" sign is introduced to have concord force and slip);
- α=arctan $\left(\frac{\mathrm{Vsy}}{|\mathrm{Vy}|}\right)$, slip angle, it constitutes the abscissa of the lateral interaction characteristic;
- γ, camber angle;
- Fz, vertical thrust exerted by the road on the wheel in correspondence of the contact patch, it coincides with the vertical load on the wheel centre;
- F_{z0}, nominal load used in the parametric identification by the manufacturer;
- λ_{Fz0}, scale factor of nominal (rated) load.
- $F_{z0}' = F_{z0}\ \lambda_{Fz0}$, vertical load scaled;
- $dFz = \frac{\mathrm{F_z - F_{z0\prime}}}{\mathrm{F_{z0\prime}}}$, load increase with respect to the nominal condition (possibly scaled).

Sometimes the interaction characteristics dictated by the MF are significantly far from the experimental points detected by the telemetry. This is due to the impossibility of faithfully reproducing in the laboratory the conditions of humidity, temperature, inflation pressure, adhesion, wear, taper which the tyre is subjected once mounted on a real vehicle.

To buffer this problem, scaling factors have been introduced that allow modulating macro parameters and modifying the shape of the curve due to experimental data. They are indicated with the letter λ and are listed in the table below [80] [81].

The default value of these factors is set equal to one (except $\lambda\mu y$ which equals zero if not used). For example, to change from a relatively high friction surface to a law friction surface the factor $\lambda\mu x$ and $\lambda\mu y$ may be given a value lower than unity.

Table 6.1– Scaling coefficient, pure slip.

Name:	Name used in tire property file:	Explanation:
λ_{Fzo}	LFZO	Scale factor of nominal (rated) load
λ_{Cx}	LCX	Scale factor of F_x shape factor
$\lambda_{\mu x}$	LMUX	Scale factor of F_x peak friction coefficient
λ_{Ex}	LEX	Scale factor of F_x curvature factor
λ_{Kx}	LKX	Scale factor of F_x slip stiffness
λ_{Hx}	LHX	Scale factor of F_x horizontal shift
λ_{Vx}	LVX	Scale factor of F_x vertical shift
$\lambda_{\gamma x}$	LGAX	Scale factor of camber for F_x
λ_{Cy}	LCY	Scale factor of F_y shape factor
$\lambda_{\mu y}$	LMUY	Scale factor of F_y peak friction coefficient
λ_{Ey}	LEY	Scale factor of F_y curvature factor
λ_{Ky}	LKY	Scale factor of F_y cornering stiffness
λ_{Hy}	LHY	Scale factor of F_y horizontal shift
λ_{Vy}	LVY	Scale factor of F_y vertical shift
$\lambda_{\gamma y}$	LGAY	Scale factor of camber for F_y
λ_t	LTR	Scale factor of Peak of pneumatic trail
λ_{Mr}	LRES	Scale factor for offset of residual torque
$\lambda_{\gamma z}$	LGAZ	Scale factor of camber for M_z
λ_{Mx}	LMX	Scale factor of overturning couple
λ_{VMx}	LVMX	Scale factor of Mx vertical shift
λ_{My}	LMY	Scale factor of rolling resistance torque

Table 6.2 – Scaling coefficient, combined slip.

Name:	Name used in tire property file:	Explanation:
$\lambda_{x\alpha}$	LXAL	Scale factor of alpha influence on F_x
$\lambda_{y\kappa}$	LYKA	Scale factor of alpha influence on F_x
$\lambda_{Vy\kappa}$	LVYKA	Scale factor of kappa induced F_y
λ_s	LS	Scale factor of Moment arm of F_x

Table 6.3 – Scaling coefficient, transient response.

Name:	Name used in tire property file:	Explanation:
$\lambda_{\sigma\kappa}$	LSGKP	Scale factor of Relaxation length of Fx
$\lambda_{\sigma\alpha}$	LSGAL	Scale factor of Relaxation length of Fy
$\lambda_{\omega r}$	LGYR	Scale factor of gyroscopic torque

6.3 MF-evo scheme

MF model provides a set of scaling factors that has been introduced to consider the influence of several external overall parameters such as road roughness, weather conditions and suspension characteristics. These scaling factors are important for a correct prediction of tyre-road contact forces but are not a function of the tyre itself.

Pacejka MF standard model does not consider the thermal effect, thus has constant tyre characteristics, meaning that if we consider a long run from a track session slip angle would have no reason to increase from one lap to another. Instead, the rise in temperature, with increasing lap number, leads to a decrease in cornering stiffness, which means that in order to have the same lateral force magnitude at the same curve the value of the slip angle must be gradually greater (figure 6.6).

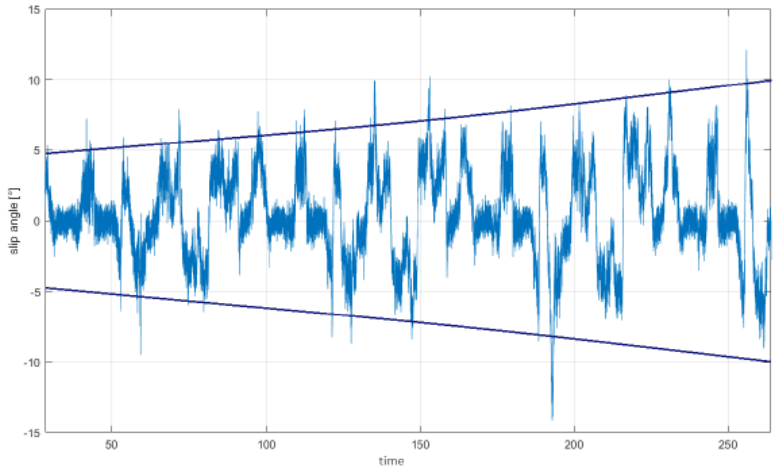

Figure 6.6 – Slip angle (time history)

Developing a multi-physics tyre model, that considers how its dynamics is influenced not only by dynamic and kinematic parameters but also by thermodynamic ones, is strongly necessary to have a complete picture of the factors that affects tyre performance.

The MF-evo version is able to modify the tyre behaviour on the basis of the thermally enriched dynamic state, making possible to consider, in real time, the variations in coefficients by means of pre-identified embedded analytic functions, developed in collaboration with Vehicle Dynamics UniNa Research Group (figure 6.7).

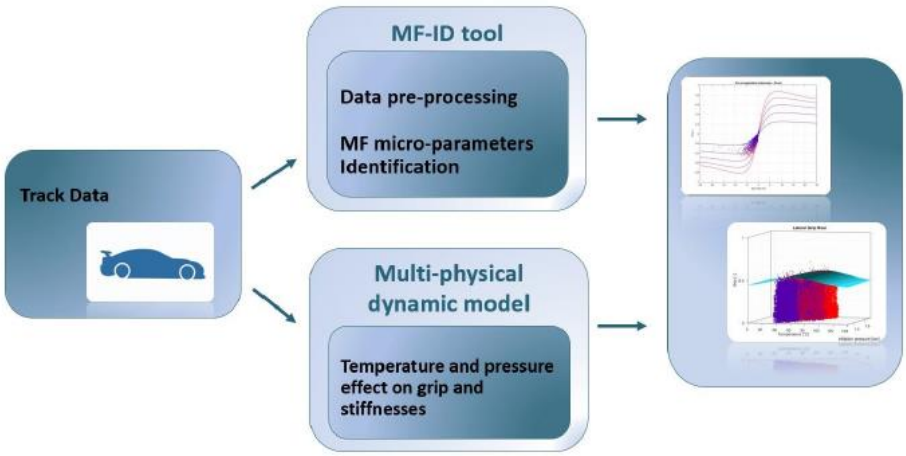

Figure 6.7 – MF-evo scheme

The variations of tyre characteristics due to temperature and pressure effects are obtained modifying the scaling factors based on the weighting functions of grip and stiffness in dependence on temperature and pressure, allowing to reproduce the variation of forces throughout the whole thermodynamic working range, making Pacejka MF-evo model sensitive to tyre temperature internal distribution and inflation pressure.

The possibility of simulating the interaction forces that the tyre exchanges with the ground throughout the whole thermodynamic working range is of fundamental importance in view of identifying the range of temperature and pressure in which grip performance is maximized.

6.3.1 Temperature effects

The importance of a tyre thermal model additional outputs can be easily deduced from figure 6.8 and figure 6.10 (normalized because of confidential agreement), where the tyre tread temperature, not available from the sensor data but provided by a tyre thermal model1, deeply modifies the tyre dynamic behaviour [82].

The difference in terms of interaction curves can be appreciated highlighting a stiffness decrease due to a higher tyre temperature for both longitudinal and lateral tyre interaction curves.

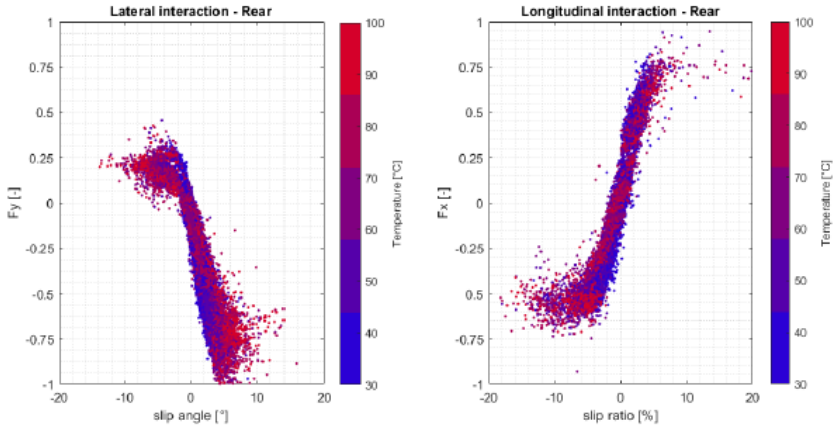

Figure 6.8 – Temperature effect on lateral and longitudinal interactions

Reference temperature used to underline the stiffness-temperature correlation is Tread Core temperature. Tread Core (in red, Figure 6.9) is situated between Tread Surface (in blue) and Tread Base (in black), whereas Tread Base represents the part of the compound in direct contact with the tyre belt layer.

By means of a tyre thermal model, it is possible to predict the temperature gradient with a high level of accuracy within the entire tyre structure. Starting from the model outputs in terms of temperatures and local thermal exchanges, the physical considerations particularly suitable to distinguish the optimal thermal range of each compound and the variation of tyre dynamic behaviour due to the thermal effect, can be further performed.

Figure 6.9 – Tyre thermal model – temperatures scheme.

Thanks to the availability of the tread temperature, it is possible to obtain much more correlations, from which optimal thermal range can be identified. Tread temperature offers the best results concerning the correlation stiffness-temperature as well as grip-temperature (figure 6.10, normalized because of confidential agreement); in fact, the external surface temperature varies with fast dynamics, which does not allow to modify in so short time the whole tread characteristics, while the inner liner temperature varies too slowly to condition the tyre performance instant by instant.

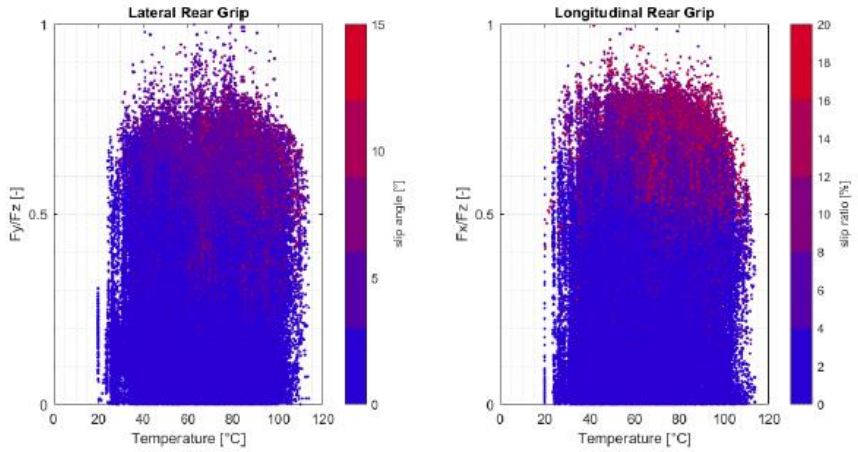

Figure 6.10 – Temperature effect on lateral and longitudinal grip

In figure 6.10 acquired data have been coloured from blue to red with increasing slip angle for the lateral grip and slip ratio for the longitudinal one.

6.3.2 Pressure effects

Changing inflation pressure even affects tyre force and moment characteristics. This happens because changes in inflation pressure alter the size, shape and contact pressure distribution in the footprint of the tyre. In general, increasing inflation pressure will cause

the size of the footprint to shrink, raise the contact pressure near the centre of the footprint and allow less tyre distortion (less footprint shape change).

Tyre-road pure lateral interactions of rear-axle acquired data at three pressure levels have been plotted with different colours in figure 6.11 (normalized because of confidential agreement).

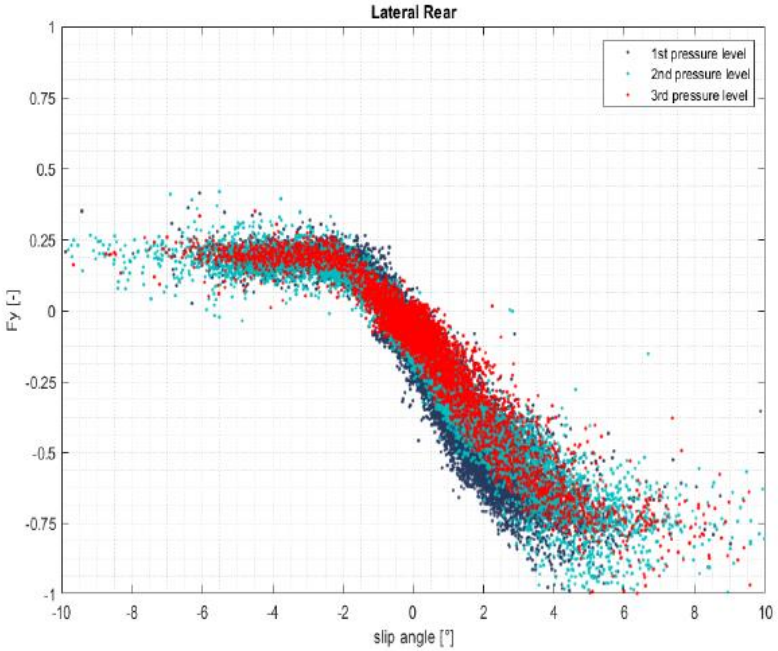

Figure 6.11 – Pressure effect on lateral interaction

A decrease in inflation pressure increases the lateral force capability of the tyre and thus the cornering stiffness, due to the increase of tyre's footprint. On contrary, a decrease of contact length (smaller surface area) results in a decrease of cornering stiffness [83] [84].

Meanwhile, a lower air pressure often brings to lower forces after the peak value, when sliding velocity begin to play a dominant role in tyre road interactions.

Increasing pressure also reduces the longitudinal force capability and the braking stiffness of the tyre, as it is shown in Figure 6.12 (normalized because of confidential agreement) where pure longitudinal interaction for acquired data have been displayed.

The influence of inflation pressure on the peak grip coefficient value doesn't seem to be very dominant with respect to internal temperature distribution. We could say that in a specific temperature range, increasing inflation pressure reduces both lateral and longitudinal grip as a results of contact patch reduction.

However, it's difficult to highlight this dependence on experimental data from handling track session since the rise in temperature leads to a direct increase in pressure too and it's not possible to discriminate the two effects. Laboratory tests should be carried out in order to study the way tyre performance is affected by tyre pressure while keeping the temperature in the different layers steady.

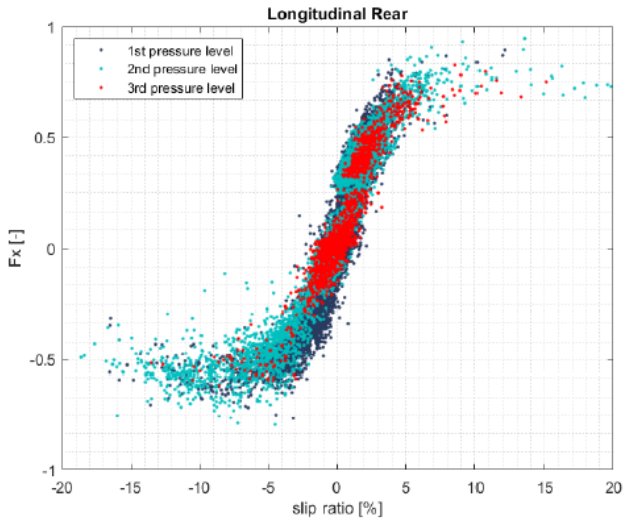

Figure 6.12 – Pressure effect on longitudinal interaction

During handling track session temperature and pressure are two phenomena closely linked to one other. As a result, with increasing pressure the temperature window in which tyre reach its maximum performance increase (Figure 6.13, normalized because of confidential agreement).

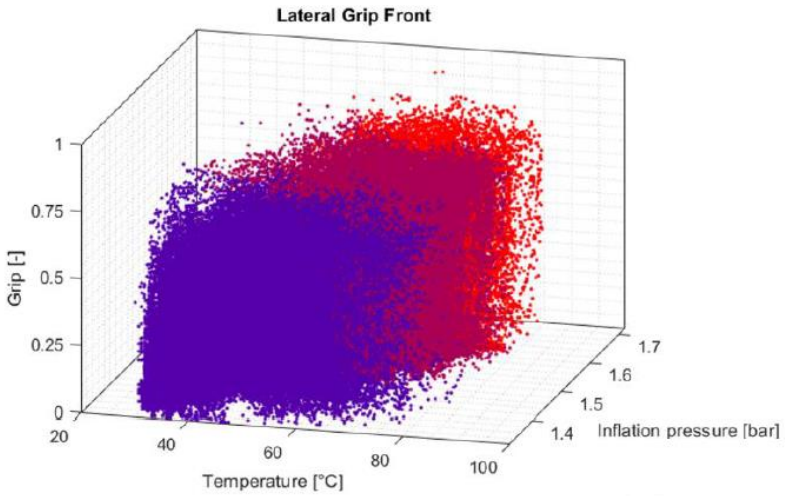

Figure 6.13 – Maximum grip-temperature variation with pressure

6.3.3 Grip Analysis

It is possible to say that grip depends on both tread-surface and tread-core temperatures.

The tyre external surface temperature varies with faster dynamics, which is not well correlated with the grip variation which does not show fast dynamics. This means that the surface temperature is not able to modify in so short time the whole tread mechanical characteristic. The grip shows an excellent correlation with a temperature weighted averages between tread surface and tread core, the tread-core layer shows a slower dynamic, so the mean average temperature dynamics have the same trend of the grip. The tyre frictional behaviour can be practically linked to the tread core-surface weighted averages temperature which can be used to optimize the compound mechanical characteristics starting from its thermal behaviour. The above temperature can clearly be evaluated only by means of a specific tyre thermal model.

After a sensitive analysis, the most suitable temperature to identify the grip variation is a weighted average between tread-surface and the tread-core, in particular:

$$T_{GRIP} = 0.25 \cdot T_{tread\ surface} + 0.75 \cdot T_{tread\ core} \tag{6.8}$$

The trend of the grip shows the presence of a temperature range in which grip reaches its maximum values. With the aim of modelling the noted trend, grip law as function of temperature has been assumed as a Gaussian function. Moreover, Gaussian function for each pressure level shows its maximum value at increasing temperature values as pressure increases.

Both lateral and longitudinal grip analysis has been done. Figure 6.14 shows the grip values as a function of temperature and inner air pressure variation (All plots are normalized for industrial confidentiality agreements).

It is possible to consider also the inner air pressure variation influence on grip level. In this case, a bidimensional model has been considered.

The identified functions are characterized by assuming a unit value at the maximum performance-temperature and pressure. In this way, it is possible to scale the Pacejka curves, identified at about maximum performance-temperature and pressure levels, and to get the interaction forces at any temperature or pressure value, multiplying the scale factor LMUY for lateral interaction and LMUX for longitudinal interaction by the gain-function output corresponding to that temperature or pressure value.

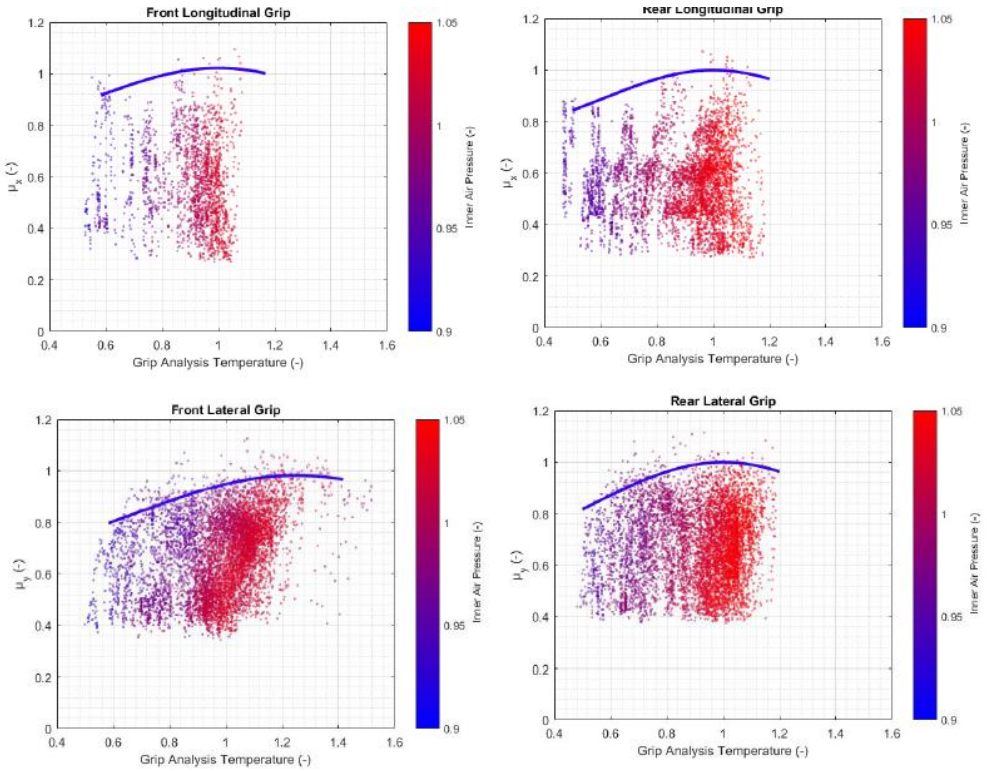

Figure 6.14 – Grip values as a function of temperature and inner air pressure variation

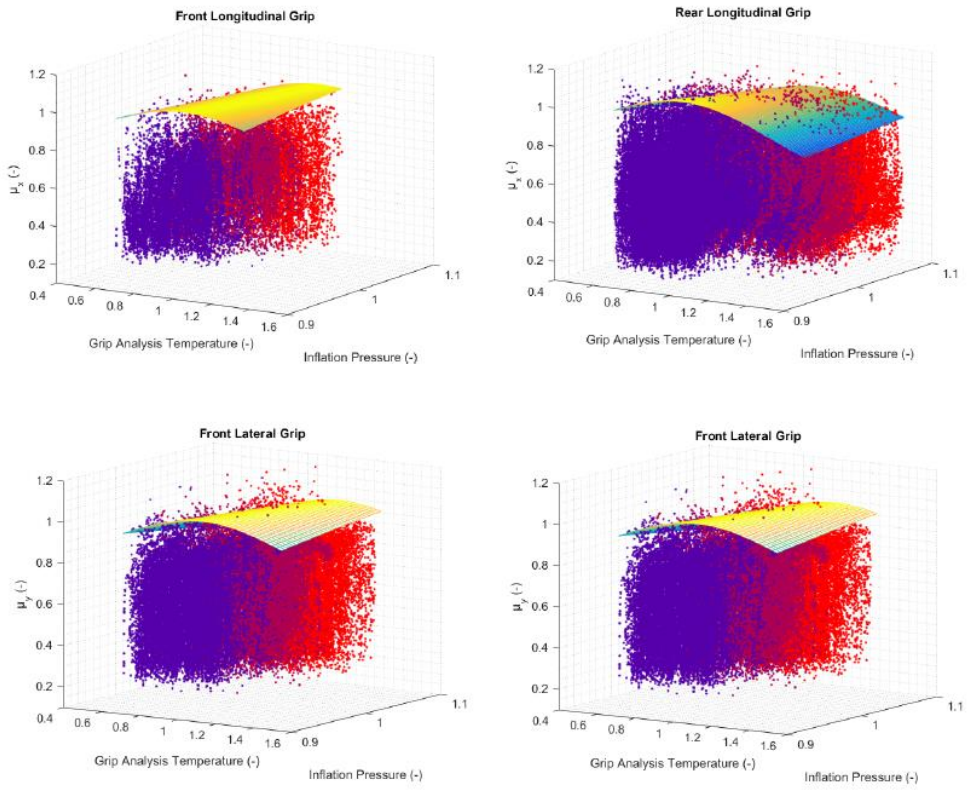

Figure 6.15 – Bidimensional grip law

6.3.4 Stiffness Analysis

It is possible to say that cornering stiffness and braking stiffness depend on both tread-base and tread-core temperatures. Thus, reference temperature for stiffness functions identification has been evaluated as a weighted average of tread-base and tread-core temperature, provided by the tyre thermal model:

$$T_{STIFFNESS} = 0.7 \cdot T_{tread\ surface} + 0.3 \cdot T_{tread\ core} \tag{6.9}$$

Per each temperature, pressure and load range, the linear range of tyre-road interaction has been isolated. Stiffness values have been identified as the slope of straight lines fitting the representative points (Figure 6.16, normalized because of confidential agreement). The colour of the experimental point is in function of the temperature, high-temperature condition in red, low temperature in blue.

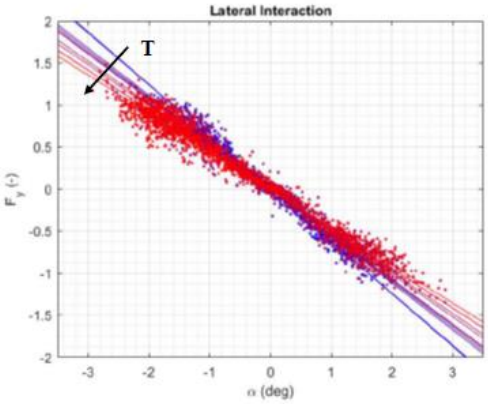

Figure 6.16 – Cornering stiffness identification

Per each load range, the slope has been represented as function of temperature and pressure (Figure 6.17).

The functions displayed assume a unitary value in correspondence with maximum performance-temperature and pressure and allows to scale Pacejka curves depending on the temperature and pressure level by multiplying the scaling factor LKY for lateral interaction and LKX for longitudinal interaction.

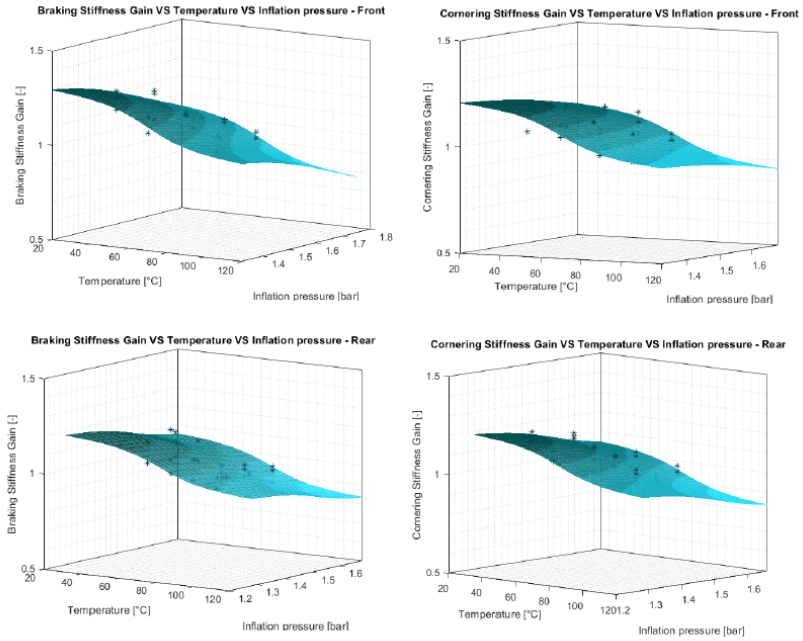

Figure 6.17 – Cornering and braking stiffness law

6.4 Introduction to VI-CarRealTime

VI-CarRealTime is a real-time vehicle simulation software based on a simplified 4 wheels model featured by 14 degrees of freedom (6 for the body and 2 for each wheel). For each wheel it is possible to enable an additional longitudinal degree of freedom (further 4 DOFs when the feature is activated for all the wheels). The software GUI is divided into 3 main sections: build, test and review. The build mode allows to import and modify the vehicle model or" system" which is further organized into "subsystems" representing the main vehicle components. A short description of the model subsystems is given in the following [85].

6.4.1 Reference system

The reference frames used in VI-CRT [86] are consistent with the standard ISO 8855 and the SAE recommended practice.

The coordinate systems needed to describe the motion of the vehicle are a global reference, a body fixed system and one system fixed in each of the wheel hubs.

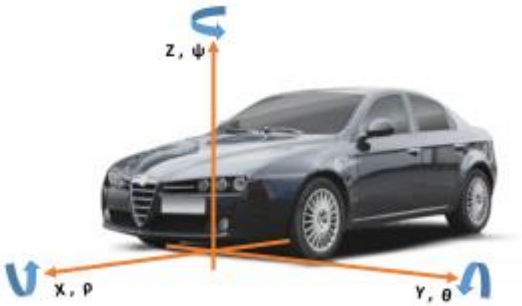

Figure 6.18 – VI-CRT - Body fixed reference frame

6.4.2 Body-fixed coordinate systems

The vehicle model movements are described with respect to the global frame that does not accelerate and does not rotate. The body-fixed frame is integral to the vehicle and is centered in the mid point of the front tyres contact patches. The X axis points towards the front of the vehicle, the Y axis toward the left and the Z axis is oriented to form a right hand reference system.

6.4.3 Wheel coordinate system

It is defined as a triad with the origin coincident to the wheel center and the same orientation as the body-fixed frame. The reference system (ISO-C axis system) that is adopted is depicted in Figure 6.19.

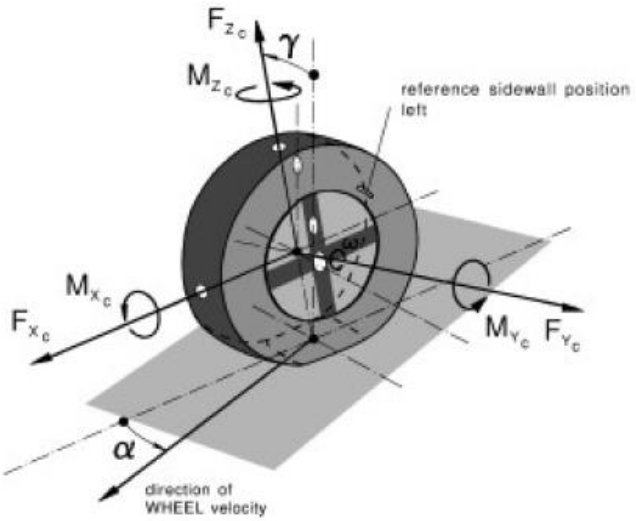

Figure 6.19 – Wheel reference frame

6.4.4 Front and rear suspension

In VI-CarRealTime the suspensions subsystems are described using a conceptual approach. There are no physical parts representing the system but each kinematic quantity is described by means of lookup tables expressed as a function of the vertical wheel jounce and, eventually, the steer angle.

Regarding the suspension kinematics and geometry, the user can describe:

- Track width
- Wheel centre longitudinal and lateral position
- Wheel orientation: camber, toe, side view (caster) angle

The effect of compliance, other than kinematics, is considered: for each kinematic entity (position and orientation) a specific spline describes the variation of that quantity as a function of the considered ground force (Fx, Fy, Mz, Fz). The effect of compliance is introduced by exploiting the superposition principle: for each suspension entity, the overall value is computed as:

$$\epsilon = \epsilon_k + \sum_{i=1}^{n} \epsilon_{i,c} \tag{6.10}$$

Where the first term is the kinematic value of the considered entity for a given suspension jounce while the second term is the sum of the effects of all the forces acting on the tyre in the considered while.

Spring elements can be defined by specifying a spline representing the spring characteristic and it is possible to set spring preload, free length and compression ratio (ratio between wheel vertical jounce and spring deflection).

In a similar way, dampers can be represented by a curve that describes the applied force as a function of the damper velocity.

Anti-roll bars are also included into the model and implemented describing the vertical anti-roll force versus wheel vertical displacement. The effect is introduced as a pair of opposite vertical forces acting between the left and right wheel centre and the sprung part of the body.

Finally, jounce and rebound bumpers can be described by specifying the clearance and the force versus jounce spline.

Suspensions are obviously one of the main components influencing vehicle safety and handling so they'll play a key role during the model validation that will be presented later on.

6.4.5 Steering system

The steering subsystem in VI-CRT is described in the same way as the suspensions. This means that specific curves can be defined in order to characterize:

- Steer wheel angle versus steer at ground
- Left and right camber angle versus steer wheel angle
- Left and right wheel longitudinal and lateral position
- Caster and kingpin angle as a function of the vertical wheel jounce and steer wheel angle
- Steering compliance

6.4.6 Body

The body section describes all the mass properties of the vehicle under examination. In particular, the section is divided into subsections through which the user can describe the properties of the vehicle starting from the sprung mass and inertia tensor until the aerodynamic characteristics of the car. It is also possible to modify the vehicle load conditions by placing additional masses where desired. This latter feature was the one that has been used to simulate the various vehicle configurations, while developing the IP logic.

6.4.7 Powertrain

The powertrain subsystem can be characterized by editing the related subsections that allow to model:

- Engine torque curve
- Vehicle drivetrain and differential
- Gear ratios
- Clutch

6.4.8 Front and rear wheels

Front and rear wheels are mainly described by a specific (".tir") input file, in which all the coefficients describing the tyre characterization are contained. Additionally, mass properties and wheel radius expressed as a function of wheel centre height can be defined.

6.4.9 Brakes

Braking system parameters can also be edited. Among those, brake pressure distribution (the equivalent of a mechanical distributor), friction coefficient between pads and disc, piston radius and pressure gain are the most significant ones.

6.5 Sensitivity analysis description

The analysis is carried out using the VI-CRT tool called *max performance*. This event in VI-CarRealTime is used to define dynamic limit velocity profile on a given track.

The event uses a specific static solver (VI-SpeedGen) to compute a velocity profile and then it uses the dynamic solver to verify if the computed speed profile is feasible. If the velocity path is unfeasible (maximum path distance exceeded, zero velocity etc.) the solver turns back to the static and computes a new velocity profile, modifying only the portion nearby the unfeasible point. The process is iterated until a feasible velocity profile is found. Basically, the vehicle model used for static prediction has no suspensions and inherits all properties from the full VI-CarRealTime model. The effect of aero forces is considered, and the effect of suspension jounce is considered by the presence of ride height maps.

Figure 6.20 shows the simulation scheme.

The various simulation-steps are as follows:

- Path Segmentation: The path is divided into a series of sections and the curvature is evaluated (Figure 6.21).
- Speed Profile generation: VI-SpeedGen algorithm is used to compute a static speed profile on a given trajectory. It uses a simplified model with respect to the one used in standard dynamic events. The simplified vehicle has no suspensions and inherits all the properties from the full VI-CarRealTime model. The effect of aero forces is considered and the effect of suspension jounce is taken into account by the presence of ride height maps. Starting from the input trajectory, the algorithm recognizes the apex of all the curves and

computes the static limit speed for each apex assuming that the vehicle is in pure lateral. From the local curvature and after computing the maximum lateral force (acceleration) the vehicle can sustain, it's possible to compute the maximum speed in pure lateral conditions. (Figure 6.22 a).

Once the speed in each apex has been computed, the forward integration phase computes the maximum acceleration the vehicle can sustain from each apex forward. Since the apex is the point with minimum speed, after the apex the vehicle must accelerate and the acceleration performance of the vehicle are retrieved from tyre and powertrain of the main vehicle. With such assumption, it's possible to draw the speed curve (red curve in the Figure 6.22 b) from each apex forward. The backward integration phase computes the maximum deceleration the vehicle can sustain from each apex backward. Since the apex is the point with minimum speed, before the apex the vehicle must be in deceleration and the deceleration performance of the vehicle are retrieved from tyre and brake system of the main vehicle. With such assumption, it's possible to draw the speed curve (blue curve in the Figure 6.22 c) from each apex backward. Finally, red curves and blue curves are connected and smoothed in order to obtain the final static speed profile.

- VI-Driver Iterations: Dynamic model is used to perform a validation on the static speed profile prediction.
- Detected unfeasibility reason: to detected unfeasibilities, the checked parameters are the Path distance, Yaw rate limits and the longitudinal speed threshold.
- Change SpeedGEn Params: The process is iterated until a feasible velocity profile is found

The vehicle used is the standard one made available by the software, the characteristics of which are shown in Figure 6.23.

The output quantities such as accelerations etc. are measured with respect to a reference system with origin in the centre of gravity as shown in Figure 6.24.

The standard use of the software allows you to use a tyre model by loading a tir file.

This type of analysis, however, is conducted using the tyre model described in 6.3.

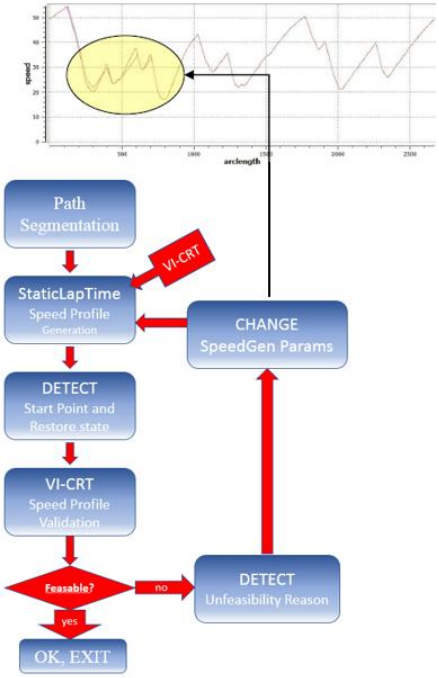

Figure 6.20 – Simulation scheme

It is therefore an advanced Pacejka model in which the effects of temperature on the response of the tyres and therefore on the dynamic behaviours of the vehicle are also considered.

For this purpose, the work carried out with the Vi-Grade company was to integrate the Vi car real time software, a thermal model and an evolved Pacejka model, both developed by the vehicle dynamics group by UniNa.

It is a software in the loop logic whose scheme is shown in Figure 6.1.

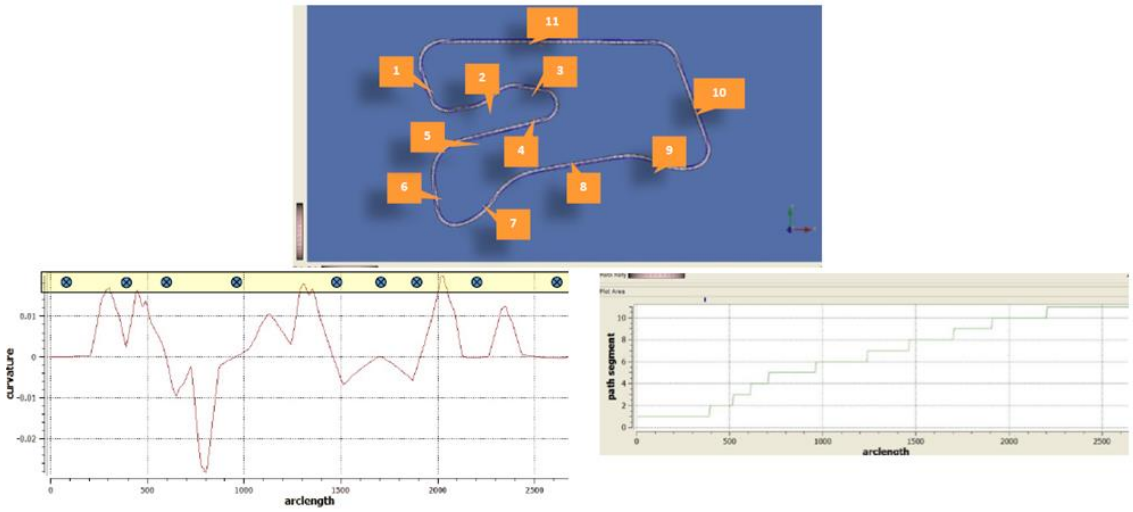

Figure 6.21 – Path segmentation

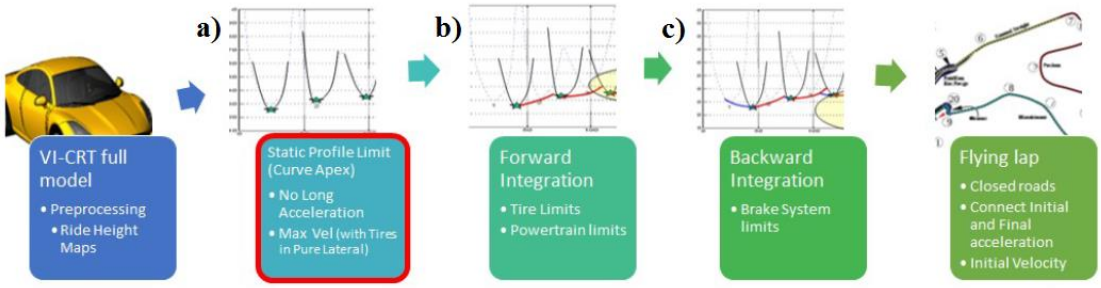

Figure 6.22 – Steps of Speed Profile generation Algorithm

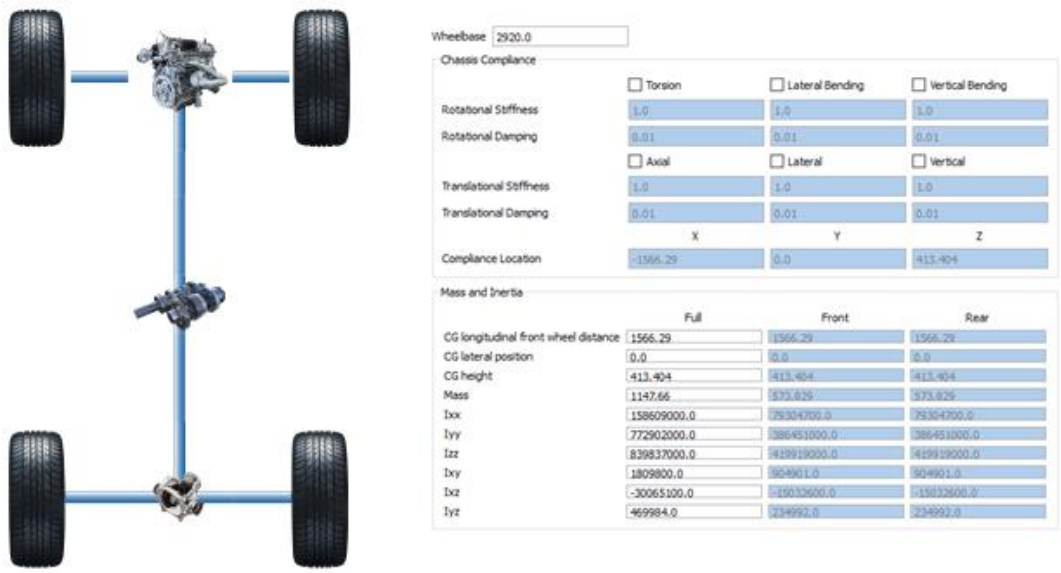

Figure 6.23 – Vehicle parameters

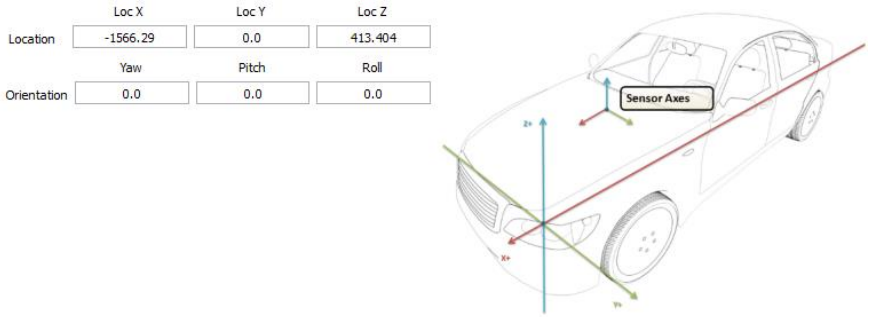

Figure 6.24 – Reference system for measurements

An investigation is carried out on the influence of some parameters of the tyre response and therefore on the behavior of the entire vehicle.

The parameters taken into consideration are:

- **Tread surface wear**: its effect on the thermal response of tyres
- **k tread surface:** thermal conductivity of the tread surface
- **cv tread surface:** thermal specific heat of the tread surface
- **stiffness law of MF-evo**
- **grip law of MF-evo**
- **road temperature**
- **external temperature**

The reference simulation has the following parameters:

Table 6.4 - Reference simulation parameters

T ambient (°C)	15
T road (°C)	15
Initial T tyre (°C)	15
Initial inflation pressure (bar)	1.3

Each simulation consists of 15 laps on the default circuit made available by the software:

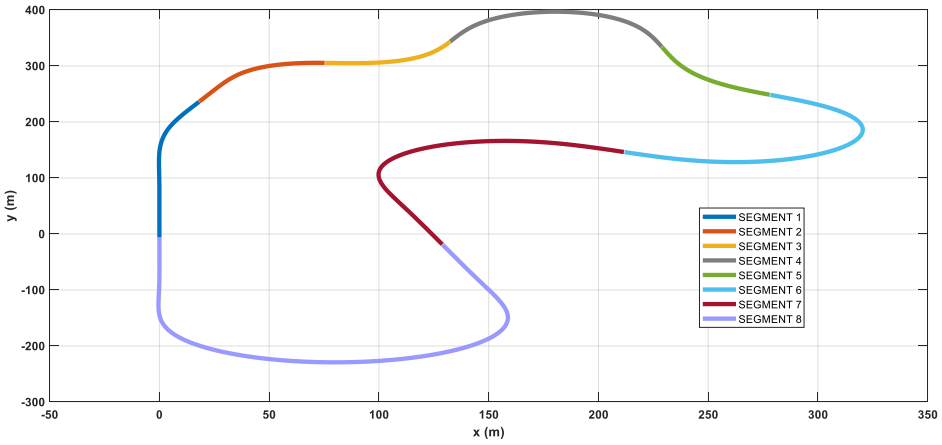

Figure 6.25 – VI track

The following quantities are evaluated:

- Time Laps
- Temperature trend
- Understeer angle

The understeer angle is defined as [87]:

$$\delta_u = \delta_{wheel} - \delta_{Aker} \tag{6.11}$$

where:

- δ_{wheel} is the steering angle of the front outside wheel
- δ_{Aker} is the Akerman steer angle: $\delta_{Aker} = \frac{l}{R}$
- l is the vehicle wheelbase
- R is defined as $R = \frac{u}{r}$
- u is the longitudinal speed
- r is the yaw rate

Starting from the understeer angle definition, is possible to define the quantity understeer gradient as [1]

$$K_G = \frac{d(\delta_{wheel} - \delta_{Aker})}{day} \tag{6.12}$$

The table 6.5 shows the test plan carried out.

Table 6.5 – Test plane

	Wear %	k (W/m)	Cv (Kj/kgK)	Low Grip	Low Stiffness	ambient Temperature (°C)	road Temperature (°C)
1	0	Nominal	Nominal	Nominal	Nominal	15°C	15 °C
2	0	+25 %	Nominal	Nominal	Nominal	15°C	15°C
3	0	+50%	Nominal	Nominal	Nominal	15°C	15°C
4	0	Nominal	+25 %	Nominal	Nominal	15°C	15°C
5	0	Nominal	+50%	Nominal	Nominal	15°C	15°C
6	+25 %	Nominal	Nominal	Nominal	Nominal	15°C	15°C
7	+50%	Nominal	Nominal	Nominal	Nominal	15°C	15°C
8	0	Nominal	Nominal	Nominal	Nominal	15°C	15°C
9	0	Nominal	Nominal	Law 1	Nominal	15°C	15°C
10	0	Nominal	Nominal	Law 2	Nominal	15°C	15°C
11	0	Nominal	Nominal	Nominal	Law 1	15°C	15°C
12	0	Nominal	Nominal	Nominal	Law 2	15°C	15°C
13	0	Nominal	Nominal	Nominal	Nominal	45 °C	15°C
14	0	Nominal	Nominal	Nominal	Nominal	10 °C	15 °C
15	0	Nominal	Nominal	Nominal	Nominal	15°C	45 °C
16	0	Nominal	Nominal	Nominal	Nominal	15°C	65 °C
17	0	Nominal	Nominal	Nominal	Nominal	15°C	15°C
18	0	Nominal	Nominal	Nominal	Nominal	15°C	15°C
19	0	Nominal	Nominal	Nominal	Nominal	15°C	15°C
20	0	Nominal	Nominal	Nominal	Nominal	15°C	15°C
21	0	Nominal	Nominal	Nominal	Nominal	15°C	15°C

6.5.1 Reference Conditions

The tyre used in the simulations has the following characteristics:

- optimum temperature range: 50 ÷ 100 °C
- optimum pressure range (at Temperature max performance): 1.1 ÷ 2.2 bar

The figure 6.26 shows the MF-evo law.

Figure 6.27 shows the simulation results in terms of lap time

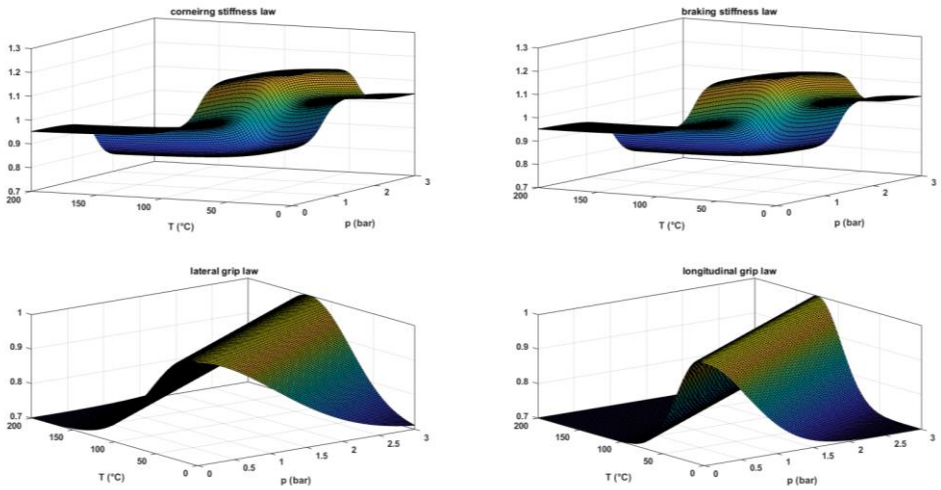

Figure 6.26 – MF-evo law

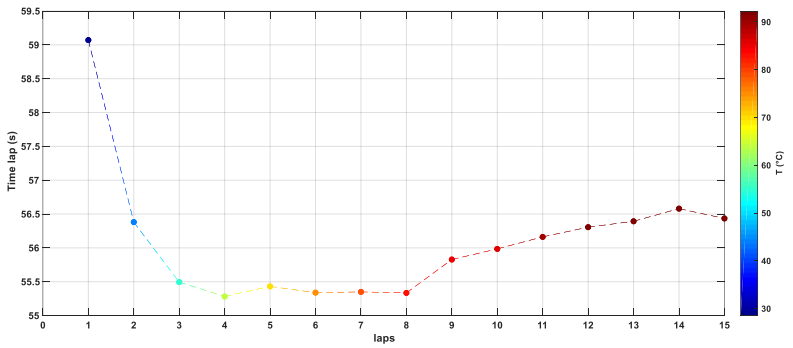

Figure 6.27 – Time Lap (Reference conditions)

The maximum lateral acceleration relative to each track sector was evaluated and the average between these values was subsequently considered (Figure 6.28).

Finally, the understeer gradient is shown in Figure 6.29.

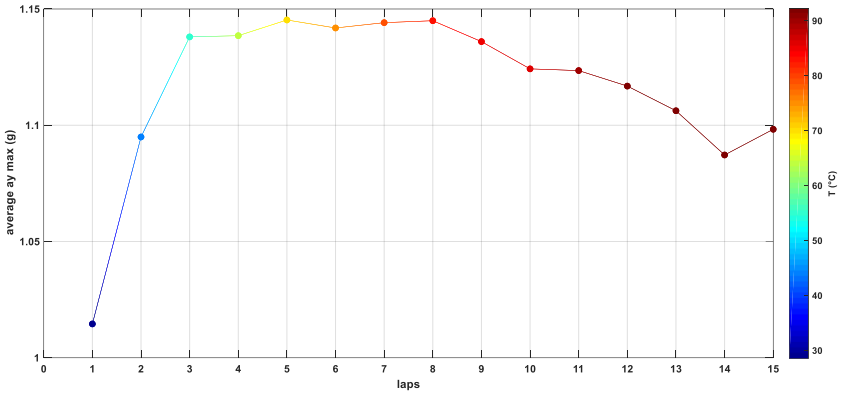

Figure 6.28 – Average max lateral acceleration

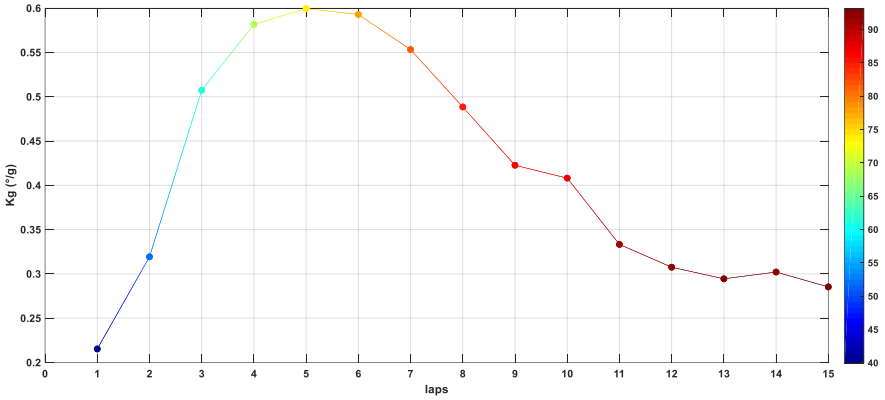

Figure 6.29 – Understeer Gradient (reference conditions)

6.5.2 Tread surface wear effect

Figure 6.9 shows the discretization of the tyre thickness in:

- Tread surface
- Tread core
- Tread base

Starting from the nominal thickness of the tread surface, the effect of wear is studied by introducing a reduction of this thickness by 25% and 50%:

Table 6.6 – Tread surface thickness

Wear %	Tread surface thickness (mm)
0	5.500
25 %	4.125
50 %	2.750

It should be noted that the effect of the wear introduced, which affects only the thermal behavior of the tyre and therefore does not consider all the other effects introduced by it.

Figure 6.30 shows the simulation results in terms of lap time.

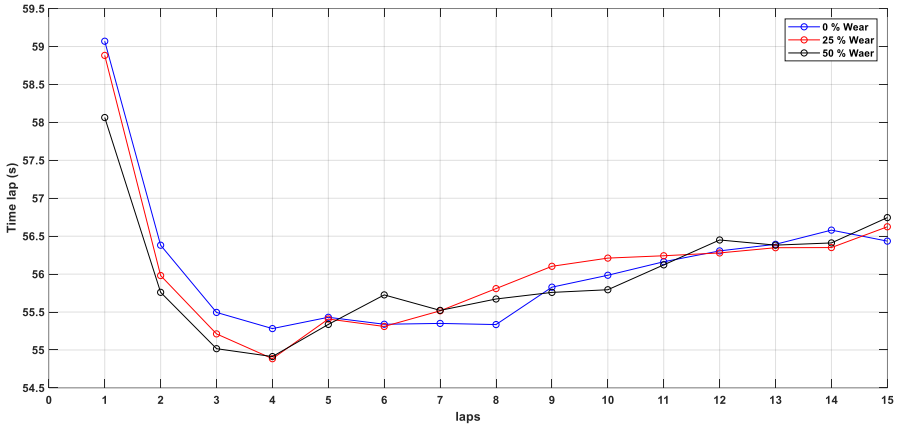

Figure 6.30 – Time laps for different wear levels

Figure 6.31 and 6.32 show the temperature trend, evaluated by 6.8 and 6.9, during the 15 laps while the figure 6.33 shows the inflation pressure trend.

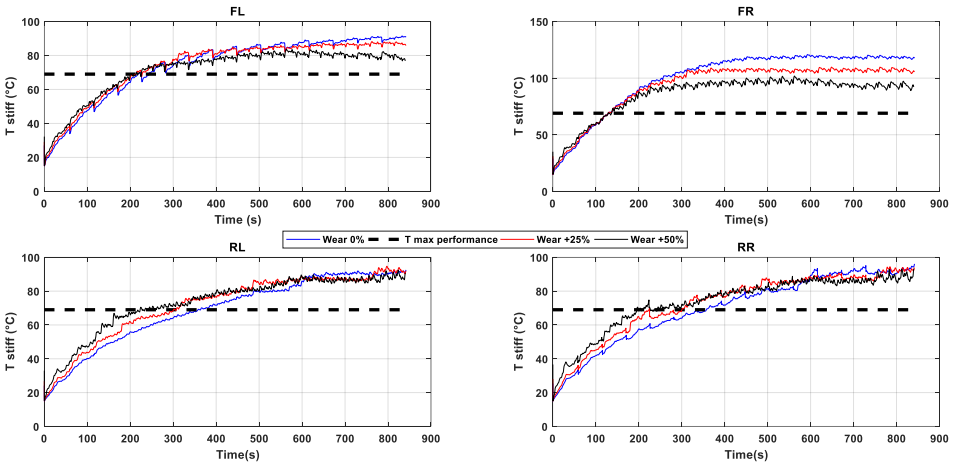

Figure 6.31 – Temperature stiff trend (Wear effect)

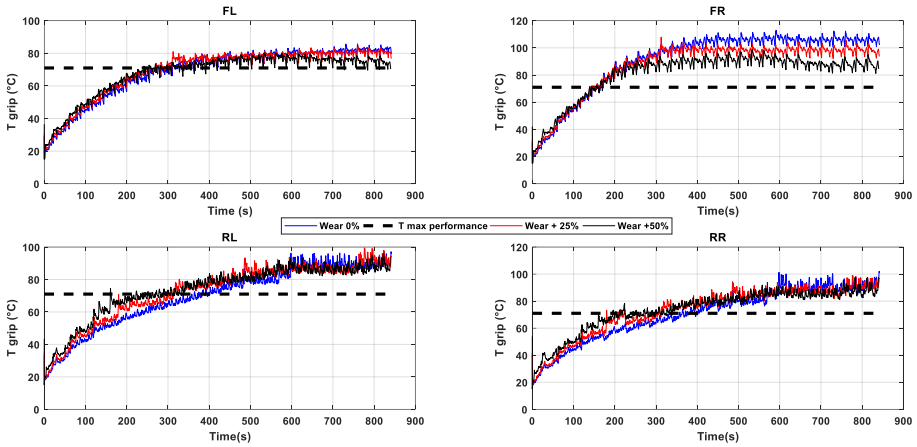

Figure 6.32 – Temperature Grip trend (Wear effect)

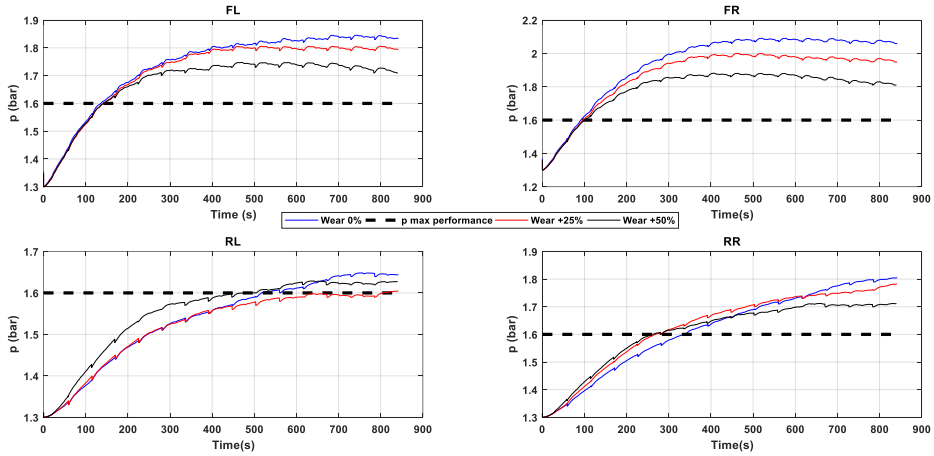

Figure 6.33 – Inflation pressure trend (Wear effect)

Figure 6.34 shows comparison of lateral accelerations while figure 6.35 shows the comparison between the understeer gradient.

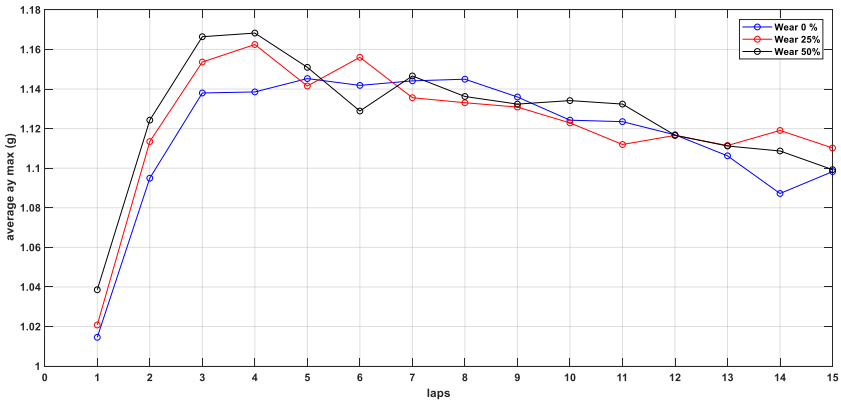

Figure 6.34 – Average max lateral acceleration compare (Wear effect)

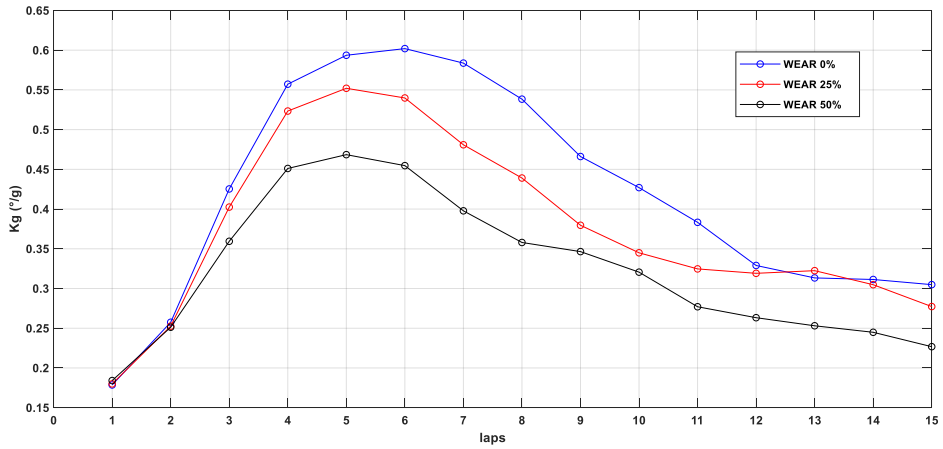

Figure 6.35 – Understeer Gradient compare (Wear effect)

The analysis shows the following results:

- the reduction in thickness causes a greater rapidity to reach the maximum performance temperature
- as wear increases, the operating temperature decreases
- as wear increases, understeer decreases

6.5.3 Conductivity surface effect

Starting from the nominal value of conductivity surface, the effect of $\pm$ 25 % and $\pm$ 50 % variations are studied (Figure 6.36).

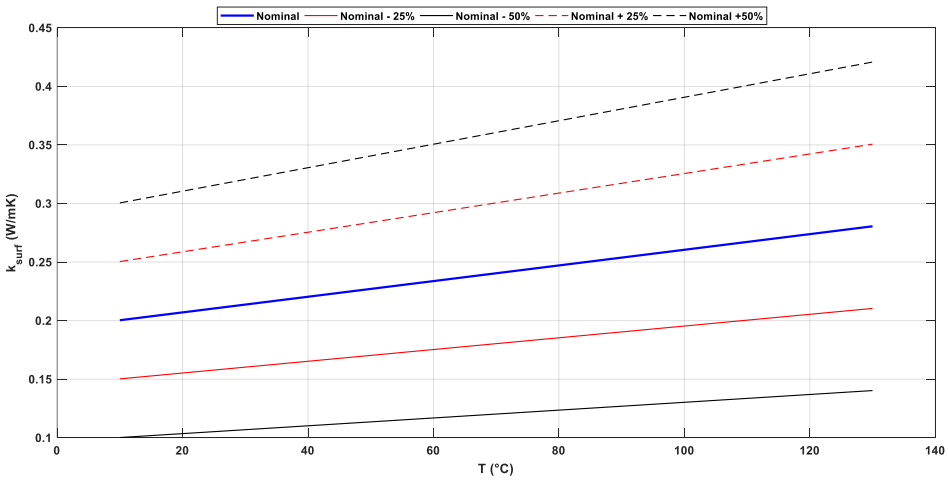

Figure 6.36 – Surface conductivity trend

Figure 6.37 shows the simulation results in terms of lap time.

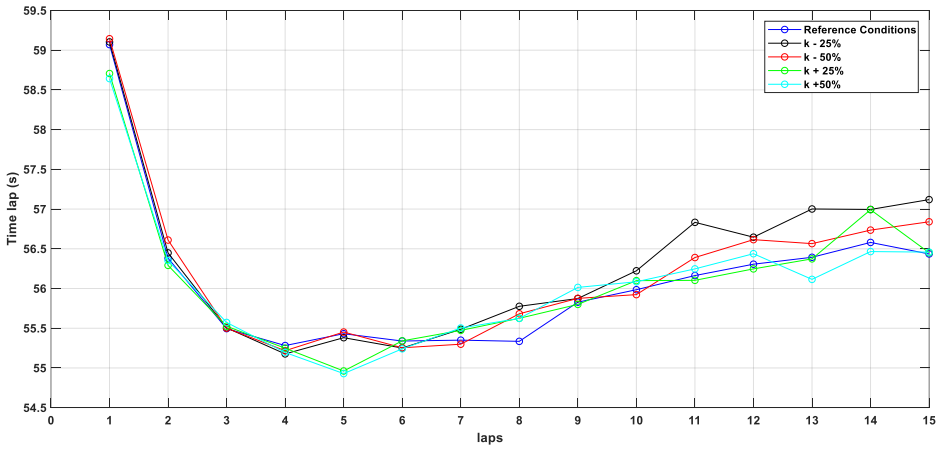

Figure 6.37 – Time laps for various k

Figure 6.38 and 6.39 show the temperature trend, evaluated by 6.8 and 6.9, during the 15 laps while the figure 6.40 shows the inflation pressure trend.

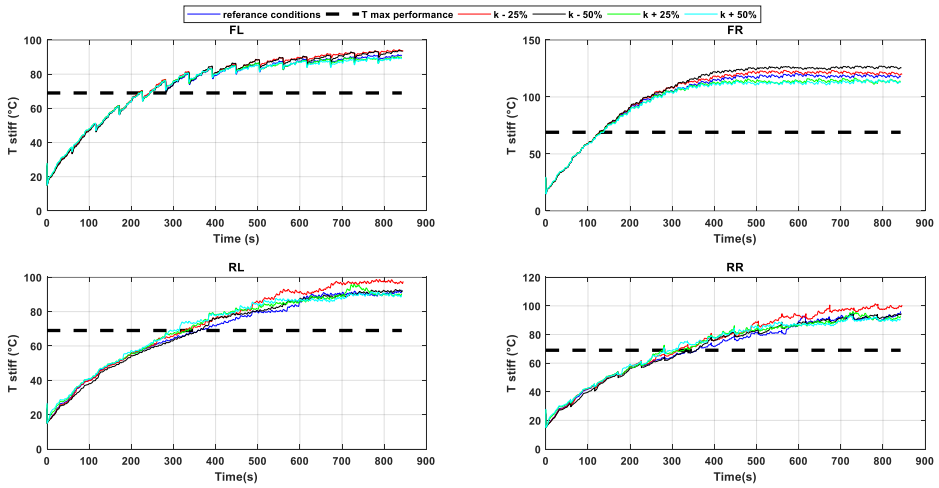

Figure 6.38 – Temperature stiff trend (conductivity effect)

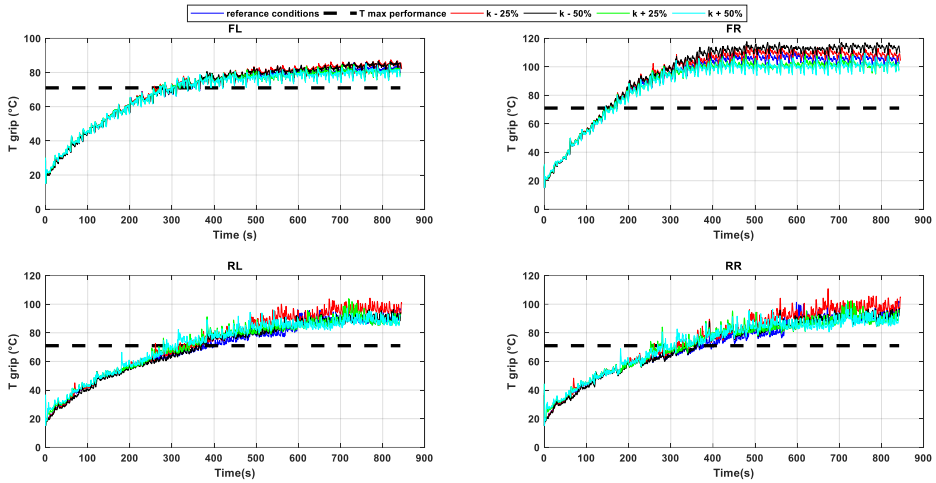

Figure 6.39 – Temperature grip trend (conductivity effect)

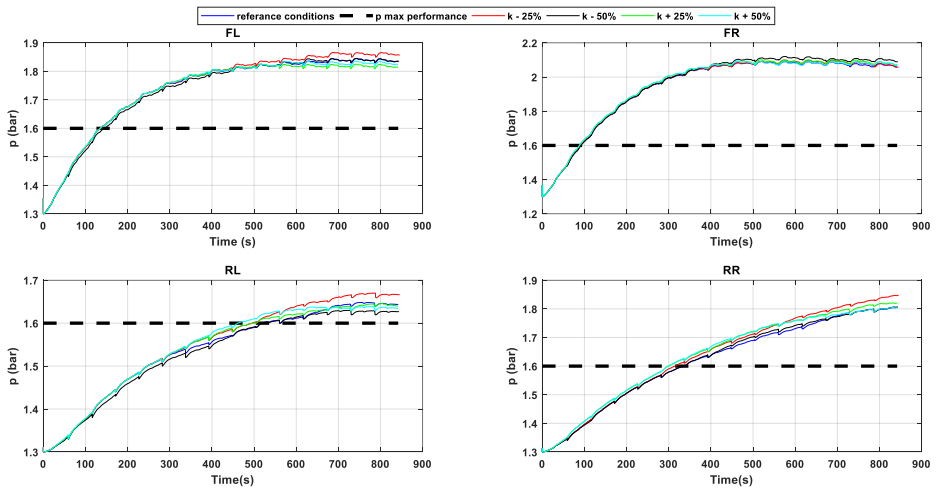

Figure 6.40 – Inflation pressure trend (conductivity effect)

Figure 6.41 shows comparison of lateral accelerations while figure 6.42 shows the comparison between the understeer gradient.

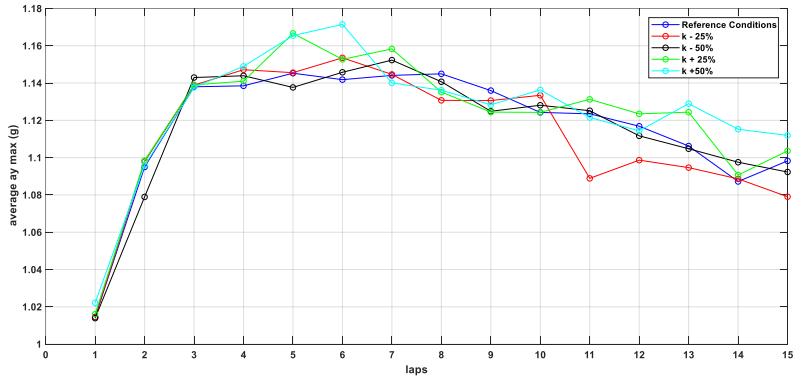

Figure 6.41 – Average max lateral acceleration compare (conductivity effect)

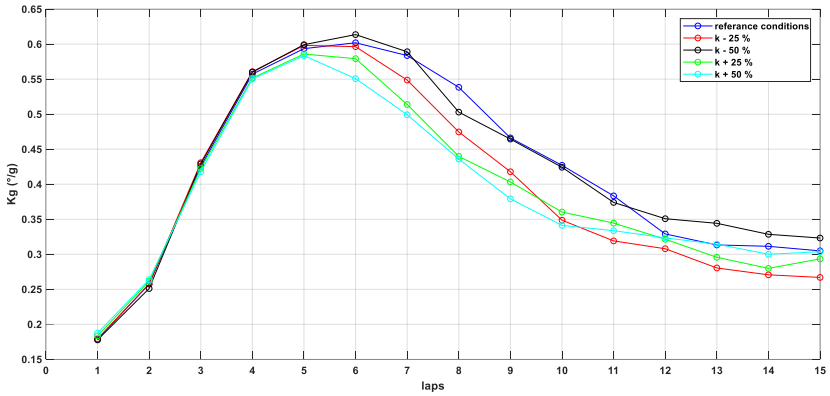

Figure 6.42 – Understeer Gradient compare (conductivity effect)

The analysis shows the following results:

- reducing the conductivity, there is a slight increase in the operating temperature
- there are no noticeable variations in terms of lap time

6.5.4 Specific heat surface effect

Starting from the nominal value of the specific heat surface, the effect of ± 25 % and ± 50 % variations are studied (Figure 6.43).

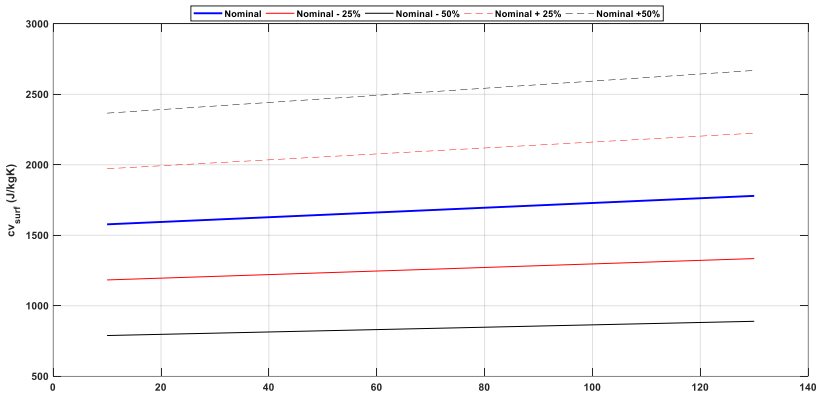

Figure 6.43 – Surface specific heat trend

Figure 6.44 shows the simulation results in terms of lap time .

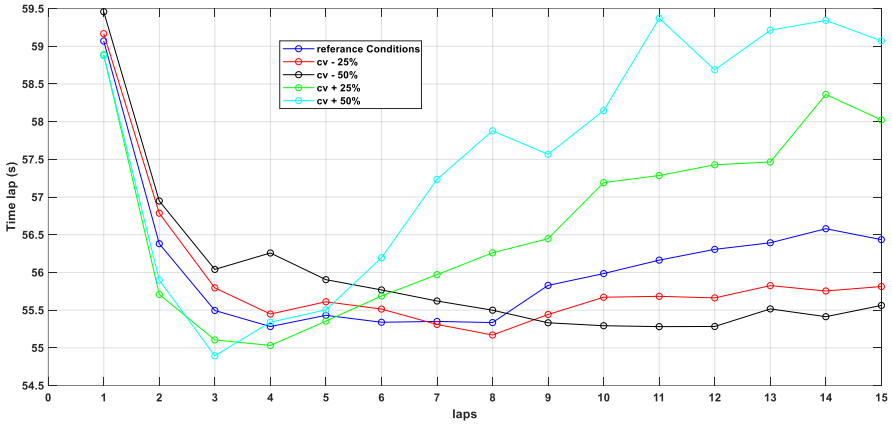

Figure 6.44 – Time laps for various cv

Figure 6.45 and 6.46 show the temperature trend, evaluated by 6.8 and 6.9, during the 15 laps while the figure 6.47 shows the inflation pressure trend.

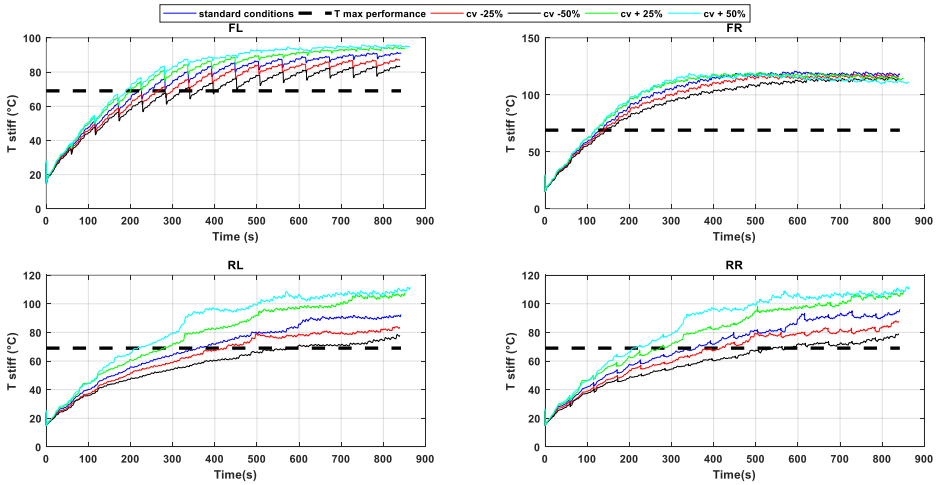

Figure 6.45 – Temperature stiff trend (specific heat effect)

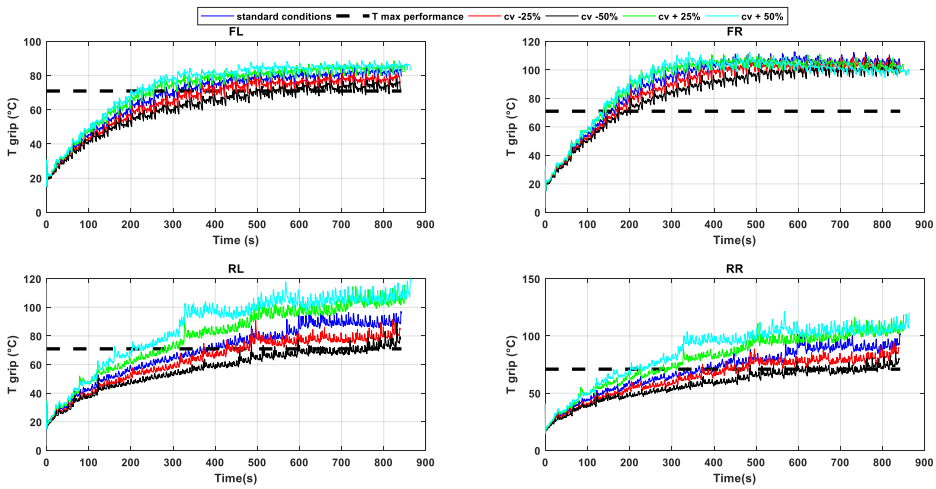

Figure 6.46 – Temperature grip trend(specific heat effect)

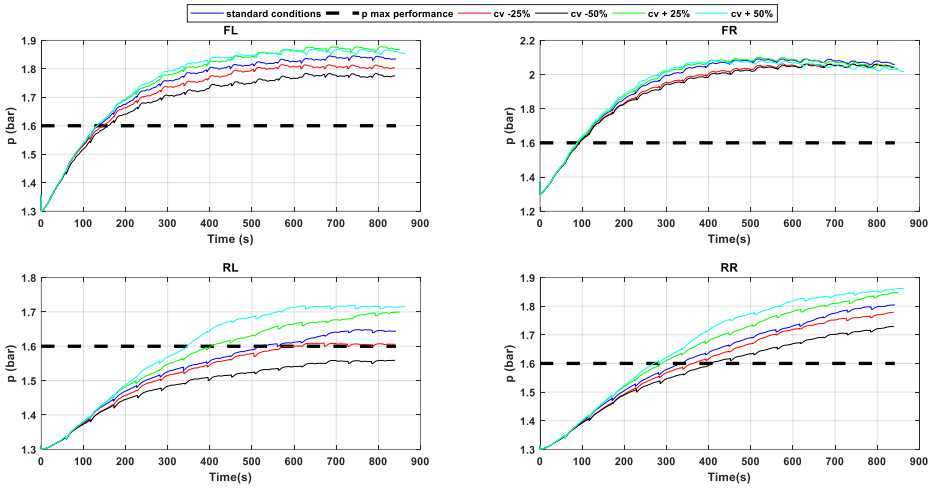

Figure 6.47 – Inflation pressure trend (specific heat effect)

Figure 6.48 shows comparison of lateral accelerations while figure 6.49 shows the comparison between the understeer gradient.

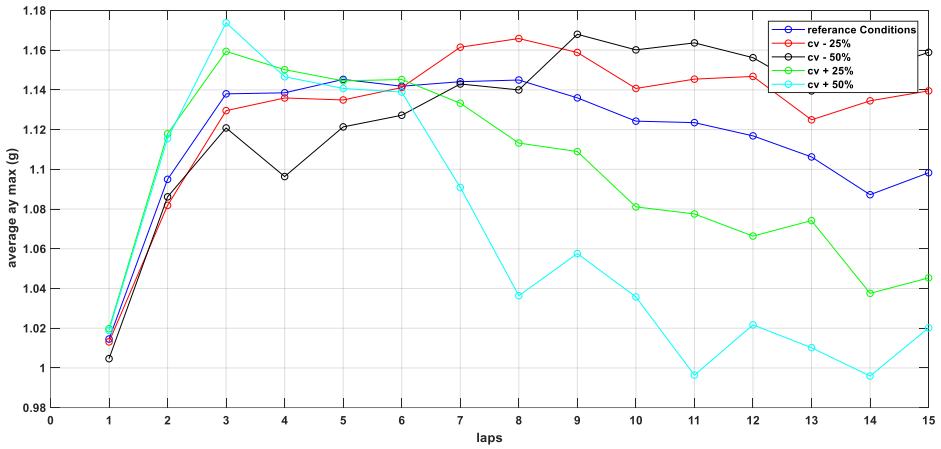

Figure 6.48 – Average max lateral acceleration compare (specific heat effect)

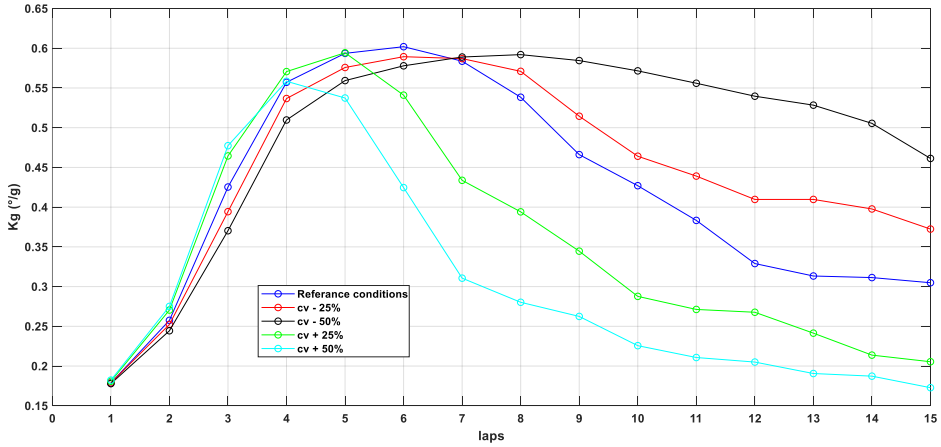

Figure 6.49 – Understeer Gradient compare (conductivity effect)

The analysis shows the following results:

- as the specific heat increases, higher temperatures are reached
- as the specific heat increases, the best lap time is reached first, but quickly moves away from the max performance condition

6.5.5 MF-evo stiffness law effect

As described in 6.3.4, the effect of temperature on stiffness is introduced by resizing the Pacejka curves through multiplicative functions that act on LKY for lateral interaction and for LKX for longitudinal interaction.

These functions can be represented as a function of temperature and pressure as shown in the figure 6.50.

The effect of the grip and stiffness function are shown in the figure 6.51.

The effect of three coefficients governing the laws is studied (figure 6.52).

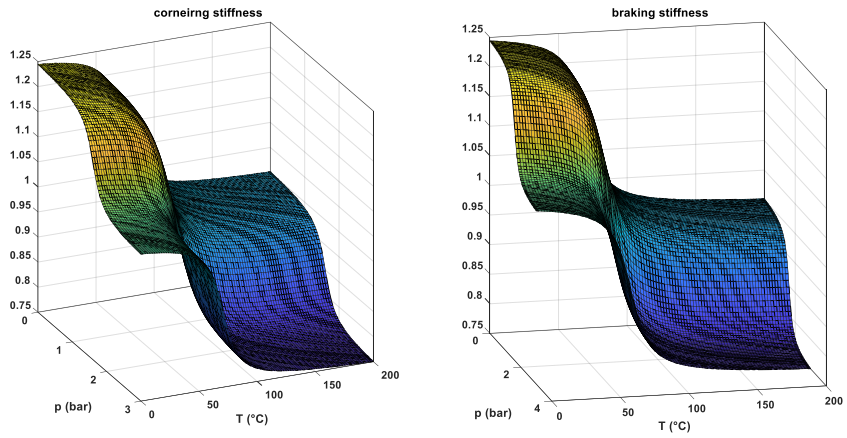

Figure 6.50 – Cornering and Braking stiffness function

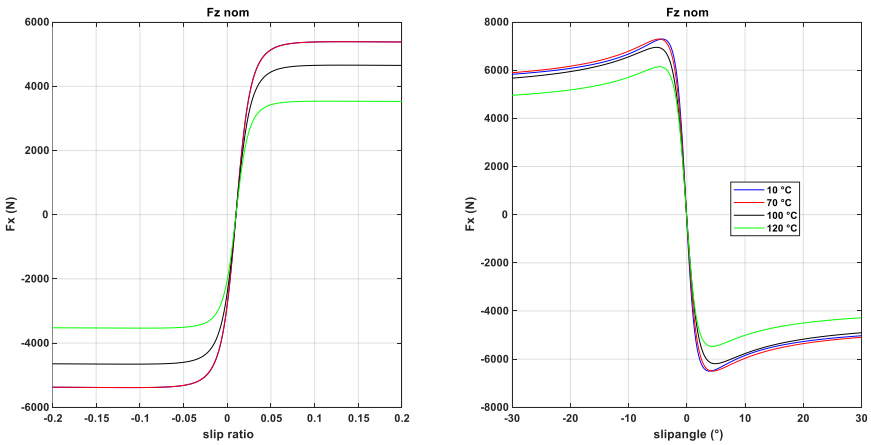

Figure 6.51 – Temperature effect on the longitudinal/lateral grip and braking/cornering stiffness

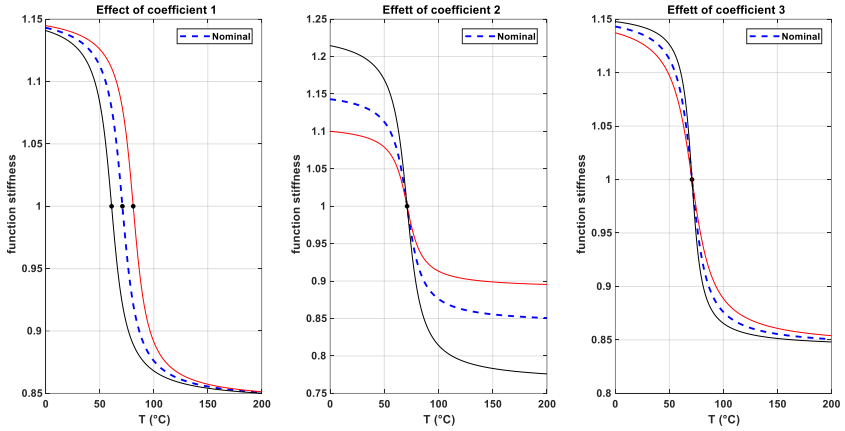

Figure 6.52 – Effect of coefficients on the function stiffness

EFFECT OF COEFFICIENT 1

Figure 6.53 shows the simulation results in terms of lap time.

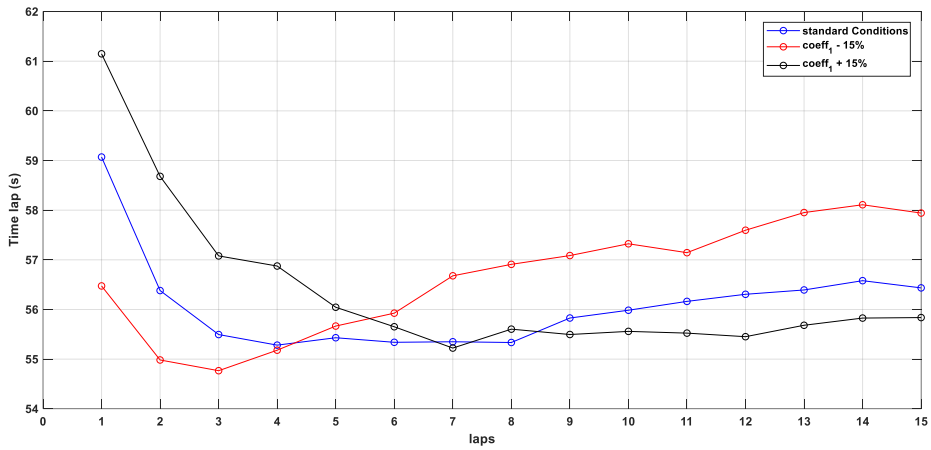

Figure 6.53 – Time laps for various stiffness coefficient 1

Figure 6.54 and 6.55 show the temperature trend, evaluated by 6.8 and 6.9, during the 15 laps while figure 6.56 shows the inflation pressure trend.

Figure 6.57 shows comparison of lateral accelerations while figure 6.58 shows the comparison between the understeer gradient.

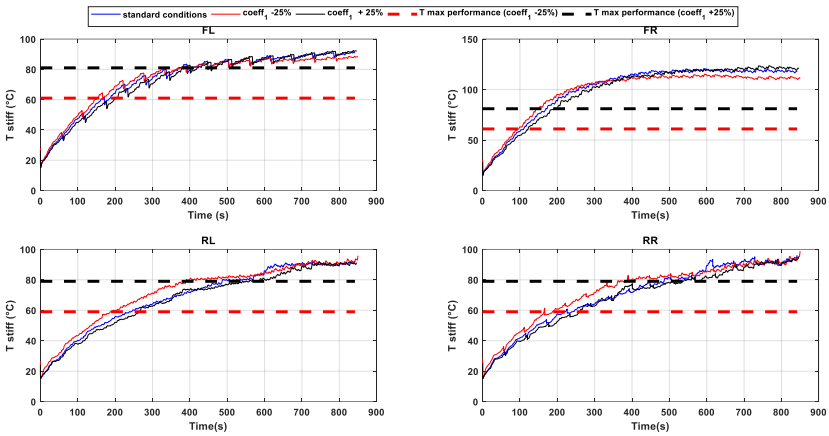

Figure 6.54 – Temperature stiff trend (coeff 1 stiffness law effect)

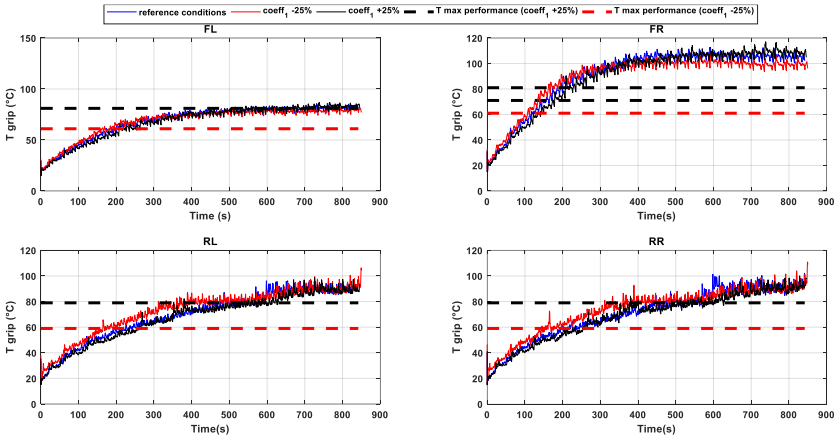

Figure 6.55 – Temperature Grip trend (coeff 1 stiffness law effect)

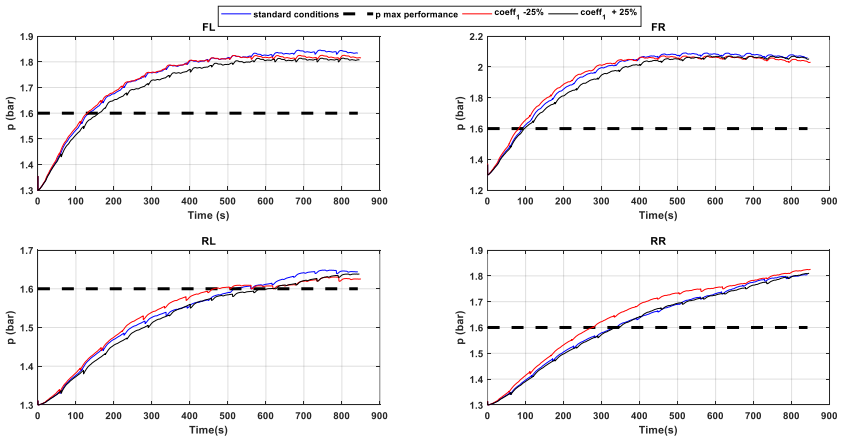

Figure 6.56 – Inflation pressure trend (coeff 1 stiffness law effect)

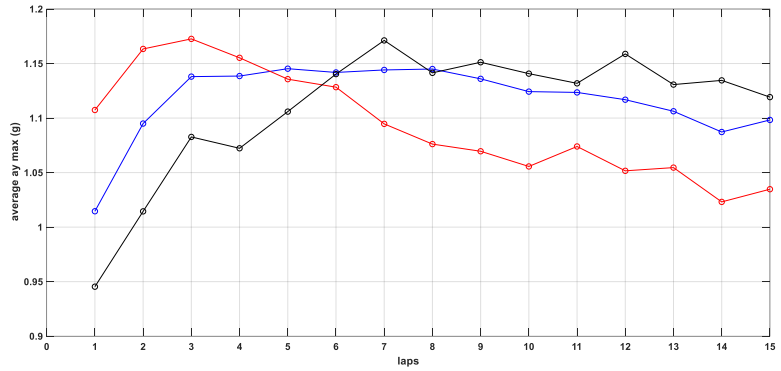

Figure 6.57 – Average max lateral acceleration compare (stiffness law coeff 1 effect)

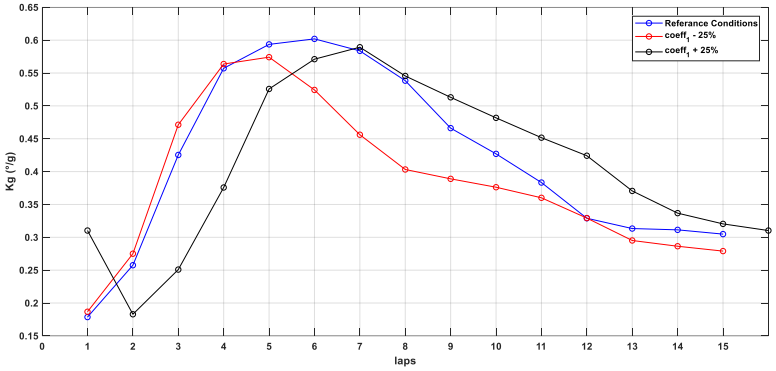

Figure 6.58 – Understeer Gradient compare (stiffness law coeff 1 effect)

- substantially the coefficient 1 represents the max performance temperature
- A lower T max performance allows you to reach the best lap time first
- if the thermal regime away from which temperature, you risk worsening performance too much

EFFECT OF COEFFICIENT 2

Figure 6.59 shows the simulation results in terms of lap time.

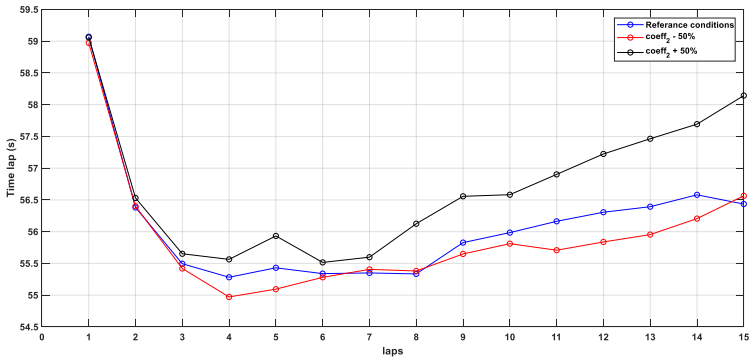

Figure 6.59 – Time laps for various stiffness coefficient 2

Figure 6.60 and 6.61show the temperature trend, evaluated by 6.8 and 6.9, during the 15 laps while figure 6.62 shows the comparison between the understeer gradients.

Figure 6.63 shows comparison of lateral accelerations while figure 6.64 shows the comparison between the understeer gradient.

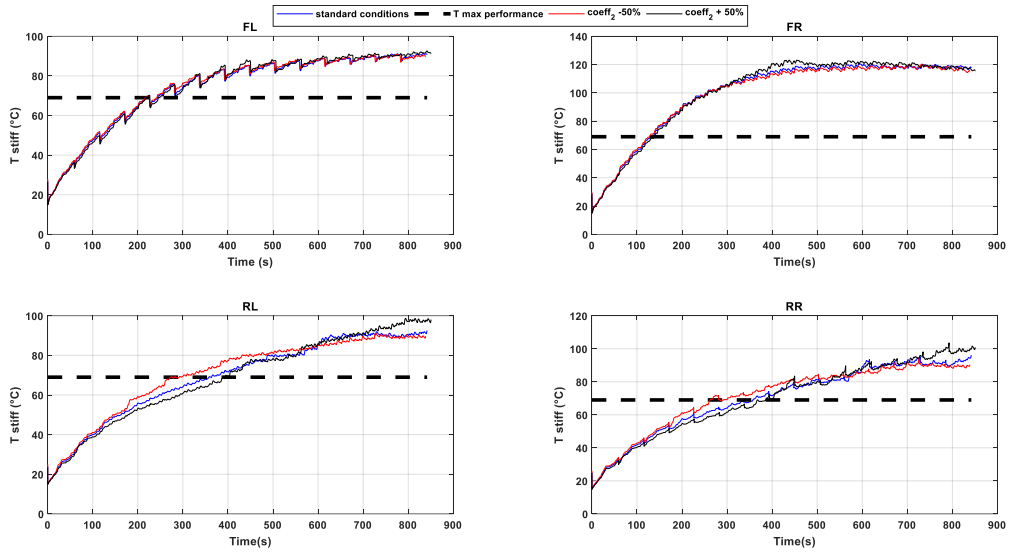

Figure 6.60 – Temperature stiff trend (coeff 2 stiffness law effect)

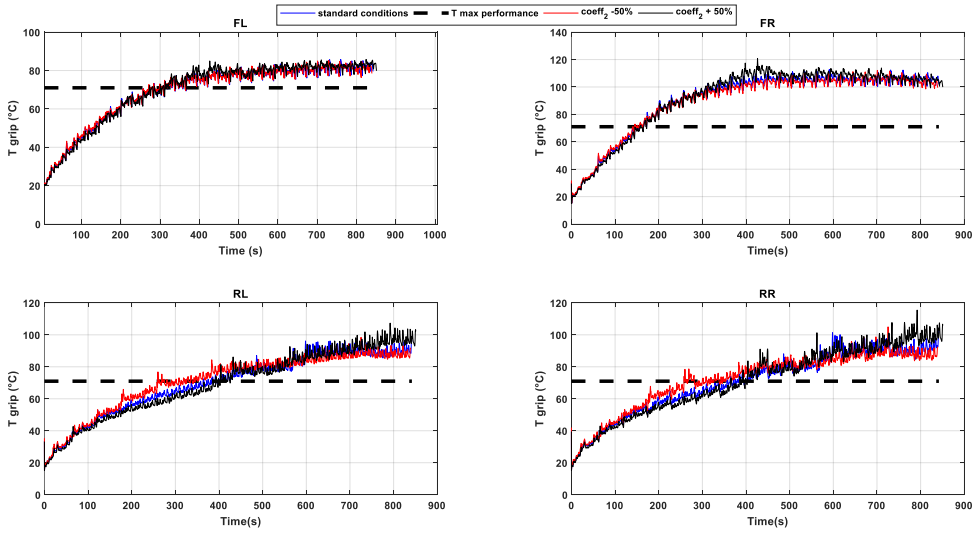

Figure 6.61 – Temperature grip trend (coeff 2 stiffness law effect)

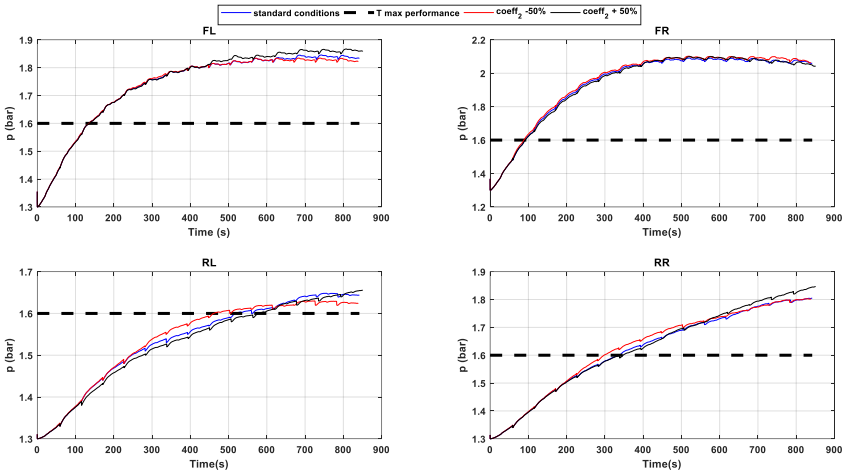

Figure 6.62 – Inflation pressure trend (coeff 2 stiffness law effect)

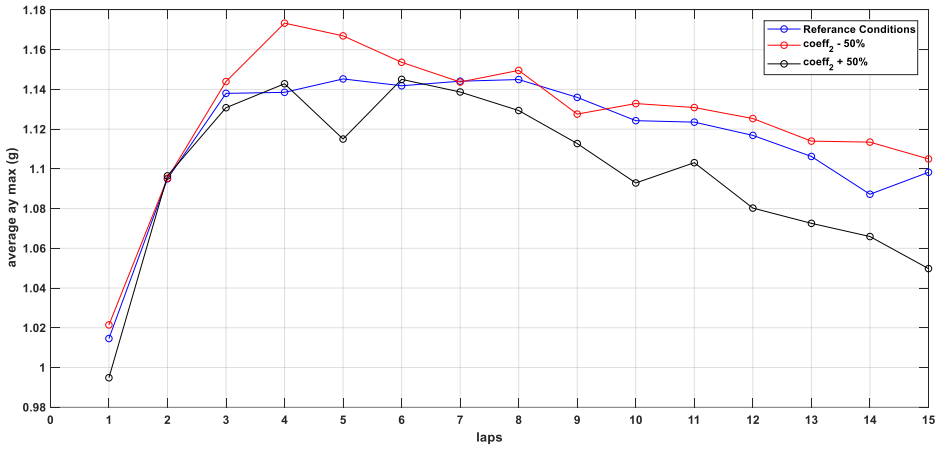

Figure 6.63 – Average max lateral acceleration compare (stiffness law coeff 2 effect)

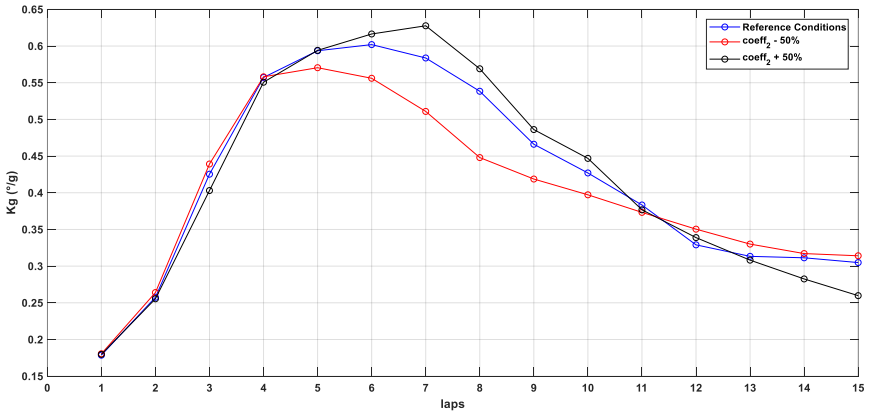

Figure 6.64 – Understeer Gradient compare (stiffness law coeff 2 effect)

The analysis shows the following results:

- the coefficient 2 represents the asymptotic value of the curve

- as this coefficient increases, performance deteriorates

EFFECT OF COEFFICIENT 3

Figure 6.65 shows the simulation results in terms of lap time.

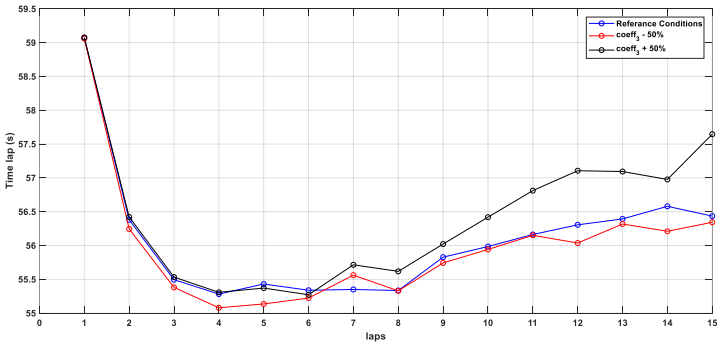

Figure 6.65 – Time laps for various stiffness coefficient 2

Figure 6.66 and 6.67 show the temperature trend, evaluated by 6.8 and 6.9, during the 15 laps while the figure 6.68 shows the inflation pressure trend.

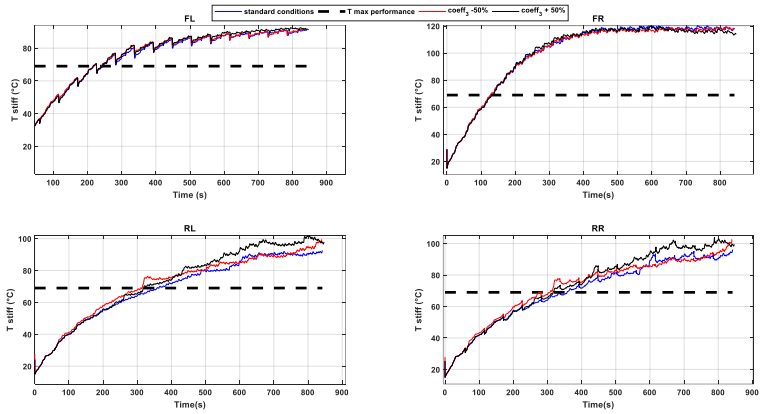

Figure 6.66 – Temperature stiff trend (stiffness law coeff 3 effect)

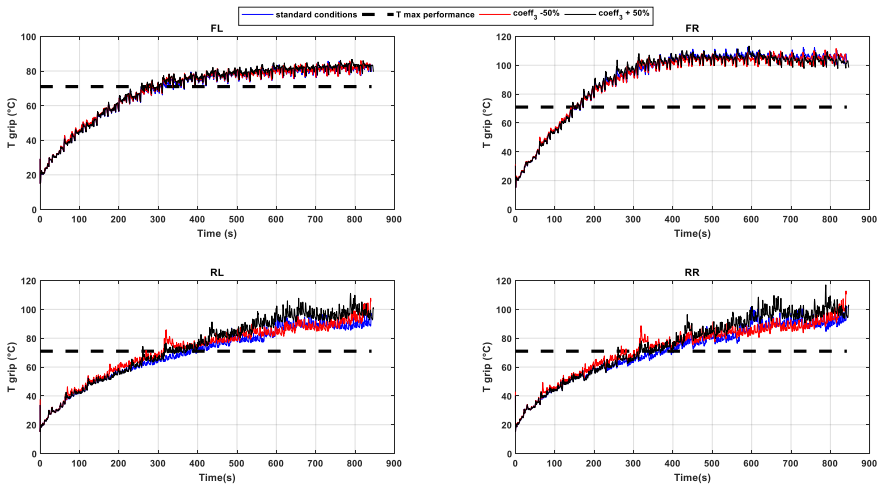

Figure 6.67 – Temperature grip trend (stiffness law coeff 3 effect)

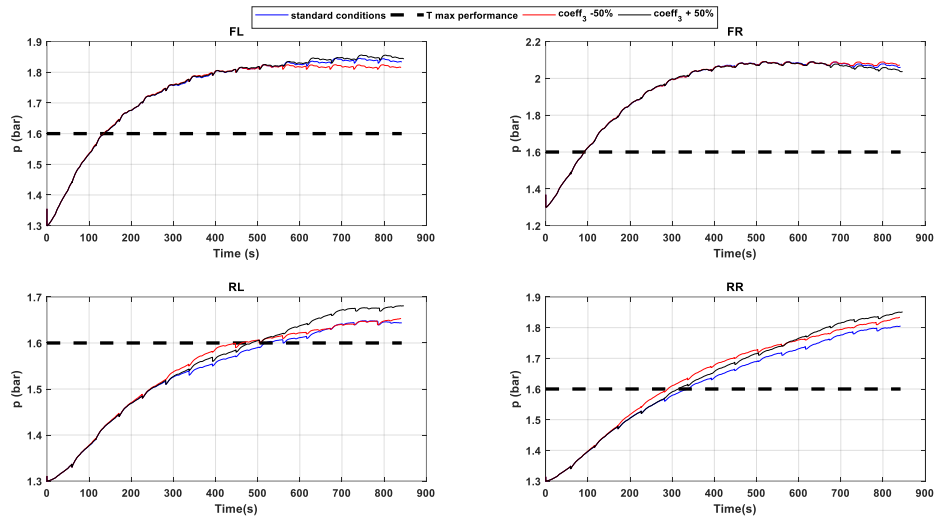

Figure 6.68 – Pressure trend (stiffness law coeff 3 effect)

Figure 6.69 shows comparison of lateral accelerations while figure 6.70 shows the comparison between the understeer gradient.

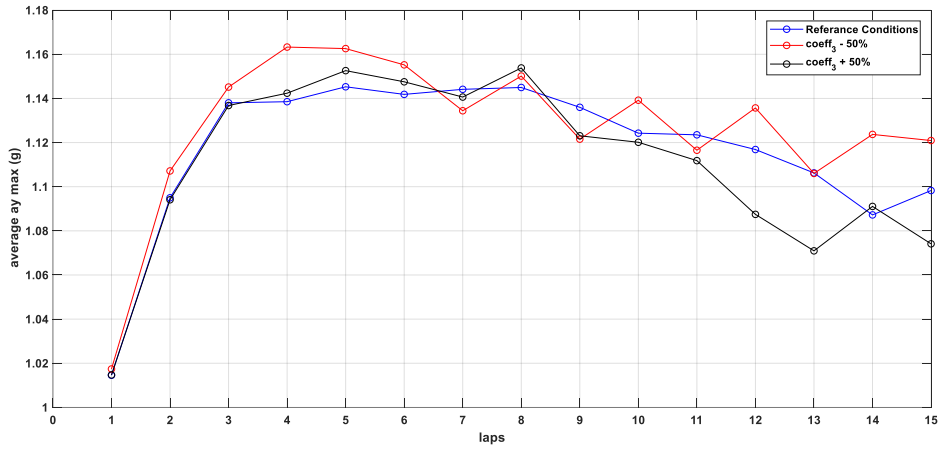

Figure 6.69 – Average max lateral acceleration compare (stiffness law coeff 3 effect)

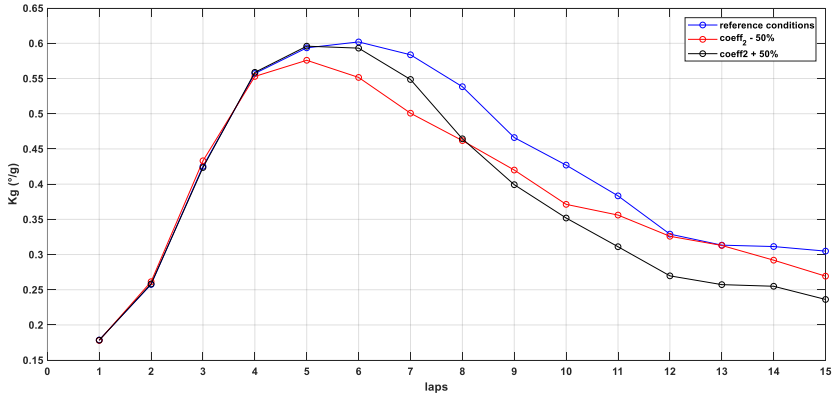

Figure 6.70 – Understeer Gradient compare (stiffness law coeff 3 effect)

The analysis shows the following results:

- the coefficient 3 represents the slope of the curve
- as coefficient 3 increases, performance deterioration is anticipated

6.5.6 MF-evo grip law effect

The effect of two coefficients governing the laws is studied (figure 6.71).

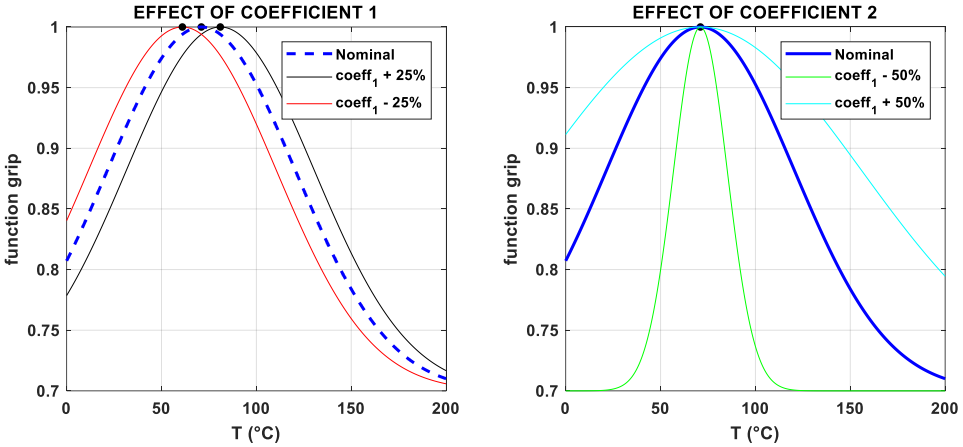

Figure 6.71 – Effect of coefficients on the function grip

Figure 6.72 shows the simulation results in terms of lap time.

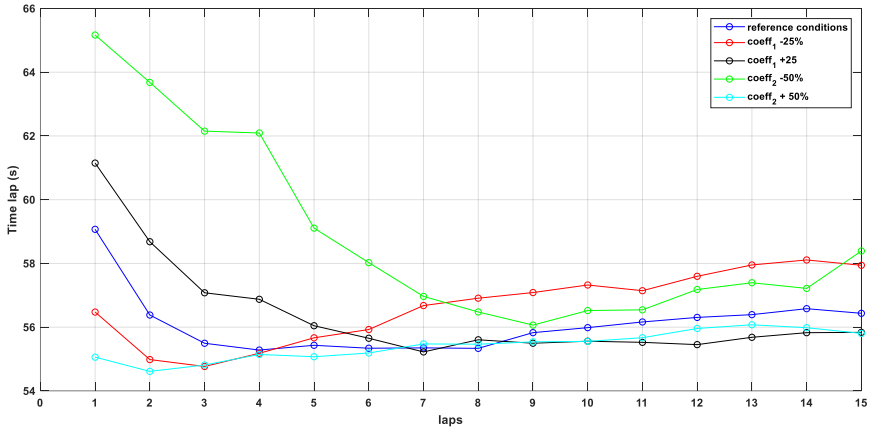

Figure 6.72 – Time laps for various grip coefficient 1

Figure 6.73 and 6.74 show the temperature trend, evaluated by 6.8 and 6.9, during the 15 laps while the figure 6.75 shows the inflation pressure trend.

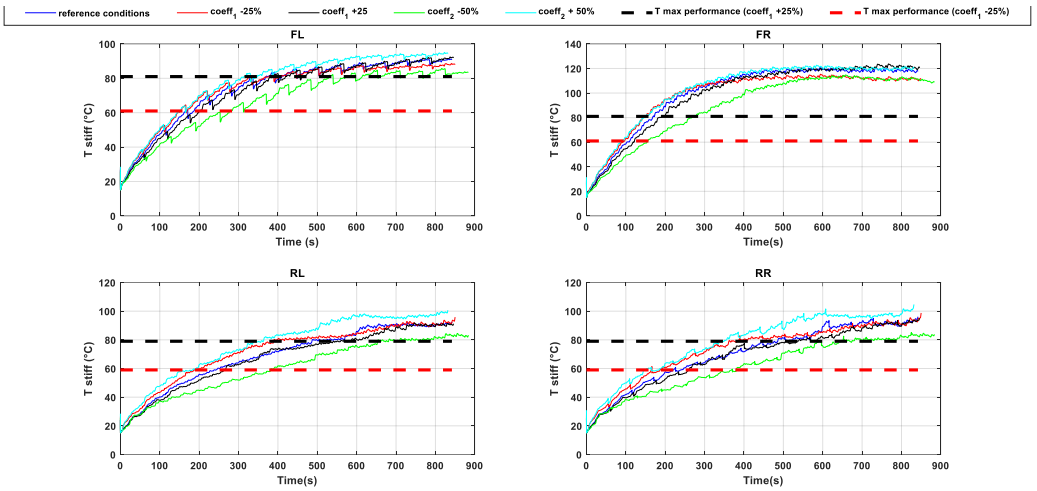

Figure 6.73 – Temperature stiff trend (grip law effect)

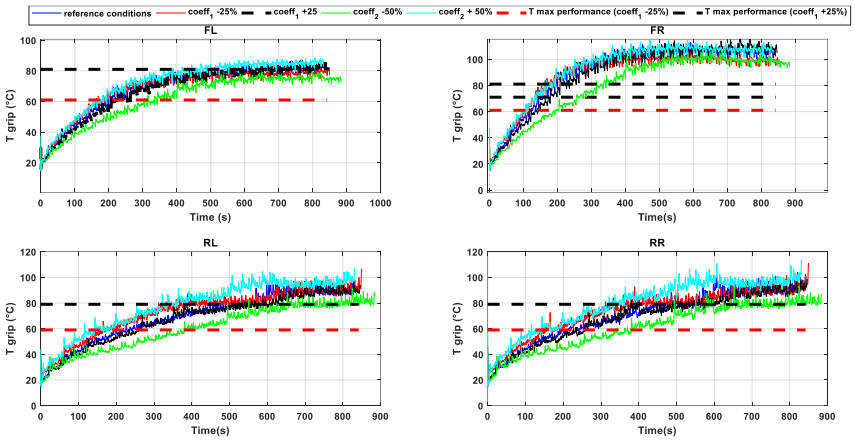

Figure 6.74 – Temperature grip trend (grip law effect)

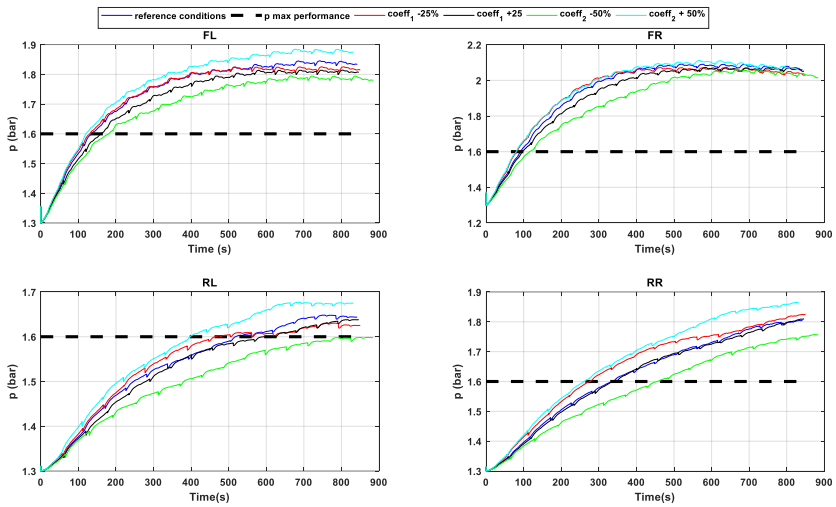

Figure 6.75 – Pressure trend (grip law effect)

Figure 6.76 shows comparison of lateral accelerations while figure 6.77 shows the comparison between the understeer gradient.

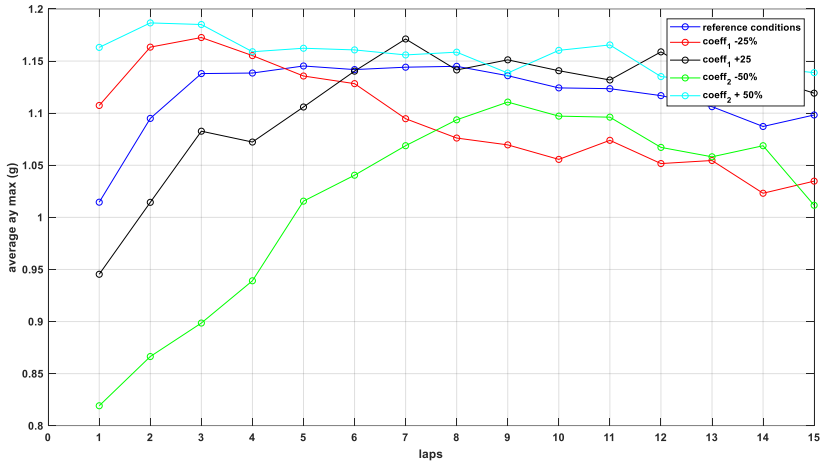

Figure 6.76 – Average max lateral acceleration compare (grip law effect)

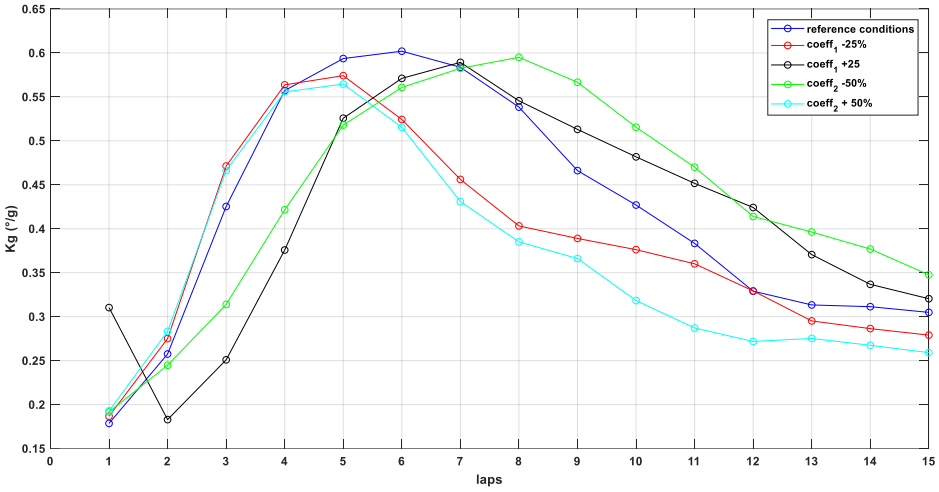

Figure 6.77 – Understeer Gradient compare (grip law effect)

- substantially the coefficient 1 represents the max performance temperature
- A lower T max performance allows you to reach the best lap time first
- if the thermal regime away from which temperature, you risk worsening performance too much
- as the coefficient 2 increases, the curve widens and the range of max performance increases

6.5.7 Road Temperature effect

The simulated road temperatures are:

- 15 °C
- 45 °C
- 65 °C

Figure 6.78 shows the simulation results in terms of lap time while the figure 6.79, 6.80 and 6.81 show the temperature (evaluated by 6.8 and 6.9) and pressure trend, during the 15 laps.

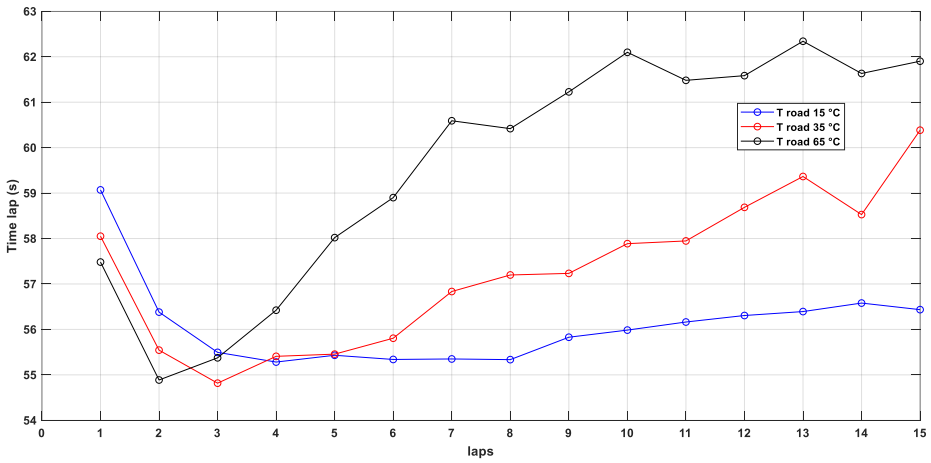

Figure 6.78 – Time laps for various road temperature

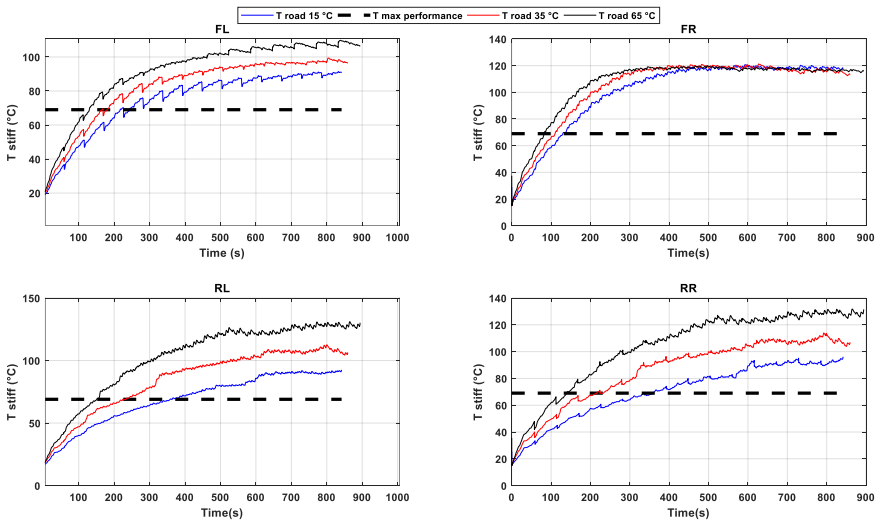

Figure 6.79 – Temperature stiff trend

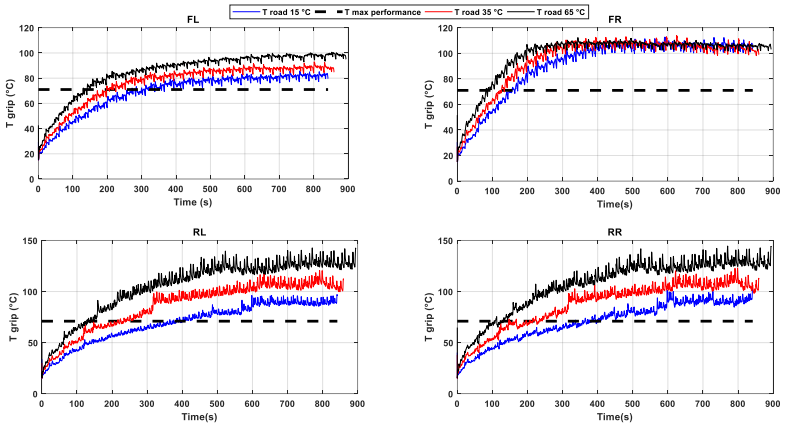

Figure 6.80 – Temperature grip trend

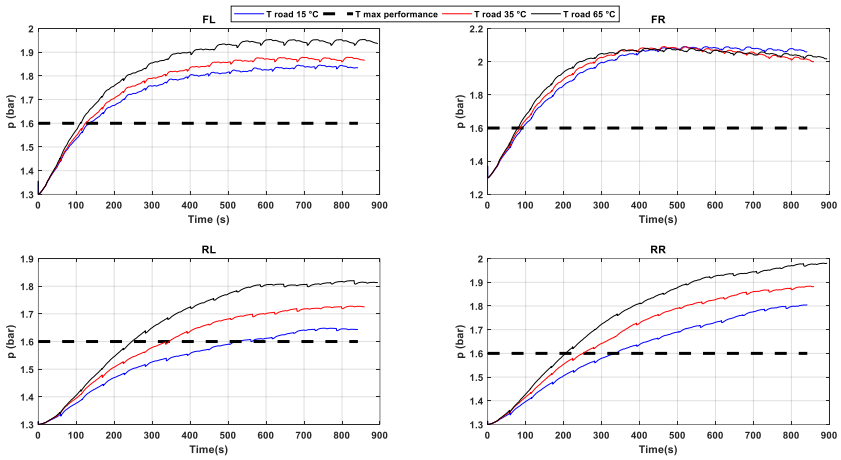

Figure 6.81 – Pressure trend (T road effect)

Figure 6.82 shows comparison of lateral accelerations while figure 6.83 shows the comparison between the understeer gradient.

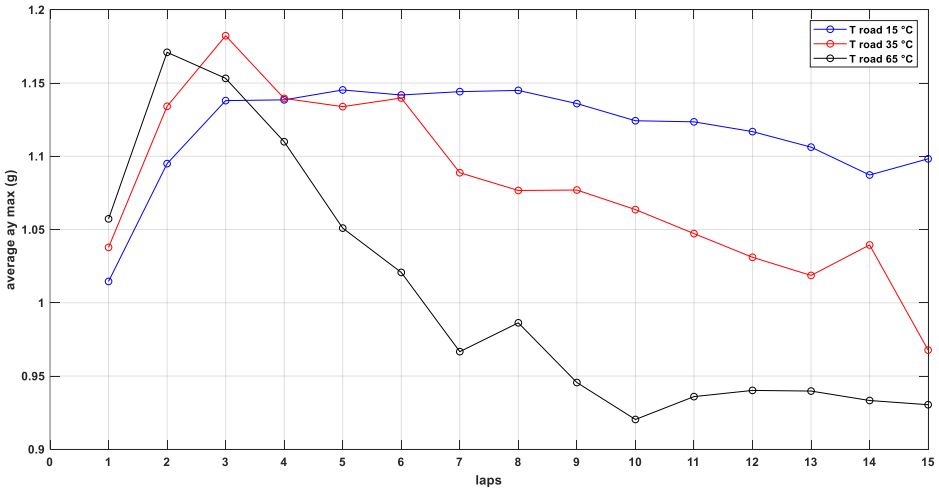

Figure 6.82 – Average max lateral acceleration compare (Temperature road effect)

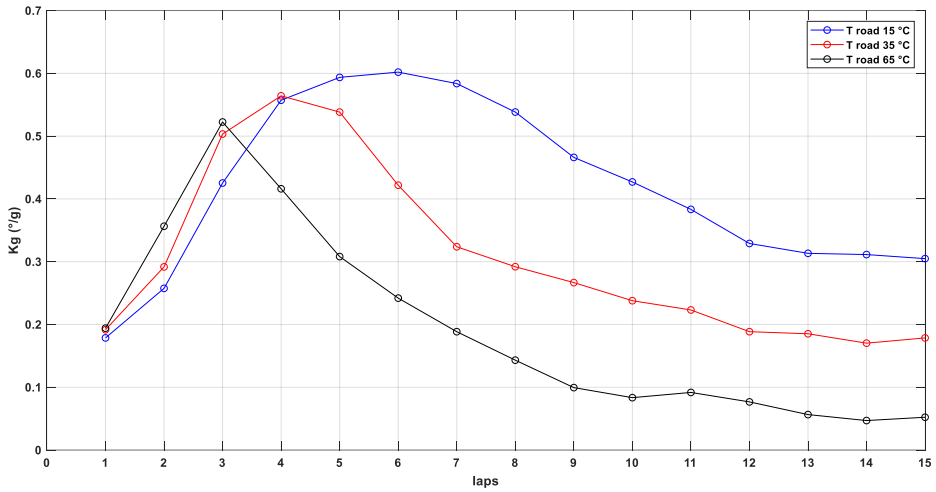

Figure 6.83 – Understeer Gradient compare (T road effect)

The analysis shows the following results:

- as the road temperature increases, the achievement of the max performance zone is anticipated
- as the asphalt temperature increases, the operating temperature increases with a consequent deterioration in performance

6.5.8 External temperature effect

The simulated external air temperature are:

- 15°C
- 35 °C
- 45 °C

Figure 6.84 shows the simulation results in terms of lap time.

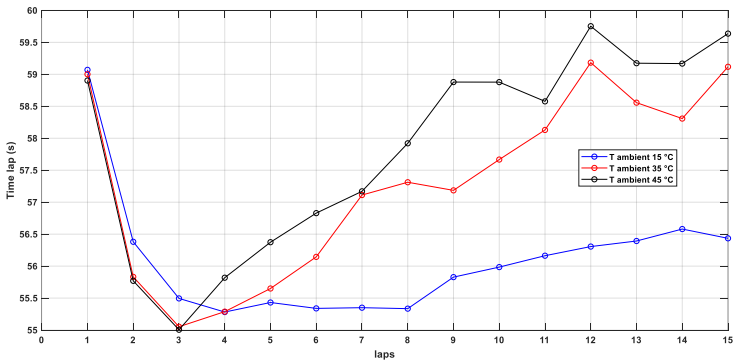

Figure 6.84 – Time laps for various ambient temperature

The figure 6.85, 6.86 and 6.87 show the temperature (evaluated by 6.8 and 6.9) and pressure trend, during the 15 laps.

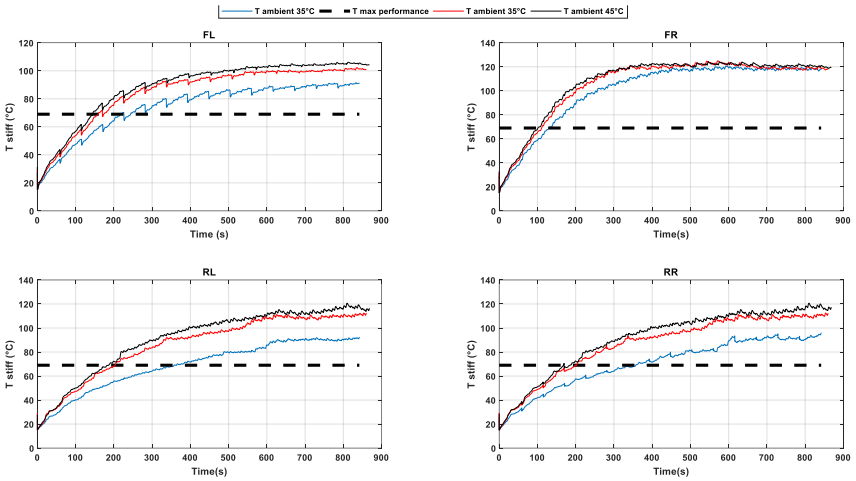

Figure 6.85 – Temperature stiff trend (T ambient effect)

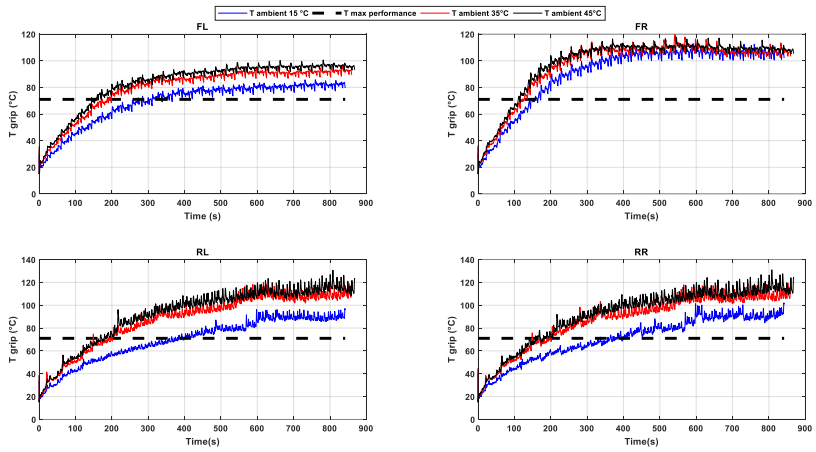

Figure 6.86 – Temperature grip trend

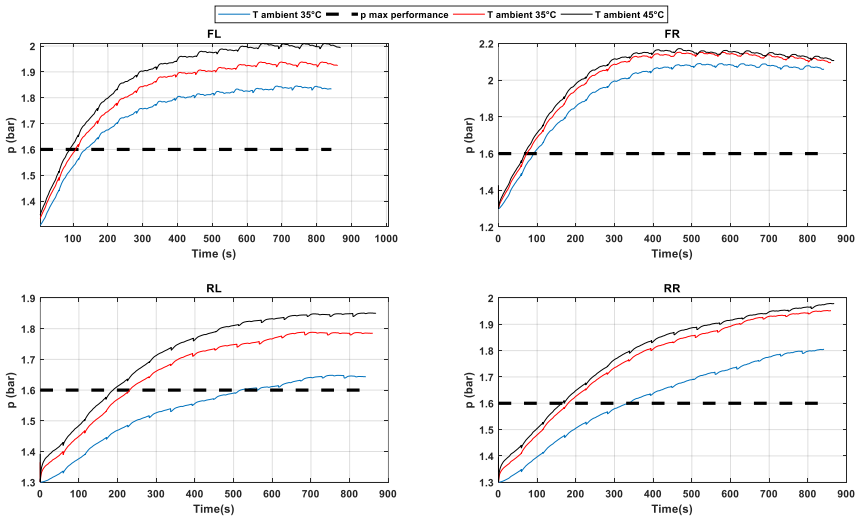

Figure 6.87 – Pressure trend (T ambient effect)

Figure 6.88 shows comparison of lateral accelerations while figure 6.89 shows the comparison between the understeer gradient.

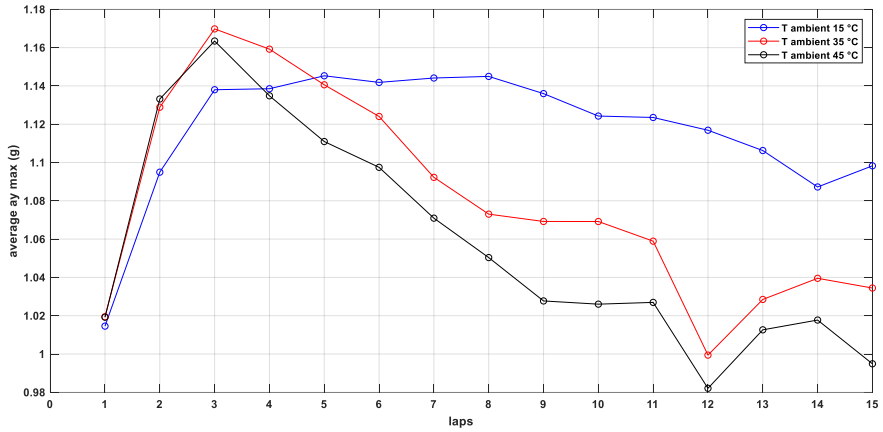

Figure 6.88 – Average max lateral acceleration compare (ambient temperature effect)

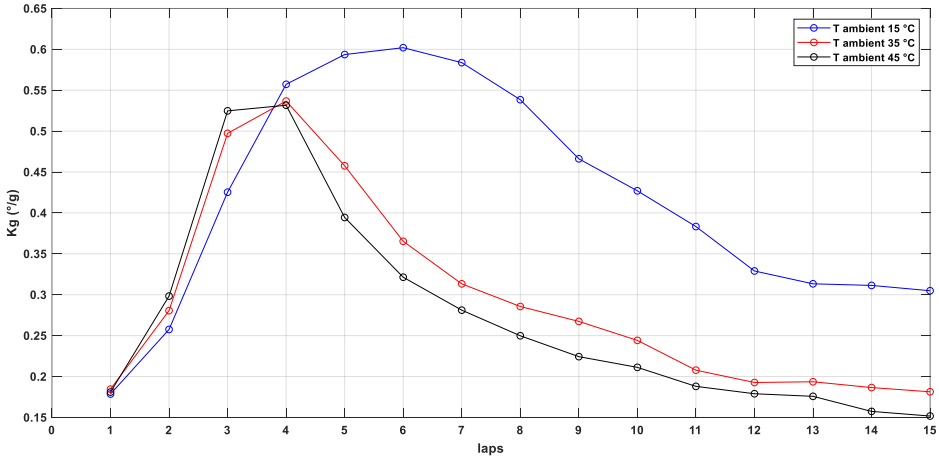

Figure 6.89 – Understeer Gradient compare (ambient temperature effect)

Similarly to the road temperature:

- as the ambient temperature increases, the achievement of the max performance zone is anticipated
- as the ambient temperature increases, the operating temperature increases with a consequent deterioration in performance

6.6 Conclusions

A sensitivity analysis of the influence of a series of quantities on the vehicle dynamic behaviour was conducted.

A series of parameters are considered:

- **Wear**
- **thermal conductivity of tread surface**
- **specific Heat of tread surface**
- **stiffness law of MF-evo**
- **grip law of MF-evo**
- **road temperature**
- **external temperature**

The work was carried out in collaboration with VI-grade which provides a simulation environment called VI-Car Real Time.

The simulations consisted of a series of laps on a track, then evaluating the response of the vehicle with the tyre temperature evolution.

For this purpose, a tyre model called Mf-evo has been implemented which considers the thermal effects in terms of stiffness (cornering and braking) and grip (longitudinal and lateral).

The comparison quantities taken into consideration were:

- Time laps
- Average of max lateral acceleration
- Understeer Gradient

The tool can be useful:

- to tyre makers to simulate the effect of changes made to tyres
- motorsport teams to simulate the various thermal conditions and choose the best configuration

The next steps will concern the introduction of the main effect of wear and therefore of the reduction in performance caused by it.

References

[1] M. Guiggiani, The Science of Vehicle Dynamics: Handling, Braking, and Ride of Road and Race Cars, Berlin, Germany : Springer Science & Business Media, 2014.

[2] H. Pacejka, Tire and Vehicle Dynamics, Elsevier, 2005.

[3] D. L. Milliken and W. F. Milliken, Race Car Vehicle Dynamics, Society of Automotive Engineers Warrendale, 1995.

[4] F. Farroni, Development of a Grip and Thermodynamics Sensitive Tyre/Road Interaction PhD Thesis, Università degli Studi di Napoli Federico II, 2014.

[5] J. D. Walter and A. N. Gent, The Pneumatic Tire, NHTSA, 2005.

[6] J. E. Mark, B. Erman and C. M. Roland, The Science and Technology of Rubber 4th ed, Academic Press, 2013.

[7] Y. Kirino and Y. Hara, "Environmental Compound Technology for Tyres," vol. 2012, no. 6, pp. 187-192, 2013.

[8] R. N. Jazar., Advanced Vehicle Dynamics, springer, 2019.

[9] R. N. Jazar, Vehicle Dynamics: Theory and Applications. 3rd ed., Springer, 2017.

[10] T. D. Gillespie, Fundamentals of Vehicle Dynamics, Society of Automotive Engineers, 1992.

[11] M. Meywerk, Vehicle Dynamics, Wiley, 2015.

[12] D. Schramm, R. Bardini and M. Hiller, Vehicle Dynamics: Modeling and Simulation, Springer, 2014.

[13] A. Sakhnevych, Multi-Physical Approach for Tyre Contact and Wear Mechanisms.PhD Thesis, Università degli Studi di Napoli Federico II, 2017.

[14] F. Calabrese , F. Farroni and F. Timpone, "A Flexible Ring Tyre Model for Normal Interaction," *Int. Rev. Modell. Simul,* vol. 6, no. 4, p. 1301–1306, 2013.

[15] H. B. Pacejka, Tyre and Vehicle Dynamics. 2nd ed. Butterworth-Heinemann, Elsevier, 2005.

[16] P. Dąbek and M. Trojnacki, "Requirements for Tire Models of the Lightweight," *Springer*, vol. 414, pp. 33-51, 2016.

[17] D. Ammon, "Vehicle Dynamics Analysis Tasks and Related Tyre Simulation Challenges," *International Journal of Vehicle Mechanics and Mobility*, vol. 43, no. 2005, pp. 30-47, 2011.

[18] E. Bakker, L. Nyborg and H. Pacejka, "Tyre Modelling for Use in Vehicle Dynamics," *SAE Technical Paper*, p. 870421, 1987.

[19] H. Dugoff, "Tire Performance Characteristics Affecting Vehicle Response to Steering and Inputs," Final report, 1969.

[20] M. Gipser, "FTire – the Tire Simulation Model for all Applications Related to Vehicle Dynamics.," *Vehicle System Dynamics*, vol. 45, pp. 139-151, 2007.

[21] G. Capone, D.Giordano, M.Russo, M.Terzo and F.Timpone, "Ph.An.Ty.M.H.A.: a Physical Analytical Tyre Model for Handling Analysis - the Normal Interaction," *Vehicle System Dynamics*, vol. 47, no. 1, pp. 15-27, 2009.

[22] D. Castagnetti, G. Scirè Mammano and E. Dragoni, "Elastostatic Contact Model of Rubber-Coated Truck Wheels Loaded to the Ground," *Proc. Inst. Mech. Eng. Part L*, vol. 222, pp. 245-257, 2008.

[23] F.Farroni, E.Rocca, R.Russo, S.Savino and F.Timpone, "Experimental Investigations about Adhesion Component of Friction Coefficient Dependence on Road Roughness Contact Pressure, Slide Velocity and Dry/Wet Conditions," in *mini Conference on vehicle system dynamics,identification and anomalies (VSDIA)*, 2012.

[24] F.Farroni, M. Russo, R. Russo and F. Timpone, "Tyre-Road Interaction: Experimental Investigations about the Friction Coefficient Dependence on Contact Pressure, Road Roughness, Slide Velocity and Temperature," in *ASME 11th Biennial Conference On Engineering Systems Design And Analysis (ESDA)*, 2012.

[25] H. Jrad, J. L. Dion, F. Renaud, I. Tawfiq and M. Haddar, "Experimental Characterization, Modeling and Parametric Identification of the Non Linear

Dynamic Behavior of Viscoelastic Components," *European Journal of Mechanics-A/Solids,* vol. 42, pp. 176-187, 2013.

[26] P. A. Smyth, Viscoelastic Behaviour of Articular Cartilage in Unconfined Compression, A Thesis Presented to The Academic Faculty, 2013.

[27] M. L. Williams, R. Robert F. Landel and J. D. Ferry, "The Temperature Dependence of Relaxation Mechanisms in Amorphous Polymers and Other Glass-forming Liquids," *Journal of the American Chemical Society ,* vol. 77, pp. 3701-3707, 1955.

[28] L. Rouleau, R. Pirk, PluymersB. and W. Desmet, "Characterization and Modeling of the Viscoelastic of a Self-Adhesive Rubber Using Dynamic Mechanical Analysis Test," *Journal of Aerospace Technology and Management,* vol. 7, pp. 200-208, 2015.

[29] B. Pawel, B. Paweł, G. Paweł and M. Jerzy, "Assessment of Mechanical Properties of Offroad Vehicle Tire: Coupons Testing and FE Model Development," *Acta Mechanica et Automatica,* vol. 6, 2012.

[30] A. Corollaro, Essentiality of Temperature Management while Modeling and Analyzing Tires Contact Forces, Ph.D. Thesis in ingegneria dei sistemi meccanici; università di Napoli Federico II, 2014.

[31] Y. J. Lin and S. J. Hwang, "Temperature Prediction of Rolling Tires by Computer Simulation," *Elsevier,* vol. 67, p. 235–249, 2004.

[32] L. Johnson, Contact Mechanics, Cambridge University Press, 1985.

[33] R. Agrawal, S. N. Saxena, G. Mathew, S. Thomas and B.K.Sharma, "Effective Thermal Conductivity of Three-Phase Styrene Butadiene Composites," *Journal of Applied Polymer Science,* vol. 76, p. 1799–1803, 2000.

[34] P. Dashora, "A Study of Variation of Thermal Conductivity of Elastomers with temperature," *Phisica Scripta,* vol. 49, pp. 611-614, 1994.

[35] A. Schallamach, "The velocity and Temperature Dependence of Rubber Friction," *Proceedings of the Physical Society,* vol. 66, no. 5, pp. 386-392, 1955.

[36] H. Kummer, "Unified Theory of Rubber and Tire Friction," in *Engineering Research Bulletin B-94,* The Pennsylvania State University College, 1966.

[37] B. N. J. Persson, “On the Theory of Rubber Friction,” *Surface Science,* vol. 401, no. 3, pp. 445-454, 1998.

[38] B. N. J. Persson, “Rubber Friction: Role of the Flash Temperature,” *Journal of Physics: Condensed Matter,* vol. 18, no. 32, 2006.

[39] T. Akasaka and S. Yamasaki, “Evaluation of Fundamental Spring Constants of Sidewall for Radial Tire,” *JARI research journal,* vol. 8, no. 10, pp. 1-10, 1986.

[40] J. Walter, “Centrifugal Effects in Inflated, Rotating Bias-Ply Tires,” *Texstile research journal,* vol. 40, no. 1, pp. 1-7, 1970.

[41] E. L. McPillan, *Improvements to a Two-Dimensional Model for Pneumatic and Non-Pneumatic Tires,* Thesis, Clemson University, 2017.

[42] Y. Nakajima, Advanced Tire Mechanics, Tokyo,: Springer, 2019.

[43] P. Hewson, “Method for Estimating Tyre Cornering Stiffness from Basic Tyre Information,” *Journal of Automobile Engineering,* vol. 219, no. 12, pp. 1407-1412, 2005.

[44] M. Mizuno, H. Sakai, K. Oyama and Y. Isomura, “Development of a Tyre Force Model Incorporating the Influence of the Tyre Surface Temperature,” *Vehicle System Dynamics,* vol. 43, pp. 395-402, 2005.

[45] K. B. Singh, “Vehicle Sideslip Angle Estimation Based on Tire Model Adaptation,” *Electronics,* vol. 8, no. 2, p. 199, 2019.

[46] S. Koskinen and P. Peussa, “Friction Final Report”, Technical Report No. FP6-IST-2004-4-027006,” European Union, Finland, Information Society Technologies (IST) Programme.

[47] G. Erdogan, L. Alexander. and R.Rajamani, “Estimation of Tire-Road Friction Coefficient Using a Novel Wireless Piezoelectric Tire Sensor,” *IEEE Sensors Journal,* vol. 11, no. 2, pp. 267-279, 2011.

[48] J. M. Bastiaan, *Design of a Smart Tire Sensor System,* Waterloo, Ontario, Canada,: thesis presented to the University of Waterloo, 2015.

[49] H. Lee and S.Taheri, “Intelligent Tires – a Review of Tire Characterization Literature,” *IEEE Intell Transp,* vol. 9, no. 2, pp. 114-135, 2017.

[50] K. Moona, H.Liang, J. Yi and B. Mika, “Tire Tread Deformation Sensor and Energy Harvester Development for “Smart Tire” Applications,” in *Proceedings*

of the Sensors and Smart Structures Technologies for Civil, Mechanical, and Aerospace System, San Diego, 2007.

[51] D. Garcia-Pozuelo, O. Olatunbosun, J.Yunta and et al, "A Novel Strain-Based Method to Estimate Tire Conditions Using Fuzzy Logic for Intelligent Tires," 2017.

[52] V. Magori, M. VR and S. N, "On-line Determination of Tire Deformation, a Novel Sensor Principle," in *Proceedings of the IEEE Ultrasonics Symposium*, Sendai, Japan, 1998.

[53] A. Tuononen, "Optical Position Detection to Measure Tyre carcass Deflections," *Veh Syst Dyn,* vol. 46, p. 471–481, 2008.

[54] Administration National Highway Traffic Safety, "Mechanics of Pneumatic Tires," United States Department of Transportation, Washington, 1981.

[55] R. Matsuzaki, T. Keating, A. Todoroki and N. Hiraoka, "Rubber-Based Strain Sensor Fabricated Using Photolithography for Intelligent Tires," *Sensors & Actuators A: Physical,* vol. 148, no. 1, pp. 1-9, 2008.

[56] M. Sallusti, *Analisi dei Segnali Accelerometrici Provenienti da uno Pneumatico Sensorizzato per l'Estrazione di Informazioni sulla Dinamica del Contatto,* Milano: Politecnico di Milano, 2014.

[57] R. Sidoti and M. Villa, *Lo pneumatico Come Sensore per il Controllo Attivo del Veicolo.,* Milano: Politecnico di Milano, 2009.

[58] L. Ariano and P. Bernardi, *Analisi ed Interpretazione dei Dati Provenienti da Sensori Inseriti nello Pneumatico per un suo Utilizzo Come Elemento Attivo per il Controllo del Veicolo.,* Milano: Tesi di laurea, Politecnico di Milano, 2005.

[59] N. Anania and M. Bettanin, *Analisi dei Segnali Provenienti da Sensori Posizionati all'interno dello Pneumatico: Riconoscimento di Condizioni Estreme e della Dinamica Laterale al Fine del Controllo Attivo del Veicolo,* Milano: Tesi di laurea, Politecnico di Milano, 2006.

[60] A. Caltaroni and P. Balordi, *Studio del Comportamento di Sensori Inseriti nello Pneumatico,* Milano: Tesi di laurea, Politecnico di Milano, 2003, 2003.

[61] A. Cosentino, *Handling Performance Control Trogh Tyre Optimal Inflation Pressure Assessed by Smart Tyre,* Milano: Tesi di laurea, Politecnico di Milano, 2017.

[62] M. Parini, *Ottimizzazione delle Procedure di Calibrazione per uno Pneumatico Smart Tyre,* Milano: Tesi di laurea, Politecnico di Milano, 2016.

[63] S. D. Val and A. Fantoni, *Utilizzo di un Approccio Statistico per la Stima di Forze di Contatto e Angolo di Camber Tramite uno Pneumatico Sensorizzato in Condizioni Stazionarie e di Transitorio,* Milano: Tesi di laurea, Politecnico di Milano, 2013., 2013.

[64] D. C. Montgomery and G. C. Runger, Applied Statistics and Probability for Engineers, 4th Edition, John Wiley & Sons Inc, 2006.

[65] M. Della Torre, *Stima delle Forze di Contatto e della Tessitura Stradale Attraverso Pneumatici Sensorizzati: Sviluppo degli Algoritmi di Elaborazione Dati e loro Appliapplicazione*, Milano: Tesi di laurea, Politecnico di Milano, 2015.

[66] F.Kreith, R. Manglik and M. Bohn, Principles of Heat Transfer, Cengage learning, 2012.

[67] S. Patankar, Numerical Heat Transfer and Fluid Flow, McGraw Hill, 1980.

[68] HISHAM A. Abdel-Aal, "On Heat Partition among Dry Sliding Anisotropic Solids," *The Annals of University "Dunarea de Jos" of Galati,* vol. 3, pp. 73-80, 2004.

[69] Allouis C., Amoresano A., Giordano D., Russo M. and Timpone F., "Measurement of the Thermal Diffusivity of a Tire Compound By Mean of Infrared Optical Technique," *International Review of Mechanical Engineering,* vol. 6, pp. 1089 - 1095, 2012.

[70] A. Corollaro, *Un Modello Termodinamico di Pneumatici da Competizione per Simulazioni Real Time in Impianti HIL,* Napoli: Master's thesis Università degli Studi di Napoli Federico II (Italian), 2012.

[71] Bosch, P., Ammon, D., and Klempau, F., "Tyre Models–Desire and Reality in Respect of Vehicle Development," *Darmstadter Reifenkolloquium,* vol. 17, p. 87–101, 2002.

[72] Putignano C., Le Rouzic J., Reddyhoff T., Carbone G. and Dini D., "A Theoretical and Experimental Study of Viscoelastic Rolling Contacts Incorporating Thermal Effects," *Journal of Engineering Tribology,* vol. 228, no. 10, p. 1112–1121, 2014.

[73] F. Farroni, Sakhnevych A. and F. Timpone, "Development of a Grip and Thermodynamics Sensitive Procedure for the Determination of Tyre/Road Interaction Curves Based on Outdoor Test Sessions," in *In Proceedings of the 4th International tyre colloquium: tyre models for vehicle dynamics analysis*, 2015.

[74] Ebbott T., Hohman R., Jeusette J. and Kerchman V., "Tire Temperature and Rolling Resistance Prediction With Finite Element Analysis," *Tire Science and Technology,* vol. 27, no. 1, pp. 2-21, 1999.

[75] Neale A., Derome D., Blocken B. and Carmeliet J., "Determination of Surface Convective Heat Transfer Coefficients by Cfd," in *11th Canadian Conference on Building Science and Technology Banff,* Alberta, 2007.

[76] Ozerdem B., "Measurement of Convective Heat Transfer Coefficient for a Horizontal Cylinder Rotating in Quiescent Air," *Int. Comm. Heat Mass transfer,* vol. 27, no. 3, pp. 389-395, 2000.

[77] B.S.Petukhov, "Heat Transfer and Friction in Turbulent Pipe Flow with Variable Physical Properties," *Advances in Heat Transfer,* vol. 6, pp. 503-564, 1970.

[78] H. B. Pacejka and I. J. M. Besselink, "Magic Formula Tyre Model With Transient Properties," *Vehicle System Dynamics,* 1997.

[79] E. Bakker, L. Nyborg and H. B. Pacejka, "Tyre Modelling for Use in Vehicle Dynamics Studies," *SAE Technical Papers,* 1987.

[80] I. J. M. Besselink, A. J. C. Schmeitz and H. B. Pacejka, "An improved Magic Formula/Swift tyre model that can handle inflation pressure changes," *Vehicle System Dynamics,* 2010.

[81] D. Arosio, F. Braghin, F. Cheli and E. Sabbioni, "Identification of Pacejka's Scaling Factors From Full-Scale Experimental Tests," *Veh. Syst. Dyn,* 2005.

[82] K. Anupam, S. Srirangam, A. Scarpas and C. Kasbergen, “Influence of Temperature on Tire–Pavement Friction: Analyses,” *Transportation Research Record,* vol. 2369, no. 1, pp. 114-124, 2013.

[83] E. Kasprzak, K. Lewis and D. Milliken, “Inflation Pressure Effects in the Nondimensional Tire Model,” *SAE International,* 2006.

[84] S. Kanwar and S. Srikanth, “An Adaptive Tire Model for Enhanced Vehicle Control Systems,” *SAE International Journal of Passenger Cars - Mechanical Systems,* 2015.

[85] Vi-Grade, *VI-CarRealTime 19.0 Documentation,* 2019.

[86] Vi-Grade, *Vi car real time 2019 https://www.vi-grade.com/en/products/vi-carrealtime/,* 2019.

[87] J. Segers, Analysis Techniques for Racecar Data Acquisition, Second Edition, SAE international, 2008.